Developing Advanced Shape Sensing Methodologies for Aerospace Applications

Politecnico di Torino

ScuDo
Scuola di Dottorato ~ Doctoral School
WHAT YOU ARE, TAKES YOU FAR

Doctoral Dissertation
Doctoral Program in Aerospace Engineering (34^{th}cycle)

Developing Advanced Shape Sensing Methodologies for Aerospace Applications

By

Rinto Roy

******

Supervisor(s):
Prof. Cecilia Surace, Supervisor
Prof. Marco Gherlone, Co-Supervisor

Doctoral Examination Committee:
Prof. C. Sbarufatti, Referee, Politecnico di Milano, Italy
Prof. S. Sorohan , Referee, Politehnica University of Bucharest, Romania

Politecnico di Torino
2022

Declaration

I hereby declare that, the contents and organization of this dissertation constitute my own original work and does not compromise in any way the rights of third parties, including those relating to the security of personal data.

Rinto Roy
2022

* This dissertation is presented in partial fulfillment of the requirements for **Ph.D. degree** in the Graduate School of Politecnico di Torino (ScuDo).

I would like to dedicate this thesis to my family for being a constant source of support and much-needed distraction during difficult times.

Acknowledgements

I would like to express my sincere gratitude to my supervisors, Prof. Cecilia Surace and Prof. Marco Gherlone, for their constant support and guidance over the past three years.

I also wish to thank Dr. Massimiliano Mattone, Eng. Marco Esposito, and Eng. Mariana Rodriguez for their help and support during the experimental activities.

Abstract

Inspection and maintenance operations are essential for the long-term operation of current and future aircraft structures, ensuring health, safety, and optimal performance. Structural Health Monitoring (SHM) systems have facilitated real-time monitoring and condition-based maintenance solutions, resulting in improved inspection efficiency and safety, and lower cost and human effort. Despite widespread SHM research, practical adoption has been limited due to the complexity of industrial structures, influence of the operational environment, high sensor requirement, etc. Developing advanced monitoring strategies to address these challenges forms the central aim of the work done.

The developmental effort is centred on the inverse Finite Element Method (iFEM), a variationally-based shape sensing approach that solves the inverse problem of reconstructing structural displacements from measured surface strains. iFEM's inherent independence of the structure's material properties and loading conditions, combined with its accuracy and robustness in producing results using a sparse set of sensors, makes it an appealing solution for the displacement, strain, or stress monitoring of future aerospace vehicles. Both 1D iFEM, for beams and frames, and 2D iFEM, for plates and shells, have been proposed in literature. The present work focuses on further development of these existing formulations to bridge the gap towards their practical adoption.

The formulation of novel 1D inverse beam elements for analysing complex aerospace structures constitutes the primary part of the work done. The complexities modelled include an accurate treatment of transverse shear and torsional deformation for beams with any general cross-section. This is achieved by introducing certain shear coefficients and functions that reconcile the cross-sectional variation of transverse shear strain with classical 1D beam theories. Numerical and experimental validation of these novel beam elements is also presented, where accuracy, robustness, and practical feasibility are discussed. An additional novelty of the work done is the experimental investigation of additively manufactured beam specimens, constituting a first of its kind in shape sensing literature. The new beam elements developed are further adapted to model thin-walled beams undergoing cross-sectional warping, necessitating an update to the interpolation order of torsional rotation within an element. The element so-developed is also validated numerically.

This work also addresses certain key limitations of the 2D iFEM: the large number of sensors required and their optimal locations to generate accurate shape-sensing results. The proposed solution involves designing simple and easily reproducible strain-sensor patterns that guarantee stable and accurate iFEM predictions. These patterns are further coupled with virtual strain expansion strategies to reduce sensor quantity. The lessons learned from the above two approaches are subsequently used to develop an efficient iFEM-based damage detection strategy for SHM applications. As both 1D and 2D iFEM have been demonstrated to be effective monitoring strategies, work also focused on maximising their benefits and minimising their limitations by developing a Multi-Resolution monitoring approach. This concept marries the low cost (sensor and computational), low-fidelity results of the 1D iFEM with the high cost and high fidelity results of 2D iFEM to create an optimised monitoring framework. This new approach is demonstrated numerically for the damage detection of a complex wing box structure, revealing the 1D iFEM as an effective tool for damage detection and 2D iFEM for damage localisation.

The iFEM-based monitoring strategies developed in this work can also be instrumental for the operation of the next generation of shape morphing structures. This work also lays the foundation for this research by developing an iFEM-based closed-loop control architecture for monitoring and controlling morphing structures instrumented with a limited number of actuators and under the effect of unknown external loads.

Contents

List of Figures

List of Tables

Chapter 1

Introduction

Over their operational life, aerospace structures can experience a depreciation in structural health, leading to reduced performance and poor levels of safety. In the case of aircraft, this loss of health can be due to component failure, wear, projectile impacts, fatigue damage, corrosion, etc. The latter two phenomena are especially relevant for ageing aircraft or those used beyond their design life. Hence, inspection and maintenance operations gain importance as aircraft age increases and contribute to a significant portion of its lifecycle cost (LCC) [1].

Existing aircraft inspections are primarily restricted to on-ground visual, eddy-current or ultrasonic inspections, commonly referred to as non-destructive testing (NDT). These inspections are performed periodically when the aircraft is removed from service and subjected to inspection after certain flight hours. As no information regarding the actual health condition of the structure is available prior to inspections, these methods are highly conservative and inefficient, incurring high costs and human effort. In contrast, strategies that prescribe maintenance operations based on the real-time health of the structure can improve inspection efficiency, aircraft safety, and reduce maintenance costs and efforts.

Recent developments in sensor technologies and data processing have facilitated integration between the health monitoring system and the structure. Sensors instrumented on the structure can be used to provide a real-time assessment of the structural integrity under various operational conditions. This approach, referred to as Structural Health Monitoring (SHM), facilitates a shift from a scheduled to a condition-based maintenance philosophy, reducing human effort and costs and improving overall structural safety. SHM has been identified as a key technology for developing advanced diagnostic and prognostic systems for the health management of future aerospace (e.g., aircraft, reusable launch vehicles), civil (e.g., buildings, bridges), and marine (e.g., offshore wind turbines) structures [2–4].

A wide spectrum of SHM methodologies has been proposed in scientific literature [5], with the primary approach to damage detection being a comparison between the damaged and healthy state of the structure. This comparison involves certain damage-sensitive mechanical features based on the structure's modal parameters, strain, stress, etc. Despite the immense quantity of research over the past few decades, the technologies developed have found very limited applicability in industrial structures. They are in direct contrast to condition-based monitoring (CBM) techniques that have been widely used for rotorcraft monitoring. Some of the main challenges facing the practical adoption of SHM are [6]:

- Complex structural geometries encountered in practical applications;
- A large number of sensors are required for monitoring large structural areas;
- Reliability of the method under environmental factors and measurement noise;
- Characterisation of damage detection and false alarm generation.

In the face of these challenges, *shape sensing* techniques offer a unique pathway to developing robust and efficient monitoring strategies. Shape sensing is defined as the inverse problem of reconstructing the deformed shape of the structure using surface strain measurements. As this constitutes an inverse problem, uniqueness, existence, and stability conditions are not necessarily satisfied. However, a wide array of approaches based on strain integration, basis functions, variational formulation, and neural networks have been developed to solve this problem [7]. As they can facilitate the development of monitoring strategies independent of the material properties or operational conditions of the structure, shape sensing has been identified to play a key role in real-time displacement, strain, or stress monitoring of future aerospace vehicles [8].

The application of shape sensing-based monitoring solutions is not limited to SHM alone. Another key domain is that of morphing structures, where recent advances have led to the development of structures whose form obeys its function [9]. Applications in the aerospace domain include morphing wing aircraft [10, 11], that use integrated sensors and actuators (e.g., shape memory alloys (SMA), piezoelectric sensors, etc.) to perform drastically different functions over a wide range of flight conditions [12]. Despite these advances, the future adoption of morphing structures is dependent on the development of certain key technologies [12, 13]:

- Small and efficient actuators for shape or state change;
- Monitoring and control algorithms to integrate sensors and actuators.

Shape sensing techniques present a unique solution to these problems. The reconstructed displacement field can be used as feedback for developing efficient control strategies that allow for real-time monitoring and control of structural shape.

Based on these discussions, the aim of the present work can be condensed into the following statement: *the development of advanced shape sensing methodologies addressing the existing challenges and meeting the requirements of future SHM*

systems and shape morphing structures. These objectives are addressed in the present work by focusing on the development of a particular shape sensing methodology: the inverse Finite Element Method (iFEM) [14]. iFEM is a variationally-based approach that solves for the displacement field by minimising an error functional defined as the least-squares error between analytical and experimentally measured strains. As it is based on the strain-displacement relations, it is inherently independent of the material properties and loading conditions of the structure and can provide accurate and robust results even using a sparse set of strain data [15]. These features make it a favourable choice compared to other competing shape sensing approaches.

Within the context of the objectives outlined previously and the capability of existing iFEM formulations to meet these requirements, the areas for further development can be deduced and are stated below:

- Development of advanced iFEM formulations for monitoring aerospace structures with complex geometries;
- Investigation of optimal sensor placement or identification of efficient sensor patterns ensuring reliable iFEM predictions;
- Application of iFEM solutions for developing robust and accurate damage detection and localisation strategies;
- Development of an iFEM-based control architecture for morphing structures.

Each chapter of this thesis is devoted to addressing one of these aims. For clarity, the basic structure of the thesis is outlined below. It begins with a survey of existing literature at the end of Chapter 1. The merits and limitations of the various shape sensing methodologies are presented, and existing applications to relevant problems in the aerospace sector are discussed. These discussions help outline the limitations of existing iFEM formulations and serve as the basis for identifying the main aims of the current work. A comprehensive discussion of the theory behind both 1D and 2D iFEM formulations is given in Chapter 2. The main theoretical contributions of this work are described in this chapter, where the limitations of existing inverse beam elements are discussed, and subsequent reformulations to handle greater geometrical complexity are presented.

Chapters 3 and 4 present the numerical validation of the new beam element formulations and an application-oriented investigation of plate shape sensing, respectively. The preliminary results of Chapter 3 are further corroborated in Chapter 5 using results from multiple experimental tests on beam specimens. Inspired from previous discussions, Chapter 6 presents a novel iFEM-based framework for controlling shape morphing structures, laying the foundation for future investigations on the topic. Finally, Chapter 7 summarises the work done and elucidates the main contributions and achievements.

The work discussed in this thesis has also resulted in the following journal and international conference publications:

- Roy, R., Gherlone, M., Surace, C.: Damage localisation in thin plates using the inverse finite element method. In Proceedings of the 13th Int. Conference on Damage Assessment of Structures, Lecture Notes in Mechanical Engineering; Springer: Singapore, 2020 [16]
- Roy, R., Gherlone, M., Surace, C.: Shape sensing of beams with complex cross sections using the inverse finite element method. In Proceeding of 12th Int. Workshop on Structural Health Monitoring, Stanford, CA, 2019 [17]
- Roy, R., Tessler, A., Surace, C., Gherlone, M.: Shape Sensing of Plate Structures Using the Inverse Finite Element Method: Investigation of Efficient Strain–Sensor Patterns. Sensors 2020, 20, 7049 [18]
- Roy, R., Gherlone, M, Surace, C.: A shape sensing methodology for beams with generic cross-sections: Application to airfoil beams. Aer. Sci. and Tech. 2021, 110, 106484 [19]
- Roy, R., Gherlone, M., Surace, C., Tessler, A.: Full-Field Strain Reconstruction Using Uniaxial Strain Measurements: Application to Damage Detection. Appl. Sci. 2021, 11, 1681 [20]

These references are not cited any further in this thesis to avoid any disruptions to the clear and organic discussion of the work done.

1.1 Literature Review

1.1.1 Structural Health Monitoring

The philosophy underlying SHM-based damage detection is a comparison between the structure's damaged and baseline healthy state. This is achieved by analysing data from sensors instrumented on the structure to obtain mechanical features sensitive to damage presence and location.

Among the SHM methodologies developed in literature, the majority are based on analysing changes in the modal parameters of the structure [5]. These investigations were pioneered by Cawley et al. [21, 22], where changes in the natural frequencies or mode shapes are used to infer damage presence and location. As modal parameters capture the health state of the entire structure, these methods can be categorised as a global, rather than local, monitoring strategy. Modal parameters can also be used as part of a numerical model updating problem to localise the precise damage location [23]. A key limitation of this approach is the sensitivity of modal parameters to the operational conditions of the structure and environmental factors such as temperature, humidity, etc. Recent research has focused on filtering the operational and environmental influences from changes produced by the damage using data-normalization procedures based on look-up tables, regression models, machine learning, etc. [24].

Analysing changes in the structural mode shapes is also a powerful damage predictor. Specifically, discontinuities in the corresponding rotation or curvature fields (i.e., the first or second derivative of the displacements) are good indicators of damage. Such techniques have also received wide attention and have been developed for one-dimensional (1D) beams or frames [25, 26], and two-dimensional (2D) plate [27, 28] structures. Additional limitations here are the large number of sensors required for a refined prediction of the vibrational mode shapes and the high sensitivity of displacement derivatives to the influence of measurement noise. Optical-based techniques or Scanning Laser Doppler Vibrometers for measuring the mode shapes can alleviate these problems to a certain extent.

Other measurable mechanical features that are sensitive to damage are the strains or displacements of the structure. In contrast to approaches based on modal parameters, these features assess the static behaviour of the structure and constitute a local, rather than a global, monitoring approach. They can be categorised as direct, where the measured strain or displacement field is analysed for any violations in the structure's compatibility or governing differential equations [29, 30], or inverse, where an objective function formulated in terms of the damage parameters is minimised and solved using the measurements [31]. These methods often require a large number of sensors and are capable of monitoring small, highly localised areas of the structure.

Advancements in fibre optics (like fibre Bragg gratings (FBG) or distributed fibre optic strain sensors (FOSS)) have made them an ideal sensor choice for long-term structural monitoring applications [32]. Features such as small size, resistance to external influences (electromagnetic or environmental), reliability, and large measurement density have meant that their adoption is only expected to increase over the coming years. They have been widely applied to monitor bridges, tunnels [33], and offshore wind turbine structures [34]. Applicability in the aerospace sector is augmented by the possibility of embedding fibre cables within structures, as illustrated by their use for monitoring inflatable space habitats [35] and composite aircraft wing box structures [36, 37].

This section provided a brief review of some of the main developments and approaches to SHM. For a more detailed introduction to the topic, interested readers are encouraged to refer to Ref. [5, 24].

1.1.2 Morphing Structure Actuation & Control

The development of shape morphing structures has received wide attention over the past few decades, with designs and control strategies often specific to the intended application [9, 11, 12, 38]. In the case of aircraft, the shape change can be on a large scale, where aircraft wing or planform area changes, or on a smaller scale, with changes in the wing sweep or cross-section (e.g., airfoil camber) [12]. Common

design and control approaches are discussed here to contrast existing work and novelties presented in the current work.

Some of the most common approaches to aircraft wing morphing are related to changes in wing camber. This shape change is often achieved using kinematic rigid link mechanisms actuated by electromechanical actuators [39–41]. The popularity of these designs is explained by the need to meet industrial standards and safety requirements. Such designs have been demonstrated for the wing flap control of civil aircraft, where the control scheme uses encoders to measure the relative rotation between links to assess the wing shape [39]. Alternate control approaches include using FBG-based strain measurements related to the bending and torsional deformations of the wing using transfer functions obtained from a priori experimental tests [40]. Morphing leading-edge wing designs for variable cruise and take-off or landing performance have also been designed [41], and shape control can also be achieved using surface instrumented accelerometer sensors coupled with a linear aeroelastic model of the structure [42].

Other actuation alternatives include piezoelectric or shape memory alloy (SMA) actuators that require more compliant wing designs due to the lower actuation force generated. Such an SMA-based airfoil design relied on a fuzzy logic-based proportional-integral-derivative (PID) controller (with pressure sensors as feedback) for controlling flow separation over the airfoil surface [43]. Piezoelectric actuators have also been used to develop a distributed trailing edge morphing concept for load alleviation and flutter suppression [44]. The use of SMA wires has been demonstrated to be effective in controlling the leading edge shape of an aircraft chevron for achieving subsonic engine noise reduction [45].

With the growing popularity of machine learning in recent decades, reinforcement learning has also emerged as a leading candidate for developing efficient control systems for the next generation of morphing structures [46].

1.1.3 Shape Sensing

Shape sensing refers to the inverse problem of reconstructing the displacement field of a structure using strain measurements from surface-mounted sensors. Depending on their approach, existing shape sensing methodologies can be sorted into four main categories as those based on [7]: integration of experimental strain measurements, displacement field modelling using basis functions or mode shapes, neural networks, and using a finite element-based variational principle. These approaches are discussed separately below.

Ko et al. [47] developed a strain integration-based shape sensing strategy using the classical beam theory, where transverse deflection and bending rotations are reconstructed at beam sections instrumented with sensors. The use of either

one or multiple sensing lines facilitated the reconstruction of torsional rotation as well, and the capabilities of this theory were demonstrated on a complex wing box structure [48]. Xu et al. [49] proposed further development of these 1D theories to analyse thin-walled beams undergoing cross-sectional warping. Integration-based approaches have also been developed for plate structures [50] and applied for monitoring shape morphing beams [51]. Their feasibility for future aeroelastic shape control was studied experimentally using cantilevered beams and plates instrumented with distributed fibre optic sensors [52]. As these approaches are based on the numerical integration of measured strains, the large number of measurements required for accurate predictions is an inherent limitation.

Methods modelling the strain or displacement fields as a weighted superposition of an a priori choice of basis functions have also received a wide range of interest [53–55]. The basis functions chosen can be a piecewise polynomial, with varying degrees of continuity enforced [56], or the vibrational mode shapes of the structure [57–59]. In the case of mode shapes, they can be estimated experimentally [57, 60, 61], using an experimental modal analysis of the structure, or extracted from high-fidelity numerical FEM models [58, 59]. They have found applications in monitoring rotating machinery, like a wind turbine tower [62, 63], and for aeroelastic shape sensing of an aircraft wing [64]. For an interesting comparison between integration and basis function-based methods for the experimental shape sensing of a swept-wing plate, refer Ref. [65]. A limitation of this approach is that the number and type of basis functions used can influence the results. When using mode shapes, there is the additional need for evaluating modal information a priori, requiring either experimental data or an accurate numerical model of the structure.

The literature on the use of neural networks for shape sensing is limited. The most prominent work is of Bruno et al. [66], where shape control of the backup truss structure for space-borne telescopes or antennas was investigated. Neural networks were used to relate strain measurements from an incomplete set of truss members to the deformed shape of the whole structure. In this case, neural net training is the most computationally intensive part of the method, with the amount and type of training data influencing the final results obtained.

A final approach to shape sensing, and the one most relevant to the current work, is based on a variational principle. Work on this topic was pioneered by Tessler and Spangler [67, 15], who developed a variational formulation for the displacement reconstruction of plates and shells. The method so developed, called the inverse Finite Element Method (iFEM), is reviewed in more detail in the next section. Interested readers are encouraged to refer to Gherlone et al. [7] for a performance comparison between the various shape sensing methodologies described above.

1.1.4 inverse Finite Element Method

iFEM is a variationally-based approach where the structural domain is discretised using finite elements. The displacement field is reconstructed by minimising an error functional described as the least-squares error between analytical and experimentally measured strains [67, 15]. These analytical strains are computed by interpolating the nodal degrees-of-freedom (DOF) using element shape functions, similar to the direct FEM, and applying the linear strain-displacement relations. Minimization of the error functional leads to a set of linear algebraic equations that can be solved to obtain the reconstructed nodal displacements of the structure. Existing iFEM formulations can broadly be classified into: 1D iFEM for beams or frames, and 2D iFEM for plates or shells.

Initial research began with the development of 2D inverse elements, the first being the three-node constant strain shell element, iMIN3, developed by Tessler et al. [14]. The element is based on Mindlin theory [68] and uses C^0-continuous anisoparametric shape functions [69], leading to improved treatment of transverse shear in the thin plate regime. Additional higher-order elements were subsequently developed by Kefal et al. [70, 71], such as the four-node quadrilateral shell element named iQS4 [70], featuring anisoparametric interpolations [72] and an additional drilling degree-of-freedom, and the eight-node curved shell element named iCS8 [71].

Research on 1D iFEM also progressed in parallel, with Gherlone et al. [73] leading the development of 1D inverse elements for the shape sensing of beam and frame structures. The beam elements are based on Timoshenko beam theory, with the error functional defined as the least-squares error between analytical and experimental sectional strains of the beam. These sectional strains represent the axial, bending, transverse shear, and torsional deformation of a beam section. The new inverse beam elements developed were demonstrated to be effective for the static and dynamic shape sensing of beams with simple cross-sections (e.g., circular). Later adaptations involve using isogeometric analysis for modelling variable section beams [74] and complex loading scenarios [75]. Beam elements based on Euler-Bernoulli beam theory have also been proposed [76], including the enhanced formulation of You et al. [77] guaranteeing robust non-singular solutions. Similarly, elements have also been developed for monitoring composite beams based on refined zig-zag theory (RZT) theory [78], curved beams [79], and beams undergoing material non-linearities [80].

Another interesting development is for structures undergoing large non-linear displacements. Paczkowski et al. [81] extended Tessler's initial formulation to model large displacement and non-linear strains using an error functional based on the Green-Lagrange strain measures. An alternate strategy based on an incremental iFEM approach was proposed by Tessler et al. [82] for plate or shell structures

and is equally applicable for beams as well. Although the author contributed to this work [82], it is not mentioned further in the present report to avoid diverting attention from the main focus of the thesis. Other works in this area have also led to the development of non-linear membrane finite elements for the shape sensing and load-reconstruction of membrane wings [83, 84].

The 1D and 2D iFEM methods developed have been subject to various numerical and experimental applications. Experimental investigations of the 1D iFEM include the shape sensing of a circular beam [85] and the real-time monitoring of a radio telescope reflector using FBG sensors [86].

A wider array of experimental investigations are available for the 2D iFEM, including the shape sensing of a wing-shaped plate [7], deformation and internal load monitoring of a test wing [87], shape sensing of a wing-shaped sandwich structure using embedded and surface mounted strain sensors [88], stiffened panel instrumented with fibre optic sensors [89], etc. Numerical investigations include those on a composite stiffened panel [90], composite wing box [91], stress monitoring of a Panamax container ship [92], and bulk carriers [93]. Numerical efforts have also been made to quantify the effects of measurement and material uncertainties [94].

Recent focus has also been directed to the use of iFEM for SHM applications [95]. Notable works include crack detection in beams using fibre optic sensors [96, 97], the definition of a load-adaptive baseline for structural damage identification in thin plates [98], damage monitoring in offshore wind turbine structures [99, 100], composite plates [101–103], and an unmanned aircraft fixed-wing [104]. Other applications include iFEM coupled with convolutional neural networks [105] and peridynamics for crack propagation monitoring [106].

Despite the vast research described above, gaps still exist in achieving the objectives outlined at the beginning of this chapter. For the 1D iFEM, there is a lack of inverse beam elements powerful enough to accurately model complex beam geometries, particularly the transverse shear and torsional deformation. This serves as one of the primary aims of the present work. In contrast with 2D iFEM, the shell inverse elements developed have proven effective despite structural complexity. However, questions remain regarding the number and optimal location of sensors used. Some attempts made to offer a solution to this problem are described below.

Kefal et al. [107] investigated the effect of number, location and orientation of strain sensors for the specific problem of shape sensing of a wing-shaped thick panel. In contrast, Esposito et al. [108] adopted genetic algorithms for identifying optimal sensor locations in plate structures. Other optimisation-based approaches include the use of Particle Swarm Optimization (PSO) [109] and eigen value analysis [110] for a wing frame. However, due to the lack of generalisability of solutions obtained from optimization-based approaches, they are not determined to be a definite solution to this problem. Hence, identifying ideal sensor locations or efficient patterns forms

another facet of this work. The present work also aims to address this topic from the perspective of applying it to a damage detection problem.

Attempts to reduce the number of sensors used have yielded reasonable success, with major efforts relying on strain extrapolation using the Smoothing Element Analysis (SEA) developed by Tessler et al. [111]. Kefal et al. [112] coupled the iFEM and the SEA for the shape sensing of multi-layered composite and sandwich structures, while Oboe et al. [113] compared SEA to polynomial fitting as a strain extrapolation strategy for shape sensing of a composite plate.

Chapter 2

Theory of Beam and Plate Shape Sensing using iFEM

This chapter introduces the underlying theory and formulation of the inverse beam and plate or shell elements used for iFEM-based shape sensing. The chapter begins with a discussion of the 1D iFEM, initially recounting existing beam elements and subsequently describing novelties to their formulations, i.e., the accurate treatment of transverse shear and torsional deformation developed as part of this work. The chapter concludes with a description of the 2D iFEM. Although no new plate or shell elements are introduced, existing formulations are recounted for interested readers, considering their relevance for later discussions.

2.1 1D inverse Finite Element Method

Several inverse beam elements are available in literature [73, 74, 77, 79], differing in the kind of beam geometry analysed, kinematic relations and element interpolation functions used, etc. This section begins with a general description of the 1D iFEM formulation, followed by a discussion on the development of individual elements.

Beam displacement reconstruction using the 1D iFEM from surface strain measurements is based on matching a vector of so-called 'analytical' sectional strains, $\mathbf{e}(\mathbf{u})$, to a vector of 'experimental' sectional strains, $\mathbf{e}^{\varepsilon}$, in a least-squares sense [73]. This is accomplished using an error functional, Φ, defined as,

$$\Phi(\mathbf{u}) = \|\mathbf{e}(\mathbf{u}) - \mathbf{e}^{\varepsilon}\|^2 \tag{2.1}$$

where $\mathbf{u}$ is the vector of kinematic variables used to describe the kinematic field of the beam and the superscript $(\bullet)^{\varepsilon}$ represents experimentally estimated strains.

The iFEM is based on a variational formulation that discretises the structural domain using a series of finite elements. For each element, an element error functional corresponding to the k^{th} sectional strain, e_k, can be derived as,

$$\Phi_k^e = \frac{L_e}{N} \sum_{i=1}^{N} [e_k(x_i) - (e_k^{\varepsilon})_i]^2 \quad , \quad (k = 1, ..., n_s) \tag{2.2}$$

where L_e is the element length, N is the total number of axial beam locations, x_i, where strains are measured, and n_s is the total number of sectional strains in the element formulation.

The total element error functional, Φ^e, can be evaluated from Eq. 2.2 as the weighted sum of contributions from n_s individual functionals,

$$\Phi^e = \mathbf{w} \cdot \mathbf{\Phi} = \sum_{k=1}^{n_s} w_k^e \Phi_k^e \tag{2.3}$$

where $\mathbf{\Phi}$ is a vector of error functionals, and $\mathbf{w}$ is a vector of weighing coefficients used for enforcing a stronger or weaker correlation between $\mathbf{e}(\mathbf{u})$ and $\mathbf{e}^{\varepsilon}$.

The calculation of $\mathbf{e}(\mathbf{u})$ is governed by the kinematic relations used for describing beam behaviour. As the methodology is based on a finite element discretisation of the structural domain, the kinematic field is obtained by interpolating the nodal DOF using suitable shape functions,

$$\mathbf{u}(x) = \mathbf{N}(x)\mathbf{u}^e \tag{2.4}$$

where $\mathbf{N}(x)$ is the matrix of shape functions, $\mathbf{u}^e$ is a vector of nodal DOF, and x is the axial coordinate of the beam. Assuming the small-strain hypothesis, the analytical sectional strains can be derived from Eq. 2.4 by applying the linear strain-displacement relations,

$$\mathbf{e}(\mathbf{u}) = \mathbf{B}(x)\mathbf{u}^e \tag{2.5}$$

where $\mathbf{B}(x)$ is a matrix of shape function derivatives. The vector $\mathbf{e}^{\varepsilon}$ is calculated from experimental strain measurements from sensors embedded on the structure. Later sections provide more details on the calculation of $\mathbf{e}^{\varepsilon}$ for each element.

Substituting Eq. 2.5 in Eq. 2.3 and minimizing the element functional with respect to the nodal DOF, $\mathbf{u}^e$, results in a set of linear of algebraic equations,

$$\mathbf{k}^e\mathbf{u}^e = \mathbf{f}^e \tag{2.6}$$

where matrix $\mathbf{k}^e$ and vector $\mathbf{f}^e$ are analogous to the element stiffness matrix and force vector in the direct FEM. They can be further defined as the weighted sum of

contributions from each sectional strain term,

$$\mathbf{k}^e = \sum_{k=1}^{n_s} w_k^e \mathbf{k}_k^e \quad , \quad \mathbf{f}^e = \sum_{k=1}^{n_s} w_k^e \mathbf{f}_k^e \tag{2.7}$$

The system matrix $\mathbf{k}^e$ is only a function of strain sensor positions within an element, while the vector $\mathbf{f}^e$ is a function of the sensor positions and the value of experimental strain measurements. They can be described in terms of the shape function derivatives as,

$$\mathbf{k}_k^e \equiv \frac{L_e}{N} \sum_{i=1}^{N} \left[\mathbf{B}_k^T(x_i) \mathbf{B}_k(x_i) \right] \quad , \quad \mathbf{f}_k^e \equiv \frac{L_e}{N} \sum_{i=1}^{N} \left[\mathbf{B}_k^T(x_i) (e_k^{\varepsilon})_i \right] \tag{2.8}$$

Applying appropriate coordinate transformations and assembling all element contributions, the global set of linear algebraic equations can be compiled,

$$\mathbf{KU} = \mathbf{F} \tag{2.9}$$

Given that the requisite boundary conditions are applied to constrain the structure against rigid-body motion and the system matrix, $\mathbf{K}$, is ensured to be non-singular, Eq 2.9 can be solved to obtain the iFEM reconstructed nodal displacements $\mathbf{U}$.

The main steps of the 1D iFEM procedure is highlighted in the flow diagram of Fig. 2.1. Interested readers can consult Gherlone et al. [73] for additional explanations.

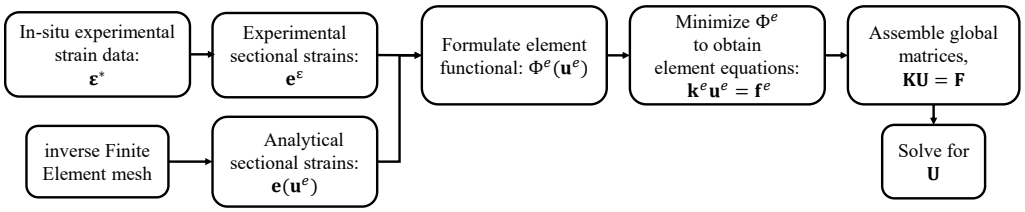

Fig. 2.1 Flow diagram of the 1D iFEM methodology highlighting the major steps involved

Although the present section described the general 1D iFEM framework, the number and definition of sectional strains, $\{\mathbf{e}(\mathbf{u}), \mathbf{e}^{\varepsilon}\}$, is specific to type of inverse beam element used. These elements are discussed in the following sections, in terms of the kinematic relations used and the corresponding sectional strains derived. Additionally, the novelties in element formulation, which forms the main focus of the current work, is also presented.

2.1.1 Euler-Bernoulli Beam Element

Considering a slender prismatic beam with any arbitrary cross-section defined in the three-dimensional Cartesian coordinates (x,y,z). The origin is assumed to located at the root of the beam, with the x-axis passing through the shear center of the beam cross-section and parallel to the beam axis, as shown in Fig. 2.2. The two transverse axes, y and z, are the principal inertia axes of the beam cross-section, with second area moments I_{yy} and I_{zz}. The beam has a length L, cross-sectional area A, and the beam material is assumed to be homogeneous and isotropic with Young's modulus E, shear modulus G, and Poisson's ratio ν.

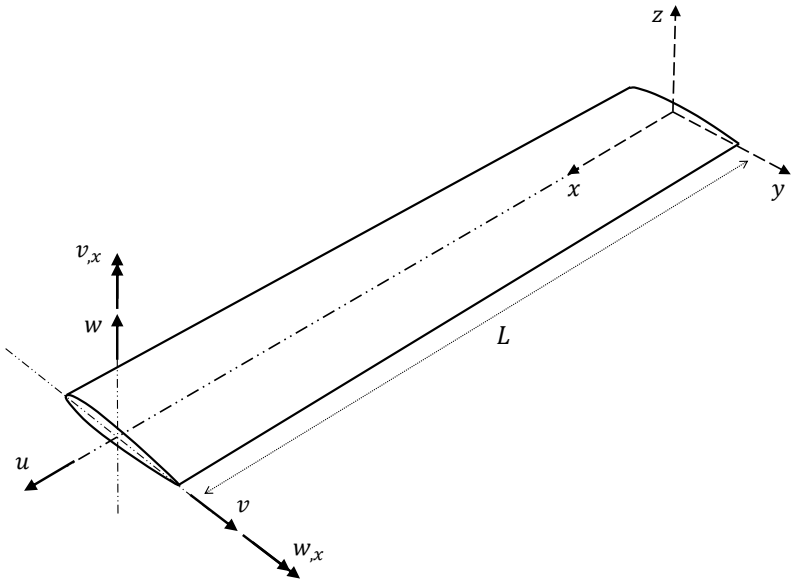

Fig. 2.2 The reference coordinate system and kinematic variables used for defining a slender prismatic airfoil beam

Kinematic Relations

Due to the slender nature of the beam, the transverse shear contribution to the beam deformation can be considered negligible. Hence, the beam element (proposed in Ref. [76]) is formulated based on the kinematic assumptions of Euler-Bernoulli beam theory [114]. The Cartesian components of the displacement vector is represented in terms of the kinematic variables u, v, w, $v_{,x}$, and $w_{,x}$ (see Figure 2.2) as,

$$\begin{aligned} u_x(x,y,z) &= u(x) + zw_{,x}(x) - yv_{,x}(x) \\ u_y(x,y,z) &= v(x) \\ u_z(x,y,z) &= w(x) \end{aligned} \tag{2.10}$$

where u_x, u_y, and u_z are the displacements of any beam point along the x, y and z-axis, respectively. The kinematic variables, u, v, and w represent the beam displacement at the shear center along the x, y and z-axis, respectively, while $v_{,x}$, and $w_{,x}$ are the corresponding derivatives. These variables can be written in vector form,

$$\mathbf{u} = \{u, v, w, , v_{,x}, w_{,x}\}^T \tag{2.11}$$

Applying small-strain hypothesis, the axial and transverse shear components of the strain field can be derived from Eq. 2.10 as,

$$\begin{Bmatrix} \varepsilon_x(x,y,z) \\ \gamma_{xz}(x,y,z) \\ \gamma_{xy}(x,y,z) \end{Bmatrix} = \begin{Bmatrix} u_{x,x} \\ u_{x,z} + u_{z,x} \\ u_{x,y} + u_{y,x} \end{Bmatrix} = \begin{Bmatrix} e_1(x) + z e_2(x) + y e_3(x) \\ 0 \\ 0 \end{Bmatrix} \tag{2.12}$$

where e_1, e_2 and e_3 are the three sectional strains ($n_s = 3$) defined along the beam axis and represent the axial stretching, and bending curvatures of the beam, respectively. In keeping with our assumption, the transverse shear strain components are seen to vanish in Eq. 2.12. The vector of analytic sectional strains can be written as,

$$\mathbf{e}(\mathbf{u}) = \begin{Bmatrix} e_1 \\ e_2 \\ e_3 \end{Bmatrix} = \begin{Bmatrix} u_{,x} \\ w_{,xx} \\ -v_{,xx} \end{Bmatrix}. \tag{2.13}$$

The weighing coefficient vector (see Eq. 2.3) for this element can be defined as,

$$\mathbf{w} = \{w_1, w_2(I_{yy}/A), w_3(I_{zz}/A)\} \tag{2.14}$$

The vector $\mathbf{e}(\mathbf{u})$ forms only one part of the error functional of Eq. 2.1. The calculation of its experimental counterpart, $\mathbf{e}^{\varepsilon}$, is discussed below.

Experimental Sectional Strains

Considering the beam surface instrumented with strain sensors, such as strain gauges or fibre optic sensors, measuring strains at N discrete axial locations x_i ($i = 1, ..., N$) and oriented along the x-axis (see Fig. 2.3). Using Eq. 2.12, the experimental strain measurements, ε^*, on the beam surface can be defined as,

$$\varepsilon^*(x_i, c) = \varepsilon_x(x_i, c) = e_1^{\varepsilon}(x_i) + z(c) e_2^{\varepsilon}(x_i) + y(c) e_3^{\varepsilon}(x_i) \tag{2.15}$$

where the superscript $(\bullet)^*$ represents the strain measured on the beam surface along any local axis, $\varepsilon^* = \varepsilon_x$ in the present case as only axial strain measurements are used to define the beam deformation, and e_1^{ε}, e_2^{ε}, and e_3^{ε} are the experimental sectional strains defined along the beam axis. The coordinate c represents the circumferential

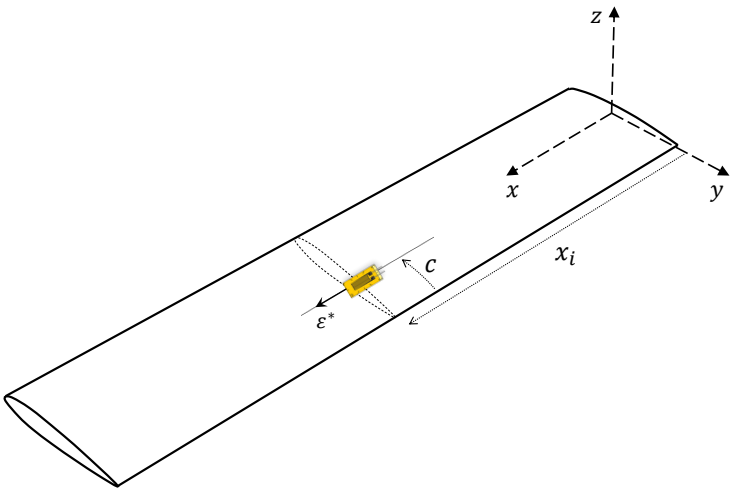

Fig. 2.3 Prismatic airfoil beam instrumented with a strain gauge; the parameters used for describing the sensor position on the beam surface have been defined in the figure

distance along the section perimeter. For the specific case of an airfoil profile (as shown in Fig. 2.3), c is the circumferential distance in the counter-clockwise direction along the beam perimeter starting from the trailing edge of the airfoil. As the experimental sectional strains are the three unknowns at any section, solution of Eq. 2.16 requires at least three experimental axial strain measurements per section, and can be written in terms of the coordinate matrix, $\mathbf{X}_c$, as,

$$\boldsymbol{\varepsilon}^* = [\mathrm{X}_c]_{3\times 3}\,\mathbf{e}^{\varepsilon} \tag{2.16}$$

where $\boldsymbol{\varepsilon}^*$ is a vector of experimental strain measurements and $\mathbf{e}^{\varepsilon}$ is the sectional strain vector,

$$\mathbf{e}^{\varepsilon} = \begin{Bmatrix} e_1^{\varepsilon} \\ e_2^{\varepsilon} \\ e_3^{\varepsilon} \end{Bmatrix} \tag{2.17}$$

Values for $\mathbf{e}^{\varepsilon}$ at any section x_i can be obtained by solving Eq. 2.16.

Element Interpolations

The present element is derived considering the case of a slender beam subjected to a concentrated tip load, leading to a constant axial force, and linear variation of bending moments along the beam length. Correspondingly, the axial strain, e_1, is a constant, while the curvatures, e_2 and e_3, are linear. Hence, the kinematic variable u is interpolated linearly, and v, and w cubically. Based on these considerations, the interpolation of kinematic variables within an element, $x \in [0, L_e]$, using the nodal

DOF can be described as,

$$\begin{aligned} u(x) =& L_1(x)u_1 + L_2(x)u_2 \\ v(x) =& M_1(x)v_1 + M_2(x)\theta_1 + M_3(x)v_2 + M_4(x)\theta_2 \\ w(x) =& M_1(x)w_1 + M_2(x)\phi_1 + M_3(x)w_2 + M_4(x)\phi_2 \end{aligned} \tag{2.18}$$

where the variables $\theta = v_{,x}$ and $\phi = w_{,x}$, and L, M represent the Lagrange and Hermitian polynomials, respectively. Refer to Appendix A for a complete description of these polynomials. The beam element developed is hereafter referred to as 'iEB2'.

2.1.2 Timoshenko Beam Element

Consider a thick prismatic beam defined in the three-dimensional Cartesian coordinates (x, y, z), as shown in Fig. 2.4. The coordinate system, geometrical and material properties of the beam are similar to those described in Section 2.1.1. In contrast to the previous problem, the contribution due to transverse shear and torsion forms an important part of beam deformation in this case, and cannot be ignored. Also, transverse shear strain is not a constant, but varies across the beam cross-section. Reconciliation of the transverse shear and torsional deformation with 1D beam theories is achieved through the use of certain coefficient and functions. The definition of these coefficients and functions for any general beam section is a central aim of the work done and is discussed in detail in the following sections.

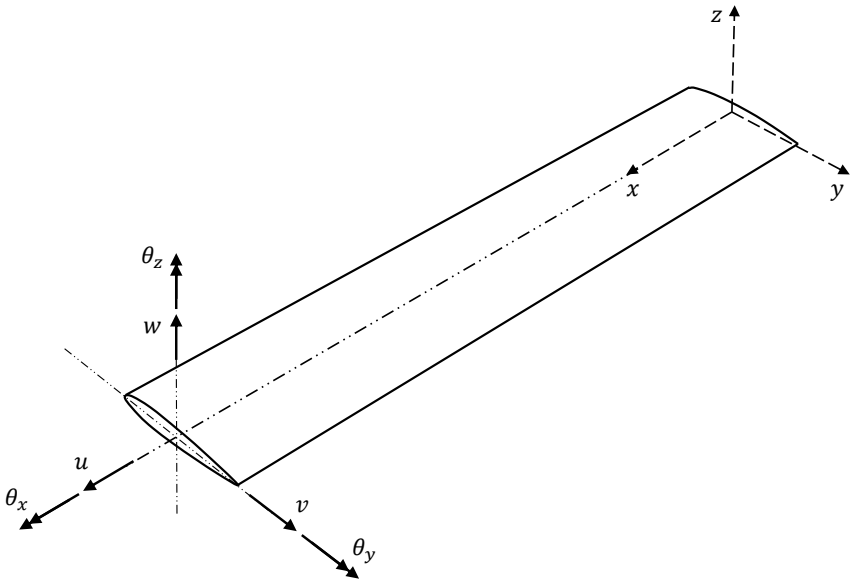

Fig. 2.4 The reference coordinate system and kinematic variables used for defining a thick prismatic airfoil beam

Kinematic Relations

Due to the importance of transverse shear deformation, the present inverse element is formulated based on the kinematic assumptions of Timoshenko beam theory [85, 114]. Alongside the transverse shear contribution, torsional deformation (ignored in iEB2 for simplicity) is also considered for this new element. In this case, the Cartesian components of the displacement vector can be defined in terms of the kinematic variables u, v, w, θ_x, θ_y and θ_z (shown in Fig. 2.4) as,

$$\begin{aligned} u_x(x,y,z) &= u(x) + z\theta_y(x) - y\theta_z(x) \\ u_y(x,y,z) &= v(x) - z\theta_x(x) \\ u_z(x,y,z) &= w(x) + y\theta_x(x) \end{aligned} \tag{2.19}$$

where u_x, u_y, and u_z are the displacements of any beam point along the x, y and z-axis, respectively. The kinematic variables, u, v and w, represent the beam displacements at the shear center, and θ_x, θ_y and θ_z are the torsional and bending rotations about the x, y and z-axis, respectively. The vector of kinematic variables can be written as,

$$\mathbf{u} \equiv \{u, v, w, \theta_x, \theta_y, \theta_z\}^T \tag{2.20}$$

Applying the linear strain-displacement relations, the axial and transverse shear strains are calculated from the displacement field of Eq. 2.19 and are given as,

$$\begin{Bmatrix} \varepsilon_x(x,y,z) \\ \gamma_{xz}(x,y,z) \\ \gamma_{xy}(x,y,z) \end{Bmatrix} = \begin{Bmatrix} u_{,x} \\ u_{,z} + w_{,x} \\ u_{,y} + v_{,x} \end{Bmatrix} = \begin{Bmatrix} e_1(x) + ze_2(x) + ye_3(x) \\ e_4(x) + ye_6(x) \\ e_5(x) - ze_6(x) \end{Bmatrix} \tag{2.21}$$

where e_i, ($i = 1, \ldots, n_s$ and $n_s = 6$) are the six sectional strains defined along the beam axis, and correspond to the axial stretching, bending curvatures, transverse shear and torsional strain of the beam, respectively. These sectional strains can be written in vector form as [73],

$$\mathbf{e}(\mathbf{u}) = \begin{Bmatrix} e_1 \\ e_2 \\ e_3 \\ e_4 \\ e_5 \\ e_6 \end{Bmatrix} = \begin{Bmatrix} u_{,x} \\ \theta_{y,x} \\ -\theta_{z,x} \\ w_{,x} + \theta_y \\ v_{,x} - \theta_z \\ \theta_{x,x} \end{Bmatrix}. \tag{2.22}$$

The weighing coefficient vector for this element (see Eq. 2.3) can be defined as,

$$\mathbf{w} = \{w_1, w_2(I_{yy}/A), w_3(I_{zz}/A), w_4, w_5, w_6(I_p/A)\} \tag{2.23}$$

where I_p is the polar area moment (or torsional constant) of the cross-section.

Here again, the vector **e** represents the analytical sectional strains of the beam and forms one part of the iFEM error functional. A main aspect of the work done is the development of theoretical equations for the calculation of experimental sectional strains for any general beam profile. The corresponding theory and a simple application, considering an airfoil beam, are discussed below.

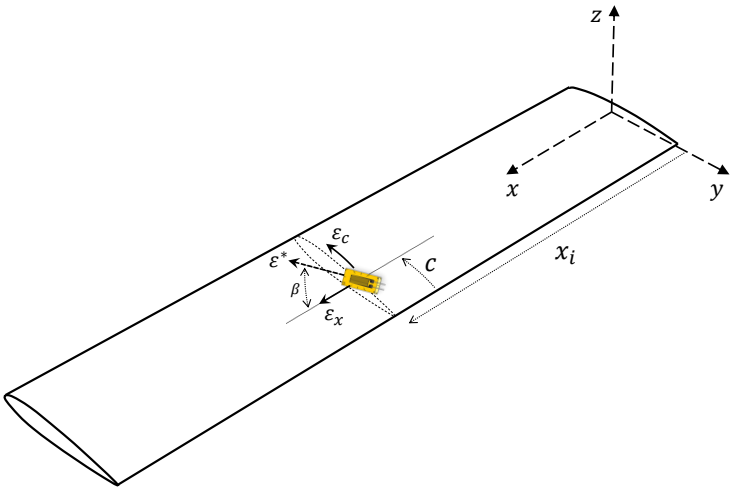

Fig. 2.5 Prismatic thick airfoil beam with a surface mounted strain gauge; the various parameters defining the sensor location and orientation are shown

Experimental Sectional Strains

Considering the beam surface to be instrumented with strain sensors, such as strain gauges or fiber optic sensors. Strains are measured at N discrete axial locations x_i ($i = 1,\ldots,N$), and sensors are oriented at any angle β with respect to the x-axis (see Fig. 2.5). The surface strain measurement ε^* can be related to axial ε_x, tangential ε_c and shear γ_{xc} strain components as ,

$$\varepsilon^*(x_i,c,\beta) = \varepsilon_x(x_i,c)\cos^2\beta + \varepsilon_c(x_i,c)\sin^2\beta + \gamma_{xc}(x_i,c)\cos\beta\sin\beta \tag{2.24}$$

where c is the circumferential coordinate defined in the previous section and shown in Fig. 2.5. If the value of Poisson's ratio for the beam material is known (commonly $\nu = 0.3$ for metals), Eq. 2.24 can be further simplified as [73],

$$\varepsilon^*(x_i,c,\beta) = \varepsilon_x(x_i,c)(\cos^2\beta - \nu\sin^2\beta) + \gamma_{xc}(x_i,c)\cos\beta\sin\beta \tag{2.25}$$

Using Eq. 2.21, axial strains ε_x on the beam surface can be defined in terms of the sectional strains along the beam axis as,

$$\varepsilon_x(x_i,c) = e_1^{\varepsilon}(x_i) + z(c)e_2^{\varepsilon}(x_i) + y(c)e_3^{\varepsilon}(x_i) \tag{2.26}$$

The tangential shear strain, γ_{xc}, is a function of c and the cross-sectional profile. Gherlone et al. [73] demonstrated the calculation of experimental sectional strains for a simple circular beam. However, these results were for a specific case and not translatable to beams with other cross-sectional profiles. The present work introduces a novel framework for experimental sectional strain calculation applicable to beams with any general profile.

The underlying theory behind this new formulation is that, for a beam under any general loading condition, the tangential shear strain, γ_{xc}, on the surface of the beam can be defined as the superposition of contributions due to transverse shear and torsional loads. Assuming a cantilevered beam loaded at the tip by a unit force along the z-axis, $\gamma_{xc}(c)$ along the perimeter of the cross-section can be written in terms of a tangential shear strain maximum, $\gamma^z_{xc,max}$, and a shear variation function, $f_1(c)$. Similarly, if the cantilevered beam is loaded by a unit tip force along the y-axis, $\gamma_{xc}(c)$ can be written in terms of a maximum, $\gamma^y_{xc,max}$, and a function, $f_2(c)$. Additionally, if the beam is subjected to a tip torsional load generating a unit rate of twist ($e^\varepsilon_6 = 1$), $\gamma_{xc}(c)$ along the perimeter is defined using the shear variation function, $f_3(c)$. The final distribution of γ_{xc} can be written as a superposition of all three load cases,

$$\gamma_{xc}(x_i, c) = \gamma^z_{xc,max}(x_i) f_1(c) + \gamma^y_{xc,max}(x_i) f_2(c) + e^\varepsilon_6(x_i) f_3(c) \tag{2.27}$$

Relating the tangential shear strain maxima, $\gamma^z_{xc,max}$ and $\gamma^y_{xc,max}$, to the corresponding sectional strains e^ε_4 and e^ε_5 is instrumental for the calculation of these latter quantities. They are related through the use of certain shear coefficients, whose calculation are described below.

Consider a cantilevered beam loaded at the tip by a force F_z along the z-axis. The shear strain energy per unit length calculated using a 3D numerical model of the beam, ϕ^{FE}_{SE}, and a Timoshenko beam model, ϕ^{TM}_{SE}, are equated through a coefficient,

$$k_{tz} = \frac{\phi^{TM}_{SE}}{\phi^{FE}_{SE}} \tag{2.28}$$

where k_t is the classical shear correction factor, and the shear strain energy,

$$\phi^{TM}_{SE} = \frac{F_z^2}{2AG} \tag{2.29}$$

Eq. 2.28 is also used to define the relation between the constant transverse shear strain defined by Timoshenko beam theory, F_z/AG, and the effective transverse shear strain of the beam cross-section, e^ε_4. This relation can be written as,

$$k_{tz} = \frac{F_z^2}{2AG\phi^{FE}_{SE}} \approx \frac{F_z/AG}{e^\varepsilon_4} \tag{2.30}$$

Similarly, for a cantilevered beam loaded at the tip by a force F_y along the y-axis, the coefficient k_{ty} can be defined as,

$$k_{ty} = \frac{\phi_{SE}^{TM}}{\phi_{SE}^{FE}} = \frac{F_y^2}{2AG\phi_{SE}^{FE}} \approx \frac{F_y/AG}{e_5^{\varepsilon}} \tag{2.31}$$

The coefficient, k_{ε}, is used to relate the tangential shear strain maxima due to transverse loading in a certain direction to the corresponding sectional strain. These coefficients for transverse loads along the z and y-axis are defined as,

$$k_{\varepsilon z} = \frac{e_4^{\varepsilon}}{\gamma_{xc,max}^{z}} = \frac{F_z/GA}{k_{tz}\gamma_{xc,max}^{z}} \quad , \quad k_{\varepsilon y} = \frac{e_5^{\varepsilon}}{\gamma_{xc,max}^{y}} = \frac{F_y/GA}{k_{ty}\gamma_{xc,max}^{y}} \tag{2.32}$$

Substituting Eq. 2.32 in Eq. 2.27, the tangential shear strains can be written in terms of the sectional strains as,

$$\gamma_{xc}(x_i,c) = \frac{1}{k_{\varepsilon z}} e_4^{\varepsilon}(x_i) f_1(c) + \frac{1}{k_{\varepsilon y}} e_5^{\varepsilon}(x_i) f_2(c) + e_6^{\varepsilon}(x_i) f_3(c) \tag{2.33}$$

Finally, substituting Eqs. 2.26 and 2.33 in Eq. 2.25, we get an equation relating the surface strain measurements to experimental sectional strains,

$$\begin{aligned} \varepsilon^*(x_i,c,\beta) = {} & \left(e_1^{\varepsilon}(x_i) + z(c)e_2^{\varepsilon}(x_i) + y(c)e_3^{\varepsilon}(x_i)\right)\left(\cos^2\beta - \nu\sin^2\beta\right) + \\ & \left(\frac{1}{k_{\varepsilon z}} e_4^{\varepsilon}(x_i) f_1(c) + \frac{1}{k_{\varepsilon y}} e_5^{\varepsilon}(x_i) f_2(c) + e_6^{\varepsilon}(x_i) f_3(c)\right)\cos\beta\sin\beta \end{aligned} \tag{2.34}$$

The shear functions, $\{f_1, f_2, f_3\}$, and coefficients, $\{k_{\varepsilon z}, k_{\varepsilon y}\}$, are only a function of the cross-sectional profile and have to be evaluated beforehand to solve Eq. 2.34. Evaluation of the unknown sectional strains requires at least six strain measurements per section. Eq. 2.34 can also be written in vector form as,

$$\boldsymbol{\varepsilon}^* = [\mathrm{X}_c]_{6\times 6}\, \mathbf{e}^{\varepsilon} \tag{2.35}$$

where $\mathbf{e}^{\varepsilon}$ is the vector of unknowns defined as,

$$\mathbf{e}^{\varepsilon} \equiv \{e_1^{\varepsilon}, e_2^{\varepsilon}, e_3^{\varepsilon}, e_4^{\varepsilon}, e_5^{\varepsilon}, e_6^{\varepsilon}\}^T \tag{2.36}$$

The shear functions and coefficients can be calculated analytically or using a numerical model of the beam. The calculation steps for a symmetric airfoil profile along with the final results for other common profiles are described in Appendix B.

Element Interpolations

The element interpolations developed by Gherlone et al. [73] is used for this work as well. Due to their relevance when discussing results in future sections, they are briefly recounted here. The interpolations correspond to the beam undergoing two different loading conditions.

In the first case, the beam is considered to be subjected to a concentrated general tip load, where e_1, e_4, e_5, and e_6 are a constant, and flexural strains e_2, and e_3 are linear across the element. The corresponding interpolations for the kinematic variables within the element are given as,

$$\begin{aligned} u(\eta) &= \sum_{i=1,2} L_i^{(1)}(\eta) u_i & \theta_x(\eta) &= \sum_{i=1,2} L_i^{(1)}(\eta)\theta_{xi} \\ v(\eta) &= \sum_{i=1,2} L_i^{(1)}(\eta) v_i - \sum_{j=1,r,2} N_j^{(3)}\theta_{zj} & \theta_y(\eta) &= \sum_{j=1,r,2} L_i^{(2)}(\eta)\theta_{yi} \\ w(\eta) &= \sum_{i=1,2} L_i^{(1)}(\eta) w_i + \sum_{j=1,r,2} N_j^{(3)}\theta_{yj} & \theta_z(\eta) &= \sum_{j=1,r,2} L_i^{(2)}(\eta)\theta_{zi} \end{aligned} \tag{2.37}$$

where $\eta \in [-1,1]$, $L_i^{(1)}$ and $L_i^{(2)}$ are the 1st and 2nd-order Lagrange polynomials, respectively, and $N_j^{(3)}$ are the anisoparametric interpolations. Refer Appendix A for a complete description of these quantities. The beam element developed based on Eq. 2.37 was called the 0th-order element in Ref. [73], but for convenience is hereafter referred to as 'iTM2D0'.

In the second case, the beam is considered to be subjected to a transverse uniform distributed load, where e_1, e_6 are a constant, e_4, and e_5 are linear, and e_2, e_3 are quadratic across the element. The corresponding interpolations for the kinematic variables within the element are given as,

$$\begin{aligned} u(\eta) &= \sum_{i=1,2} L_i^{(1)}(\eta) u_i & \theta_x(\eta) &= \sum_{i=1,2} L_i^{(1)}(\eta)\theta_{xi} \\ v(\eta) &= \sum_{k=1,q,r,s,2} L_i^{(4)}(\eta) v_i & \theta_y(\eta) &= \sum_{j=1,2} L_i^{(1)}(\eta)\theta_{yi} + \sum_{k=1,q,r,s,2} M_j^{(3)} w_k \\ w(\eta) &= \sum_{i=1,q,r,s,2} L_i^{(4)}(\eta) w_i & \theta_z(\eta) &= \sum_{j=1,r,2} L_i^{(2)}(\eta)\theta_{zi} - \sum_{k=1,q,r,s,2} M_j^{(3)} v_k \end{aligned} \tag{2.38}$$

where $L_i^{(4)}$ are the 4th-order Lagrange polynomials, and $M_j^{(3)}$ are the anisoparametric interpolations (refer Appendix A). The beam element developed based on Eq. 2.38 (called the 1st-order element in Ref. [73]) is hereafter referred to as 'iTM2D1'.

2.1.3 Timoshenko Beam Element for Non-Prismatic Beams

A further generalisation of the beam formulation of Section 2.1.2 is presented here, where it is extended to non-prismatic geometries, i.e., for beams with variable profiles. Considering a non-prismatic beam defined in the three-dimensional Cartesian coordinate system (x,y,z), as shown in Fig. 2.6. The location of the coordinate system origin and the beam material properties is similar to previous cases. The cross-sectional profile of the beam is assumed to vary along its length, and the section properties at any axial location, x_i, is $\{A, I_{yy}, I_{zz}, I_p\}_i$.

For non-prismatic beams, the kinematic relations used and the calculation of $\mathbf{e}(\mathbf{u})$ is similar to those described in Section 2.1.2, and is not reiterated here. However, $\mathbf{e}^{\varepsilon}$ is a function of the beam profile and cannot be computed accurately using Eq. 2.34. The requisite changes to these equations are the basis of the following discussions.

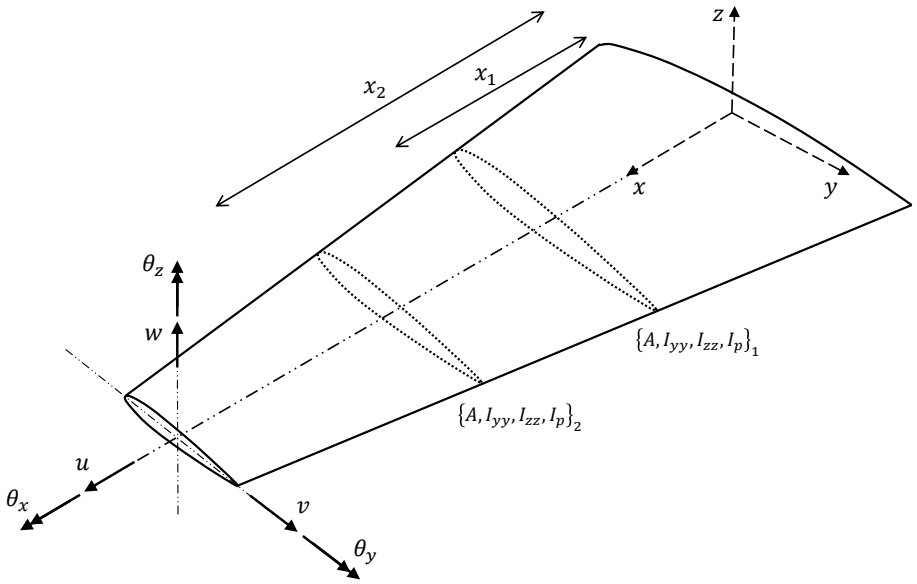

Fig. 2.6 The reference coordinate system and kinematic variables used for defining a tapered airfoil beam; the varying sectional properties at different beam sections is also shown

Experimental Sectional Strains

Considering a non-prismatic beam instrumented with strain sensors, the strain measurement by a sensor placed at any axial location x_i, and circumferential location c, and oriented at an angle β can be written as,

$$\varepsilon^*(x_i,c,\beta) = \varepsilon_x(x_i,c)(\cos^2\beta - \nu\sin^2\beta) + \gamma_{xc}(x_i,c)\cos\beta\sin\beta \tag{2.39}$$

where c is the circumferential coordinate. In the case of a tapered airfoil beam, as shown in Fig. 2.6, c is defined with respect to the local airfoil profile at each section x_i. The axial component of strain is written as,

$$\varepsilon_x(x_i,c) = e_1^{\varepsilon}(x_i) + e_2^{\varepsilon}(x_i)z(x_i,c) + e_3^{\varepsilon}(x_i)y(x_i,c) \tag{2.40}$$

where $(y(x_i,c),z(x_i,c))$ represents the general point coordinates corresponding to the beam profile at any section. Similarly, the tangential shear strain component can be written in a generalised form as,

$$\gamma_{xc}(x_i,c) = \frac{1}{k_{\varepsilon z}(x_i)} e_4^{\varepsilon}(x_i) f_1(x_i,c) + \frac{1}{k_{\varepsilon y}(x_i)} e_5^{\varepsilon}(x_i) f_2(x_i,c) + e_6^{\varepsilon}(x_i) f_3(x_i,c) \tag{2.41}$$

where functions $\{f_1, f_2, f_3\}$ and coefficients $\{k_{\varepsilon z}, k_{\varepsilon y}\}$ are now defined as a function of the beam profile at any section x_i.

Substituting Eqs. 2.40 and 2.41 in Eq. 2.39, we get,

$$\begin{aligned}\varepsilon^*(x_i,c,\beta) = (e_1^{\varepsilon}(x_i) + e_2^{\varepsilon}(x_i)z(x_i,c) + e_3^{\varepsilon}(x_i)y(x_i,c))\,(\cos^2\beta - \nu\sin^2\beta) + \\ \left(\frac{1}{k_{\varepsilon z}(x_i)} e_4^{\varepsilon}(x_i) f_1(x_i,c) + \frac{1}{k_{\varepsilon y}(x_i)} e_5^{\varepsilon}(x_i) f_2(x_i,c) + e_6^{\varepsilon}(x_i) f_3(x_i,c)\right)\cos\beta\sin\beta\end{aligned} \tag{2.42}$$

The solution of Eq. 2.42 requires the calculation of shear functions and coefficients depending on the beam profile at those axial locations where the strain measurements are made. For the simple case of a tapered beam, these coefficients and functions remain the same as the profile is only scaled up or down at each section.

As the element interpolations and nodal DOF are similar to those described for iTM2D0 and iTM2D1, the present formulation is not categorised as a new element, but rather a minor update to the previous one.

2.1.4 Timoshenko Beam Element with Warping

The final beam formulation presented in this section concerns thin-walled beams where torsion of the beam is accompanied by cross-sectional warping. Considering a thin-walled beam defined in the three-dimensional Cartesian coordinate system (x,y,z), as shown in Fig. 2.7. The location of the coordinate system origin and the beam properties are similar to those described in Section 2.1.2. The beam is assumed to be subjected to a general load, involving torsion. The axial displacements and strains due to warping influences the calculation of sectional strains and can lead to inaccurate solutions. The present section proposes a further improvement of previous formulations for the shape sensing of structures undergoing cross-sectional warping deformation as well.

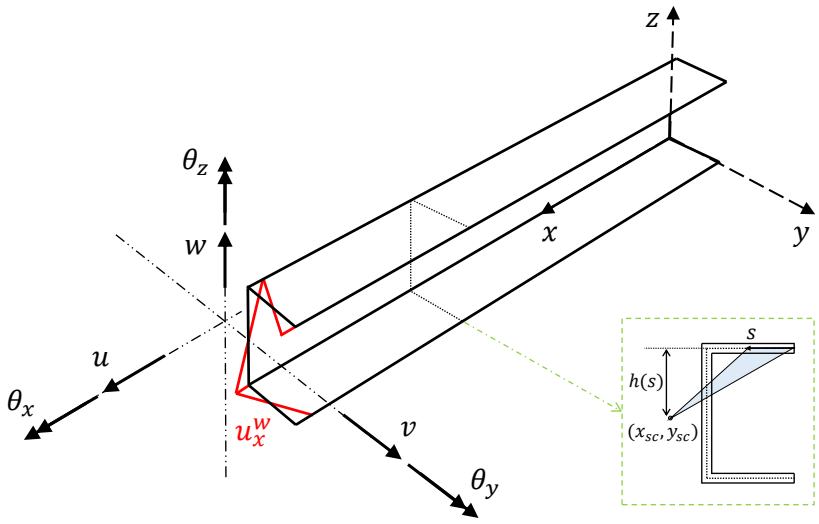

Fig. 2.7 The reference coordinate system and kinematic variables used for defining a thin-walled beam; an illustration of cross-sectional warping (red lines) is also shown

Kinematic Relations

For an open section thin-walled beam under constrained warping, the axial displacement along the midline of the flange cross-section, u_x^w (see Fig. 2.7), can be defined as [115],

$$u_x^w(x,s) = -\omega(s)\theta_{x,x}(x) \tag{2.43}$$

where $\theta_{x,x}$ represents the rate of twist, and s is the distance measured along the midline of the flange cross-section. The function, $\omega(s)$, is the sectorial area defined by the integral [116],

$$\omega(s) = \int_0^s h(s)ds \tag{2.44}$$

where h is the perpendicular distance from the center of rotation (shear center in this case) to the tangent at any point, $(y(s), z(s))$, on the flange midline (see Fig. 2.7).

The Cartesian components of the displacement vector, considering this additional warping contribution, is written as,

$$\begin{aligned} u_x(x,s) &= u(x) + z(s)\theta_y(x) - y(s)\theta_z(x) - \omega(x,s)\theta_{x,x}(x) \\ u_y(x,s) &= v(x) - z(s)\theta_x(x) \\ u_z(x,s) &= w(x) + y(s)\theta_x(x) \end{aligned} \tag{2.45}$$

where u, v, w, θ_x, θ_y, and θ_z are the kinematic variables defined in Fig. 2.7.

The axial and transverse shear strains are derived from Eq. 2.45 by applying the linear strain-displacement relations,

$$\left\{\begin{array}{c}\varepsilon_x(x,s)\\ \gamma_{xz}(x,s)\\ \gamma_{xy}(x,s)\end{array}\right\}=\left\{\begin{array}{c}u_{,x}\\ u_{,z}+w_{,x}\\ u_{,y}+v_{,x}\end{array}\right\}=\left\{\begin{array}{c}e_1(x)+z(s)e_2(x)+y(s)e_3(x)-\omega_{,x}(x,s)e_7\\ e_4(x)+y(s)e_6(x)-\omega_{,z}(x,s)e_6\\ e_5(x)-z(s)e_6(x)-\omega_{,y}(x,s)e_6\end{array}\right\} \tag{2.46}$$

where e_i, $(i=1,...,n_s$, and $n_s=7)$ are the new sectional strains defined along the beam axis. The quantity, e_7, represents the second derivative of the torsional rotation and is directly proportional to the axial strain due to warping. These sectional strains are written in vector form,

$$\mathbf{e}(\mathbf{u})=\left\{\begin{array}{c}e_1\\ e_2\\ e_3\\ e_4\\ e_5\\ e_6\\ e_7\end{array}\right\}=\left\{\begin{array}{c}u_{,x}\\ \theta_{y,x}\\ -\theta_{z,x}\\ w_{,x}+\theta_y\\ v_{,x}-\theta_z\\ \theta_{x,x}\\ \theta_{x,xx}\end{array}\right\}. \tag{2.47}$$

Similar to the updated analytical sectional strain vector, $\mathbf{e}(\mathbf{u})$, the calculation of its experimental counterpart is also affected by warping. Modelling the warping component in the measured surface strains serves as the basis for an accurate evaluation of $\mathbf{e}^{\varepsilon}$ and is discussed below.

Experimental Sectional Strains

Considering an open section thin-walled beam instrumented with strain sensors, the surface strain measurement, ε^*, at any point s in the section x_i can be related to the axial, ε_x, and shear γ_{xs} strain components as,

$$\varepsilon^*(x_i,s,\beta)=\varepsilon_x(x_i,s)(\cos^2\beta-\nu\sin^2\beta)+\gamma_{xs}(x_i,s)\cos\beta\sin\beta \tag{2.48}$$

where the axial component is defined with the additional warping strain contribution as (based on Eq. 2.46),

$$\varepsilon_x(x_i,s)=e_1^{\varepsilon}(x_i)+z(s)e_2^{\varepsilon}(x_i)+y(s)e_3^{\varepsilon}(x_i)-\omega(s)e_7^{\varepsilon}(x_i) \tag{2.49}$$

The distribution of γ_{xs} is similar to that defined in Eq. 2.33 and is not reiterated here. Substituting Eq. 2.49 in Eq. 2.48, we get,

$$\begin{aligned}\varepsilon^*(x_i,s,\beta) = &(e_1^\varepsilon(x_i)+e_2^\varepsilon(x_i)z(s)+e_3^\varepsilon(x_i)y(s)-\omega(s)e_7^\varepsilon(x_i))\,(\cos^2\beta-\nu\sin^2\beta)\\ &+\left(\frac{1}{k_{\varepsilon z}}e_4^\varepsilon(x_i)f_1(s)+\frac{1}{k_{\varepsilon y}}e_5^\varepsilon(x_i)f_2(s)+e_6^\varepsilon(x_i)f_3(s)\right)\cos\beta\sin\beta\end{aligned} \tag{2.50}$$

where the seven unknown experimental sectional strains, e_i^ε $(i=1,\ldots,7)$, are written in vector form,

$$\mathbf{e}^\varepsilon \equiv \{e_1^\varepsilon, e_2^\varepsilon, e_3^\varepsilon, e_4^\varepsilon, e_5^\varepsilon, e_6^\varepsilon, e_7^\varepsilon\}^T \tag{2.51}$$

Solution of Eq. 2.50 requires at least seven strain measurements per section, but due to the interdependence between e_6^ε and e_7^ε, it cannot be directly solved by matrix inversion and requires an iterative solution procedure. A simple solution of Eq. 2.50 can be achieved through an assumption of the interpolation order of θ_x within the beam element. The solution for a quadratic interpolation is discussed here.

Assuming that within an element the distribution of θ_x is defined using the quadratic polynomial,

$$\theta_x(x) = a_0 + a_1 x + \frac{a_2}{2}x^2 \tag{2.52}$$

where a_0, a_1 and a_2 are unknown coefficients. The sectional strains, e_6^ε and e_7^ε, are calculated directly from Eq. 2.52,

$$\begin{aligned}e_6^\varepsilon(x) &= a_1 + a_2 x\\ e_7^\varepsilon(x) &= a_2\end{aligned} \tag{2.53}$$

Substituting Eq. 2.53 in Eq. 2.50, we get,

$$\begin{aligned}\varepsilon^*(x_i,s,\beta) = &(e_1^\varepsilon(x_i)+e_2^\varepsilon(x_i)z(s)+e_3^\varepsilon(x_i)y(s))\,(\cos^2\beta-\nu\sin^2\beta)\\ &+\left(\frac{1}{k_{\varepsilon z}}e_4^\varepsilon(x_i)f_1(s)+\frac{1}{k_{\varepsilon y}}e_5^\varepsilon(x_i)f_2(s)\right)\cos\beta\sin\beta\\ &+a_1 f_3(s)\cos\beta\sin\beta+a_2(x_i f_3(s)\cos\beta\sin\beta-\omega(s)(\cos^2\beta-\nu\sin^2\beta))\end{aligned} \tag{2.54}$$

where e_i^ε $(i=1,\ldots,5)$, a_1, and a_2 are the seven unknowns. Eq. 2.54 can be solved though matrix inversion by combining strain measurements from at least two sections (due to the linear interpolation assumed), with at least six surface strain measurements per section.

With the values of a_1 and a_2 evaluated, $e_6^\varepsilon(x_i)$ and $e_7^\varepsilon(x_i)$ can now be calculated at any section within the element using Eq. 2.53. Due to the assumption of Eq. 2.52,

these calculated quantities are linked, in terms of a value and its slope. If the element error functional of Eq. 2.3 is formulated using $\mathbf{e}^{\varepsilon}$ evaluated at two or more sections within an element, the minimisation constraint imposed by both e_6^{ε} and e_7^{ε} terms are similar, and thus redundant. Hence, the contribution due e_7^{ε} can be safely omitted from the element error functional without any loss of accuracy.

It should be noted that Eq. 2.54 presents a specific solution for a quadratic interpolation of θ_x (Eq. 2.52). Higher order polynomials can also be used depending on the end conditions of the beam and axial variation of torsional strain, e.g. in the case of non-uniform torsion. However, this leads to an increase in the number of unknown coefficients, a_i, in Eq. 2.54 and necessitates additional strain measurements. Such cases are not explored here and are left for future investigations.

Element Interpolations

The interpolation of the kinematic variables for the present beam formulation is similar to those proposed in Eqs. 2.37 and 2.38 for the iTM2D0 and iTM2D1 elements. The only difference is the introduction of the warping contribution, that leads to a corresponding increase in the interpolation order of torsional rotation. Based on the assumption of Eq. 2.52, θ_x within the element is now defined as,

$$\theta_x(\eta) = \sum_{i=1,r,2} L_i^{(2)}(\eta)\theta_{xi} \tag{2.55}$$

Eq. 2.55 serves as an update to Eqs. 2.37 and 2.38 and will vary depending on the order of the polynomial assumed in Eq. 2.52. The interpolation of all other kinematic variables, for both elements, remain the same. The two beam elements thus developed with the additional warping contribution is hereafter referred to as 'iTM2D0W' and 'iTM2D1W'.

2.2 2D inverse Finite Element Method

Although the novel formulation of the beam inverse elements is the main theoretical contribution of this work, existing 2D iFEM formulation for plates, and shells [14, 15] is also briefly discussed here due to its relevance when describing results in later sections.

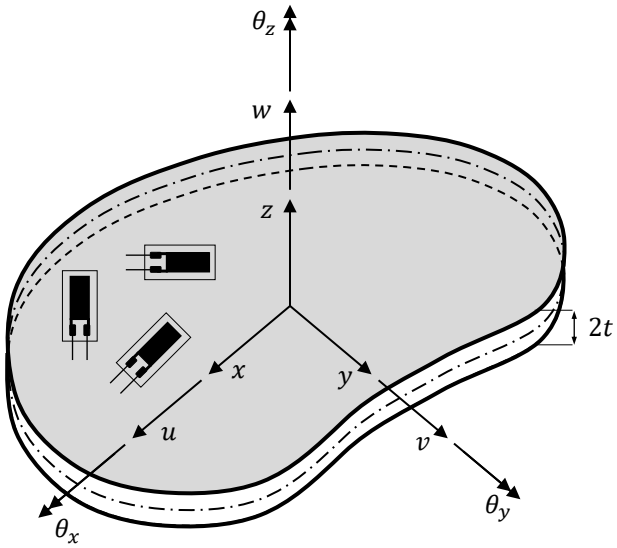

Fig. 2.8 Plate geometry instrumented with strain sensors and the kinematic variables used for defining the plate kinematics

2.2.1 Mindlin Plate Element

Considering a plate structure defined in the three dimensional Cartesian coordinate system (x,y,z) (shown in Fig. 2.8). The plate has an area A, thickness $2t$ and the origin of the z-axis lies on the plate mid-plane.

Plate Kinematics

The iFEM formulation for plates or shells is based on the kinematic assumptions of Mindlin theory [68], where the displacement field is defined using five kinematic variables: $\{u,v,w,\theta_x,\theta_y\}$ (see Fig. 2.8). The Cartesian components of the displacement vector in the orthogonal mid-plane coordinates $\mathbf{x} \equiv \{x,y\}$ of the plate can be represented in terms of the kinematic variables as,

$$\begin{aligned} u_x &= u(\mathbf{x}) + z\theta_y(\mathbf{x}) \\ u_y &= v(\mathbf{x}) - z\theta_x(\mathbf{x}) \\ u_z &= w(\mathbf{x}) \end{aligned} \tag{2.56}$$

where u and v are the in-plane displacements along the x and y-axis, respectively, θ_x and θ_y are the bending rotations about the x and y-axis, respectively, and w is the average transverse deflection across the plate thickness.

The linear strain-displacement relations are used for deriving the strain field of the plate from Eq. 2.56. The in-plane strains of the plate can be described as,

$$\begin{Bmatrix} \varepsilon_{xx} \\ \varepsilon_{yy} \\ \gamma_{xy} \end{Bmatrix} = \begin{Bmatrix} u_{x,x} \\ u_{y,y} \\ u_{x,y}+u_{y,x} \end{Bmatrix} = \begin{Bmatrix} u_{,x} \\ v_{,y} \\ u_{,y}+v_{,x} \end{Bmatrix} + z \begin{Bmatrix} \theta_{y,x} \\ -\theta_{x,y} \\ -\theta_{x,x}+\theta_{y,y} \end{Bmatrix} = \mathbf{e} + z\mathbf{k} \tag{2.57}$$

where **e** are the three membrane strain measures and represent the in-plane stretching of the mid-plane, while **k** are the curvature strain measures and represent the bending of the plate mid-plane.

The transverse shear strains can be described based on Mindlin theory as,

$$\begin{Bmatrix} \gamma_{xz} \\ \gamma_{yz} \end{Bmatrix} = \begin{Bmatrix} u_{z,x}+u_{x,z} \\ u_{z,y}+u_{y,z} \end{Bmatrix} = \begin{Bmatrix} w_{,x}+\theta_y \\ w_{,y}-\theta_x \end{Bmatrix} = \mathbf{g} \tag{2.58}$$

where **g** are the two transverse shear strain measures of the plate.

The strain measures **e**, **k**, and **g** are the eight analytical strain measures of the plate and form one part of the total error functional.

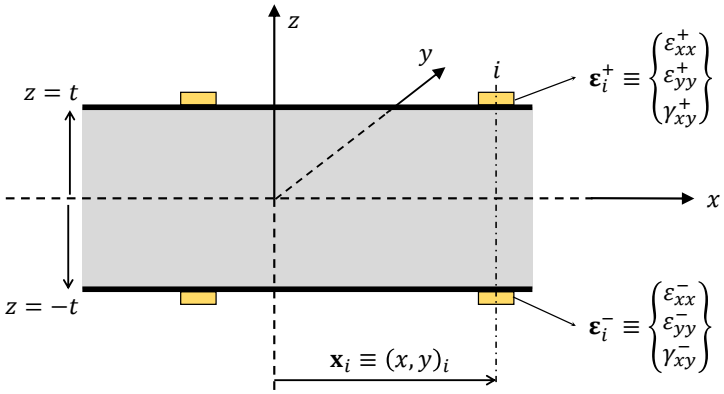

Fig. 2.9 Illustration of the plate thickness instrumented with strain sensors on the top and bottom surfaces; location of the sensors and strain components measured are also shown

Experimental Strain Measures

Assuming the plate to be instrumented with strain sensors, like strain gauges or fiber optic sensors, at discrete locations $\mathbf{x}_i = (x,y)_i$, on its top ($z = t$) and bottom ($z = -t$) surfaces (shown in Fig. 2.9). The strain measures defined in the reference mid-plane coordinates of the plate can be evaluated experimentally using strain measurements on the top, $\boldsymbol{\varepsilon}_i^+ = \{\varepsilon_{xx}^+, \varepsilon_{yy}^+, \gamma_{xy}^+\}_i^T$, and bottom, $\boldsymbol{\varepsilon}_i^- = \{\varepsilon_{xx}^-, \varepsilon_{yy}^-, \gamma_{xy}^-\}_i^T$, surfaces of the

plate as,

$$\mathbf{e}_i^{\varepsilon} = \frac{1}{2}\left(\begin{Bmatrix}\varepsilon_{xx}^{+}\\ \varepsilon_{yy}^{+}\\ \gamma_{xy}^{+}\end{Bmatrix} + \begin{Bmatrix}\varepsilon_{xx}^{-}\\ \varepsilon_{yy}^{-}\\ \gamma_{xy}^{-}\end{Bmatrix}\right)_i \tag{2.59}$$

$$\mathbf{k}_i^{\varepsilon} = \frac{1}{2t}\left(\begin{Bmatrix}\varepsilon_{xx}^{+}\\ \varepsilon_{yy}^{+}\\ \gamma_{xy}^{+}\end{Bmatrix} - \begin{Bmatrix}\varepsilon_{xx}^{-}\\ \varepsilon_{yy}^{-}\\ \gamma_{xy}^{-}\end{Bmatrix}\right)_i \tag{2.60}$$

The shear strain measures $\mathbf{g}^{\varepsilon}$ cannot be obtained directly from experimental strains. The absence of these quantities can be treated with the choice of appropriate weighing coefficients as discussed in the next section.

Error Functional

The iFEM formulation for plates or shells is based on discretising the structural domain using a series of finite elements with element areas, A^e. For each element, e, a functional described as the weighted least-squares error between the analytical and experimental strain measures is formulated as [14, 15],

$$\Phi^e \equiv \mathbf{w}_m\mathbf{\Phi}_m + \mathbf{w}_b\mathbf{\Phi}_b + \mathbf{w}_s\mathbf{\Phi}_s \tag{2.61}$$

where the individual error functionals Φ_m, Φ_b, and Φ_s correspond to the membrane, curvature and shear strain measures, respectively. The row vectors, $\mathbf{w}_m$, $\mathbf{w}_b$, and $\mathbf{w}_s$, are vectors of weighing coefficients defined as,

$$\mathbf{w}_m = [w_1, w_2, w_3], \mathbf{w}_b = [w_4, w_5, w_6], \mathbf{w}_s = [w_7, w_8] \tag{2.62}$$

The individual error functionals can be defined as,

$$\begin{aligned}
\mathbf{\Phi}_m &\equiv \begin{Bmatrix}\phi_1\\ \phi_2\\ \phi_3\end{Bmatrix} = \frac{1}{A^e}\int_{A^e}[\mathbf{e}_i - \mathbf{e}_i^{\varepsilon}]^2 dA \\
\mathbf{\Phi}_b &\equiv \begin{Bmatrix}\phi_4\\ \phi_5\\ \phi_6\end{Bmatrix} = \frac{(2t)^2}{A^e}\int_{A^e}[\mathbf{k}_i - \mathbf{k}_i^{\varepsilon}]^2 dA \\
\mathbf{\Phi}_s &\equiv \begin{Bmatrix}\phi_7\\ \phi_8\end{Bmatrix} = \frac{1}{A^e}\int_{A^e}\mathbf{g}^2 dA
\end{aligned} \tag{2.63}$$

The iFEM solution involves minimizing the element functional of Eq. 2.63 with respect to the nodal DOF of the element to obtain a set of linear algebraic equations,

$$\mathbf{k}^e\mathbf{u}^e = \mathbf{f}^e \tag{2.64}$$

where the matrix $\mathbf{k}^e$ is a function of the strain-sensor positions, and the vector $\mathbf{f}^e$ is a function of the strain-sensor positions and measured strain data. These matrices are analogous to the stiffness and force matrices seen in the direct FE method. The contribution from all the elements are assembled with appropriate coordinate transformations to obtain the global set of equations,

$$\mathbf{KU} = \mathbf{F} \tag{2.65}$$

The requisite boundary conditions are applied for the solution of Eq. 2.65 to constraint the structure against rigid-body motion and ensure that the system matrix $\mathbf{K}$ is non-singular. Subsequently, Eq. 2.65 can be solved to obtain the reconstructed nodal displacements, $\mathbf{U}$, of the structure.

The flow diagram of the entire 2D iFEM procedure is shown in Fig. 2.10. For additional discussions of three and four node shell elements developed and nodal interpolations used, consult Refs. [69, 70, 72].

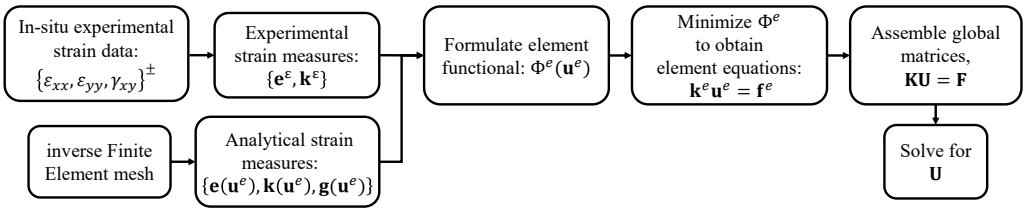

Fig. 2.10 Flow diagram highlighting the major steps for implementing the 2D iFEM procedure

2.2.2 Virtual Sensor Approach for iFEM

As shape sensing strategies are dependent on data obtained from surface-mounted strain sensors, a sufficient number of strain measurements must be ensured to adequately describe the displacement field of the structure. In this aspect, a key limitation of the 2D iFEM is the large number of strain sensors required for accurate shape sensing predictions. Using a low number of strain sensors or absence of measurements at key structural locations can potentially lead to a breakdown of the iFEM procedure.

A solution to this problem is the use of virtual sensing, where a limited set of physical strain measurements are expanded to unmeasured locations. Techniques such as the Smoothing Element Analysis (SEA) [111, 117, 118] or modal expansion can be used for expanding measured strains or strain measures. The success of virtual sensing is dependent on the number and location of physical sensors available, accuracy of the virtual sensing strategy adopted, and also on the complexity of the

strain field investigated. Hence, a suitable virtual sensing scheme can be chosen based on the problem investigated.

Considering a set of expanded or 'smoothed' experimental strain measures, $\{\mathbf{e}_i^{\varepsilon}\}^{(s)}$ and $\{\mathbf{k}_i^{\varepsilon}\}^{(s)}$, the error functional of Eq. 2.61 can be reformulated as,

$$\Phi^e \equiv \mathbf{w}_m \mathbf{\Phi}_m^{(s)} + \mathbf{w}_b \mathbf{\Phi}_b^{(s)} + \mathbf{w}_s \mathbf{\Phi}_s \tag{2.66}$$

where the new individual error functionals are described as,

$$\begin{aligned} \mathbf{\Phi}_m^{(s)} &\equiv \begin{Bmatrix} \phi_1 \\ \phi_2 \\ \phi_3 \end{Bmatrix} = \frac{1}{A^e} \int_{A^e} [\mathbf{e}_i - \{\mathbf{e}_i^{\varepsilon}\}^{(s)}]^2 dA \\ \mathbf{\Phi}_b^{(s)} &\equiv \begin{Bmatrix} \phi_4 \\ \phi_5 \\ \phi_6 \end{Bmatrix} = \frac{(2t)^2}{A^e} \int_{A^e} [\mathbf{k}_i - \{\mathbf{k}_i^{\varepsilon}\}^{(s)}]^2 dA \end{aligned} \tag{2.67}$$

where the superscript (s) indicates smoothed or expanded quantities.

The remaining steps and equations of the iFEM procedure are similar to those explained previously. A flow diagram of the complete coupled iFEM procedure (using SEA for virtual sensor expansion) is shown in Fig. 2.11.

Virtual sensor expansion serves as a useful tool for reducing the number of strain sensors required for a particular shape sensing problem or for avoiding a breakdown of the iFEM procedure in cases with insufficient strain measurements.

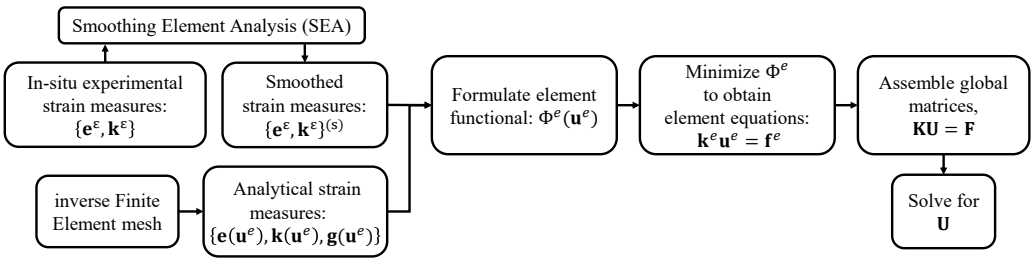

Fig. 2.11 Flow diagram of the coupled iFEM-SEA highlighting the major steps involved

Chapter 3

Beam Shape Sensing: Numerical Studies

The novel inverse beam elements formulated in Chapter 2 are validated numerically in this chapter. Commercial finite element method (FEM) codes are used to model various simple and complex beam structures under different loading conditions. The resulting FEM strains are used as input for the iFEM procedure. Subsequently, the accuracy of iFEM reconstructed displacements is compared against the reference FEM displacements. Preliminary investigations using numerical strains are useful for establishing a benchmark iFEM accuracy without considering the influence of measurement errors, experimental noise, etc.

This section begins with an investigation of the effect of sensor position on shape sensing accuracy for beams with complex cross-sections. The inferences from this study are applied to later problems where different beam geometries, increasing in complexity from prismatic to tapered, solid to thin-walled cross-sections, are studied. For each case, the reconstruction accuracy of the major displacement and rotation components are quantified, based on which conclusions are derived on the efficacy of these new elements in predicting the axial, bending, shear and torsional deformations of the beam.

3.1 Optimal Sensor Placement

Calculation of the experimental sectional strains (e.g. using Eq. 2.15) is influenced by the position and orientation of strain sensors on the beam surface. An optimal sensor position maximises the quantity and quality of measured strain information. Hence, configurations with sensors placed extremely near or far from one another or in the close vicinity of a free or fixed end of the beam are not suitable. For

beams with complex cross-sections, like an airfoil with one or no symmetry planes, the optimal choice of sensor locations is not obvious. Hence, an iterative study is performed to identify suitable sensor locations that guarantee high reconstruction accuracy for the various displacement components of the beam.

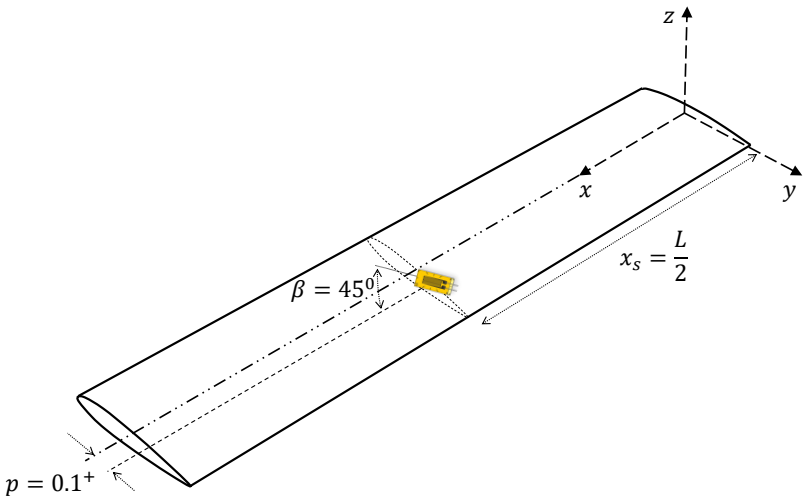

Fig. 3.1 Illustration of an airfoil beam showing the parameters, p, x_s, and β, that describe the position and orientation of strain sensors instrumented on the beam surface; sensor in the present case is described by the notation: $[0.1^+, \frac{L}{2}, 45]$

To aid this optimal sensor placement effort, it is useful to establish convenient and efficient notations for describing the position and orientation of strain sensors instrumented on the beam surface. As the present section aims to investigate beams with airfoil profiles, the notation proposed is $[p^{\pm}, x_s, \beta]$, where p is the distance (measured along the chord line of the airfoil) between the sensor location and the centroid, and normalized with respect to the chord length. Here, the superscript represents sensor positions on either the upper $(+)$ or lower $(-)$ surface of the airfoil profile. The axial position of the sensor, measured from the root, is denoted by x_s, and the angle β describes sensor orientation with respect to the beam axis. These parameters are described graphically in Fig. 3.1.

The sensor shown in Fig. 3.1 is described by the notation, $[0.1^+, \frac{L}{2}, 45]$, indicating a sensor on the upper surface of the profile and placed 10% of the chord length from the section centroid, at half the beam length from the root, and oriented at an angle of 45^0 with respect to the x-axis. Although the present notation is developed primarily focusing on airfoil profiles, it is expected to be translatable, with minor adaptations, to other profiles.

Table 3.1 Geometrical and material properties of the airfoil beam investigated

Material	Young's Modulus (GPa)	Poisson's Ratio	Density (kg/m^3)
Aluminium	73	0.3	2700

The present study aims to identify the optimal sensor locations for a prismatic beam with a solid symmetric airfoil profile (NACA 0016). The beam is cantilevered and loaded at the tip by unit concentrated loads oriented along the transverse y and z axes. The beam is made of an aluminium alloy with material properties described in Table 3.1. The size of the beam geometry, along with the loading and boundary conditions, are shown in Fig. 3.2.

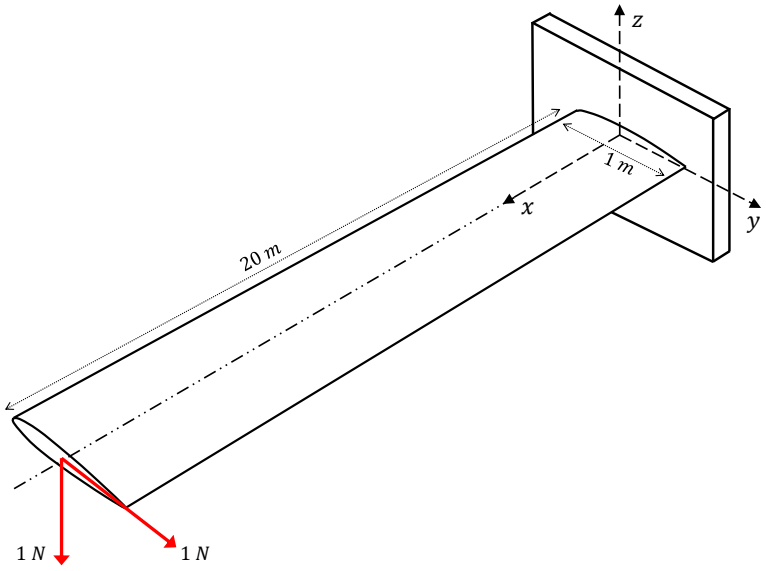

Fig. 3.2 Illustration of the airfoil beam problem used for the optimal sensor placement effort; values for beam and chord length are shown along with the fixed root and transversely loaded tip (the drawing and dimensions are only representative and not to scale)

For the present problem, the influence of axial position is not investigated, and hence, x_s is not an optimization variable. Two fixed axial locations are used, $x_s = \frac{L}{3}, \frac{2L}{3}$, equally distant from the tip, root and one another. At each section, x_s, the parameter, p, is iterated to evaluate three suitable positions along the beam perimeter, where sensors oriented at $\beta = 0^0$ and $\beta = 45^0$ are instrumented. Two additional requirements are also imposed, i.e. the sensor positions are symmetric and equally spaced with respect to the beam centroid. Additionally, the absolute value of p is constrained within the limits of 5% and 35% to avoid sensor positions excessively close to the leading or trailing edge of the airfoil section. Based on these conditions, the

sensor configuration for this study can be described as: $[(\pm p^{+}, 0^{-}), (\frac{L}{3}, \frac{2L}{3}), (0, 45))]$, where p is the only parameter iterated and a total of 12 strain gauges (six at each section) are instrumented on the beam (see Fig. 3.3).

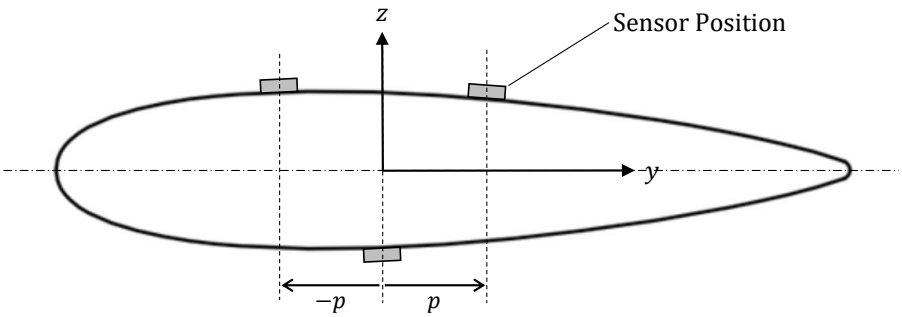

Fig. 3.3 Sensor configuration for the optimal sensor placement effort defined with respect to the iteration parameter p (each sensor position is composed of two strain gauges oriented at 0^0 and 45^0 with respect to the beam axis)

The numerical strain data required for the iFEM analysis are obtained from a high-fidelity direct FEM beam model implemented in ABAQUS. Details of FEM model discretisation for the current and subsequent problems are provided in Appendix B.1. For each value of p, the numerical strains corresponding to the sensor positions are extracted and used for the iFEM analysis. Shape reconstruction is performed using one iTM2D0 element. Reconstructed results are compared against reference FEM displacements to evaluate the percentage error in axial and transverse tip displacements based on the equation,

$$u_1^{err} = \frac{u_1^{FEM} - u_1^{iFEM}}{u_1^{FEM}} \times 100 \tag{3.1}$$

where, $u_1 \in \mathbf{u} \equiv \{u, v, w, \theta_x, \theta_y, \theta_z\}^T$ are the nodal displacements and rotations of the beam element. Results of the iterative study are presented as plots of tip displacement error as a function of p and these results are shown in Figs. 3.4 and 3.5.

The results of Fig. 3.4 demonstrate a conflicting behaviour where u^{err} decreases and v^{err} increases with increase in sensor distance from the centroid. Fig. 3.5a shows a similar behaviour where w^{err} also increases with p. It should be noted that the errors observed are very small, i.e. $< 2\%$, with different magnitudes for each component. Due to the asymmetrical nature of the beam profile, for the present loading case, w is the major deflection component (because $I_{zz} > I_{yy}$) and hence reports a lower error compared to u and v.

Due to the contrasting behaviour and magnitudes of each displacement error component, the individual error plots are normalized such that the error range lies

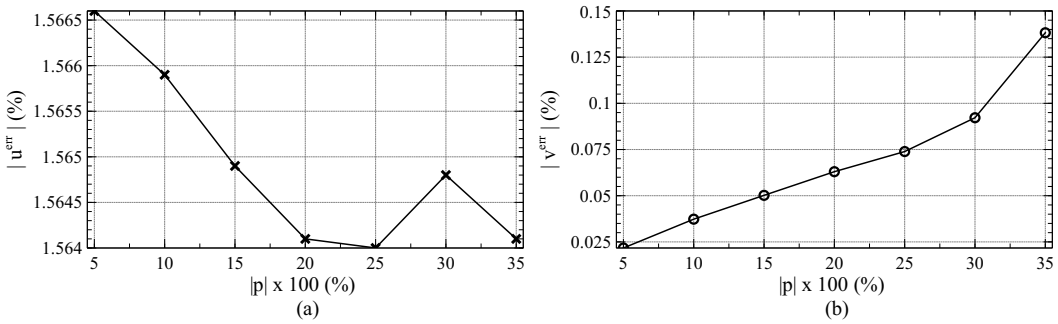

Fig. 3.4 Absolute value of percentage error in tip displacement components: (a) u, and (b) v, plotted as a function of the parameter p (horizontal axis is multiplied by 100 to plot the absolute value of p as a percentage of chord length)

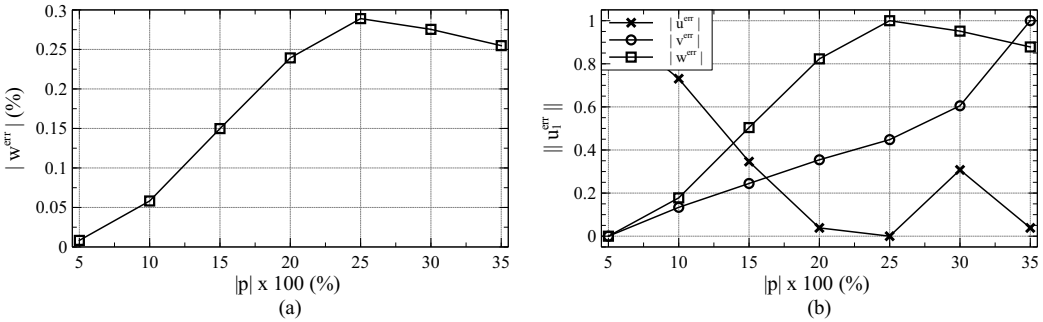

Fig. 3.5 Results of the iterative study showing: (a) absolute value of percentage error in tip deflection w, and (b) normalized error of all three tip displacement components, plotted as a function of the parameter p

within the interval $[0,1]$ using,

$$||u_1^{err}|| = \left(\frac{u_1^{err} - u_1^{err}|_{min}}{u_1^{err}|_{max} - u_1^{err}|_{min}} \right) \tag{3.2}$$

where the notations $|_{max}$ and $|_{min}$ represents the maximum and minimum value of the displacement error. For ease of interpretation, the normalized errors in u, v, and w are combined into a single plot and shown in Fig. 3.5b. An ideal value of p minimises all three displacement components. However, due to the conflicting nature of their behaviours, that is challenging. Based on Fig. 3.5, $|p| = 0.1 - 0.2$, i.e., sensors placed 10-20% of the chord length from the beam centroid present a suitable trade-off between all three errors and is identified as optimal. The axial position of the sensors is not investigated in the present study because, aside from strain measurements near the beam tip and root that are affected by their vicinity to these fixed and loaded ends, iterating sections sufficiently far away are not expected to produce any significant changes in iFEM predictive capabilities.

The results of the present study are instructive and inspire those sensor configurations used in subsequent numerical and experimental shape sensing investigations involving prismatic and non-prismatic airfoil beams.

3.2 Prismatic Beam Problems

Numerical shape sensing problems involving solid and thin-walled beam geometries with symmetric and cambered airfoil profiles are addressed in this section. The main emphasis is on evaluating transverse deflection and torsional rotation reconstruction accuracies. Additionally, beams subjected to different concentrated and distributed load cases are also investigated to contrast iFEM performance between the iTM2D0 and iTM2D1 inverse elements.

3.2.1 Concentrated Load Case

The first problem explored evaluates the use of iTM2D0 for the shape sensing of a solid prismatic beam with a cambered airfoil profile (NACA 6516). The beam is cantilevered at the root and subjected to a generalised tip load applied at the beam centroid and composed of concentrated forces and moments of magnitude, $F = 1$ N, and $M = 1$ Nm. The beam material is an aluminium alloy with properties described in Table 3.1. The size of the beam, along with the boundary and loading conditions, are shown in Fig. 3.6. Application of such a generalised load causes axial, bending, shear and torsional deformation of the beam and allows for an assessment of the reconstruction accuracy of all six kinematic variables.

The numerical strain data are obtained from a high fidelity FEM model of the beam developed in ABAQUS and meshed using linear brick elements, C3D8R (mesh details in Appendix B.1). The numerical strain data are extracted at sensor locations identified based on the results of Section 3.1 (shown in Table 3.2). Despite the cambered nature of the profile in the present problem, the previous conclusions regarding sensor positions are expected to remain effective as the degree of airfoil camber is not significant. iFEM analysis using only one iTM2D0 element and 12 strain measurements are expected to provide accurate results for the present structure because the nature of loading corresponds well with the interpolation order of kinematic variables within the element [73].

The results of the iFEM analysis are shown in Fig. 3.7, where the reconstructed displacements and rotations along the beam axis are plotted against reference FEM solutions. These plots help in assessing reconstruction accuracy throughout the entire beam. Additionally, the percentage error is computed at the beam tip (as the highest magnitude of each component is obtained at the tip), and these values are given in

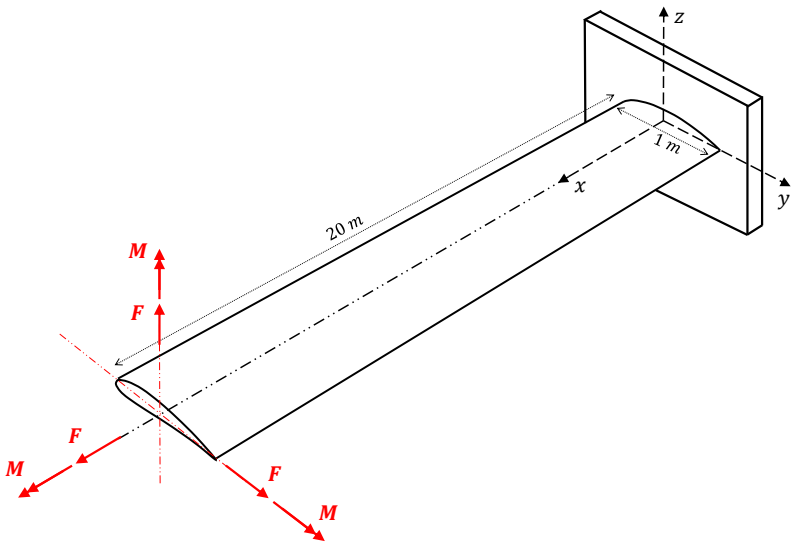

Fig. 3.6 Illustration of the cambered airfoil beam problem showing the values of beam and chord length; cantilever condition and tip loading is also shown (the drawing and dimensions are only representative and not to scale)

Table 3.2 Sensor positions used and the absolute value of percentage error in the tip displacements and rotations for the solid NACA 6516 airfoil beam are reported

Sensor Position	$\lvert u^{err}\rvert$	$\lvert v^{err}\rvert$	$\lvert w^{err}\rvert$	$\lvert \theta_x^{err}\rvert$	$\lvert \theta_y^{err}\rvert$	$\lvert \theta_z^{err}\rvert$
$[(\pm 0.1^+, 0^-), (\frac{L}{3}, \frac{2L}{3}), (0, 45))]$	0.06	0.05	1.56	0.12	1.71	0.01

Table 3.2. The results presented above show the iFEM predictions to be very accurate. The percentage error values reported in Table 3.2 reveal a maximum tip displacement or rotation error less than 2%. Due to the asymmetrical nature of the beam profile, the moments of inertia of the cross-section are not equal ($I_{zz} > I_{yy}$). This is reflected in the magnitude of transverse deflections as well, i.e. $w > v$. However, there is no significant difference in accuracy between v and w, with both reconstructions equally accurate. The high accuracy of torsional rotation ($\theta_x^{err} = 0.12\%$) is the most important aspect of these results as it provides the first independent verification of the novel treatment of shear strains in the iTM2D0 element.

The plot of Fig. 3.7a also reveals dissimilarities in the axial distribution of the iFEM and FEM results. However, this is explained by the low iFEM discretisation employed in the present problem. As iTM2D0 interpolates u linearly, and only one inverse beam element is used, the iFEM results are consistent with the element formulation. A finer inverse element mesh with more iTM2D0 elements is expected to lead to a more accurate u distribution prediction.

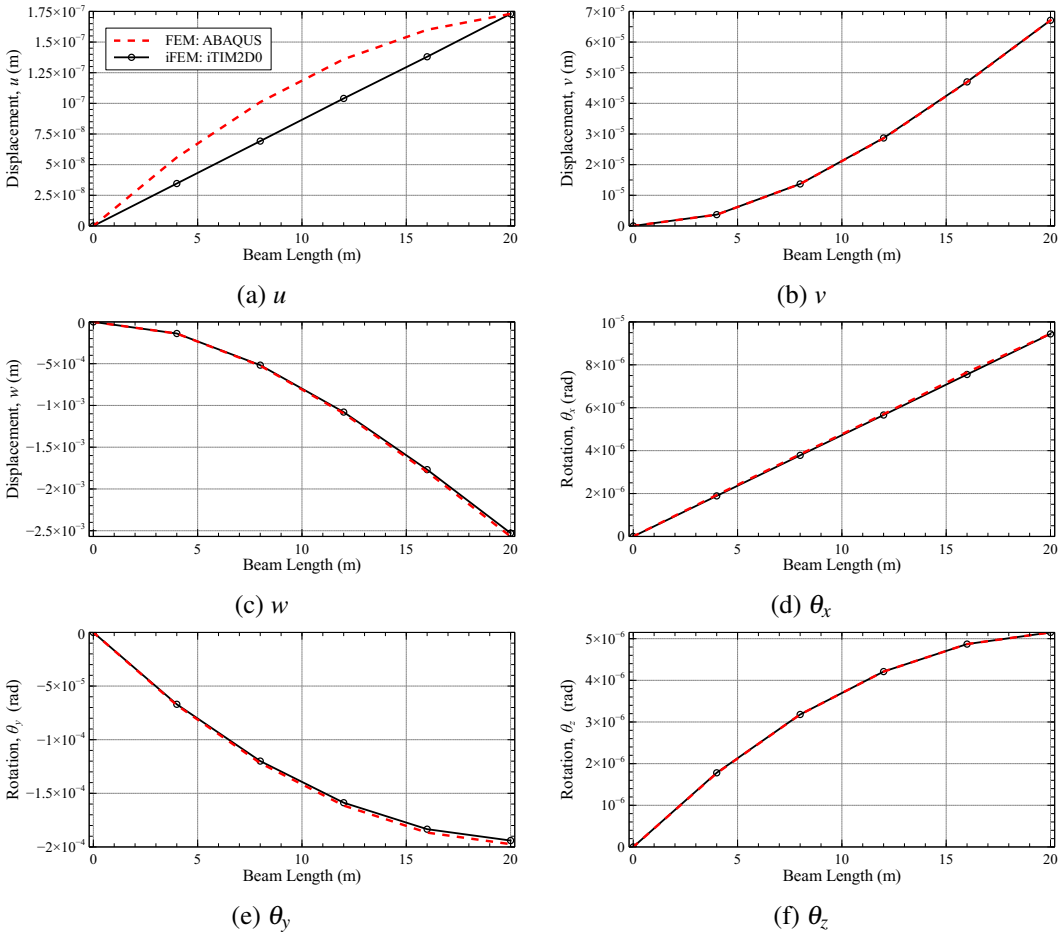

(a) u (b) v

(c) w (d) θ_x

(e) θ_y (f) θ_z

Fig. 3.7 iFEM reconstructed axial distribution of displacements and rotations for the solid NACA 6516 airfoil beam compared against the reference FEM results

3.2.2 Distributed Load Case

The second problem of this section compares the performance of iTM2D0 and iTM2D1 elements for the shape sensing of thin-walled prismatic beams. Two separate beam models are investigated: the first with a symmetric (NACA 0016) and the second with a cambered (NACA 6516) airfoil profile, each with a thickness of 5 mm. The beams are cantilevered at the root and subjected to uniform and non-uniform distributed loads. Compared to the problem of Section 3.2.1, the presence of distributed loads is expected to produce differences in reconstruction performance between the two elements.

The NACA 0016 airfoil beam is subjected to a uniform distributed load of magnitude, $P_1(x) = 1$ N/m, while the NACA 6516 airfoil beam is subjected to a

non-uniform distributed load of magnitude,

$$P_2(x) = \frac{1}{L^2}\left(L^2 - x^2\right) \quad \text{N/m} \tag{3.3}$$

where L is the beam length and $0 < x < L$. The load distribution, P_2, is parabolic and models the aerodynamic load distribution experienced on the wing of an aircraft, where the load is highest at the root ($P_2(0) = 1$ N/m) and vanishes at the tip. The material for both beams is an aluminium alloy with properties described in Table 3.1. The size of the two beams, along with the boundary and loading conditions, are shown in Fig. 3.8.

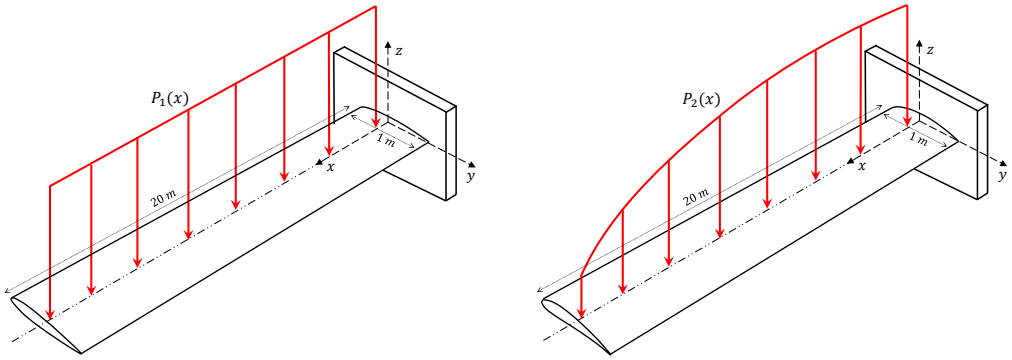

(a) (b)

Fig. 3.8 Illustration of the thin-walled beam (5 mm thick) with: (a) NACA 0016 profile and under uniform distributed loading (P_1), and (b) NACA 6516 profile under non-uniform distributed loading (P_2); the values of beam and chord length are indicated (the drawing and dimensions are only representative and not to scale)

The numerical strain data are obtained from high fidelity FEM models of the beams developed in ABAQUS, where the thin-walled geometries are meshed using the four-node shell element, S4R (mesh details in Appendix B.1). The sensor locations used and the number of strain measurements extracted from the numerical model depend on the inverse element employed. These details are provided in Table 3.3. Compared to the sensor positions of Section 3.2.1, the sensors here are positioned further from the beam centroid ($p = 0.2$) but are still within the range proposed by the sensor placement study. Due to the higher-order shape functions used in iTM2D1, the element requires more strain measurements (18, at three different sections) than the iTM2D0 element (12, at two different sections). Refer to Section 2.1.2 for further discussions regarding element interpolations.

The shape sensing results for the thin-walled NACA 0016 airfoil beam are shown in Fig. 3.9, where the major transverse deflection and bending rotation (corresponding to the loading along z-axis) reconstructed using both inverse elements are plotted against reference FEM solutions. The other displacement components are

over one order of magnitude lower and hence considered negligible. Additionally, the percentage error in reconstruction results, calculated at the beam tip, are given in Table 3.4.

Table 3.3 Number and location of strain gauges used for the two inverse beam elements implemented in the present distributed loading problem

Beam Element	No. of Strain Gauges	Sensor Position
iTM2D0	12	$[(\pm 0.2^+, 0^-), (\frac{L}{3}, \frac{2L}{3}), (0, 45))]$
iTM2D1	18	$[(\pm 0.2^+, 0^-), (\frac{L}{4}, \frac{L}{2}, \frac{3L}{4}), (0, 45))]$

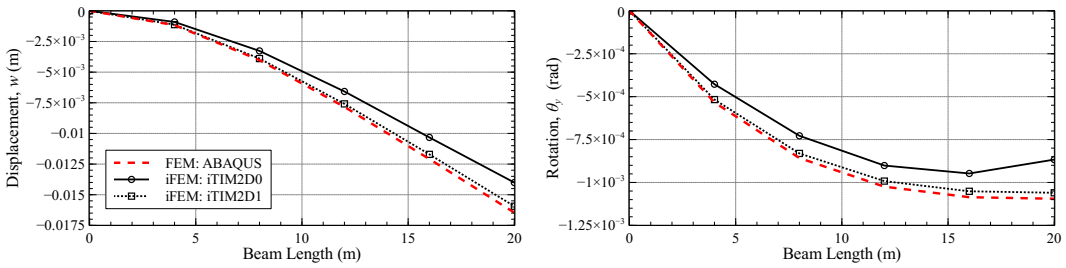

(a) w (b) θ_y

Fig. 3.9 iFEM results for the thin-walled NACA 0016 airfoil beam under a uniform distributed load; reconstructed (a) transverse deflection, and (b) bending rotation, along the beam axis is compared against the reference FEM results

As the present problem deals with beams under distributed loading, the higher-order interpolations of the iTMD1 element are expected to produce more accurate results. The iFEM results back this assertion with the use of only one iTM2D1 element sufficient to produce results with a tip error < 4 %. The plots of Fig. 3.9 also demonstrate that the iTM2D1 results are accurate across the beam length. However, it must be stated that this increase in accuracy is achieved at the cost of a greater number of strain measurements. In comparison, results using one iTM2D0 element reported higher errors (> 10 %) and can be considered inaccurate. A finer iFEM mesh using more iTM2D0 elements could be a viable strategy for improving the accuracy of the present problem.

The shape sensing results for the thin-walled NACA 6516 airfoil beam using both inverse elements are shown in Fig. 3.10 and the tip errors are reported in Table 3.4. These results present similar conclusions, with the iTM2D0 element producing errors as high as 20%, while the iTM2D1 element is much more accurate (errors less than 5%). It is interesting to note that despite the difference in the sectional profiles between the two beams, the results obtained are very similar. The lower accuracy of

iFEM results in this latter case is attributed to the greater complexity of the beam profile and loading condition.

Table 3.4 Absolute value of percentage error in tip deflection, w, and rotation, θ_y, for the two beam models under distributed loading, calculated based on the iTM2D0 and iTM2D1 element results

NACA Profile	Loading	$\lvert w^{err} \rvert$		$\lvert \theta_y^{err} \rvert$	
		iTM2D0	iTM2D1	iTM2D0	iTM2D1
0016	P_1	14.90%	3.15%	13.41%	3.17%
6516	P_2	21.27%	0.31%	16.65%	4.16%

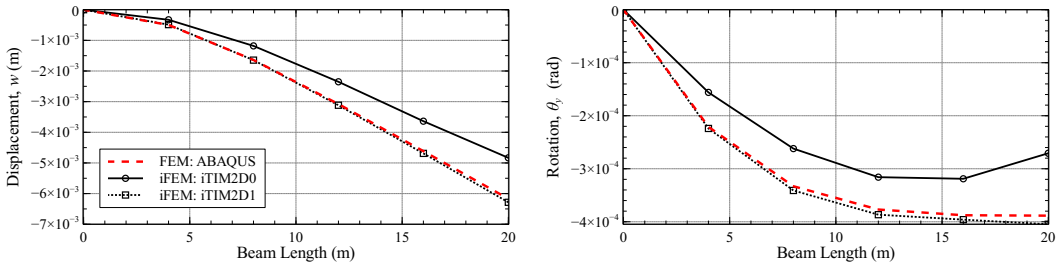

(a) w (b) θ_y

Fig. 3.10 iFEM results for the thin-walled NACA 6516 airfoil beam under a non-uniform distributed load; reconstructed (a) transverse deflection, and (b) bending rotation, along the beam axis is compared against the reference FEM results

This section concludes with a short discussion on the main conclusions derived:

- A key achievement is the numerical validation of the shear strain treatment in the new beam elements developed;
- Accuracy of deflection results for different airfoil beam models also points to the general applicability of these elements for different beam profiles;
- Finally, the choice of the inverse element used is critical in determining the iFEM accuracy for the problem investigated. The lower-order iTM2D0 element is accurate for concentrated loading scenarios, while the higher-order iTM2D1 element is more accurate for distributed loading scenarios.

3.3 Non-Prismatic Beam Problems

The beam problems investigated in the previous sections were all prismatic. To assess the limits of shape sensing performance for the beam elements formulated,

it is of interest to expand our investigations further to non-prismatic geometries, e.g., like an aircraft wing where the airfoil profile varies along the wingspan. Such geometries were the main inspiration behind the updated experimental sectional strain calculation described in Section 2.1.3. This section presents a preliminary investigation of non-prismatic beams considering the problem of shape sensing tapered airfoil beams, where the same profile is tapered from the root to the tip. The main aim is to draw distinctions with previous results regarding changes in sensor quantity and reconstruction accuracy.

Two thin-walled airfoil beam geometries are considered: the first with a symmetric (NACA 0016) and the second with a cambered (NACA 6516) airfoil profile, each with a thickness of 5 mm. Both beams are cantilevered at the root and subjected to uniform (P_1) and non-uniform (P_2) distributed loads, similar to the load cases explored in Section 3.2.1. The material for the beams is an aluminium alloy with properties described in Table 3.1. The dimensions, loading, and boundary conditions of the two beams are shown in Fig. 3.11. The ratio of root to tip chord lengths for the beams in this case is 3:1.

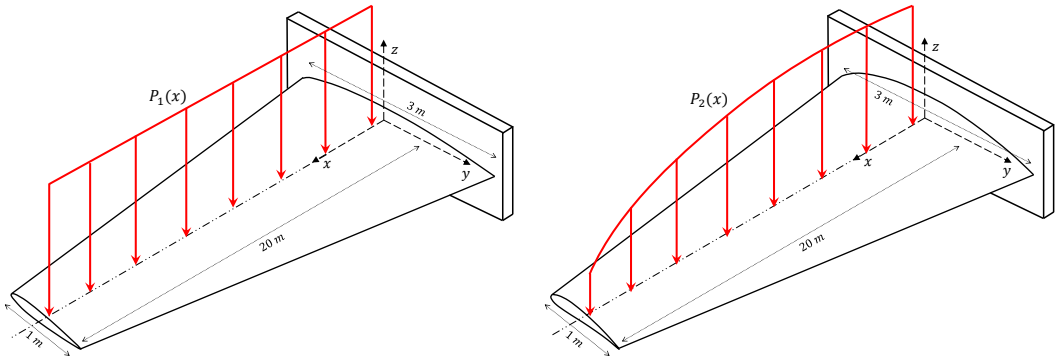

(a) (b)

Fig. 3.11 Illustration of the thin-walled (5mm thick) tapered beams with: (a) NACA 0016 profile and under a uniform distributed load (P_1), and (b) NACA 6516 profile and under a non-uniform distributed load (P_2); the values of beam, root chord, and tip chord lengths are indicated (the drawing and dimensions are only representative and not to scale)

Similar to previous problems, the numerical strain data are obtained from high-fidelity FEM models. The iFEM mesh uses one inverse element, either iTM2D0 or iTM2D1, and the number and location of strain measurements correspond to the sensor positions described in Table 3.3. As the airfoil profile changes in size along the beam span, the parameter p is defined with respect to the local airfoil chord length at each axial section. The iFEM results are presented as plots of the major transverse deflection component along the beam length, shown in Fig. 3.12, and percentage errors in tip deflection are reported in Table 3.5. For both cases, the results using both beam elements are accurate across the beam length. Compared

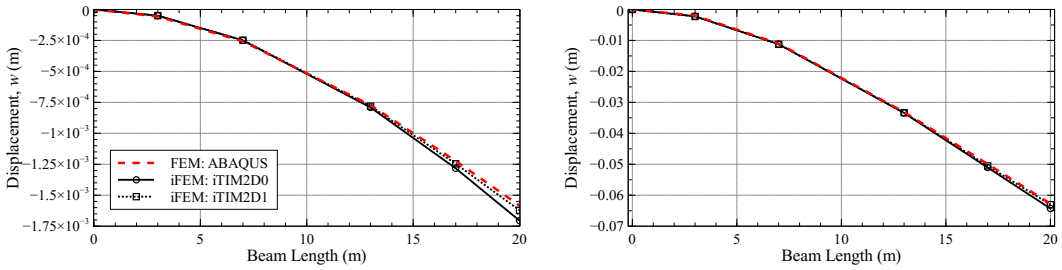

Fig. 3.12 iFEM reconstructed transverse deflection plots, compared against reference FEM results, for the tapered thin-walled: (a) NACA 0016 airfoil beam, and (b) NACA 6516 airfoil beam, under distributed loading

to the results of Section 3.2.2, the iTM2D0 results see an improvement in accuracy ($< 8\%$), while the iTM2D1 results are similar ($< 3\%$). Again, the iTM2D1 element is more accurate, but at the cost of an increased number of sensors required.

Table 3.5 Absolute value of percentage error in tip deflection, w, for the two tapered beam models under distributed loading, calculated based on iTM2D0 and iTM2D1 element results

NACA Profile	Loading	$\lvert w^{err} \rvert$	
		iTM2D0	iTM2D1
0016	P_1	7.60%	2.40%
6516	P_2	2.46%	0.47%

These results further reinforce the conclusions of the previous section, i.e., the superior accuracy of the iTM2D1 element. However, it also highlights that the iTM2D0 element, although less accurate, is still a viable option requiring less number of sensors. The reason behind the difference in iTM2D0 accuracy between the prismatic and non-prismatic beam cases is not evident and warrants further investigation. Nonetheless, these results validate the formulation of Section 2.1.3 and suggest that these elements can potentially be used for the shape sensing of more complex variable sections or swept beams. Some of these cases are explored in later chapters.

3.4 Thin-Walled Beam Problems

The final section of this chapter investigates the shape sensing of thin-walled beams, particularly the effect of cross-sectional warping caused by torsion. A more detailed scrutiny of thin-walled structures is relevant as their low mass and high stiffness has

made them highly appealing for aerospace applications. The presence of warping affects the axial displacement distribution across the beam cross-section. Correspondingly the strains measured on the beam surface are also affected. The iTM2D0W element (see Section 2.1.4) was formulated considering the effect of warping in the sectional strain calculation and uses a higher-order interpolation for torsional rotation. The present section investigates the use of the new iTM2D0W element for the numerical shape sensing of thin-walled beams undergoing warping. The performance of this novel beam element is evaluated by comparing it with iTM2D0 element results.

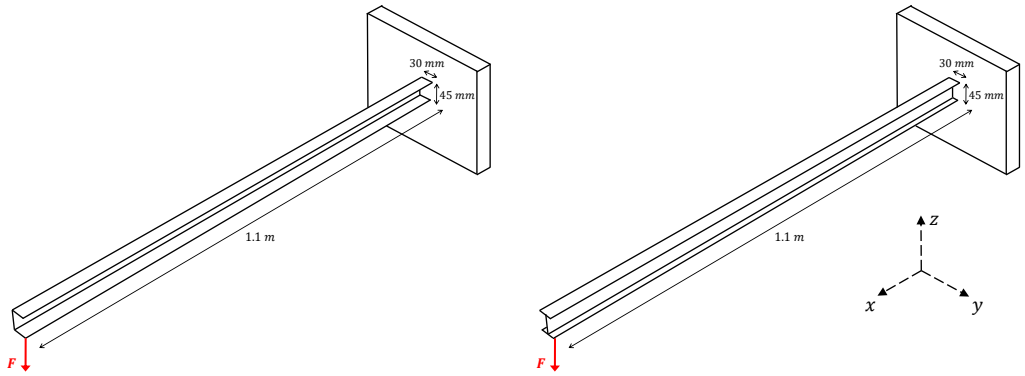

Fig. 3.13 Illustration of the thin-walled (2 mm thick) beams with a: (a) C profile, and (b) I profile, under an off-centric concentrated tip load; the beam dimensions and boundary conditions are shown

Two different beams, with a C and I profile, respectively, are considered, each having a flange thickness of 2 mm. Both beams are cantilevered and loaded by a concentrated transverse force of magnitude 100 N. In both cases, the force is applied away from the shear center (15 mm from the midpoint of the vertical flange), leading to combined bending and torsional deformation. The dimensions, boundary, and loading conditions of the beams are shown in Fig. 3.13. The material of the beams is an aluminium alloy with properties described in Table 3.1.

The numerical strain data are obtained from high-fidelity FEM models developed in ABAQUS, where the geometries are meshed using four-node shell elements (S4R). The C beam is meshed using a total of 924 elements (21 per cross-section and 44 along the length), and the I beam with 880 elements (20 per cross-section and 44 along the length). A total of 12 numerical strain measurements are used per element, and the corresponding sensor positions are described in terms of their three-dimensional coordinates in Table 3.6 and shown graphically in Fig. 3.14.

Table 3.6 Number and location of strain sensors used for the two thin-walled beams; the sensor coordinates are described with respect to a coordinate system positioned on the middle of the vertical flange and located at the root of the beam (all dimension are in mm)

Beam Profile	Sectional Positions (y,z) $\beta = 0^0$	$\beta = 45^0$	Axial Positions
C	$(21.8, 22.5)$ $(-1.0, 9.6)$ $(7.3, -22.5)$	$(7.3, 22.5)$ $(-1.0, -9.6)$ $(21.8, -22.5)$	$L/3$, $2L/3$
I	$(12.5, 22.5)$ $(-12.5, 22.5)$ (2.5,-22.5)	$(12.5, 20.5)$ $(-12.5.0, 20.5)$ $(2.5, -20.5)$	$L/3$, $2L/3$

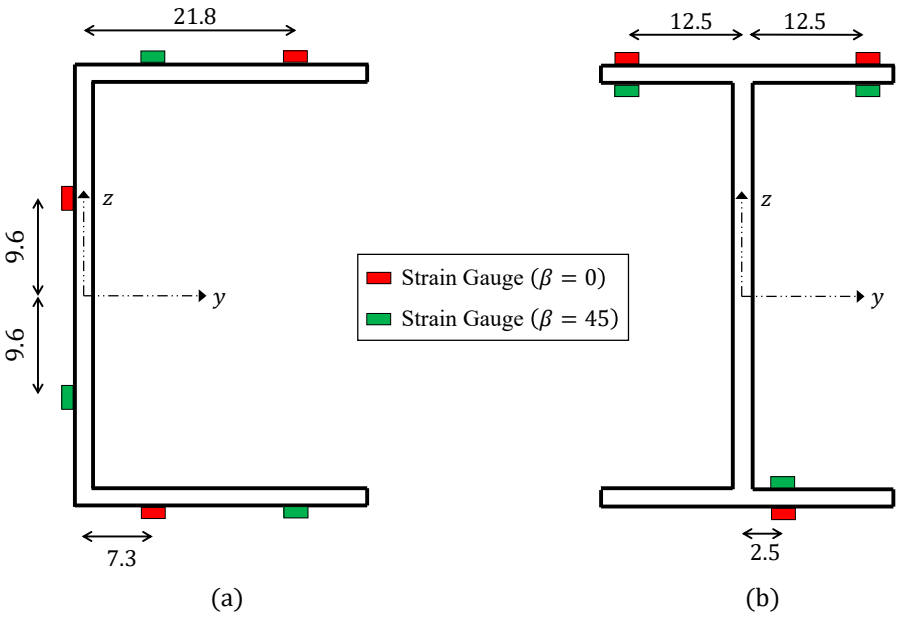

Fig. 3.14 Strain gauge positions at each axial section (as described in Table 3.6) for the thin-walled: (a) C, and (b) I beam (all dimensions are in mm)

iFEM reconstruction for each beam is performed using one iTM2D0 and one iTM2D0W element. The iFEM results for both beams are shown in Figs. 3.15 and 3.16, and the percentage error in the tip deflection and rotation components are reported in Table 3.7. These results are interesting as it shows that, for the C beam, the use of the iTM2D0W element leads to a decrease in w and an increase in θ_x reconstruction accuracy. It should also be noted that the change in tip error magnitude is greater for θ_x (-12.6%) than for w (5%). The results indicate that

improvement in θ_x accuracy is at the cost of w prediction, illustrating the coupling due to the introduction of the warping contribution.

Another interesting aspect of the results is the axial distribution of θ_x, as shown in Fig. 3.15b. As the iTM2D0 element uses a linear interpolation of θ_x, the results are also linear. However, the reference θ_x is non-linear. A key objective of this effort is the modelling of this non-linear distribution using the higher-order interpolations of the iTM2D0W element. Although it produced more accurate results at the tip, the internal distribution of θ_x is inaccurate and could be improved by increasing the number of inverse elements used.

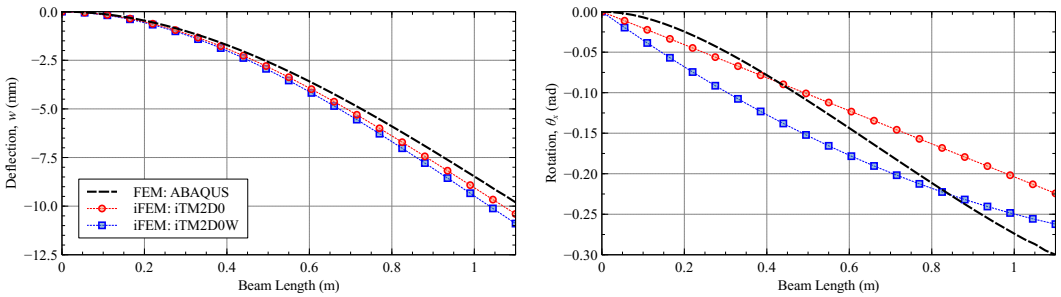

(a) w (b) θ_x

Fig. 3.15 iFEM results for the thin-walled C beam under a concentrated tip load; reconstructed: (a) transverse deflection, w, and (b) torsional rotation, θ_x, distribution along the beam length and compared against reference FEM solutions

Table 3.7 Absolute value of percentage error in transverse deflection, w, and torsional rotation, θ_x, for the two thin-walled beams using the iTM2D0 and iTM2D0W elements

Beam Profile	Loading	$\lvert w^{err} \rvert$		$\lvert \theta_x^{err} \rvert$	
		iTM2D0	iTM2D0W	iTM2D0	iTM2D0W
C	F	6.07%	11.11%	25.22%	12.56%
I	F	1.90%	1.19%	6.01%	6.04%

The iFEM results for the I beam are equally interesting as no substantial difference is observed between iTM2D0 and iTM2D0W element results. This is intriguing considering the previous case explored, and a possible explanation is that depending on the beam cross-section, the degree or magnitude of warping is different. If warping is negligible, the influence on surface strain measurements is also small and is a limit case for the iTM2D0W element, where it approaches iTM2D0 element behaviour. In the present case, as both beams are subject to loads of similar magnitude, the higher torsional stiffness of the I beam can be an explanation for the results obtained. An encouraging aspect is that despite these observations, the errors for tip

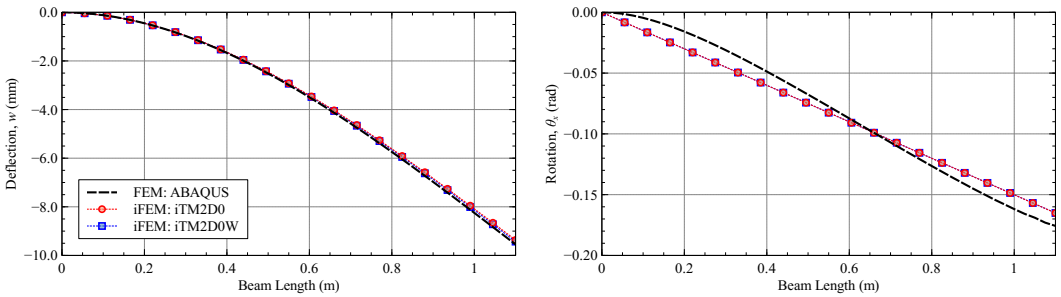

(a) w (b) θ_x

Fig. 3.16 iFEM results for the thin-walled I beam under a concentrated tip load; reconstructed: (a) transverse deflection, w, and (b) torsional rotation, θ_x, distribution along the beam length and compared against reference FEM solutions

deflection ($<$2%) and torsional rotation (6%) are already small for both elements. Hence, it can be argued that using the iTM2D0W element is not imperative in this case.

This section presented a preliminary study on using the iTM2D0W element for modelling thin-walled beams undergoing warping. Despite improvements observed in the prediction of torsional rotation, it is concluded that additional investigations are required. The equation for axial displacement due to warping for open sections (Eq. 2.43) was derived based on the assumption that shear strain vanishes on the flange midline [115]. The validity of this assumption will affect the accuracy of the iFEM results. More complex cases where the structure is under non-uniform torsion [116] require improved models to describe the distribution of warping displacement and torsional strain and are left for future work.

Chapter 4

Shape Sensing Applied for SHM Applications

This chapter presents several numerical studies investigating the use of 1D, and 2D iFEM approaches for Structural Health Monitoring (SHM) applications. The numerical studies are aimed at:

- Identifying optimal strain sensor positions or patterns for efficient shape sensing using 2D iFEM;
- Developing damage detection and localisation strategies based on iFEM.

At the end of the chapter, the conclusions from these studies are combined to develop an integrated iFEM-based real-monitoring framework for aerospace structures.

4.1 Efficient Strain Sensor Patterns

The number and location of strain sensors used are two important factors that influence the accuracy of iFEM results. This was addressed in a limited manner for beam shape sensing problems in Section 3.1. However, compared to 1D iFEM, a key limitation of 2D iFEM is the large number of strain sensors required to generate accurate shape sensing results. Hence, it is imperative to identify optimal sensor locations or simple sensor patterns that reduce the number of sensors required without compromising 2D iFEM accuracy. Although optimisation techniques are commonly proposed for this problem [108, 109], the results are often specific to the structure or loading condition investigated and are not easily generalisable. The present section investigates the design of simple and easily reproducible strain-sensor patterns that can guarantee stable and accurate iFEM predictions of the deformed shape of the structure.

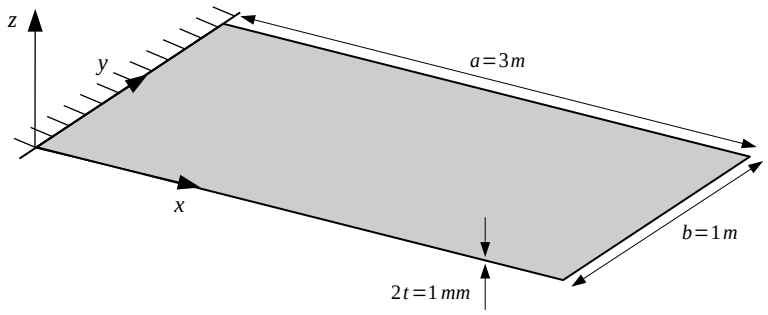

Fig. 4.1 Illustration of the cantilevered plate problem used for identifying efficient sensor patterns; plate dimensions and boundary conditions are shown

The investigation of efficient strain sensor patterns is performed numerically, considering the problem of shape sensing the vibrational modes of a cantilevered rectangular plate. The plate has a length, $a = 3$ m, width, $b = 1$ m, and thickness, $2t = 1$ mm, and is clamped at one of its short ends as shown in Fig. 4.1. The material of the plate is an aluminium alloy of Young's modulus $E = 73$ GPa, Poisson's ratio $\nu = 0.3$, and density $\rho = 2700$ kg/m^3 (Table 3.1). The displacement fields corresponding to the first six vibration modes of the plate serve as the reference for this study and are shown in Figs. 4.2 and 4.3.

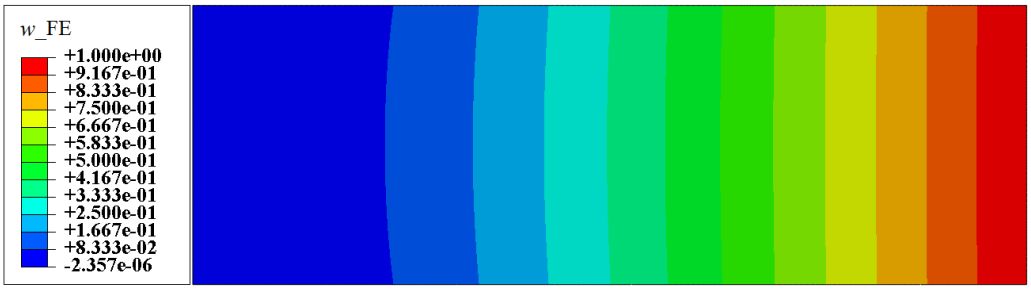

(a)

(b)

Fig. 4.2 The reference FEM contour plots of transverse deflection corresponding to the vibrational modes: (a) Mode 1, and (b) Mode 2

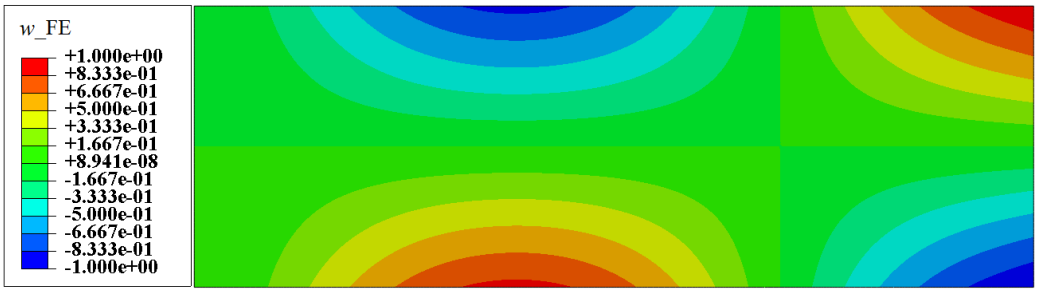

(a)

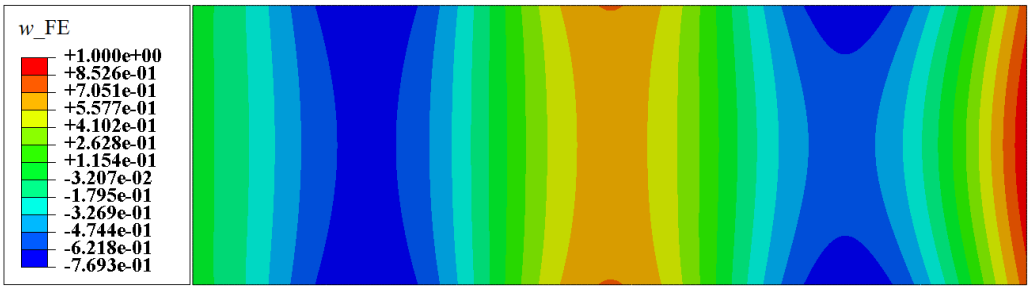

(b)

Fig. 4.3 The reference FEM contour plots of transverse deflection corresponding to the vibrational modes: (a) Mode 5, and (b) Mode 6

The FEM model of the plate is developed in ABAQUS, using a high-fidelity mesh of 7550 S4R elements, which is a four-node shell element with a bi-linear displacement field and reduced integration of the transverse shear strain energy. The numerical strain data for the iFEM analysis are extracted from the FEM model. At the same time, the FEM computed nodal displacements (shown in Figs. 4.2 and 4.3) and rotations serve as reference results for assessing the accuracy of iFEM results.

The 2D iFEM is used to reconstruct both the lower, i.e., the first and second (Fig. 4.2), and higher, i.e., the fifth and sixth (Fig. 4.3), vibrational mode shapes of the plate. The first two modes are the first bending and torsional modes of the plate, respectively, and represent relatively simple displacement fields useful for obtaining a preliminary assessment of iFEM accuracy. The other two are the second torsional and fourth bending modes, respectively. These higher modes involve more complex deformation fields, capturing varying degrees of structural response.

These plate deformations represent pure linear bending or twisting of the plate, based on Mindlin theory, where the contribution of in-plane kinematic variables is negligible. Therefore, the membrane strain measures are zero, and the distribution of in-plane strains along the plate thickness is anti-symmetric with respect to the plate mid-plane. Hence, strain sensors placed either on the top or bottom surface of the plate are sufficient to compute the experimental strain measures. In the present study, only the top surface strains are considered.

The iFEM analysis of the plate is performed using the iQS4 element [70], a four-node shell element with bi-quadratic interpolation of in-plane and transverse displacements, and bi-linear interpolation of bending rotations. The plate is discretised using a regular iFEM mesh with 60 subdivisions along the plate length and 20 along its width, resulting in a total of 1200 elements. Only one strain-sensor position is considered per element, located at the element centroid, and the value of strain measured at the centroid is assumed to be a constant throughout the element. For elements with in-situ strain sensors, the weighting coefficients of Eq. 2.62 are assigned a value of unity, while for those without, a small value, $<< 1$, is used (10^{-4} in this case). As the shear strain measures cannot be evaluated experimentally, the corresponding weights are small for all elements, $\mathbf{w}_s = [10^{-4}, 10^{-4}]$. For the iQS4 element, the 3×3 Gauss quadrature scheme is required for an exact numerical integration of the error norms of Eq. 2.63 [70]. However, for the problems considered in the present study, the 2×2 Gauss quadrature is deemed sufficient to produce accurate iFEM results with lower computational effort and is therefore used.

4.1.1 Preliminary Patterns

A few preliminary strain rosette patterns are proposed (see Fig. 4.4) to minimise the number of sensors required and maximise the accuracy and stability of iFEM predictions. The patterns are inspired by the shape of commonly used load-bearing frame structures. The sparse sensor patterns, listed in increasing order of complexity, are (shown in Fig. 4.4):

- Configuration A (CFG-A): sensors are instrumented only along the boundaries of the plate;
- Configuration B (CFG-B): supplements the previous pattern with additional internal sensors along the plate diagonals, i.e., along zig-zag paths;
- Configuration C (CFG-C): the boundary sensors are combined with sensors along all the cross-diagonal paths of the plate.

Several common features are evident from these patterns, the key being the sensor instrumentation along the plate boundaries, especially along elements where the nodal boundary conditions are prescribed. This ensures a comprehensive measurement of boundary strains which are instrumental for an accurate iFEM prediction. The presence of additional internal sensors in patterns CFG-B and C are expected to improve iFEM predictions further but at the cost of sensor quantity. Another key feature is the continuity of the strain-sensor distributions, i.e., adjacent elements of the inverse mesh are instrumented with sensors. Discontinuous strain-sensor distributions are avoided as they can lead to a singular system matrix $\mathbf{K}$ and a breakdown of the iFEM analysis. Adopting such a design philosophy for current and future sensor patterns is useful for ensuring the robustness of iFEM results.

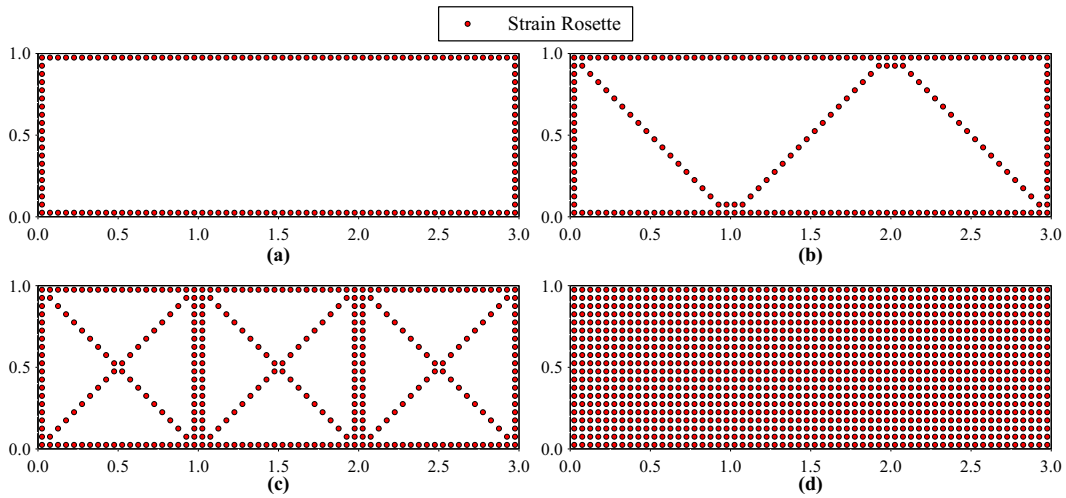

Fig. 4.4 The various strain sensor patterns proposed: (a) CFG-A, (b) CFG-B, (c) CFG-C, and (d) CFG-D (each red dot indicates a strain rosette)

An additional sensor pattern, Configuration D (CFG-D shown in Fig. 4.4), is also proposed, simulating a case where all inverse elements are instrumented with strain sensors. CFG-D is expected to produce the maximum iFEM accuracy obtained for an investigated displacement field and is considered a reference for future comparisons. The breakdown of the different sensor patterns in terms of the number of strain rosettes used is shown in Table 4.1.

Table 4.1 The number of strain rosettes used for each proposed sensor configuration

Sensor Configuration	Number of strain rosettes
CFG-A	156
CFG-B	214
CFG-C	336
CFG-D	1200

The iFEM results are presented as line and contour plots of transverse deflection and bending rotations. The results are evaluated along certain sections of the plate, e.g., along the long or short edges of the plate and certain internal sensor paths, as shown in Fig. 4.5. These sections correspond to plate locations coinciding with an absolute maximum or minimum in the transverse deflection and rotations fields for each mode. Percentage errors at specific nodes of the iFEM mesh are also calculated to investigate the influence of sensor quantity on iFEM accuracy. Finally, additional investigations are proposed based on the conclusions and inferences derived from this preliminary study.

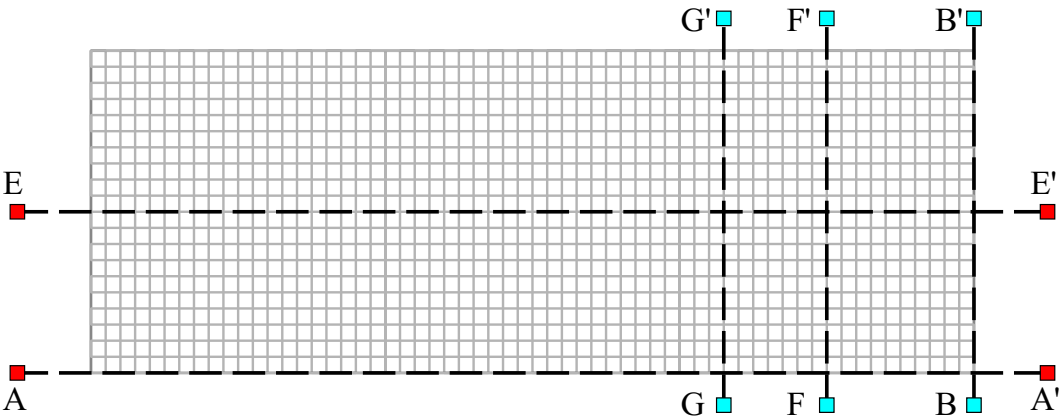

Fig. 4.5 The definition of the sections where iFEM results are reported; the iFEM mesh used is also shown (in light gray), consisting of 60 subdivisions along the plate length and 20 along the plate width

Shape Sensing of Modes 1 and 2

The first two modes correspond to the vibration frequencies, 0.094 Hz and 0.58 Hz, respectively. The first mode represents a relatively simple case of plate bending where w and θ_y are dominant (Fig. 4.2a). Similarly, the second mode is a relatively simple case of plate twisting where w and θ_x are dominant (Fig. 4.2b). These two modes provide a preliminary investigation of iFEM performance, where reconstruction of all major bending deformation components is evaluated and used to establish an upper limit of iFEM accuracy using the sparse sensor patterns.

The contour and line plots of iFEM results for the first two modes are shown in Figs. 4.6 and 4.7, respectively. The line plots compare iFEM results along specific plate sections where deflection or rotation is a maximum and iFEM is likely to generate the greatest errors. Hence, the sections chosen depend on the mode shape and are different for each mode. Additionally, the maximum value of percentage error calculated along the results of each section is given in Tables 4.2 and 4.3. The main conclusions derived from the iFEM results of both modes are:

- CFGs-A, B, C and D yield highly accurate reconstructions of the w, θ_x and θ_y fields, with a maximum percentage error $< 1\%$ across the plate;
- Accuracy increases with increase in the number of sensors used.

These results demonstrate that all three sparse sensor patterns are equally suited for the shape sensing of the first two modes. More complex plate deformations are required to discriminate the performance between these patterns and are the focus of the following sections.

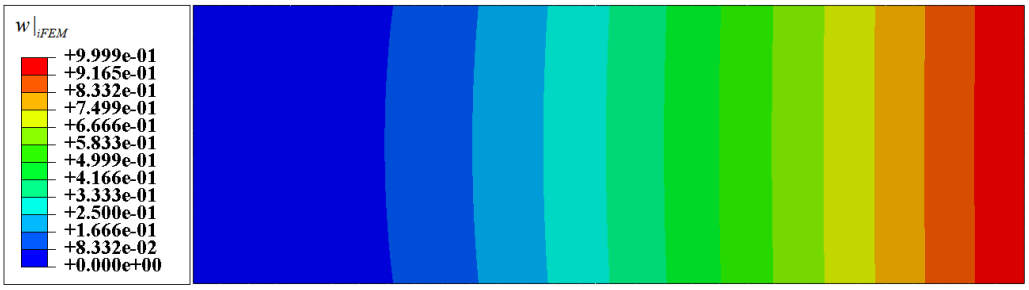

(a) Contour plot of transverse deflection for Mode 1 using CFG-D

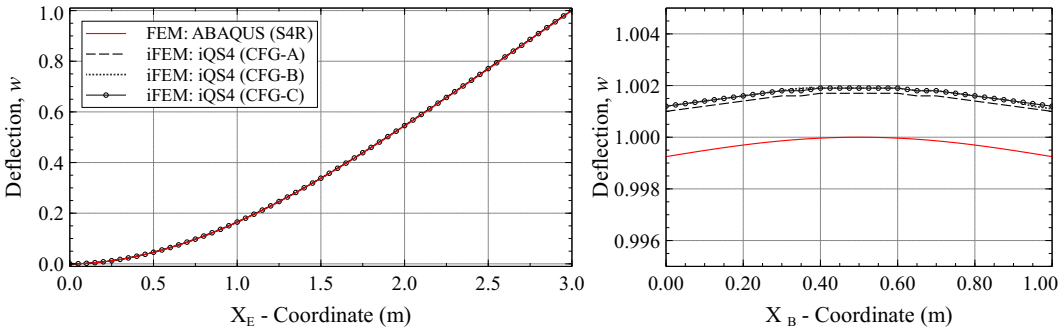

(b) Line plots of transverse deflection, w, along sections E-E' and B-B'

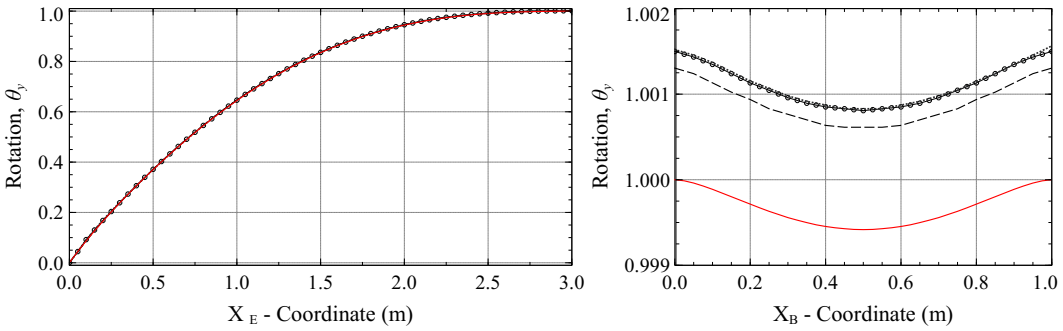

(c) Line plots of rotation, θ_y, along sections E-E' and B-B'

Fig. 4.6 Contour and line plots of iFEM reconstructed transverse deflection and rotation fields for Mode 1 (results normalized with respect to maximum FEM values along each path)

Table 4.2 Maximum error in CFG-A, B, C and D results along each section for Mode 1

Error	Section E-E'				Section B-B'			
	A	B	C	D	A	B	C	D
$w^{err}\|_{max}$	0.17%	0.19%	0.19%	0.01%	0.18%	0.20%	0.20%	0.01%
$\theta_y^{err}\|_{max}$	0.21%	0.42%	0.53%	0.06%	0.13%	0.16%	0.15%	0.02%

(a) Contour plot of transverse deflection for Mode 2 using CFG-D

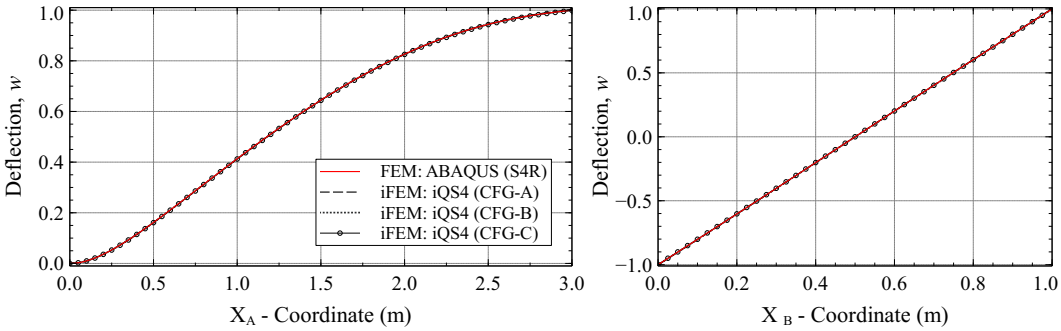

(b) Line plots of transverse deflection, w, along sections A-A' and B-B'

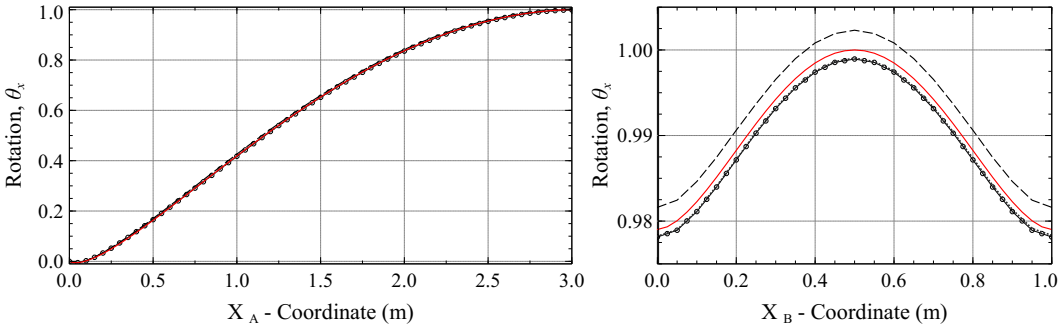

(c) Line plots of rotation, θ_x, along sections A-A' and B-B'

Fig. 4.7 Contour and line plots of iFEM reconstructed transverse deflection and rotation fields for Mode 2 (results normalized with respect to maximum FEM values along each path)

Table 4.3 Maximum error in CFG-A, B, C and D results along each section for Mode 2

Error	Section A-A'				Section B-B'			
	A	B	C	D	A	B	C	D
$w^{err}\|_{max}$	0.25%	0.07%	0.13%	0.01%	0.25%	0.25%	0.11%	0.01%
$\theta_x^{err}\|_{max}$	0.76%	0.37%	0.32%	0.02%	0.27%	0.11%	0.12%	0.02%

Shape Sensing of Modes 5 and 6

The fifth and sixth modes correspond to the vibration frequencies, 1.84 Hz and 3.27 Hz, respectively. Mode 5 (the second torsional mode, shown in Fig. 4.3a) presents a complex case of plate torsion, where all three kinematic variables, w, θ_x and θ_y, play a prominent role is describing the antisymmetric deformation field. The case is similar for Mode 6 (the fourth bending mode, shown in Fig. 4.3b), where although w and θ_y are prominent, the contribution of θ_x cannot be neglected. The deformation fields corresponding to these modes are significantly more complex and are expected to provide a more realistic assessment of the sparse sensor patterns.

The contour and line plots of iFEM results are shown in Figs. 4.8 and 4.9, respectively. Also, the maximum value of percentage error calculated using the results of each section is given in Tables 4.4 and 4.5. Compared to the previous case, major differences in sensor pattern performance are observed.

The main observations from the iFEM reconstruction of Mode 5 are:

- CFG-A results for w and θ_y are highly accurate (error $< 1.5\%$), but inaccuracies are observed for θ_x results (error ~ 3 %, see Table 4.4);
- CFGs-B and C are very accurate in reconstructing Mode 5, with errors $< 1.5\%$ for w, θ_x and θ_y (see Table 4.5);
- The internal diagonal sensor paths aided CFGs-B and C in θ_x reconstruction (see Fig. 4.8c), due to the greater quantity of κ_y strain measurements (absent in CFG-A, where κ_y is measured only along the boundaries);
- Accuracy increases with sensor quantity, with CFG-D the most accurate.

Despite the minor inaccuracies observed for CFG-A, all patterns are deemed to be sufficiently accurate in reconstructing Mode 5.

The main observations from the iFEM reconstruction of Mode 6 are:

- CFG-A is unable to accurately reconstruct Mode 6; high errors ($> 7\%$) observed for w, θ_x and θ_y (see Fig. 4.9);
- Deformation reconstruction using CFG-A at internal plate locations is inaccurate, indicating a potential lack of internal strain sensors;
- CFGs-B and C are very accurate in reconstructing w and θ_y (errors $< 1\%$); θ_x less accurate (errors $< 4\%$) and is attributed to its lower magnitude (less prominent for Mode 6);
- Asymmetries are observed in iFEM results along the plate tip (see Fig. 4.9d); most likely due to the asymmetry of sensor patterns used;
- Accuracy is seen to improve with number of sensors used per pattern.

An encouraging aspect of these results is that CFGs-B and C maintain a relatively high level of iFEM accuracy (similar to CFG-D), despite the reduction in sensors used. However, CFG-A is inadequate for this case.

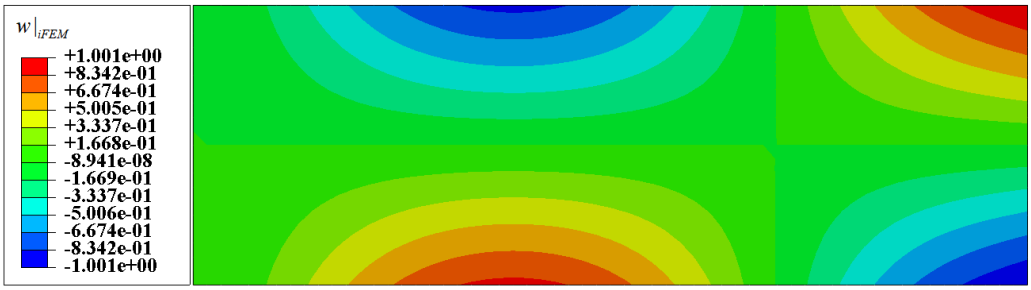

(a) Contour plot of transverse deflection for Mode-5 using CFG-D

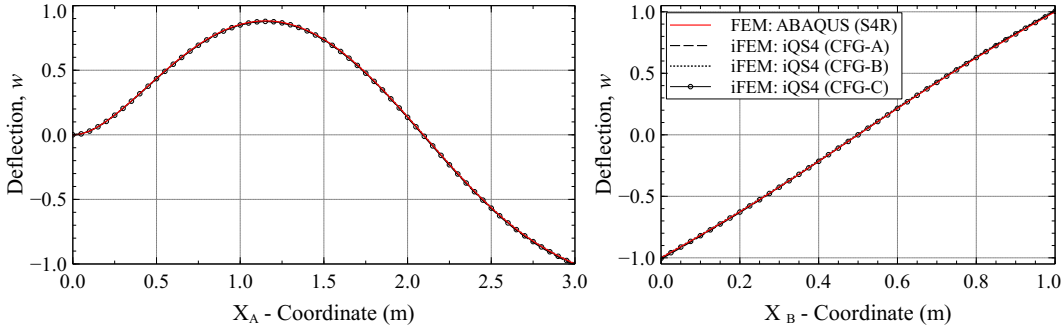

(b) Line plots of transverse deflection, w, along sections A-A' and B-B'

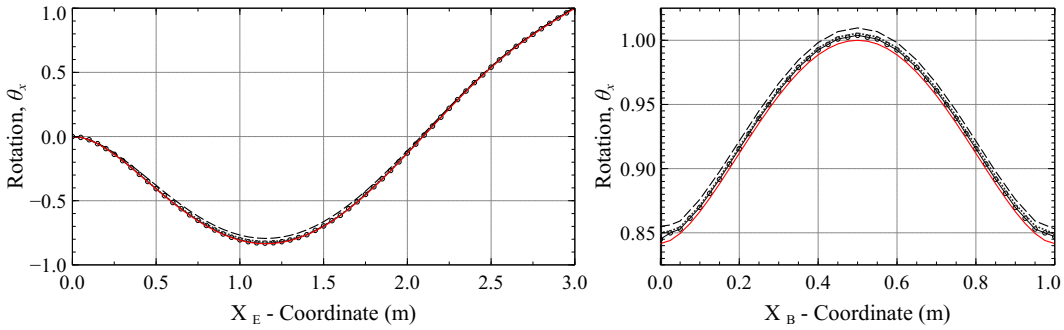

(c) Line plots of rotation, θ_x, along sections E-E' and B-B'

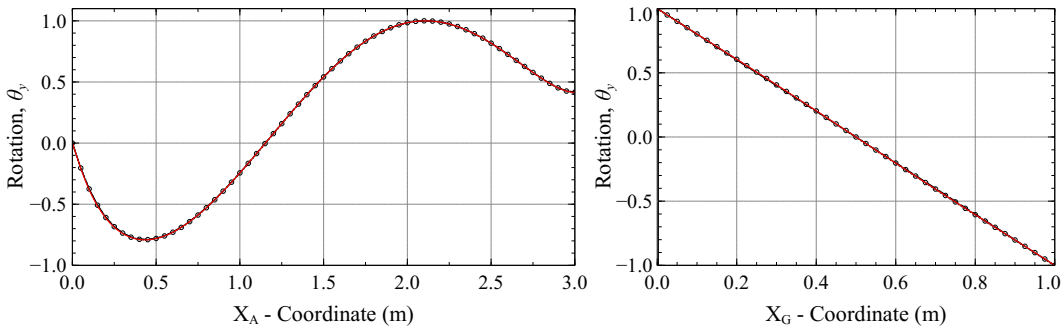

(d) Line plots of rotation, θ_y, along sections A-A' and G-G'

Fig. 4.8 The contour and line plots of iFEM reconstructed transverse deflection and rotation fields for Mode 5 (results normalized with respect to maximum FEM values along each path)

Some general conclusions on the design of efficient sensor patterns are derived from these iFEM results:

- The main and obvious conclusion is the increase in iFEM accuracy with the number of sensors used per pattern (CFG-A, the least, and CFG-D, the most accurate);
- However it is inferred that not just quantity but the orientation of the sensors paths are also important; this is well documented from the results of θ_x where the internal diagonal sensor paths provided additional κ_y measurements;
- Despite the complexity of the deformation field investigated, iFEM reconstruction along paths instrumented with sensors is seen to be accurate; the accuracy decreases with an increase in distance from the sensor path;
- Despite the symmetry in the mode shapes investigated, asymmetries are observed in the iFEM results, specifically CFG-A; this is most likely explained by the design of the sensor pattern used and the corresponding asymmetric locations of strain data measured;
- Alongside high accuracy, the number of sensors used is also deemed a major factor in selecting a sensor pattern for practical shape sensing applications; among the patterns investigated, CFG-B is identified to provide the best compromise between accuracy and sensor quantity.

These investigations provided a preliminary look into using simple strain sensor patterns for plate shape sensing. Based on the conclusions derived from these results, several strategies for optimising the sensor patterns were identified. These discussions are presented in Section 4.1.2.

Table 4.4 Maximum error in CFG-A, B, C and D results along each section for Mode 5

Error	Section A-A'				Section B-B'			
	A	B	C	D	A	B	C	D
$w^{err}\|_{max}$	1.06%	0.34%	0.48%	0.11%	1.06%	1.31%	0.41%	0.11%
$\theta_x^{err}\|_{max}$	2.78%	0.97%	0.85%	0.26%	1.20%	0.83%	0.59%	0.06%
$\theta_y^{err}\|_{max}$	1.21%	1.01%	1.08%	0.02%	0.44%	0.61%	0.27%	0.29%

Table 4.5 Maximum error in CFG-A, B, C and D results along each section for Mode 6

Error	Section A-A'				Section B-B'			
	A	B	C	D	A	B	C	D
$w^{err}\|_{max}$	0.98%	0.96%	0.75%	1.31%	0.75%	0.65%	0.35%	1.31%
$\theta_x^{err}\|_{max}$	7.13%	3.41%	3.43%	0.14%	0.46%	0.69%	0.35%	0.51%
$\theta_y^{err}\|_{max}$	0.78%	0.80%	0.74%	0.23%	0.19%	0.19%	0.13%	0.10%

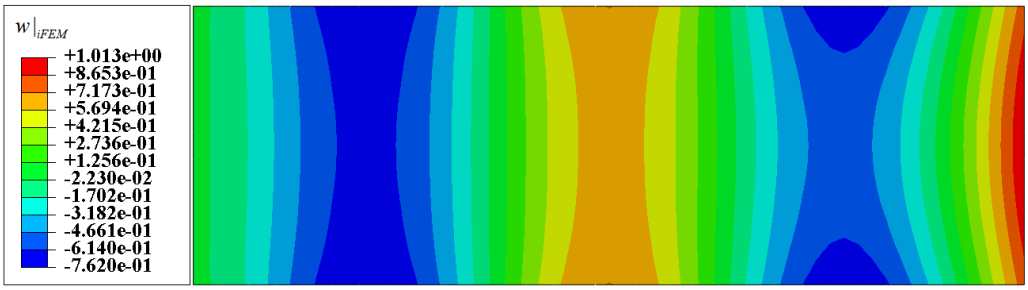

(a) Contour plot of transverse deflection for Mode 6 using CFG-D

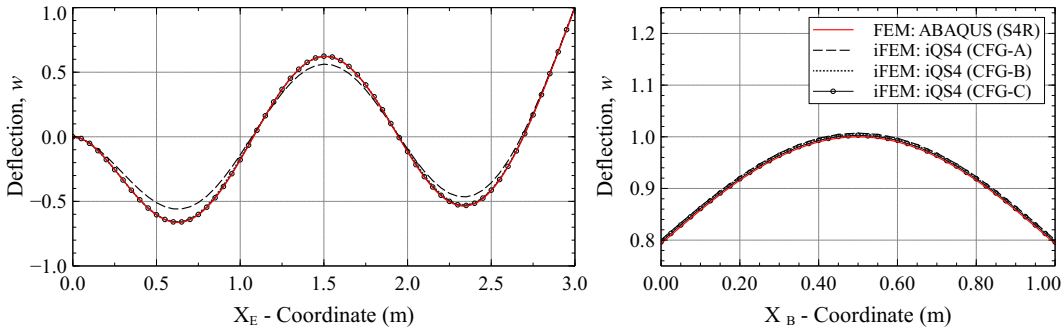

(b) Line plots of transverse deflection, w, along sections E-E' and B-B'

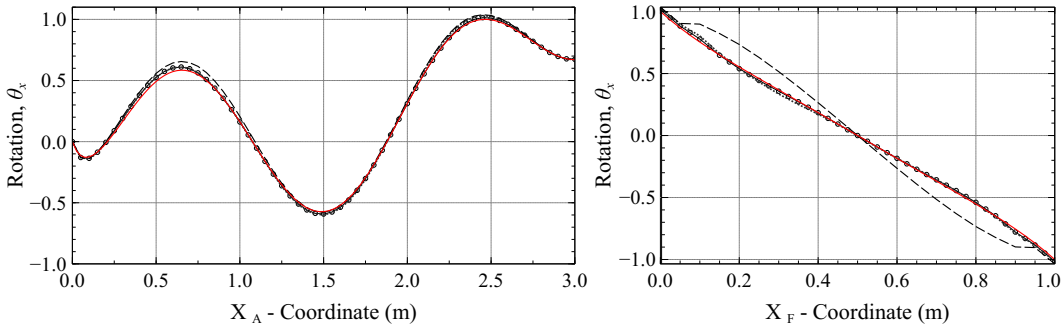

(c) Line plots of rotation, θ_x, along sections A-A' and F-F'

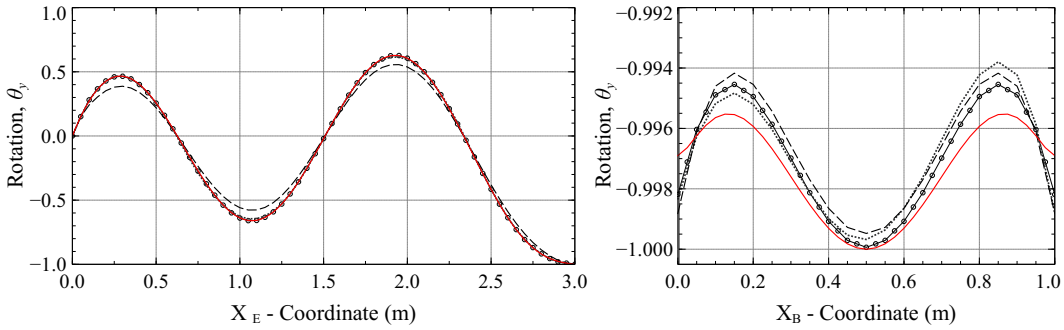

(d) Line plots of rotation, θ_y, along sections E-E' and B-B'

Fig. 4.9 The contour and line plots of iFEM reconstructed transverse deflection and rotation fields for Mode 6 (results normalized with respect to maximum FEM values along each path)

Investigating Convergence of iFEM Predictions

The iFEM results using the preliminary patterns are further evaluated to understand the influence of inverse element type and the total number of sensors on iFEM reconstruction performance. The iFEM results obtained using the iQS4 element are compared against those obtained using the iMIN3 element [14], which is a three-node constant strain shell element. This study aims to understand the influence of varying discretisation schemes and element interpolation (corresponding to the element selected) on the iFEM results.

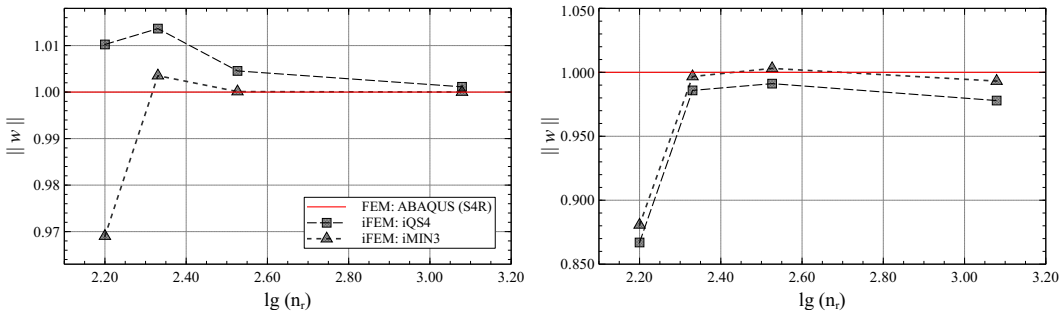

(a) Mode 5: Deflection, w

(b) Mode 6: Deflection, w

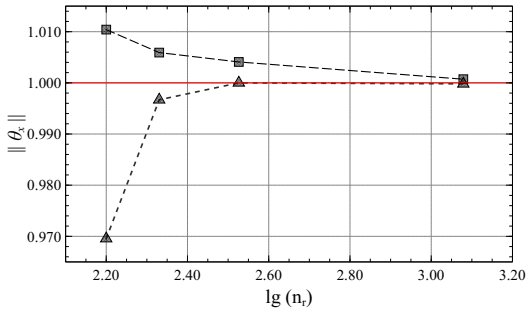

(c) Mode 5: Rotation, θ_x

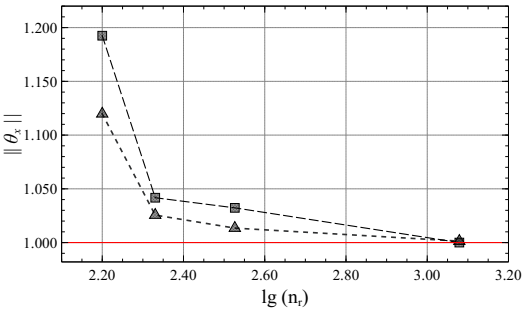

(d) Mode 6: Rotation, θ_x

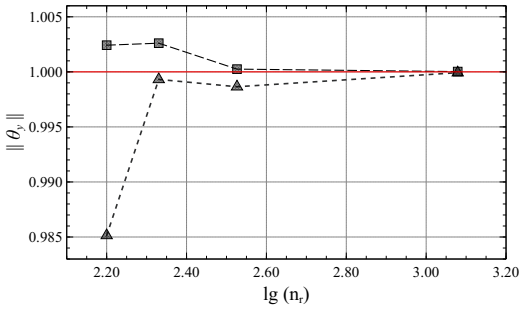

(e) Mode 5: Rotation, θ_y

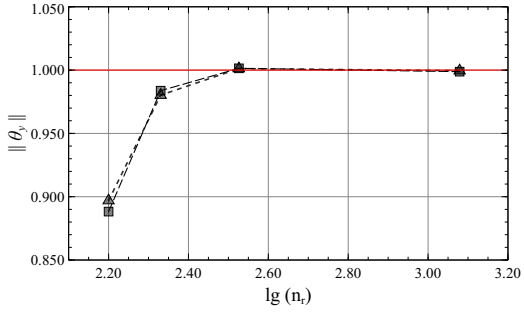

(f) Mode 6: Rotation, θ_y

Fig. 4.10 Convergence plots of iFEM results, for Modes 5 and 6, as a function of the number of strain rosettes used, n_r (results normalized with respect to reference FEM values)

The iQS4 element mesh (shown in Fig. 4.5) is adapted and used for the iFEM analysis using iMIN3 elements. Each quadrilateral element is subdivided along its cross-diagonals into four triangular elements. The strain measured at the quadrilateral element centroid is assumed to be a constant throughout the element and used at the centroids of the triangular elements. Hence, although the iMIN3 mesh uses four times the number of elements, it uses the same set of measured strain data.

The iFEM results at specific nodes of the plate, corresponding to the location of the global maximum in the deflection and rotation components of each mode, are used for this study. For Mode 5, the maxima for w, θ_x and θ_y occur at the nodes located at (x, y) coordinates: $(2.95, 0.95)$, $(2.95, 0.50)$ and $(2.00, 0.95)$, respectively. Similarly, the maxima for Mode 6 occur at nodes located at $(2.35, 0.50)$, $(2.50, 0.90)$ and $(2.00, 0.50)$. The normalized value of deflection and rotation is plotted as a function of the number of strain rosettes (n_r) used for each sensor pattern and is compared against reference FEM results. These plots are shown in Fig. 4.10.

The results demonstrate the convergence of iFEM predictions to reference FEM values as n_r increases. This convergence leads to a corresponding increase in iFEM accuracy, as demonstrated in previous results. Also, no significant difference is observed between iFEM predictions using the iMIN3 and iQS4 elements. A possible explanation is the similar treatment of strain data, i.e., an assumption of constant strain within each quadrilateral element domain is considered for both iFEM analyses.

4.1.2 Reduced Sensor Patterns

Although the sensor patterns of Section 4.1.1 proved effective in reconstructing both simple and complex plate deformations, they are not efficient for practical shape sensing applications as the number of sensors required is still relatively high. This section attempts to optimise these preliminary patterns further by reducing the number of sensors used without depreciating iFEM accuracy. Sensor quantity is reduced using virtual sensor expansion, where a limited number of physical strain measurements are expanded to unmeasured locations. Although multiple virtual sensing approaches are available in existing literature, the Smoothing Element Analysis (SEA) is used for the current work.

The preliminary patterns of Fig. 4.4 are modified to propose novel patterns where the number of in-situ strain measurements along each sensor path is reduced. The SEA is used along these reduced sensor paths to smooth in-situ strain measurements and generate continuous strain distributions for the iFEM analysis. A detailed description of the SEA is not provided in this work; interested readers are encouraged to consult the following references: Ref. [111, 117, 118].

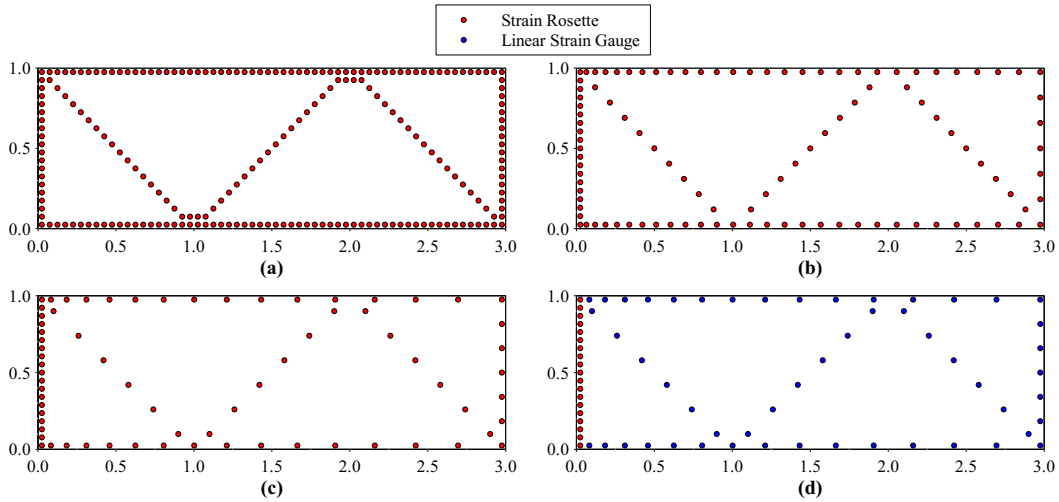

Fig. 4.11 Reference pattern: (a) CFG-B, and the novel reduced patterns derived from it: (b) Reduced Set-1 (R1), (c) Reduced Set-2 (R2), and (d) Reduced Set-3 (R3)

Based on the conclusions of the previous study, CFG-B was identified to provide an optimal trade-off between sensor quantity and iFEM accuracy. Hence, it is considered the reference for this study, i.e., the basic sensors paths are retained, but the distribution, number, and type of sensors along each path are optimised to derive three new patterns (shown in Fig. 4.11):

- Reduced Set-1 (R1): the number of strain rosettes along each path is reduced, and sensor positions are skewed with a higher density towards the fixed end. Also, a high sensor density is retained along the clamped end;
- Reduced Set-2 (R2): similar to R1 but with a further reduction in sensor positions along the plate length (distribution still skewed);
- Reduced Set-3 (R3): similar sensor locations as R2 are used, but strain rosettes are instrumented only along the clamped end. All other locations use strain gauges oriented parallel to the sensor path (measuring uni-axial strains).

The high sensor density along the clamped end emphasises the importance of the boundary strains, which are instrumental for accurate iFEM predictions. The number of sensors used for each case is described in Table 4.6.

For all these new reduced patterns, the SEA is used to smooth the in-situ strains and generate smoothed strains at element centroids corresponding to the instrumented elements of CFG-B. Hence, despite the difference in the number of in-situ strain data used, the number of smoothed strain data generated is similar for all reduced patterns. This section evaluates the use of these new patterns for the shape sensing of Modes 5 and 6. A more detailed description of the use of SEA and the accuracy of the smoothed strains obtained is provided in Appendix C.1.

Table 4.6 The number of sensors used for the reference and reduced sensor patterns

Sensor Configuration	No. of sensor positions (n_r)	No. of uniaxial strain measurements (n_{uni})
CFG-B	214	642
CFG-B | R1	107	321
CFG-B | R2	72	216
CFG-B | R3	72	112

Shape Sensing of Modes 5 and 6

In Section 4.1.1, the iFEM reconstruction of Modes 5 and 6 using CFG-B was demonstrated to be highly accurate. These results are considered a reference for the present study and used to evaluate any depreciation in iFEM accuracy in the new reduced patterns.

The line and contour plots of the coupled SEA-iFEM results (referred to in the results as iFEM$^{(s)}$) are shown in Figs. 4.12 and 4.13. The contour plots show the iFEM results using R3, which is the limiting case using the least number of in-situ strain sensors, and for which iFEM is expected to be the least accurate. The maximum value of percentage error in reconstructed deflection and rotations along the various sections are reported in Table 4.7 and 4.8.

The main observations from the results of Modes 5 and 6 are summarised below:

- R1 and R2 are observed to be very accurate in reconstructing Mode 5 with errors $<$1.5% for w, θ_x, and θ_y (see Table 4.7); higher errors are observed in Mode 6 results, with errors $<$7.5% for θ_x (see Table 4.8), but the results are still deemed accurate;
- R3 produced the least accurate results, especially in reconstructing θ_x for both modes (shown in Appendix C.2), indicating a lack of κ_y strain data for this pattern; this is explained by the fact that internal plate locations are dominated by κ_x strains, measured along the plate length, while κ_y strains are measured only along the plate tip. Although, $\kappa_{x,45}$, measured along the zig-zag paths, attempts to bridge this gap, it is clearly insufficient;
- Some features from previous results are also observed here: high reconstruction accuracy along sensor paths and minor asymmetry in results along the plate tip (due to the asymmetry of sensor patterns).

These results indicate that R1 and R2 can retain a similar level of iFEM accuracy, as observed for CFG-B, but using a significantly lower number of strain sensors (less than half).

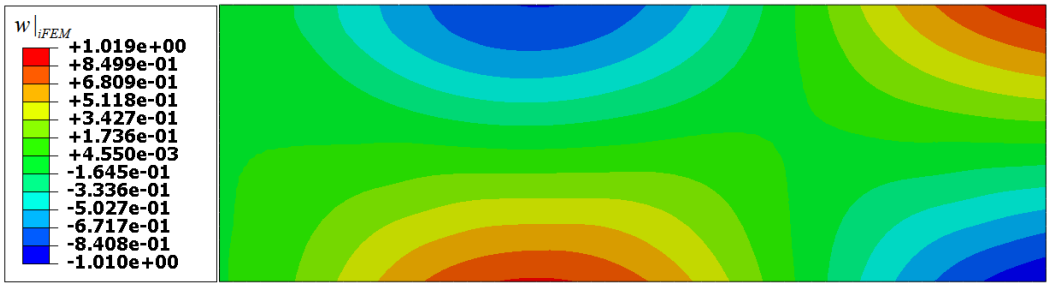

(a) Contour plot of transverse deflection for Mode 5 using R3

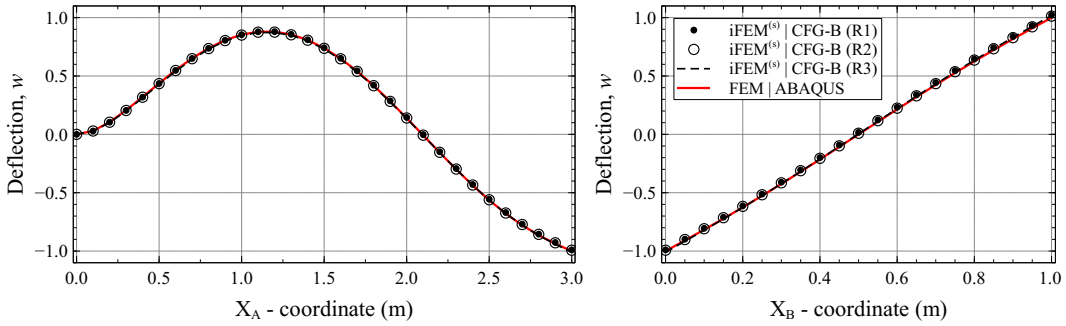

(b) Line plots of transverse deflection, w, along sections A-A' and B-B'

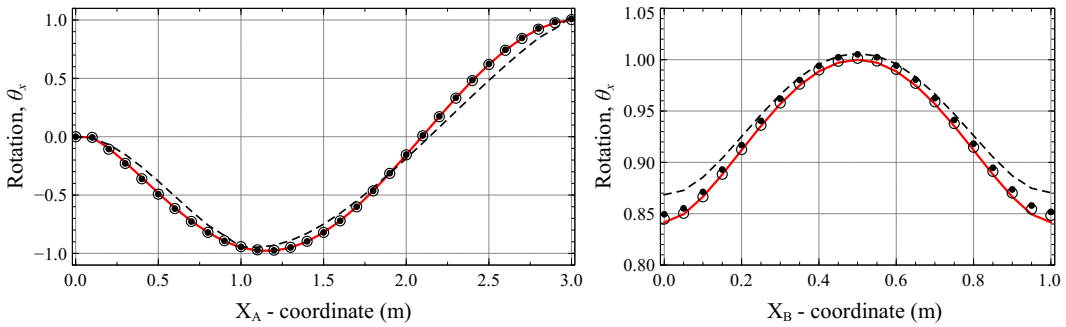

(c) Line plots of rotation, θ_x, along sections A-A' and B-B'

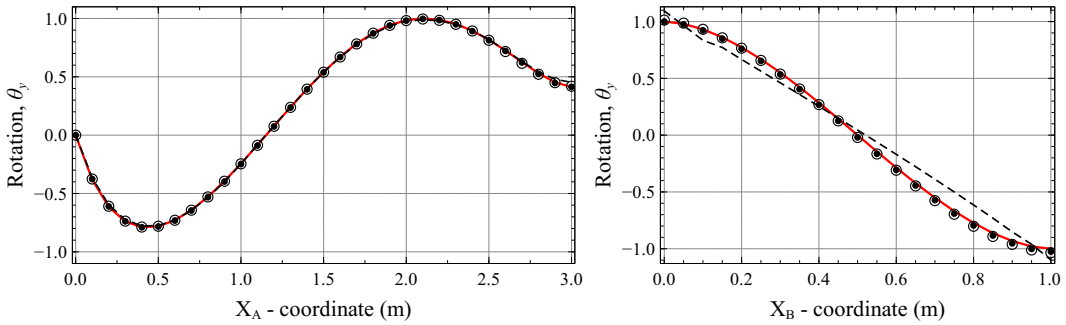

(d) Line plots of rotation, θ_y, along sections A-A' and B-B'

Fig. 4.12 The contour and line plots of transverse deflection and rotation for Mode 5 reconstructed using the SEA coupled iFEM approach

Table 4.7 Percentage error in SEA coupled iFEM results along each section for Mode 5

Variable	Section A-A'			Section B-B'		
	R1	R2	R3	R1	R2	R3
$w^{err}\|_{max}$	1.05%	0.75%	0.98%	2.34%	1.28%	1.90%
$\theta_x^{err}\|_{max}$	1.04%	1.00%	13.67%	1.01%	0.68%	2.88%
$\theta_y^{err}\|_{max}$	0.56%	1.08%	3.87%	2.52%	3.47%	16.4%

Table 4.8 Percentage error in SEA coupled iFEM results along each section for Mode 6

Variable	Section A-A'			Section B-B'		
	R1	R2	R3	R1	R2	R3
$w^{err}\|_{max}$	1.67%	2.52%	1.85%	1.32%	1.88%	1.22%
$\theta_x^{err}\|_{max}$	3.72%	7.49%	47.80%	0.24%	6.44%	3.79%
$\theta_y^{err}\|_{max}$	0.33%	1.13%	1.18%	0.40%	1.91%	1.87%

Based on the results of this study, conclusions can be drawn regarding the reduced sensor patterns proposed and the SEA coupled iFEM approach used:

- The SEA is capable of generating accurate smoothed curvature distributions from a sparse set of in-situ strain data (demonstrated in the results of Appendix C.1) and is deemed an effective virtual sensor expansion strategy;
- The SEA coupled iFEM approach also proved effective, as demonstrated by the results of R1 and R2, where accurate iFEM predictions of the deflection and rotation fields were obtained (similar to CFG-B) but using a significantly lower number of sensors; R3 offered relatively good deflection, but poor rotation predictions;
- Accuracy of each pattern must be contrasted against the number of sensors used in each case: R1 and R2 require 107 and 72 strain rosettes, respectively. In contrast, R3 requires 19 strain rosettes and a fibre optic cable, highlighting that a trade-off is necessary between sensor quantity and iFEM accuracy.

A further improvement of R3 can help reduce some of the inaccuracies (due to insufficient κ_y measurements) observed in the iFEM results. The current set of patterns are more oriented toward κ_x measurements, allowing for more accurate w and θ_y reconstructions. The use of internal cross-diagonal sensor paths can increase the amount of κ_y information, leading to a better integration of boundary and internal strains and thereby generating more accurate iFEM results. Another strategy is to instrument distributed fibre optic sensors along uni-axial strain sensor paths to significantly increase the total number of in-situ strain data points available for the iFEM analysis. Such investigations are left for future works.

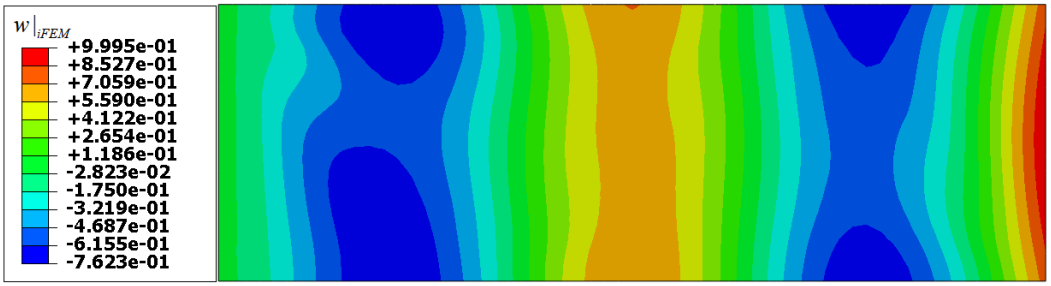

(a) Contour plot of transverse deflection for Mode 6 using R3

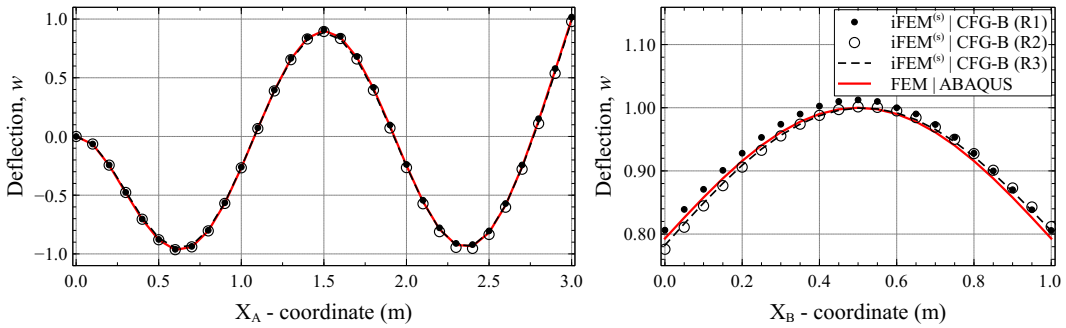

(b) Line plots of transverse deflection, w, along sections A-A' and B-B'

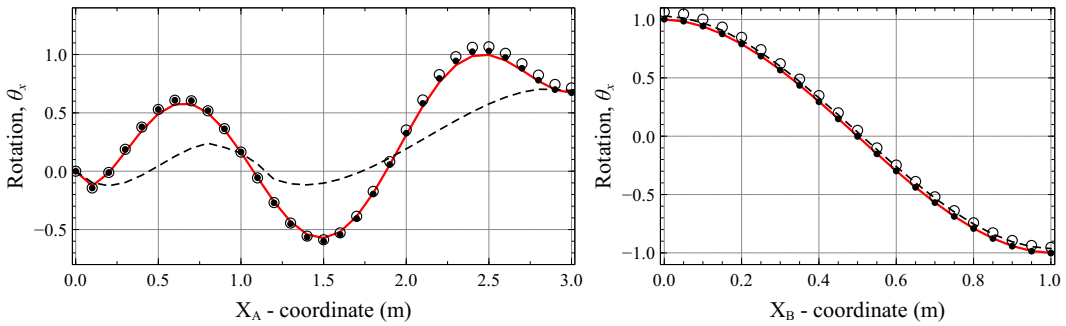

(c) Line plots of rotation, θ_x, along sections A-A' and B-B'

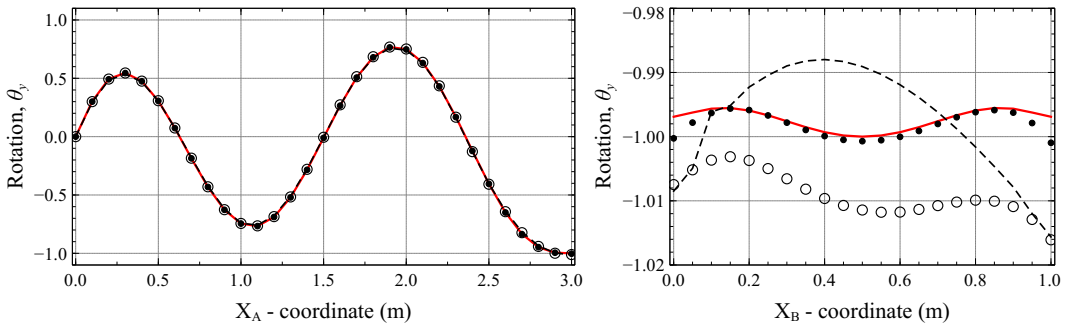

(d) Line plots of rotation, θ_y, along sections A-A' and B-B'

Fig. 4.13 The contour and line plots of transverse deflection and rotation for Mode 6 reconstructed using the SEA coupled iFEM approach

Root Mean Square Error Plots

Similar to the convergence plots of Section 4.1.1, the change in iFEM accuracy as a function of sensor quantity is also evaluated. The Root Mean Square (RMS) error of iFEM reconstructed nodal deflections and rotations for the reduced sensor patterns is evaluated to obtain a global picture of accuracy across the entire plate domain. The RMS error of each deformation component, p, can be calculated as,

$$e_{RMS}(p) = \sqrt{\sum_{i=1}^{N_{nod}} \frac{1}{N_{nod}} \left(\frac{p_i^{FEM} - p_i^{iFEM}}{p^{FEM}|_{max}} \right)^2} \times 100 \tag{4.1}$$

where $p \in \{w, \theta_x, \theta_y\}$, and N_{nod} is the total number of nodes of the iFEM mesh. The RMS errors for Modes 5 and 6 are plotted against the number of uni-axial strain measurements, n_{uni} (see Table 4.6)), for each pattern and are shown in Fig. 4.14.

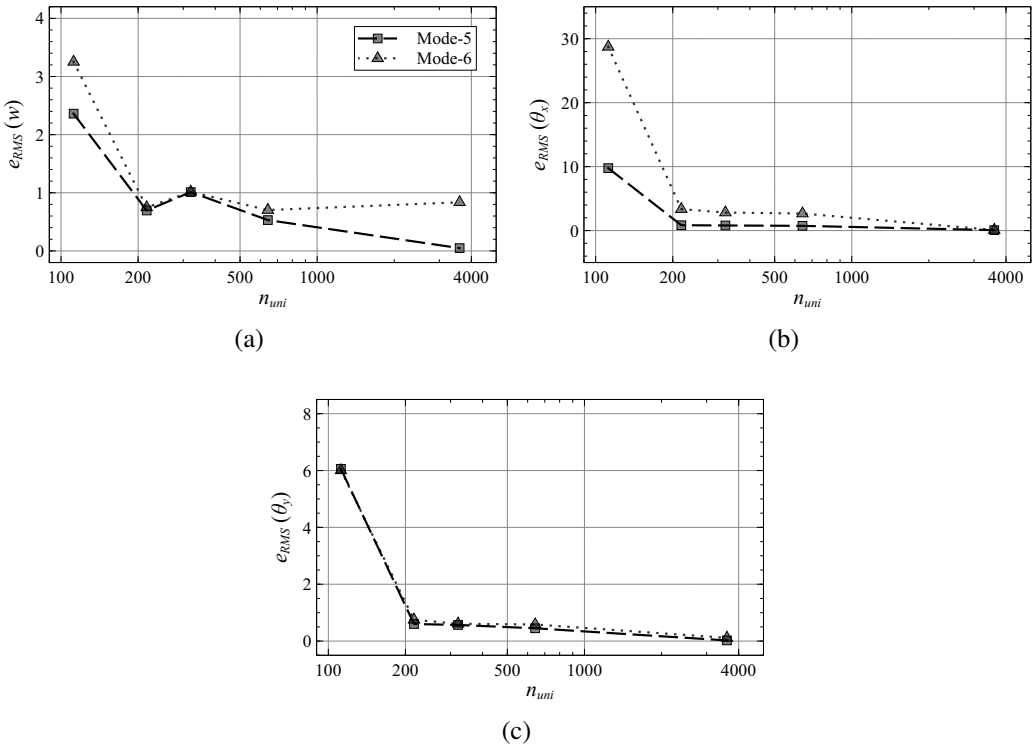

Fig. 4.14 RMS error in iFEM reconstructed (a) w, (b) θ_x, and (c) θ_y fields, as a function of the number of uni-axial strain measurements

The plots present an expected behaviour where e_{RMS} reduces with increase in n_{uni}. The highest errors correspond to R3 results ($e_{RMS}(\theta_x) =\sim 30\%$) as discussed in the previous sections. The magnitude of the errors for w and θ_y are quite small ($e_{RMS} < 6\%$) indicating a reasonably accurate reconstruction across the plate domain.

4.2 Damage Localisation in Thin Plates

The present section addresses the second of the two main aims of this chapter: investigating the use of 2D iFEM for developing an effective damage detection and localisation strategy for plate structures. The presence of damage on a structure leads to local strain perturbations, and the magnitude of these perturbations decreases with an increase in distance from the damage site. An accurate reconstruction of these strain perturbations from surface strain measurements forms the basis of the strategy developed. The main steps the iFEM-based damage detection strategy are highlighted in Fig. 4.15.

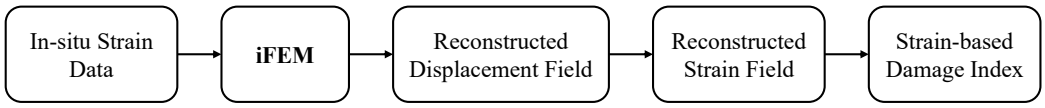

Fig. 4.15 Flowchart illustrating the major steps of the iFEM-based damage detection strategy

Considering a structure with some internal damage and instrumented with a discrete set of strain sensors, strain measurements from sensors located far from the damage site are representative of the undamaged benchmark strain field of the structure, while closer to the damage site, local strain perturbations influence measurements. The iFEM is used to reconstruct the structure's continuous displacement and strain field from this discrete set of surface strain measurements. In essence, it acts as a strain interpolation technique. However, as the iFEM is based on the strain-displacement relations, the interpolation considers plate kinematics and is expected to be more accurate. Regions of high strain concentration in the iFEM reconstructed strain field are used to reveal the presence and location of the damage on the structure. Hence, it is imperative that the in-situ strain measurements reflect both the baseline and damaged strain fields of the structure.

Strain-based damage indices are used to identify possible damage sites from the iFEM strain field results. The present work uses the maximum principal strain, ε_p, to condense the reconstructed strain tensor into a single damage sensitive variable,

$$\varepsilon_p^{iFEM} = \frac{\varepsilon_{xx}^{iFEM} + \varepsilon_{yy}^{iFEM}}{2} + \sqrt{\left(\frac{\varepsilon_{xx}^{iFEM} + \varepsilon_{yy}^{iFEM}}{2}\right)^2 + (\gamma_{xy}^{iFEM})^2} \tag{4.2}$$

where ε_{xx}^{iFEM}, ε_{yy}^{iFEM}, and γ_{xy}^{iFEM} are the iFEM reconstructed normal and shear strains at the element integration points.

A normalized damage index, I_D, based on ε_p^{iFEM} can be also defined,

$$I_D = \frac{\varepsilon_p^{iFEM} - \varepsilon_p^{iFEM}|_{min}}{\varepsilon_p^{iFEM}|_{max} - \varepsilon_p^{iFEM}|_{min}} \tag{4.3}$$

where $\varepsilon_p^{iFEM}|_{min}$ and $\varepsilon_p^{iFEM}|_{max}$ indicate the minimum and maximum values of iFEM reconstructed maximum principal strain.

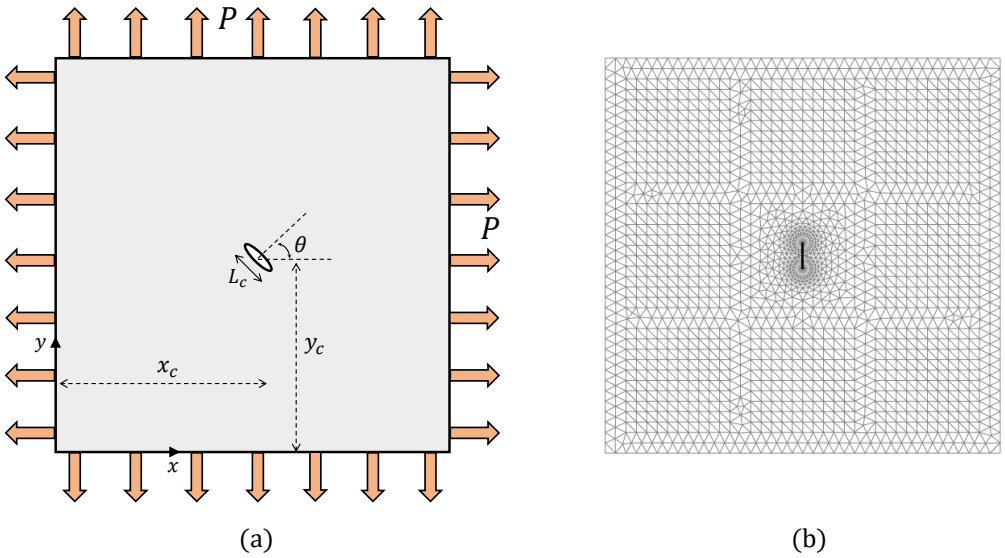

Fig. 4.16 The damaged plate structure showing: (a) the uniform bi-axial loading of the plate along with the parameters highlighting the position, size and orientation of the crack, and (b) the FEM mesh of the plate with a central crack

This novel iFEM-based damage detection strategy is investigated numerically using the problem of a square thin plate subjected to bi-axial loading. The plate has a side length of 3.8 m, thickness, 3.8 mm, and is made of an aluminium alloy with Young's modulus, $E = 73$ GPa, Poisson's ratio, $\nu = 0.3$, and density, $\rho = 2700$ kg/m^3. The plate is under uniform biaxial loading of magnitude, $P = 10^5$ N/m, as shown in Fig. 4.16. An internal crack is used to simulate damage on the plate. The various parameters defining the crack position, orientation and size are described in Fig. 4.16. The numerical strains for the iFEM analysis are extracted from a high-fidelity FEM model of the plate developed in ABAQUS. The internal crack is modelled using the seam feature, where nodes on the crack mouth are isolated. The model is meshed using the three-node shell element (called S3R), with a more refined mesh near the crack tip and a coarser mesh further from it (shown in Fig. 4.16). The finer mesh used is instrumental in accurately capturing the local strain concentration caused by the crack.

The new damage detection strategy is evaluated on three damage cases involving different iterations of crack parameters. These cases have been defined in Table 4.9: Damage Case-1 describes a 25 cm long vertical crack at the center of the plate, Damage Case-2 describes a 10 cm long vertical crack located near the corner of the plate, and Damage Case-3 describes a 25 cm long crack positioned at the center and oriented at an angle of 45^0 with the horizontal. These cases help the study understand the influence of damage size, position, and orientation on damage detection performance.

Additionally, the numerical strain data are also contaminated with artificial noise to simulate the influence of experimental errors or environmental factors that affect practical strain measurements. The noise is introduced based on a Gaussian distribution with zero mean and the value of three standard deviations equal to 5%. The magnitude of noise introduced significantly influences iFEM predictions and is studied in more detail in later sections.

Table 4.9 The crack parameters for the different damage cases investigated

Damage Case	Crack Length L_c (m)	Crack Position x_c, y_c (m)	Crack orientation θ_c (deg)
1	0.25	1.90 , 1.90	0
2	0.10	2.85 , 2.85	0
3	0.25	1.90 , 1.90	45

4.2.1 Benchmark Results: Strain Rosette Grid

For a preliminary evaluation of damage detection performance, a high-density strain rosette grid is employed for the iFEM analysis. Due to the large number of sensors used, these results are considered a benchmark for future comparisons. The plate is subdivided into square grid cells with strain rosettes placed only along the boundaries of each cell, as shown in Fig. 4.17. On the cell boundary, sensors measure higher strain perturbations when the cell encloses a damage than when no damage exists. Correspondingly, in the iFEM reconstructed strain field, the strain distribution within a damaged cell is greater than in a healthy cell. This comparison between cells is used to identify and localise the damage. Consequently, in such a method, the damage is localised to a cell, and so the level of discretisation using grid cells determines the precision of the damage localisation strategy. For the present problem, the plate is discretised into nine grid cells, as shown in Fig. 4.17a, with a total of 440 strain rosette locations.

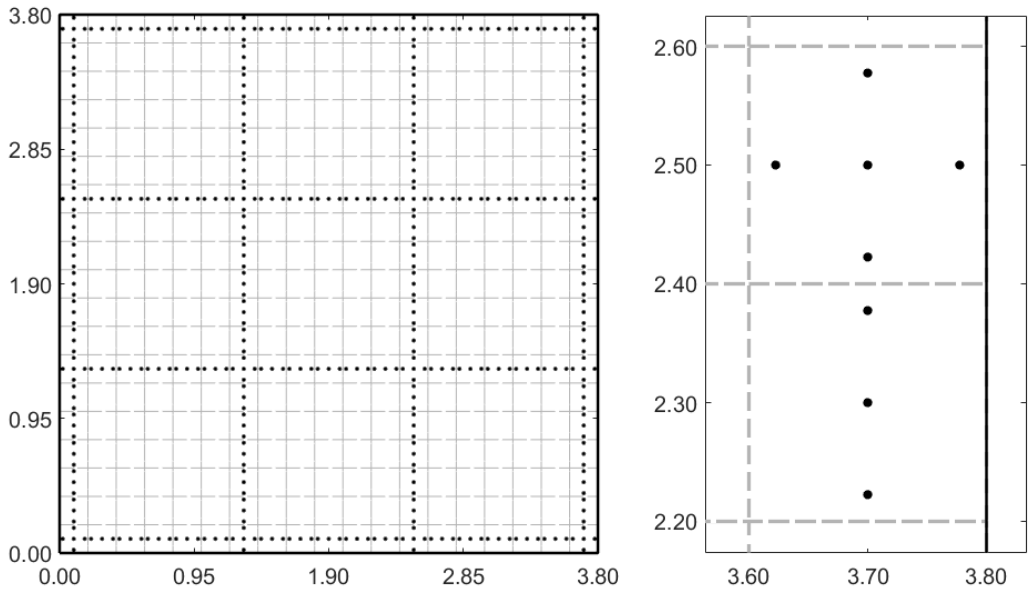

(a) (b)

Fig. 4.17 The iFEM model of the plate showing: (a) the 16×16 quadrilateral element mesh (in light gray) along with the strain sensor positions (each black dot represents a strain rosette), and (b) magnified view of sensor positions within an element

For the iFEM analysis, a regular mesh with 256 iQS4 elements (16 along each side of the plate) is used and shown in Fig. 4.17a. Sensor locations within an element coincide with some of the 3×3 Gauss integration points and differ for each element to ensure the continuity of the sensor paths. Fig. 4.17b shows a magnified view of sensor positions with certain elements, with a minimum of three and a maximum of five strain rosettes per element. The 3×3 Gauss quadrature is used to integrate the error norms of Eq. 2.63. As the plate is only under in-plane loading, only the membrane strain measures exist. Hence, sensors placed only on the top (or bottom) surface of the plate are sufficient for calculating the experimental strain measures as per Eq. 2.59.

For Damage Case-1, the iFEM reconstructed contour plot of the damage index (calculated using Eq. 4.3) is shown in Fig. 4.18a. A higher strain magnitude is immediately visible at the center of the plate, close to the actual damage site. This strain field is not overly concentrated but rather quite diffuse. This feature is due to the lack of any strain sensors in the close vicinity of the damage; instead, strains are measured further away where the magnitude of the perturbations is low. Experimental noise also contributes to this diffusion and any asymmetries in an otherwise symmetric problem. Despite these minor limitations, the results present a clear qualitative picture of the presence and location of the damage on the structure.

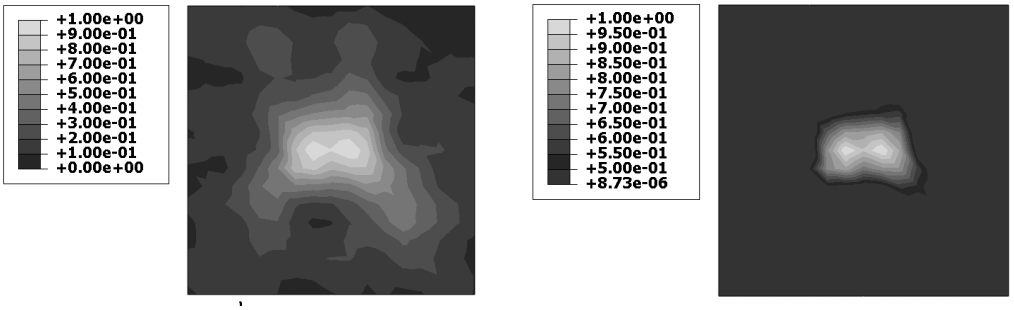

(a) (b)

Fig. 4.18 iFEM results using the strain rosette grid for Damage Case-1: (a) contour plot of damage index, I_D, and (b) the contour plot with a 50% threshold enforced

The location of damage can be further isolated through the use of a threshold value, $I_d|_{ts}$, for the damage index. Potential damage locations are those where $I_d > I_d|_{ts}$. In the present case, the value of threshold used is $I_d|_{ts} = 0.5$. The threshold enforced contour plot is shown in Fig. 4.18b. The results show that the use of a threshold allowed for clear discrimination between regions with and without damage, filtering out unwanted influences due to experimental noise. Fig. 4.18b also reveals dual strain peaks, which could be misdiagnosed as two separate damages. However, these peaks can be considered a feature of the proposed methodology.

These preliminary results are promising and highlight successful damage detection even using strain data contaminated with noise. Before presenting similar results for Damage Cases-2 and 3, a further optimisation of the benchmark strain rosette grid, using virtual sensor expansion to reduce the number of sensors used, is discussed. Subsequently, iFEM results using these new and benchmark sensor configurations for all three damage cases are presented.

4.2.2 Damage Detection using Uniaxial Strain Measurements

The benchmark sensor grid is an ideal case that is difficult to replicate experimentally due to the large number of sensors required. The present section investigates simpler patterns that reduce the number of sensors used and guarantee effective damage detection and localisation performance. The new configurations adopted utilise fibre optic strain sensors (FOSS) due to the high measurement density offered along the fibre length. The only limitation is that, in contrast to strain rosettes that measure tri-axial strains, fibre optic measurements are uniaxial, measuring strains oriented along the local tangent to the fibre. Although FOSS enabled an augmentation in the number of strain measurements, it corresponds with depreciation in quality. Based on previous studies, certain characteristics of these FOSS-based patterns are also identified: continuity of sensor paths and instrumentation of boundary elements.

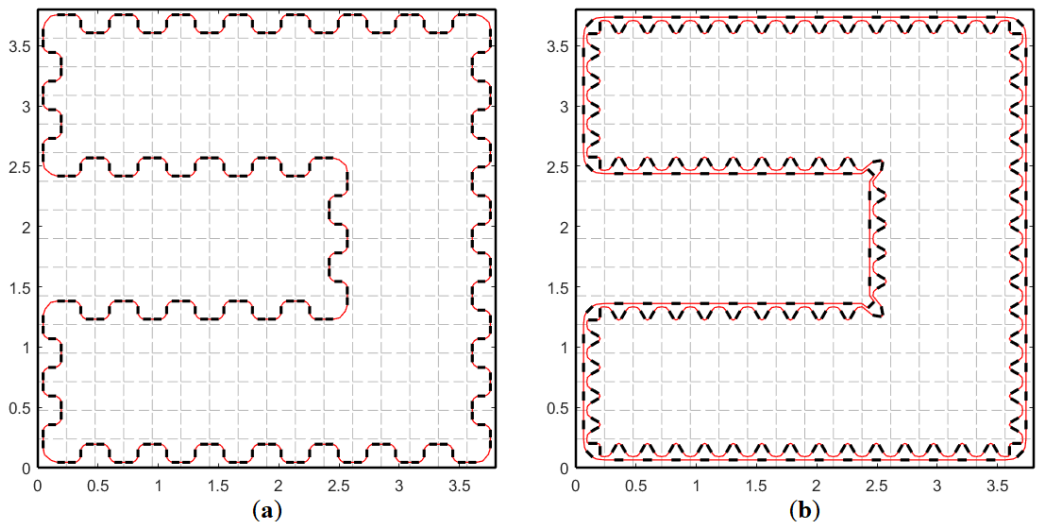

Fig. 4.19 The two novel FOSS-based sensor patterns: (a) Configuration-1, and (b) Configuration-2, proposed for the iFEM-based damage detection strategy

Two FOSS-based sensor patterns are proposed in an attempt to recreate the basic layout of the benchmark sensor grid (see Fig. 4.19):

- Configuration-1 (CFG-1): a single continuous fibre is arranged in a wave-like pattern. The fibre pattern within an element is referred to as 'Unitcell-1' (shown in Fig. 4.20), as the same pattern is repeated across the entire plate to achieve the overall pattern. The strain measurements are located at the 3×3 Gauss integration points, with at most three strain measurements per element. At any measurement point, either the $\varepsilon^{\varepsilon}_{x0}$ or $\varepsilon^{\varepsilon}_{y0}$ component of strain is measured;
- Configuration-2 (CFG-2): two continuous fibers are arranged to recreate a strain rosette within each element. This elemental arrangement is referred to as 'Unitcell-2' (shown in Fig. 4.20) and, similar to the previous case, is repeated across multiple elements. The three uni-axial measurements which constitute the rosette are oriented along angles 0^0 and $\pm 60^0$, respectively. These three uniaxial measurements are used to calculate the triaxial components of strain at the element centroid.

The inverse mesh proposed in Section 4.2.1 (with 256 iQS4 elements) is used for the present iFEM analysis as well. For CFG-1, the 3×3 Gauss scheme is used to numerically integrate the error norms, while for CFG-2, the 2×2 Gauss scheme is used, with the same centroidal strains applied at all the integration points. This scheme also facilitates an interesting comparison between two different numerical integration schemes for the same problem, the former producing greater accuracy and the latter offering lower computational effort.

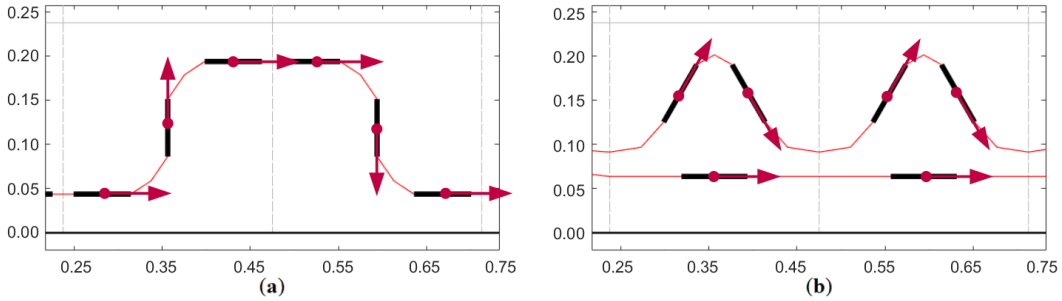

Fig. 4.20 The fiber arrangements and uni-axial strain measurements within each inverse element corresponding to: (a) Unitcell-1, and (b) Unitcell-2

The complete set of in-situ strain measurements corresponding to the two FOSS-based sensor configurations is shown in Fig. 4.21. Although the FOSS-based patterns attempted to recreate all the sensor paths in the benchmark sensor grid, the in-situ strains measured were insufficient to guarantee an accurate iFEM reconstruction and could potentially lead to a breakdown of the iFEM procedure.

The use of virtual sensor expansion strategies offers a solution to this problem (as discussed in Section 4.1.2). In the present case, the 1D SEA is used to expand the in-situ strain measurements and generate continuous smoothed strain distributions along each sensor path of the grid. A more detailed explanation of the use of 1D SEA for the current problem is provided in Appendix C.3. Although 1D SEA results are not discussed, smoothed strains are essential for generating more robust iFEM solutions. These are discussed in the following sections.

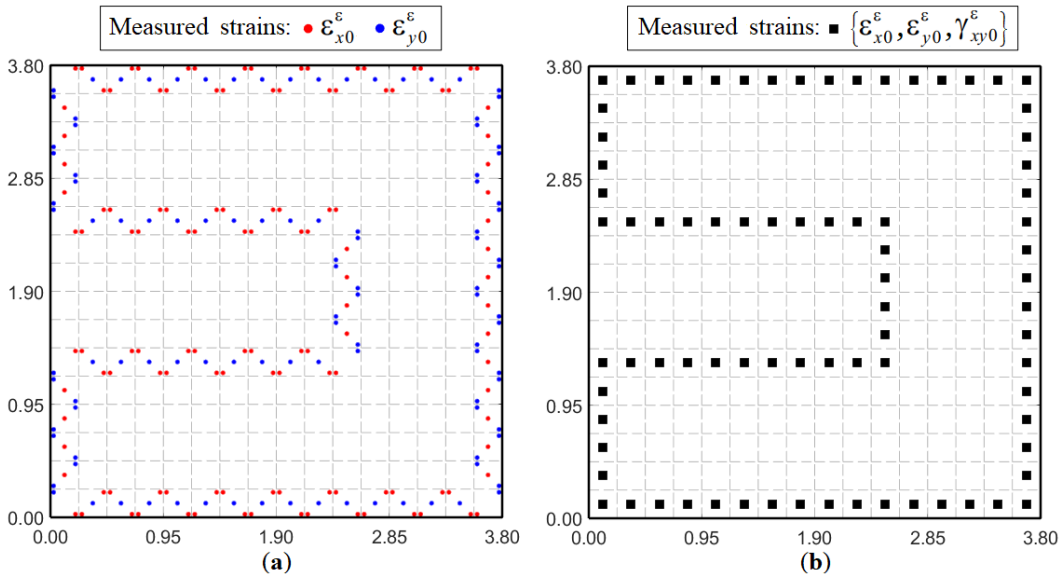

Fig. 4.21 The complete set of strain components measured within the plate by the arrangements: (a) Unitcell-1, and (b) Unitcell-2

Results for Damage Case-1

The two FOSS-based sensor patterns are applied for reconstructing the damaged strain field of Damage Case-1, and the results are shown in Figs. 4.22a and 4.23a. Compared to previous results, clear differences are observed; CFG-2 results are comparable to the benchmark case, while those of CFG-1 are deficient. Although both cases predicted a strain concentration near the center of the plate, the strain distribution of CFG-1 is asymmetric, aligned closer to the actual fibre path on the right. Also, compared to the benchmark results, these strain distributions are more dispersed. This is attributed to the much lower number of sensors used than in the benchmark case. For isolating and better representing all possible damage sites, a damage threshold ($I_D > I_D|_{ts}$, where $I_D|_{ts} = 0.5$) is enforced and these results are shown in Figs. 4.22b and 4.23b.

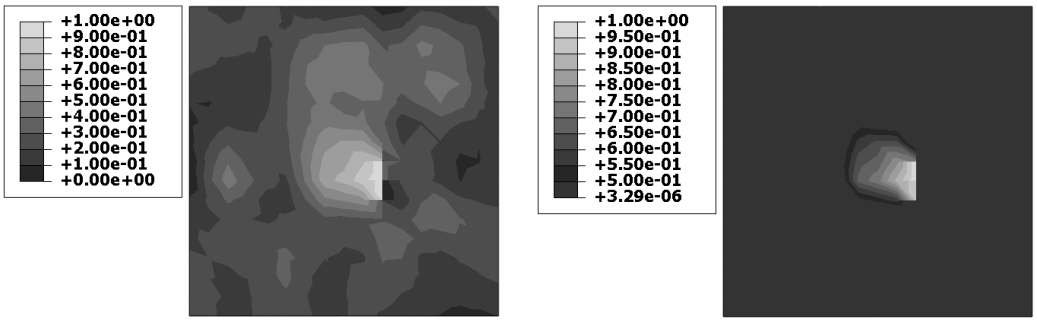

(a) I_D (b) $I_D|_{ts} = 0.5$

Fig. 4.22 iFEM results using CFG-1 for Damage Case-1: (a) contour plot of damage index, I_D, and (b) threshold enforced contour plot with $I_D|_{ts} = 0.5$

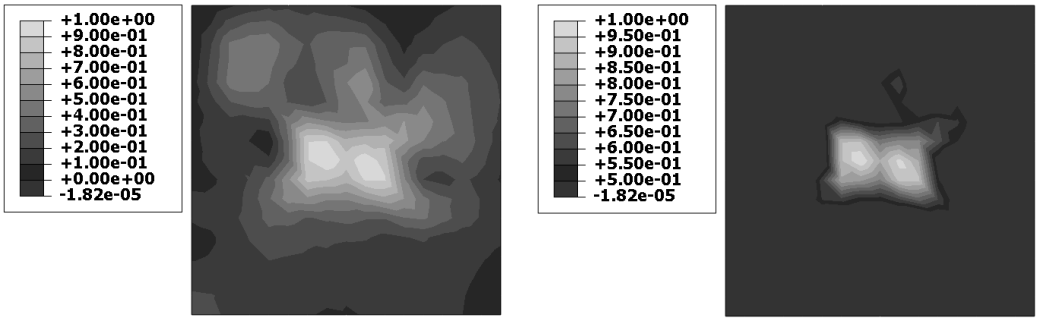

(a) I_D (b) $I_D|_{ts} = 0.5$

Fig. 4.23 iFEM results using CFG-2 for Damage Case-1: (a) contour plot of damage index, I_D, and (b) threshold enforced contour plot with $I_D|_{ts} = 0.5$

As seen in the results of Section 4.2.2, the application of a threshold aids in discriminating between damaged and undamaged regions of the plate. In the regions isolated by the threshold, the damage peaks are not exactly at the plate center for CFG-1, and multiple peaks are observed for CFG-2. These peculiar strain distributions are influenced by the design of the sensor pattern used and the magnitude of noise in the strain field. As reasoned previously, they can be considered a feature of the selected sensor configuration. Using a threshold to isolate plausible damage regions rather than localising a specific damage point is expected to constitute a more reliable and accurate damage detection strategy.

Any minor limitations observed should also be contrasted against the number of sensors required to recreate each FOSS-based pattern. Compared to benchmark results, CFGs-1 and 2 use a significantly lower number of strain sensors (maximum two FOSS), which is highly appealing from a practical perspective.

Damage Case-1 results presented a successful preliminary assessment of damage detection using iFEM-based strategies. The iFEM reconstructed strain fields provided information regarding the presence and location of damage on the plate, even under the influence of external noise. Hence, this study is pushed further, and Damage Cases-2 and 3 are also investigated to understand the influence of damage size, location and orientation on iFEM predictions. These results are shown in Sections 4.2.3 and 4.2.4.

For Damage Case-2, as the damage is smaller and positioned close to a corner of the plate, the strain perturbations are more localised with a lower magnitude. The measured strains are also influenced by end effects due to their location close to a free edge of the plate. In addition to these factors, the strain measurements are also influenced by the artificial noise introduced. The main observation from the results of Damage Case-2 are described below:

- All three cases achieved different levels of success in accurately detecting the damage site, as shown by Fig. 4.24;
- In contrast to results for Damage Case-1, no single and obvious damage location (indicated by a corresponding strain concentration) exists; multiple strain peaks at various locations of the plate are observed for all three cases;
- Due to the presence of multiple possible damage sites, the use of a threshold proved to be essential in filtering out false positives;
- The benchmark results are the most accurate, with the greatest strain peak located close to the actual damage site; it should be noted that even the enforcement of a threshold ($I_D|_{ts} = 0.5$) is not sufficient to rule out multiple false positives (see Fig. 4.24b). A possible solution is the use of a higher threshold value;
- Results for CFG-1 and 2 are inaccurate with the strain peaks not coinciding with the damage location. This indicates that the influence of measurement noise overpowers the strain perturbations due to the crack.

4.2.3 Damage Index Plots for Damage Case-2

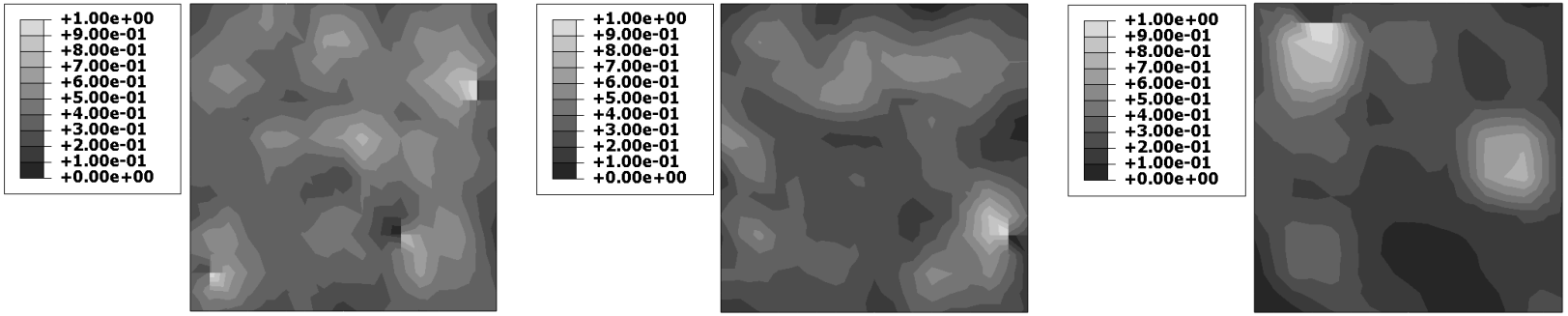

(a) Benchmark I_D plot (b) I_D plot for CFG-1 (c) I_D plot for CFG-2

Fig. 4.24 Contour plots of iFEM reconstructed damage index, I_D, using the various sensor patterns for Damage Case-2

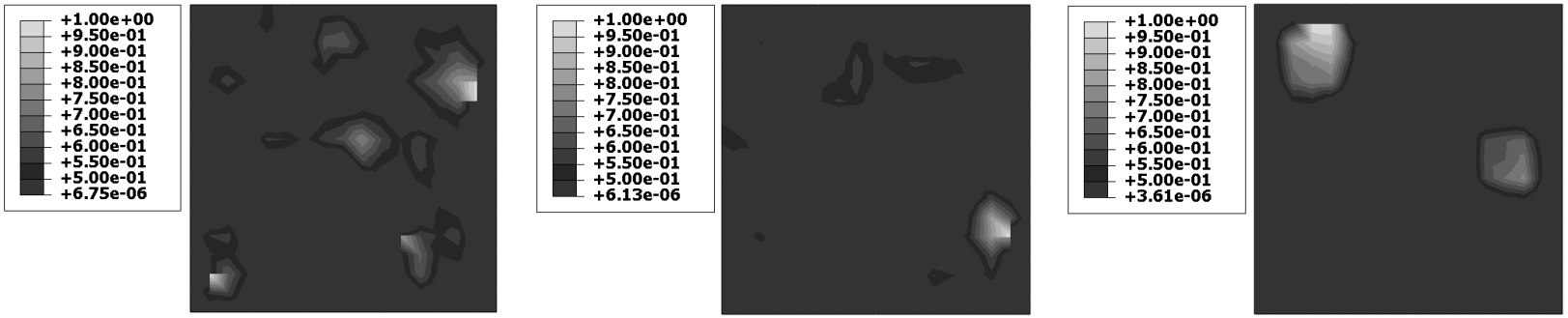

(a) Benchmark I_D plot (b) I_D plot for CFG-1 (c) I_D plot for CFG-2

Fig. 4.25 Threshold enforced contour plots of iFEM reconstructed damage index, I_D, for Damage Case-2 ($I_D|_{ts} = 0.5$)

4.2.4 Damage Index Plots for Damage Case-3

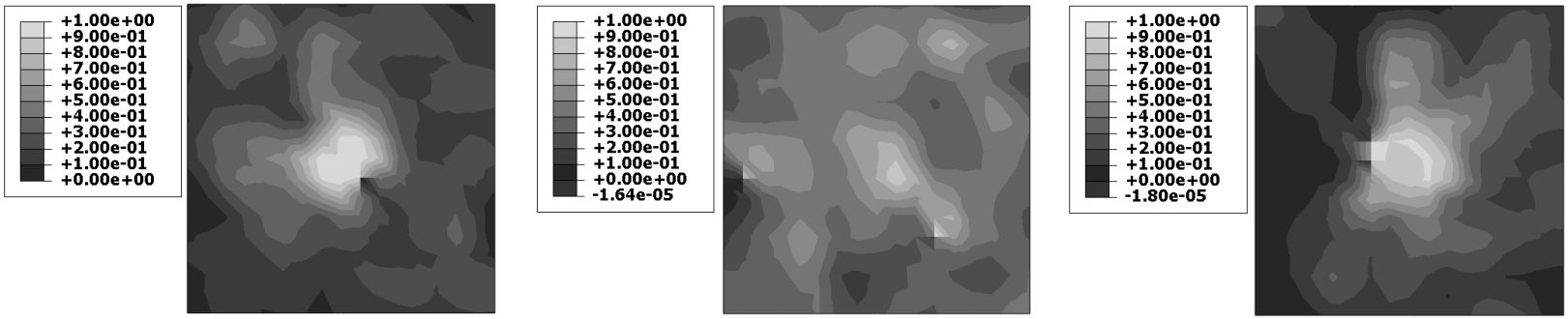

(a) Benchmark I_D plot (b) I_D plot for CFG-1 (c) I_D plot for CFG-2

Fig. 4.26 Contour plots of iFEM reconstructed damage index, I_D, using the various sensor patterns for Damage Case-3

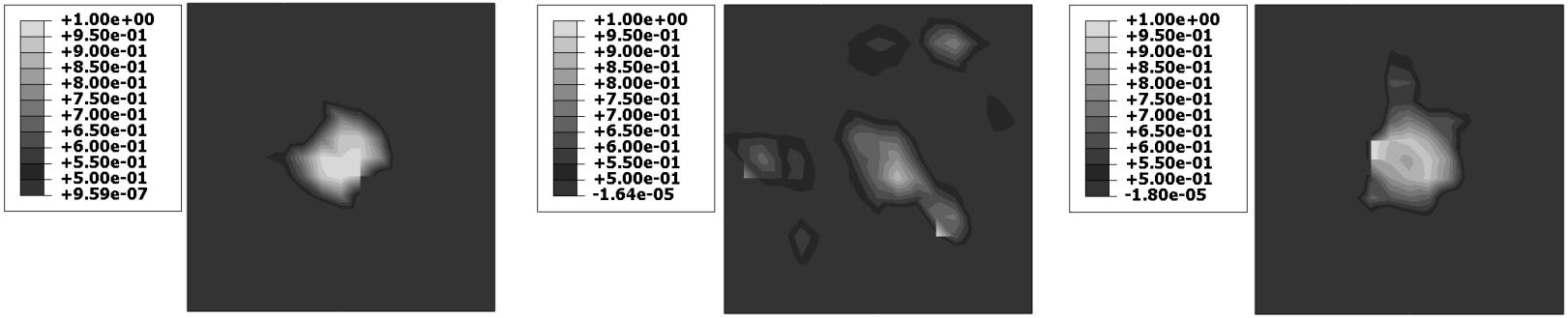

(a) Benchmark I_D plot (b) I_D plot for CFG-1 (c) I_D plot for CFG-2

Fig. 4.27 Threshold enforced contour plots of iFEM reconstructed damage index, I_D, for Damage Case-3 ($I_D|_{ts} = 0.5$)

Damage Case-3 introduces an additional variable to the problem, i.e., the orientation of the damage. As the crack is oriented at an angle of 45^0 with respect to the horizontal axis, the strain perturbations and the measured strains are also expected to be influenced. The main observation from the iFEM results of Damage Case-3 (shown in Section 4.2.4) are summarised below:

- For all three cases, the distribution of strains in iFEM reconstructed results (Fig. 4.26) reflect the damage orientation as well;
- The transfer of orientation information from the measured strains to the iFEM results is very encouraging, especially because it provides information on how the damage is likely to develop over time;
- The original damage index plots of Fig. 4.26 reveal multiple potential damage peaks; however, the threshold enforced plots of Fig. 4.27 accurately filter unwanted sites for all three cases;
- Benchmark and CFG-2 are very effective, with the results correctly indicating the damage position. Damage orientation can also be inferred from the strain distributions of Figs. 4.27a and 4.27c;
- CFG-1 results are less accurate, providing only positional information. Minor peaks at other locations can also be seen in Fig. 4.27b.

Based on the results from all three damage cases, certain general conclusions are derived about the iFEM-based damage detection strategy and the sensors patterns used:

- The iFEM-based strategy is effective in detecting and localising damages using a sparse set of surface strain measurements;
- There is a lower limit of damage size that can be successfully detected. This limit is influenced by the sensor pattern used, damage location, and the magnitude of measurement noise. When strain perturbations due to the damage are lower than perturbations caused by measurement errors or environmental factors, successfully damage detection is not possible. The damage position relative to a sensor path is also a factor, with a small crack located near a path generating greater strain perturbations than a larger crack located further away (discussed more in following sections);
- Definition of a suitable damage index threshold is instrumental for successful damage detection; a lower threshold can lead to false positives, while a very high threshold might filter true positives;
- Among the FOSS-based sensor patterns, CFG-2 provided the most accurate results (comparable to the benchmark case) using just a fraction of the in-situ strain measurements. This is attributed to its ability to provide information on all three components of strain within an element;
- A key distinction between the two configurations is the treatment of in-plane shear strains. CFG-2 used shear strain measurements from the centroid of each instrumented element. In contrast, CFG-1 assumed a constant shear

strain throughout the plate. As shear contribution is significant in defining the damaged strain field near the crack, the case providing the most accurate estimation of shear strains (CFG-2) yielded the more accurate results;

- Comparison between the two integration schemes also yielded interesting conclusions. CFGs-1 and 2 used the 3×3 and 2×2 Gauss schemes, respectively. More robust and accurate results are obtained using CFG-2, revealing that the 2×2 Gauss scheme is sufficient for an accurate numerical integration for the present problem. These results, combined with the lower computation effort and low number of in-situ strain sensors required, make their use more appealing for future applications;
- Finally, the virtual sensing strategy used influences the iFEM results. More elaborate investigations on optimal smoothing meshes or virtual sensing strategies are left for future works.

4.2.5 Noise Sensitivity Study

Results of Section 4.2.4 highlighted the influence of measurement noise on damage detection performance. This is investigated in the present section through a sensitivity study, where the change in damage detection performance with increasing noise levels is evaluated. The most promising case among the previous results, i.e., Damage Case-1 and using CFG-2, is used, and numerical strain measurements are contaminated with eight different noise levels, from 2.5% to 20%.

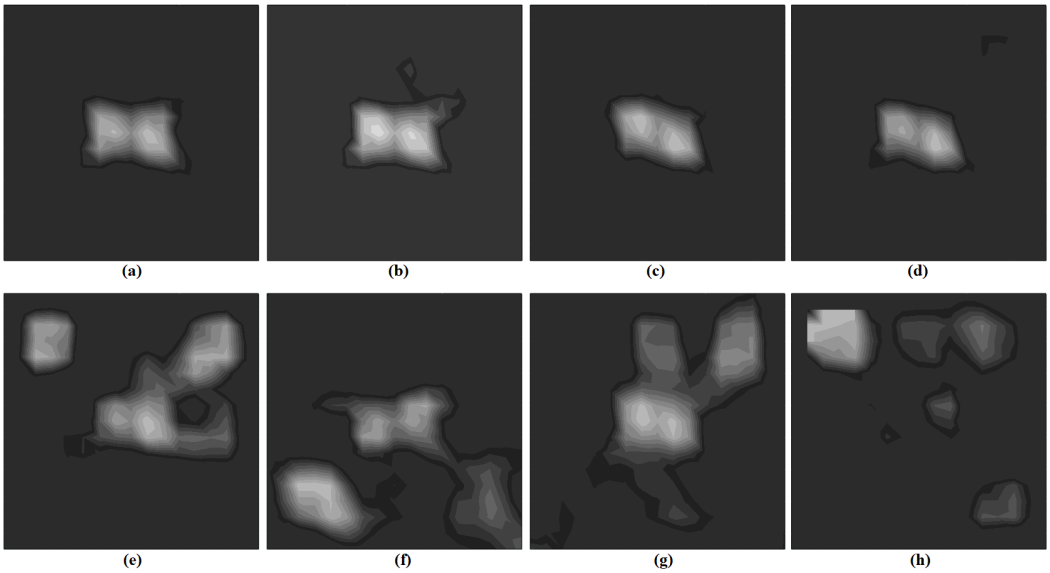

Fig. 4.28 Contour plots of threshold enforced I_D using CFG-2 for Damage Case-1 corresponding to the noise levels: (a) 2.5%, (b) 5.0%, (c) 7.5%, (d) 10.0%, (e) 12.5%, (f) 15.0%, (g) 17.5%, and (d) 20.0%

The results of the sensitivity study are given in Fig. 4.28, where the threshold enforced ($I_D|_{ts} = 0.5$) contour plots of the damage index are shown. As expected, the results deteriorate as the noise level increases. Till a noise level of 10%, strain concentration is correctly reconstructed at the center of the plate, and successful damage detection and localisation are possible. Over a noise level of 10%, in addition to the central peak, other damage peaks are generated. Even in such cases (i.e., noise levels from 12.5 to 17.5%), a higher threshold can be used to isolate the prominent peak at the center. However, as the noise level reaches 20%, results are inaccurate and successful damage detection is no longer possible. In such cases, the strain perturbations due to the noise are significantly higher than those produced by the damage.

The results of the sensitivity study are encouraging as they highlight the robustness of the iFEM-based approach and the FOSS-based pattern, CFG-2. Robustness is a key feature for a damage detection strategy to monitor structures under challenging environmental and operational conditions, and in this regard, the results presented are encouraging.

4.3 Probabilistic Assessment of Monitoring Strategies

Aside from measurement noise (investigated in Section 4.2.5), other factors that influence damage detection performance are the size, position, and orientation of damage on the plate. Section 4.2.2 investigated three discrete damage cases varying each of these parameters. However, such a limited investigation is insufficient to draw general conclusions regarding the effectiveness of a strategy. For example, Section 4.2.3 showed the iFEM-based approach to be ineffective for Damage Case-2, possibly indicating that the strategy is ineffective for damages of that size or smaller. Instead, a similar-sized damage positioned closer to a sensor path can lead to improved predictions. Hence, additional effort is required in quantifying the effectiveness of the iFEM-based damage monitoring strategy.

This section investigates probability-based metrics for characterising a damage detection strategy. In particular, two metrics are used:

- Probability of Detection (POD): the conditional probability that a monitoring strategy will detect the damage, given that it exists on the structure. POD is calculated as a function of damage characteristics (e.g. crack length);
- Probability of False Alarms (PFA): the conditional probability that a monitoring strategy detects a damage, even though it does not exist.

A low POD represents an ineffective strategy, unable to detect existing cracks, while a high PFA leads to unwanted maintenance costs and efforts. An ideal damage detection strategy should guarantee a high POD with a low PFA.

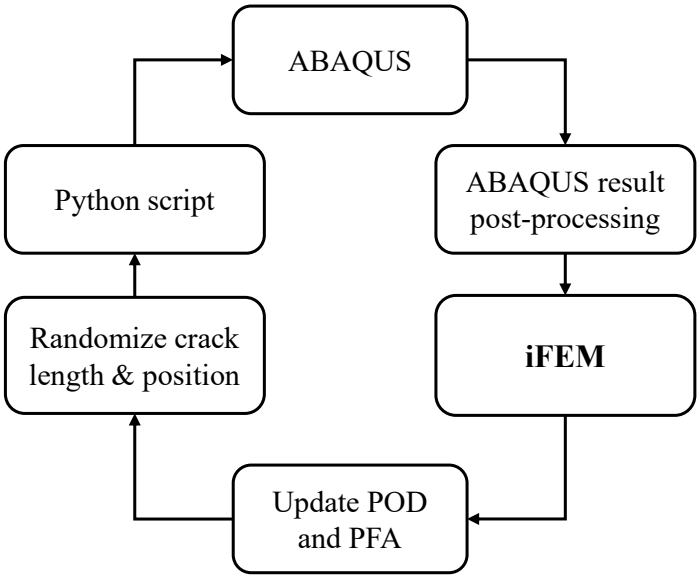

Fig. 4.29 Flow diagram of the iterative procedure used for computing the POD and PFA curves for the iFEM-based damage detection strategy

The benchmark sensor pattern of Section 4.2 is characterised using these two probability-based metrics. As calculating these probabilities requires numerous damage cases to be explored, an iterative model-based approach using numerical strains extracted from a high-fidelity FEM model developed in ABAQUS is used. The main steps of this mode-based approach are described in Fig. 4.29.

The plate problem of Section 4.2 is investigated, where the parameters defining the crack, i.e., the length L_c and position (x_c, y_c) are now iterated. For each value of crack length, the crack position is randomised using a uniform distribution function to obtain 500 different iterations of damage scenarios. Each iterated damaged plate case is modelled in ABAQUS with the aid of the python scripting functionality, and numerical strains are extracted at sensor locations corresponding to the benchmark sensor pattern of Fig. 4.17 and used for the iFEM analysis.

For an objective evaluation of the effectiveness of iFEM results, the reconstructed strain field is post-processed as:

- Calculate the value of damage index (I_D) at the centroid, (x_e, y_e), of all elements not instrumented with strain sensors;
- Damage detection is successful if there exists a point, (x_e, y_e), satisfying the criteria: $I_D(x_e, y_e) > I_D|_{ts}$, and damage location, (x_m, y_m), is determined as the mean of all points, (x_e, y_e), obeying this criteria;
- Damage localisation is deemed successful if, $|(x_m, y_m) - (x_c, y_c)| < R_c$, where the radius R_c determines the precision required for the damage detection strategy (R_c =10% plate length in the present case).

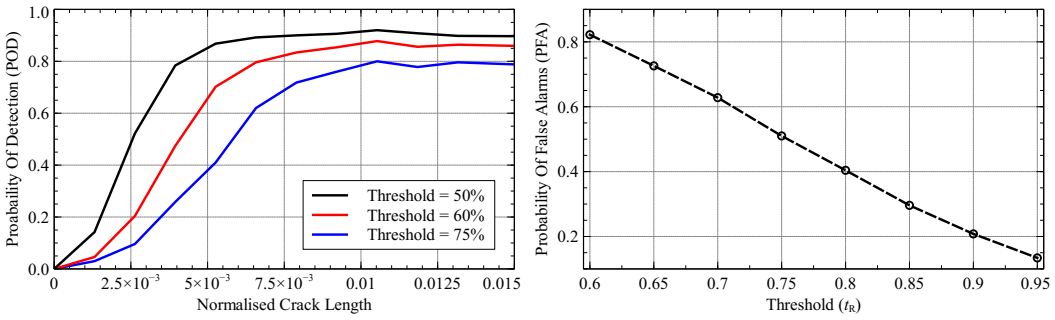

(a) (b)

Fig. 4.30 Results of the model-based process, showing the plot of (a) POD as a function of the crack length (for different thresholds), and (b) PFA as a function of the threshold level

For all damage cases with crack length, L_c, the value of POD is calculated as the ratio of the number of successful detections to the total number of damage cases. For very small values of L_c, POD tends to zero, while for very high L_c, POD converges to 1. Avoiding both extremes, suitable values of L_c in the range of 0.1% to 1.5% of the plate length are used, and different damage thresholds are also investigated. PFA is evaluated by iterating different scenarios of the undamaged plate, with strain measurements contaminated by noise following a Gaussian distribution with the third standard deviation equal to 5%. PFA is computed similar to POD but as a function of the damage threshold used. The results of the iterative study are shown as plots of POD and PFA in Fig. 4.30.

Fig. 4.30a demonstrates that POD increases with an increase in crack length, as larger-sized damages are easier to detect, eventually converging to 1 (not shown in the figure). The threshold value used has a significant impact, with POD increasing with decrease in threshold. As a lower threshold value is less discriminative to potential damage sites, the probability of damage detection also increases. However, this comes with a corresponding increase in PFA, as shown in Fig. 4.30b, due to the detection of false positives. For a value of threshold offering the highest POD, $I_D|_{ts} = 0.5$, the value of PFA is seen to be very high (PFA> 0.8), which is not very encouraging. Similarly, although a threshold value of $I_D|_{ts} = 0.95$ can guarantee a very low PFA ($=\sim 0.1$), the corresponding POD is low. A suitable damage detection strategy is adopted considering an optimal trade-off between these two quantities. Usually, the objective is to minimise PFA, thus avoiding unwanted maintenance costs and activities.

These results constituted preliminary investigations into alternative ways to qualify the effectiveness of the monitoring approach. Based on the results, it can be determined that the iFEM-based monitoring approach using the benchmark sensor pattern guarantees a high probability ($> 80\%$) of detecting cracks with lengths $L_C > 1\%$ of the plate length located anywhere on the plate.

4.4 Multi-Resolution Monitoring

Chapters 2, 3, and 4 were aimed at describing the different iFEM approaches and outlooks, both 1D and 2D, to the problem of shape sensing and investigating possible solutions to some of the common problems hindering their widespread adoption. Subsequently, a specific application of these strategies for the case of damage detection was also described in Section 4.2. Despite the broad range of topics covered, these efforts were all oriented towards a common aim, i.e., developing an efficient strategy for monitoring complex structural geometries and generating robust results using the least number of sensors required. This section presents a culmination of these efforts, proposing a common integrated framework based on a 'Multi-Resolution' approach to structural monitoring.

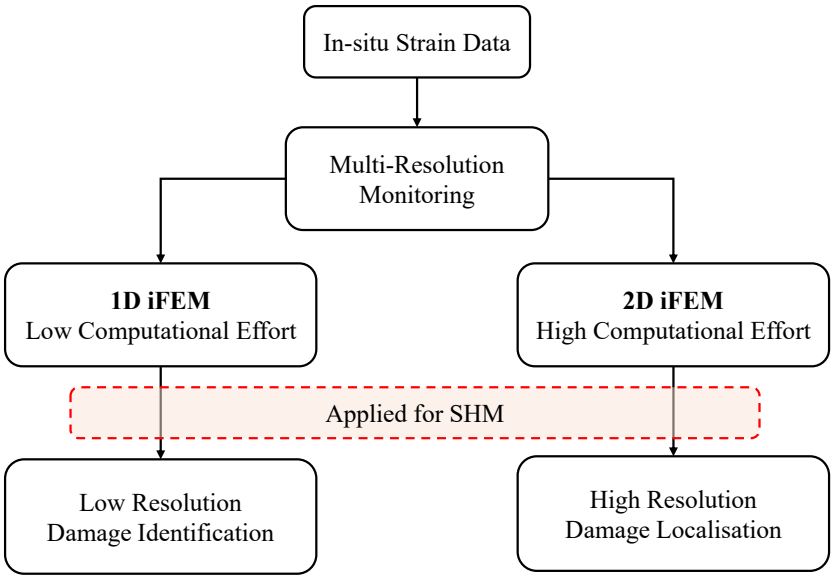

Fig. 4.31 Illustration of the Multi-Resolution monitoring framework describing the advantages and limitations of both 1D and 2D iFEM approaches for the specific case of SHM

The crux of the Multi-Resolution approach is the integration of both 1D and 2D shape sensing strategies, which otherwise had been investigated separately, under a common framework. Such an integration is based on maximising the benefits and minimising the limitations of each strategy. Due to the lower fidelity of finite element discretisation involved, the 1D iFEM can generate shape sensing results using a relatively low number of in-situ strain measurements and requiring low computational effort. However, the results produced are of a 'lower' resolution, i.e., the kinematic variables are reconstructed only along the beam axis and displacement at a point is calculated based on the kinematic assumptions used. These results prove

more effective in monitoring the global deformation field of the structure rather than capturing any local nuances.

In contrast, 2D iFEM uses a high-fidelity finite element discretisation of the structure, thus requiring a higher computational effort and a larger number of sensors to produce shape sensing results. Correspondingly, the results produced are of a 'higher' resolution, capable of capturing any local nuances in the deformation field of the structure. From the perspective of SHM, 1D iFEM is an effective tool for damage detection, while localisation is restricted to a single coordinate, i.e., along the beam axis. In contrast, the 2D iFEM is an effective tool for damage detection and accurate localisation due to the finer discretisation of the structure.

Based on the advantages and limitations of both approaches described above, the 'Multi-Resolution' framework can now be understood from the flowchart of Fig. 4.31. The 1D iFEM is the initial low-resolution monitoring tool, utilizing only a small subset of in-situ strain measurements. Due to the low computational effort required, it is an efficient and flexible tool for real-time monitoring. Any damage sensitive features or anomalous deformation behaviour detected from the initial analysis is subject to higher-resolution monitoring using the 2D iFEM for a more precise assessment of the anomalies detected (i.e., to identify crack size and location). The following sections describe a preliminary numerical demonstration of the Multi-Resolution monitoring approach.

4.4.1 Wing box Monitoring

The Multi-Resolution approach is investigated numerically using a cantilevered swept wing box structure. The wing box comprises of a top and bottom plate, with three longitudinal spars running along its length. It has a length, $L = 5$ m, width, $w = 1$ m, height, $h = 0.25$ m, and is swept by an angle of 30^0 as shown in Fig. 4.32. The thickness of the top, bottom plates and the spars are 5 mm. The material used is an aluminium alloy with Young's Modulus, E=73 GPa, Poisson's ratio, ν=0.3, and density, ρ= 2700 kg/m^3 (Table 3.1).

The wing box is fixed at the root and allowed to deform under the influence of gravity, leading to both bending and torsional deformation in the structure. Real-time monitoring is performed using strain measurements from sensors instrumented on the surface of the structure. For the present problem, the top and bottom plates of the wing box are instrumented with fibre optic strain sensors (on both sides of each plate), measuring in-plane and curvature strains. Such a sensor scheme measures strains along four separate sensor paths, two on the top plate and two on the bottom plate, respectively, and spaced 0.5 m apart. Sensor positions are illustrated (in red) in Fig. 4.32, and this sensor scheme produces a common set of in-situ strain measurements useful for both 1D and 2D shape sensing.

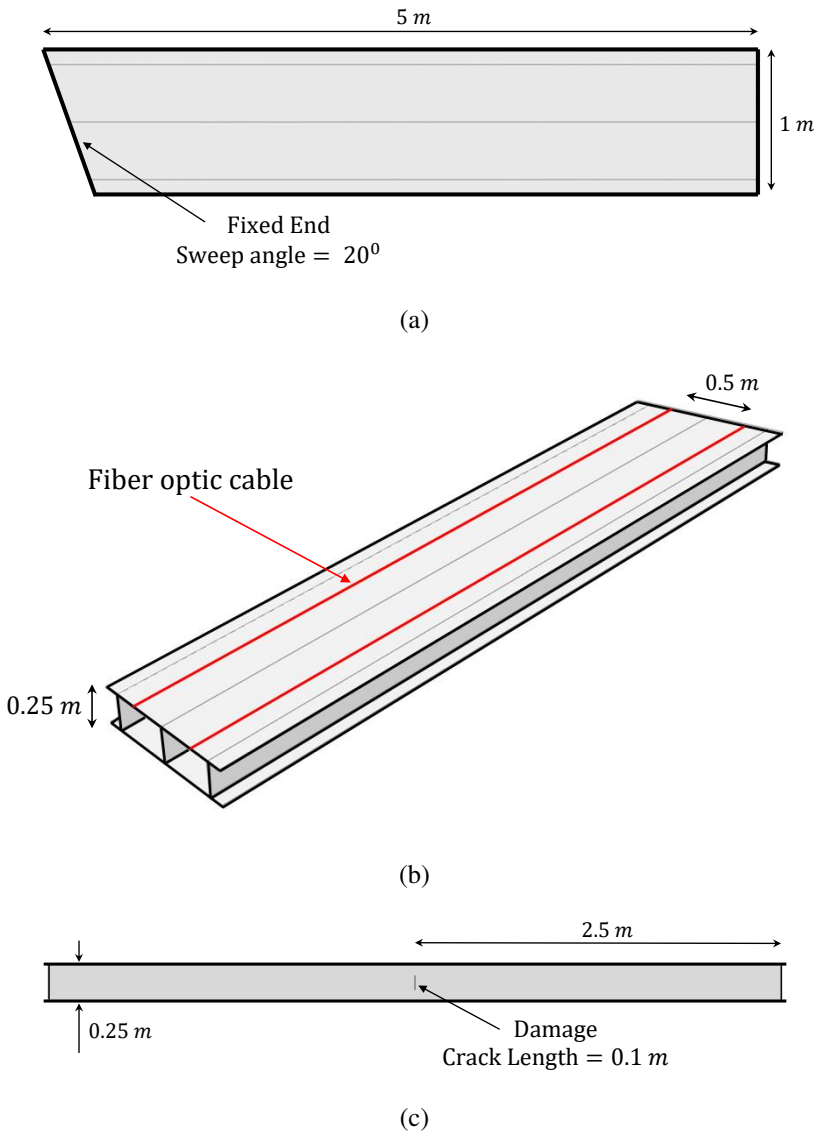

Fig. 4.32 Model of the swept wing box structure: (a) top view showing the the dimensions and swept end, (b) isometric view showing the fiber optic sensors. and (c) right-side view showing the position and size of the damage

As described in the Multi-Resolution monitoring approach, both 1D and 2D iFEM are used for the numerical shape sensing of the wing box. Numerical strains required for the iFEM are obtained from a high-fidelity FEM model of the wing box developed in ABAQUS and meshed using a total of 21201 S4R elements. The FEM strain and displacement fields are also used as a reference for iFEM results. For the iFEM analysis, two different inverse element meshes are used for discretising the wing box structure (shown in Fig. 4.33).

The 1D mesh uses a total of 40 iEB2 elements, positioned along the mid-plane of the central spar of the wing box, as shown in Fig. 4.33a. The choice of number and type of inverse beam elements used is influenced by the nature of in-situ strain measurements; FOSS offers a high measurement density, but all the measurements are uniaxial and oriented parallel to the beam axis (no shear measurements). Along each sensing line, axial strains are measured with a density of one per 5 cm, resulting in a total of 93 axial sections where strains are measured. A minimum of 2 and a maximum of 3 measurement sections are used per inverse beam element.

To reduce computational effort for the 2D iFEM analysis, only the top plate of the wing box is discretised using 2D finite elements. Such an analysis is deemed sufficient for the present problem, for accurately reconstructing wing box deformations. The top plate is discretised using 480 iQS4 elements, forming a regular quadrilateral element mesh as shown in Fig. 4.33b. For shell elements lying along a fibre sensor line, strains measured at the element centroid (on both sides of the top plate) are used for the iFEM analysis. Hence, strains measured at the centroid of a total of 96 iQS4 elements are used, with 48 along each sensing line (creating a continuous sensor path from the root to the tip).

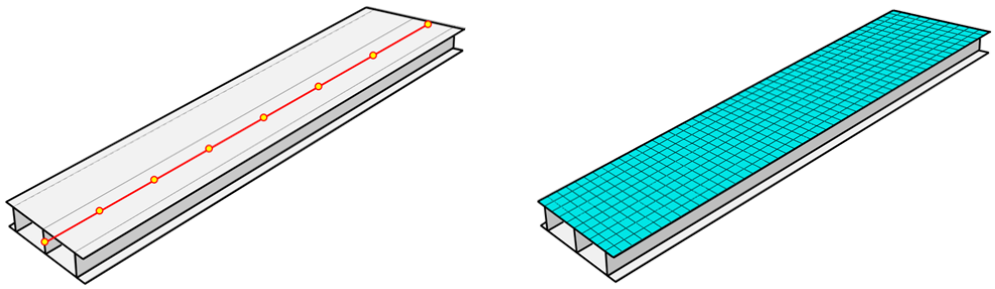

(a) (b)

Fig. 4.33 The iFEM meshes used for wing box shape sensing: (a) discretisation using inverse beam elements (figure not representative of the actual number of elements used), and (b) top plate discretised using iQS4 elements

The wing box iFEM results are evaluated for shape sensing and damage detection performance. Hence, two different wing box geometries are considered: an undamaged and damaged model. The healthy wing box is used to assess iFEM shape sensing accuracy and define a set of baseline results for damage detection. For modelling the damaged case, a 0.1 m crack is introduced on the right spar and located 2.5 m from the root of the wing box (shown in Fig. 4.32c). The iFEM results for the damaged wing box are compared against the baseline results. The presence of any damage is illustrated by any deviation from this baseline and is expected to constitute a more robust damage detection strategy.

The reference and iFEM reconstructed transverse deflection for the damaged wing box are shown in Figs. 4.34. Both iFEM approaches are accurate; 1D iFEM is less accurate with an error of 17%, while the 2D iFEM is more accurate with an error of $< 2\%$, as expected. The lower accuracy of the 1D iFEM is attributed to the absence of transverse shear deformations, combined with the complexity of the geometry investigated. The corresponding iFEM axial strain field is calculated using the strain-displacement relations. The undamaged and damaged iFEM results are used to calculate the baseline reduced strains as follows,

$$\Delta\varepsilon_{xx} = \varepsilon_{xx}|_{\text{dmg}} - \varepsilon_{xx}|_{\text{base}} \tag{4.4}$$

where $\varepsilon_{xx}|_{\text{dmg}}$ and $\varepsilon_{xx}|_{\text{base}}$ represent the damaged and baseline axial strains, respectively. The reference FEM axial strains is shown in Fig. 4.35a, while the baseline reduced axial strains using the 1D and 2D iFEM are shown in Figs. 4.35b and 4.35c, respectively. Both baseline reduced plots provide different levels of damage information, as discussed previously.

The $\Delta\varepsilon_{xx}$ distribution over the top plate, obtained using the 1D iFEM, is shown in Fig. 4.35b. Although 1D iFEM provides reconstruction results throughout the whole wing box structure, for an equivalent comparison with 2D iFEM, only the results on the top plate are presented here. Two strain peaks are evident at the wing box mid-length, correctly indicating the presence of damage. However, due to the presence of the dual peaks, a precise damage location is not evident; only the axial position is assured (hence termed 'low-resolution' results). In contrast, the $\Delta\varepsilon_{xx}$ distribution over the top plate, obtained using the 2D iFEM (shown in Fig. 4.35c), shows a precise strain peak above the actual damage site, i.e. wing box mid-length, above the right spar (hence termed 'high-resolution' results).

Although both approaches provide an accurate assessment of damage presence, the 2D iFEM is more effective in localising the damage precisely. The nature of discretisation involved explains this difference between the two approaches. The inverse shell elements can be used for a finer discretisation of the structural geometry, consequently enhancing the capability of 2D iFEM to model local strain distributions accurately. 1D iFEM lacks that capacity, as the discretisation is only 1D in nature. Any changes in the strain field due to the damage will only be reflected as a function of the axial coordinate. However, these results should be put in perspective considering the number of sensors used and the computational effort required for each case.

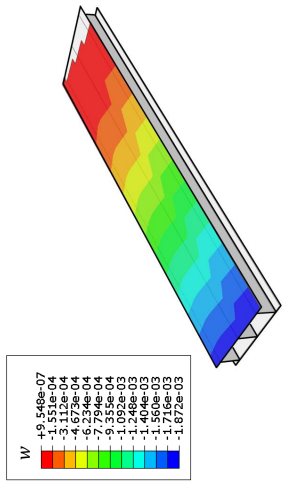

(a) FEM: Deflection, w

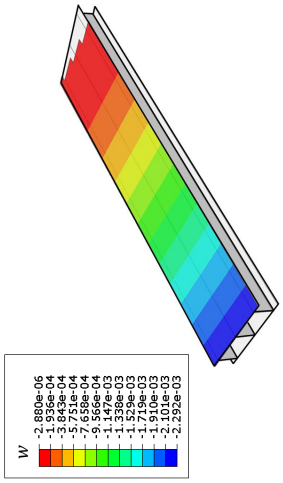

(b) 1D iFEM: Deflection, w

(c) 2D iFEM: Deflection, w

Fig. 4.34 Contour plots of transverse deflection for the damaged wing box under self weight

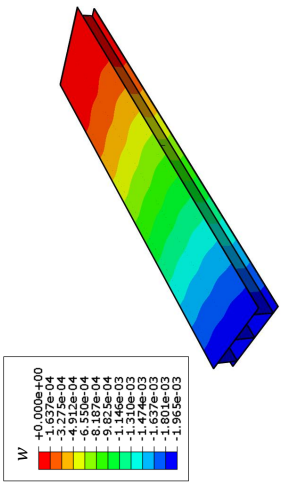

(a) FEM: Strain, ε_{xx}

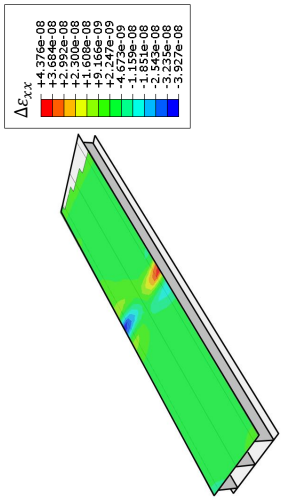

(b) 1D iFEM: Strain, $\Delta\varepsilon_{xx}$

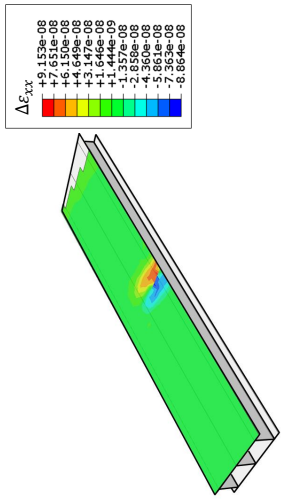

(c) 2D iFEM: Strain, $\Delta\varepsilon_{xx}$

Fig. 4.35 Contour plots of axial strain for the damaged wing box under self weight

A further investigation is also proposed where both 1D and 2D iFEM results are superposed (linear summation). The aim is to assess if such a combination can produce a more accurate representation of the damaged strain field. These results are shown in Fig. 4.36, where both baseline reduced axial strain on the top plate and its absolute value is shown. Fig. 4.36b reveals that $|\Delta\varepsilon_{xx}|$ is more accurate in localising the damage. Although not drastically different from the results of Fig. 4.35c, the combination of the two cases helps reinforce the axial strain peak of the 1D iFEM with the more localised 2D iFEM strain peak.

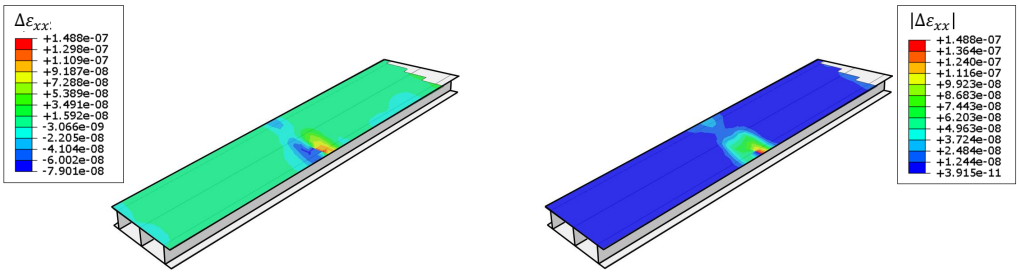

(a) $\Delta\varepsilon_{xx}$ (b) $|\Delta\varepsilon_{xx}|$

Fig. 4.36 Contour plots of (a) baseline reduced axial strain, and (b) absolute value of baseline reduced axial strain, computed using a combination of both 1D and 2D iFEM results

It must be stated that such a combination of 1D and 2D results is not an essential component of this monitoring strategy and is performed only for scientific curiosity. The 1D results are sufficient for damage detection, while for precise localisation, the 2D results are sufficient. These preliminary results help demonstrate the inspiration, features, and benefits of the Multi-Resolution monitoring approach proposed. Although demonstrated here for SHM, this novel monitoring framework also has numerous applications for the monitoring and control of shape morphing structures. Further discussions on this topic are presented in Chapter 6.

The investigations and results of this section are not meant to be exhaustive but constitute only a preliminary demonstration of the Multi-Resolution monitoring framework. Some avenues for further improvements are also identified:

- In addition to in-situ axial strains, measurement of shear strains will allow the use of iTM2D0 or iTM2D1 elements for accurate deflection and torsional rotation prediction of the wing box, improving damage detection performance;
- Use of more efficient sensor patterns (inspired by Section 4.1), possibly augmented by virtual sensor expansion strategies;
- Damage indexes based on maximum principal or Von Mises strain for a better representation of the reconstructed damaged strains (as shown in Section 4.2).

These investigations, as well as further developments of this monitoring framework, are left for future work.

Chapter 5

Beam Shape Sensing: Experimental Studies

The development of efficient 1D inverse elements for the shape sensing of beams with complex cross-sections has been a core aim of the present work. The theoretical formulation of these elements, presented in Section 2, was validated numerically in Section 3. This section presents a further validation using displacements and strains obtained from experimental test campaigns performed on different beam specimens. Experimental data is affected by factors such as imperfect boundary conditions, imprecise sensor positions, noisy sensor measurements, experimental errors, etc., which the numerical models fail to consider. Hence, the present investigation is an ideal scenario to evaluate the robustness of iFEM results. It also assesses the practical feasibility of the methodology in terms of the number of sensors used and the accuracy reported and is a logical next step in the maturation of a monitoring strategy. Three beam specimens are investigated. All experimental tests were conducted at the LAQ-AERMEC (Aeromechanical Structural Systems) lab in the Department of Mechanical and Aerospace Engineering of Politecnico di Torino.

5.1 Cantilevered Aluminium Beam

The preliminary investigation of this section discusses the use of iFEM for the experimental shape sensing of a thin-walled beam with a C profile. The material of the beam is an aluminium 6060 alloy with Young's Modulus, $E = 68.03$ GPa, Poisson's ratio, $\nu = 0.335$, and density, $\rho = 2700$ kg m^3. The beam is 1.1 m long, with a thin-walled C cross-section, roughly 45 mm high and 30 mm wide, and with a flange thickness of 2 mm. The actual beam dimensions are slightly different due to manufacturing tolerances involved and have been indicated in Fig. 5.1a. The beam is fixed at the root and is loaded using a concentrated transverse load at the tip. To

experimentally recreate an effective cantilever condition, a beam length of roughly half of the free length is fixed.

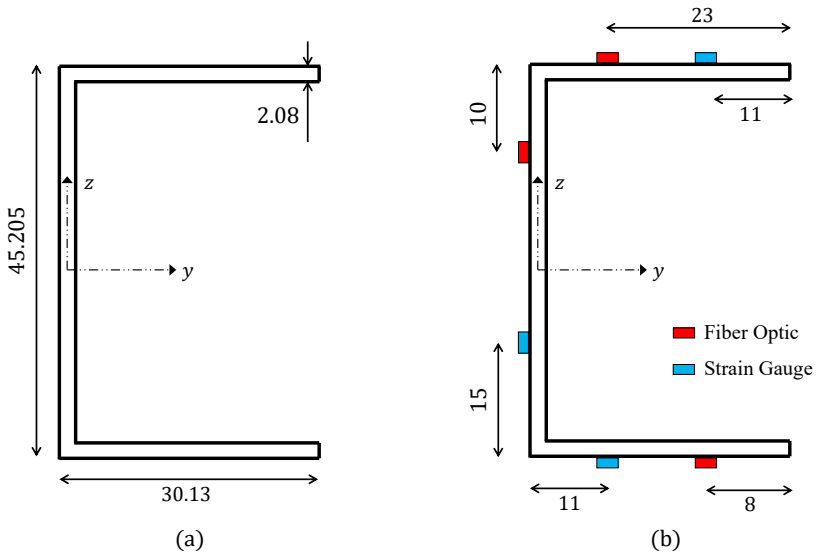

Fig. 5.1 The C beam profile of the aluminium beam specimen: (a) flange dimensions and thickness, and (b) location of the strain sensors (all dimensions are in mm)

The beam is instrumented with a combination of fibre optic sensors and strain gauges (see Figs. 5.1b and 5.2). A high-definition fibre optic sensing system provided by Luna Innovations is used for the present test. It combines an optical distributed strain sensor with an interrogator, allowing high-resolution strain measurements at a gauge pitch of 1.3 mm with an acquisition frequency of 40 Hz. A 5 m long cable is used, instrumented longitudinally (from beam root to the tip) for measuring the axial strains along the beam axis. One strain sensing line is used per flange, the locations of which are shown in Fig. 5.1b. In addition to the fibre optic cable, strain gauges are also instrumented on each flange of the beam. A total of 12 strain gauges are used, instrumented at four axial sections: $x = L/6$, $L/3$, $2L/3$, and $5L/6$ from the beam root (where L represents the beam length), with three sensors per section. The strain gauges are all oriented at an angle of 45^0 with respect to the beam axis, capturing the shear strain contributions along each flange and facilitating the use of iTM2D0 and iTM2D1 elements for the present shape sensing problem.

A loading setup is devised for applying the concentrated load at the tip of the beam (shown in Fig. 5.3a). It consists of three aluminium plates: top, bottom, and a core, for constraining the tip cross-section, essentially acting as a rib. This setup also allows the possibility of adjusting the horizontal location of the load point (with respect to the shear center) for investigating different cases of beam deformation involving both bending and torsion. The top plate also serves as a flat surface for measuring the experimental tip deflection of the beam. Two Linear Variable

Displacement Transducers (LVDTs) are used for measuring the tip deflections, positioned at the two ends of the top plate as shown in Fig. 5.3b. Both transverse tip deflection and torsional rotation can be computed from the LVDT measurements.

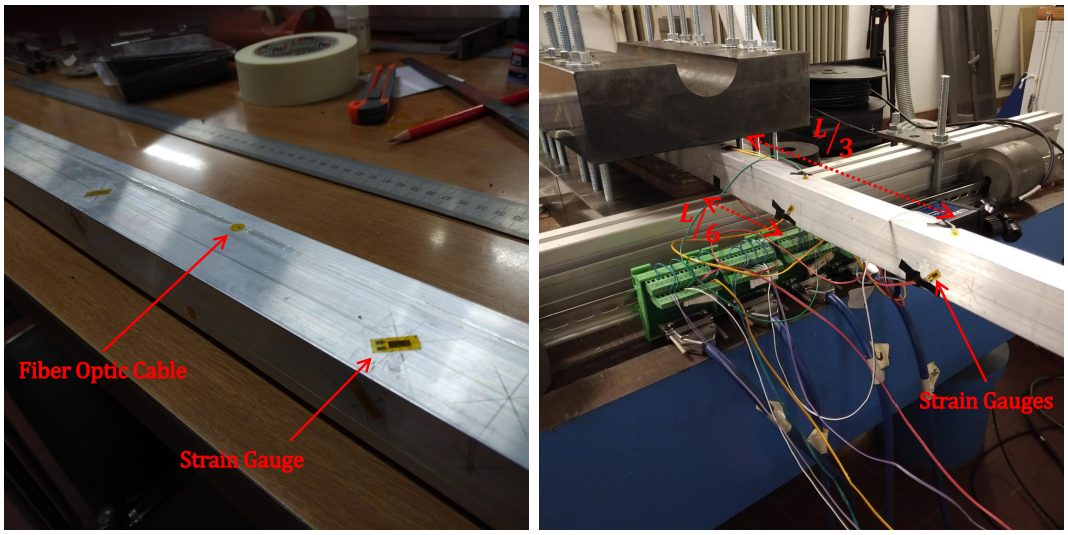

(a) (b)

Fig. 5.2 Images of the aluminium C beam instrumented with sensors: (a) strain gauges and fiber cable are shown, and (b) two initial sections of the beam instrumented with sensors

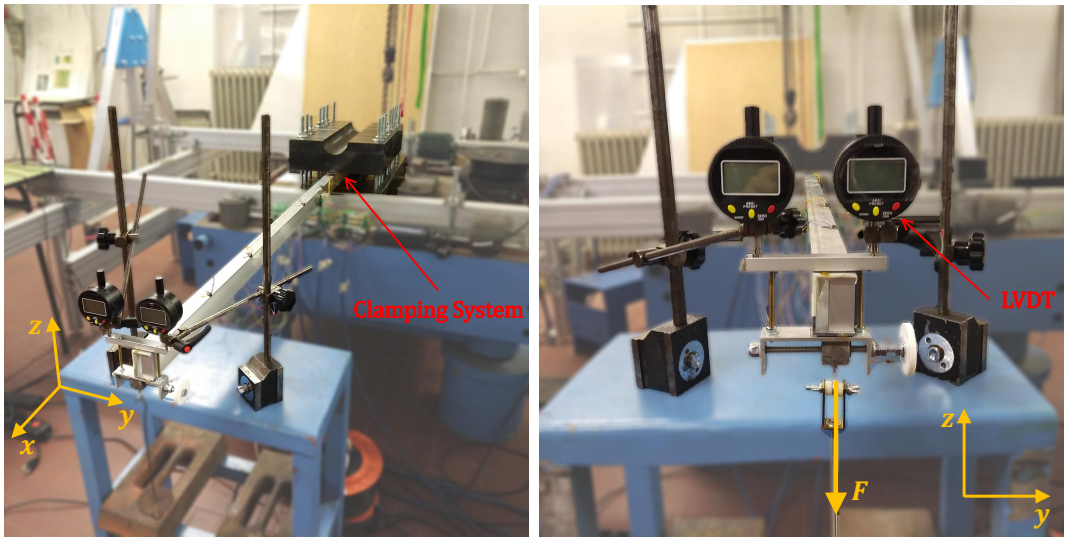

(a) (b)

Fig. 5.3 Images of the aluminium cantilevered C beam during tests in the laboratory: (a) isometric view with the clamping setup shown, and (b) front view with the loading setup and LVDT measurement positions shown.

5.1.1 iFEM Reconstruction

The experimental shape sensing is performed using the various inverse beam elements presented in Chapter 2. The high-density axial strain data obtained from the fibre optic sensor can be used alongside a finely discretised iEB2 element mesh. Alternatively, for iFEM analysis using the iTIMDO or iTM2D1 elements, strain gauge measurements are combined with point strains measured at specific fibre locations. As strain gauges are instrumented at four axial locations of the beam, a maximum of two iTM2D0 elements or one iTM2D1 element can be utilized. The accuracy of iFEM predictions is evaluated only at those locations where experimental deflections and rotations are measured, i.e., at the tip. These investigations constitute the first experimental validation of the novel formulations discussed in Section 2.1.2.

Table 5.1 Number and location of strain sensors for each inverse beam element, defined with respect to the coordinate system of Fig. 5.1 (all dimension are in mm)

Elements	No. of Sensors	Sectional Positions (y,z) $\beta=0^0$	Sectional Positions (y,z) $\beta=45^0$	Axial Positions
iTM2D0	12	$(6.13,22.6)$	$(18.13,22.6)$	$\frac{L}{3}, \frac{2L}{3}$
		$(-1.01,12.5)$	$(-1.01,-7.6)$	
iTM2D1	24	$(21.13,-22.6)$	$(10,-22.6)$	$\frac{L}{6}, \frac{L}{3}, \frac{2L}{3}, \frac{5L}{6}$

Results for Pure Beam Bending

When the beam is loaded at its shear center ($y_{sc} = -11.56$ mm from the vertical flange), no torsional deformation is generated on the beam. This case is analysed in the present section (using a tip load up to 88.3 N) and the performance of the various inverse beam elements developed in Chapter 2 are compared. Preliminary shape reconstruction is performed with either one iTM2D0 or one iTM2D1 element, using strain measurements defined in Table 5.1. A comparison of iFEM results between these two elements plotted as a function of the load applied is shown in Fig. 5.4.

Fig. 5.4a shows that both elements are accurate in reconstructing transverse deflection, with the iTM2D1 element offering better results. To quantify this accuracy, the percentage error in tip deflection is computed (using Eq. 3.1) and shown in Fig. 5.4b. Both elements report an error $<10\%$, with iTM2D1 (average $w^{err} \sim 7\%$) clearly more accurate than iTM2D0 (average $w^{err} \sim 8\%$). This higher accuracy of iTM2D1 is attributed to the higher interpolation order and the larger number of sensors used (see Table 5.1). However, the difference between these two elements is marginal, indicating that iTM2D0 can be considered an ideal choice for this tip loading problem. Another interesting feature is the improvement in iFEM accuracy with increased load, which is attributed to the higher magnitude of measured strains

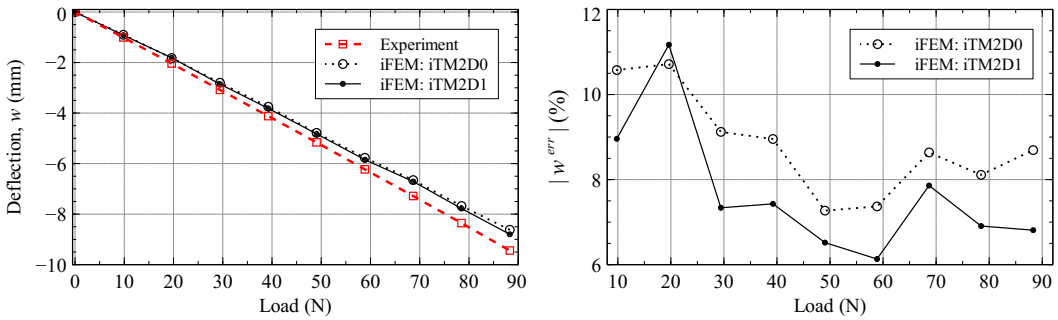

(a) w (b) $|w^{err}|$

Fig. 5.4 iFEM results, obtained using iTM2D0 and iTM2D1, for the C beam compared against experimental results: (a) tip deflection, w, (b) percentage error in tip deflection, w^{err}

and deflections at larger loads. These measurements are more reliable at higher magnitudes due to the lower influence of noise or measurement errors, leading to improved predictions.

The same beam problem is also analysed using the iEB2 element. Due to the abundance of axial strain measurements along the beam length (measured by the fibre optic strain sensors), the beam can be discretised using multiple iEB2 elements. In addition to serving as an evaluation of element performance, the influence of element quantity on iFEM accuracy can also be assessed. All axial strain measurements along the beam length are utilised (avoiding those close to the root and free ends), and various discretisation levels, up to seven uniform iEB2 elements, are investigated. The iFEM results using iEB2 elements for a tip load of 88.3 N are shown in Fig. 5.5.

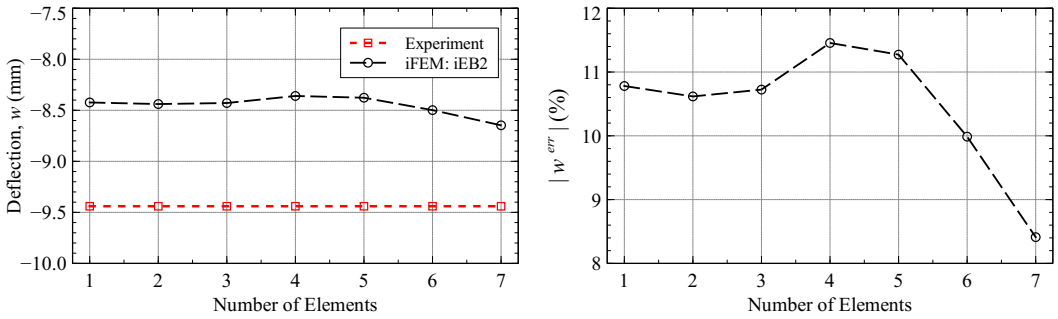

(a) w (b) $|w^{err}|$

Fig. 5.5 iFEM results, obtained using iEB2, for the C beam loaded using a 88.3 N tip load and compared against experimental results: (a) tip deflection, w, and (b) percentage error in tip deflection, w^{err}, plotted as a function of the number of elements used

Various interesting features are observed from these plots, the principal of which is the improvement in iFEM accuracy with an increase in the number of elements

used. This is expected as a finer discretisation of the beam can lead to a more accurate representation of the strain and deflection distribution along the beam length. Fig 5.5b shows that the tip deflection error reduces from ∼11% using one iEB2 element, to ∼8.5% when using seven elements. Further increase in the number of elements used is expected to lead to smaller improvements in the results, eventually converging to a specific solution.

These results can also be compared with iTM2D0 and iTM2D1 element solutions to assess the performance of each element for the same shape sensing problem. Comparison of iFEM results obtained using one inverse element of each type reveals increasing levels of accuracy from iEB2 ($w^{err} \sim 11\%$) to iTM2D1 ($w^{err} \sim 7\%$). The lower accuracy of the iEB2 is expected as it does not consider the effect of transverse shear deformation, which is expected to be non-negligible for the present problem. A strategy for improving iEB2 results is the use of multiple elements as discussed above, achieving similar levels of accuracy with up to seven iEB2 elements.

The accuracy observed in each case should be contrasted against the number of in-situ strain measurements used. The parametric study of Fig. 5.5 used strain measurements from over 100 axial sections of the beam (increasing depending on the number of elements used). In contrast the iTM2D0 and iTM2D1 elements can be implemented using measurements from at least two, and three sections, respectively (see Table 5.1). Also, the increase in computational effort with an increase in the number of elements used should be considered. In conclusion, the iTM2D0 element provides an optimal trade-off between high reconstruction accuracy and low sensor requirement for the present shape sensing problem. These results provide a preliminary validation of the novel element formulations, specifically for accurately modelling the effect of transverse shear deformation in beam deflection.

Results for Combined Beam Bending and Torsion

Transverse loading of the beam at any point not coincident with the shear center leads to a combined bending and torsional deformation. A single iTM2D0 element is used for shape sensing the present problem, and the corresponding iFEM results obtained are compared against experimental measurements. The transverse beam deflection plotted as a function of the load applied is shown in Fig 5.6.

Fig 5.6a demonstrates the iFEM reconstruction of transverse deflection to be very accurate. This conclusion is reinforced by the percentage error plot of Fig. 5.6b, where a maximum error of 3.5% and an average of around 1% is observed. A novelty of the present case is the prominence of the torsional rotation at the tip, the results of which are shown in Fig. 5.6c. The reconstructed rotations are also seen to be very accurate, with a percentage error reducing from 7% to less than 2% as the load is increased to 49 N (shown in Fig. 5.6c). As torsional rotation reconstruction

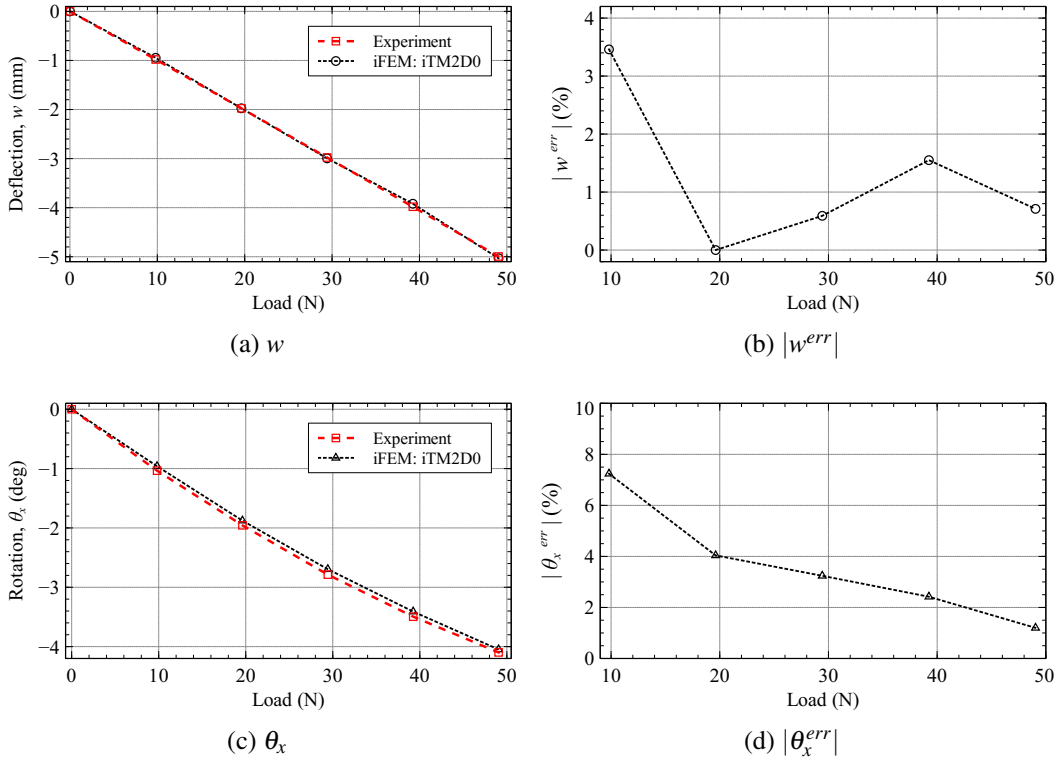

Fig. 5.6 iFEM results for the cantilevered results compared against experimental results: (a) tip deflection, w, (b) percentage error in tip deflection, w^{err}, (c) tip torsional rotation, θ_x, (d) percentage error in tip torsional rotation, θ_x^{err}

is entirely predicated on in-situ shear strain measurements and the treatment of transverse shear deformation by the element (in Section 2.1.2), the accuracy of these results serves as an experimental validation of the novel formulations.

5.1.2 Digital Image Correlation Results

Evaluating iFEM accuracy by comparing with LVDT measurements is limited in scope as comparisons are only possible at discrete locations of the beam. For a more elaborate experimental deflection measurement over a larger area (or over the entire beam), a dedicated measurement system based on Digital Image Correlation (DIC) is used. DIC is a non-contact optical-based technique capable of measuring 3D displacement and strain fields over a monitored area. A commercial DIC system provided by Correlated Solutions was used in the present experimental test campaign. It consists of high-resolution cameras for image acquisition and software (VIC-3D) for post-processing the acquired images and calculating the measured strains and displacements. In contrast to LVDTs, the DIC system offers significantly higher

measurement quantity, numerous points over an entire area, and quality, 3D strain and displacement components.

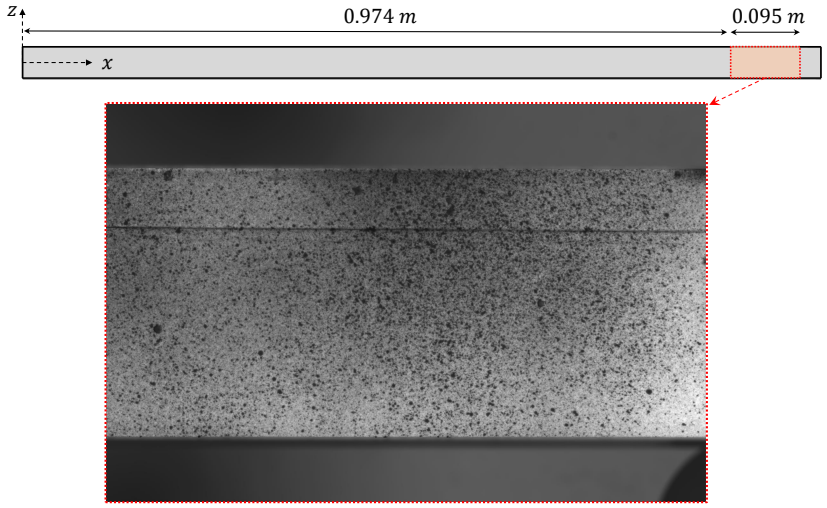

Fig. 5.7 The vertical flange of the beam monitored using the DIC system; a dense grid of points on the surface (required for DIC application) can be seen

In the experimental test, the DIC system is used to interrogate a 95.5×41 mm^2 rectangular area on the vertical flange of the beam (close to the beam tip) as shown in Fig. 5.7. The choice of the monitored area is influenced by the resolution of the cameras, size of the specimen and measurement precision required. The DIC system is used to measure displacements, u_x, u_y and u_z, when the beam is subjected to a 19.6 N tip load, generating both bending and torsional deformation in the beam. These measurements are shown in Figs. 5.8a, 5.8c, and 5.8e, respectively. Fig. 5.8a demonstrates beam bending, as the axial displacement varies linearly along the z-axis. The effect of torsion is also evident in 5.8e, as transverse deflection, u_z, is no longer a constant at each section. It should be mentioned that due to the nature of the load applied, deflection u_z is predominant (over one order of magnitude greater than u_y) and hence more emphasis is given to its accurate reconstruction.

The iFEM analysis is performed using one iTM2D1 element with in-situ strain measurements corresponding to Table 5.1. The displacement field over the monitored area is calculated from the reconstructed components along the beam axis using the kinematic relations of Eq. 2.19. The iFEM results are shown as contour plots of u_x, u_y and u_z in Figs. 5.8b, 5.8d, and 5.8f, respectively. The results are accurate, both in terms of magnitude and distribution. The sole exception is u_y, which, being the displacement along the unloaded transverse axis, is more susceptible to the influence of noise or measurement errors. As the DIC results provide displacement measurements at a high-density set of data points, iFEM accuracy can be evaluated

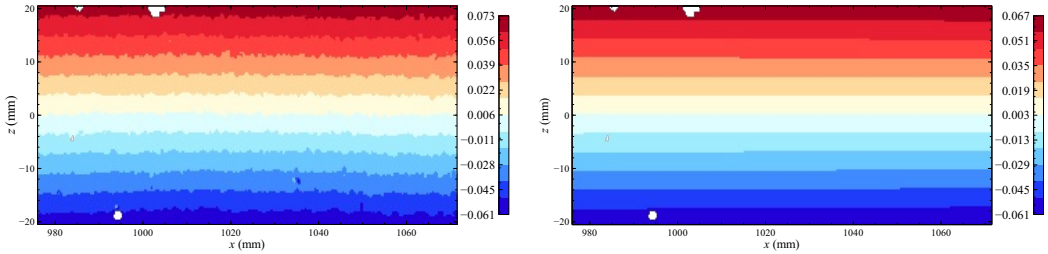

(a) $u_x|_{DIC}$

(b) $u_x|_{iFEM}$

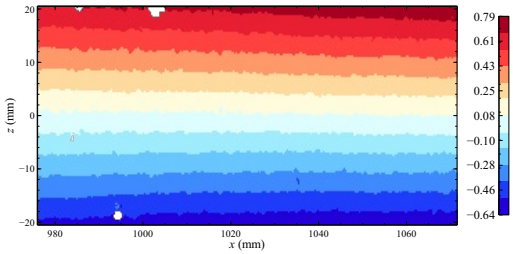

(c) $u_y|_{DIC}$

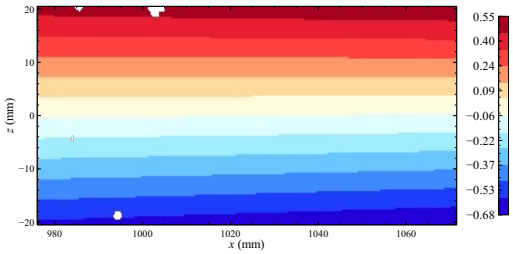

(d) $u_y|_{iFEM}$

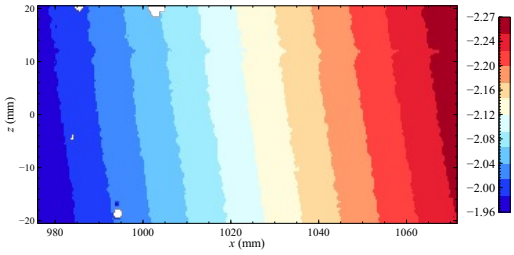

(e) $u_z|_{DIC}$

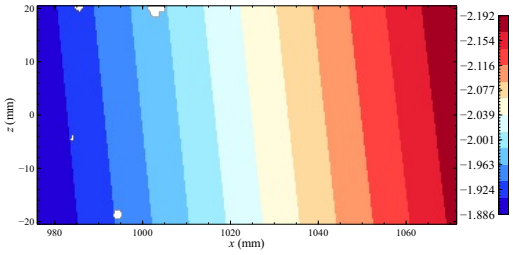

(f) $u_z|_{iFEM}$

Fig. 5.8 Contour plots of DIC and iFEM (iTM2D1) displacements for the beam under a tip load of 19.6 N (origin of the horizontal coordinate, x, is the beam root, and that of coordinate, z, is the middle of the vertical flange; all dimensions and values are in mm)

by computing the percentage error in reconstructed displacement at each point. The corresponding error plots are shown in Fig. 5.9.

These error plots present some interesting conclusions. The error plot of the major deflection, u_z, is shown in Fig. 5.9c and reveals the iFEM results to be highly accurate with a maximum error of $\sim$4%. Similarly, the plot of u_x^{err}, shown in Fig. 5.9a, reveals the axial displacement reconstruction to be accurate with an error less than 5% over the majority of the monitored area. However, several peaks with errors as high as $\sim$10% are also observed. The presence of these highly localised peaks is attributed to the low magnitude of u_x combined with noise or experimental errors. In earlier discussions, displacement, u_y, was observed to be inaccurate, and the contour plot of Fig. 5.6b backs these conclusions showing a maximum error

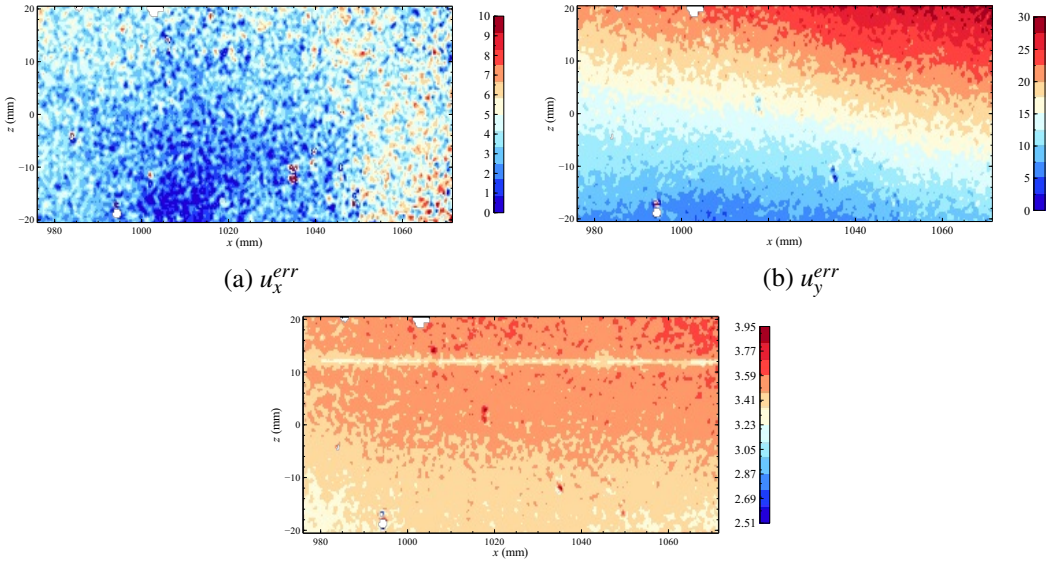

(a) u_x^{err} (b) u_y^{err}

(c) u_z^{err}

Fig. 5.9 Contour plots of percentage error in iFEM reconstructed axial and transverse displacements over the monitored area on the vertical flange of the beam

of 30%. An interesting feature is also observed in Fig. 5.9c, where a horizontal line is visible in the plot corresponding to the location of the fibre optic sensors instrumented on the beam flange, illustrating the sensitivity of the DIC acquisition. The results of this section serve as another layer of validation for the new beam formulations. As u_z accuracy is contingent on an accurate iFEM reconstruction of both w and θ_x, the accuracy observed for the former demonstrates the accuracy of the latter two quantities as well. It should also be remarked that in contrast to previous comparisons, the iFEM accuracy is assessed not just at a point but over an entire area, further demonstrating its effectiveness.

The experimental test campaign on the aluminium C beam produced a set of encouraging iFEM results, assisting the aim of developing an efficient shape sensing technique for beams with complex cross-sections. The investigations continue by analysing beam specimens involving more complex geometries next.

5.2 Additively Manufactured Beams

Encouraged by the success of previous results, further experimental investigations are proposed. As the novel beam formulations of Chapter 2 are principally aimed at investigating beams with more complex profiles, like the airfoil beams of Chapter 3, similar beam specimens are designed. However, manufacturing these specimens is

challenging, especially as their geometrical complexity increases. Normal manufacturing methods would be inefficient in terms of the cost or the amount of material required. Additive manufacturing (commonly called 3D printing or rapid prototyping) techniques are a viable alternative that has received widespread attention in recent years. They are also increasingly used in the aerospace industry to develop lightweight, high-performance parts. As it is based on generating parts by depositing material layer upon layer, complex geometric shapes can be manufactured. Hence, they are adopted for the following investigations, where the exact additive manufacturing strategy used influences the material of the beam specimen.

5.2.1 Polymer Beam Specimen

As additively manufactured parts are a relative unknown in shape sensing research (where conventional metallic or composite parts are the norm), a preliminary investigation is proposed to understand the specimen behaviour. The beam specimen designed is a scaled-down version of the thin-walled NACA 0016 airfoil beam of Chapter 3, with a beam length of 125 mm, airfoil chord length of 56 mm and wall thickness of 1.46 mm. The exact dimensions of the beam are shown in the engineering drawings of Fig. 5.10.

Stereolithography (SLA) is chosen as a simple, fast, and low-cost manufacturing option for printing this prototype beam specimen. SLA uses an ultraviolet laser to trace the shape of the beam profile in a basin of photosensitive resin. Interaction of the laser with the resin leads to resin hardening and is repeated layer-by-layer to create the final part. Although the part is built layer-wise, the material properties are nearly isotropic, i.e., there is no significant difference in tensile strength between the in-plane (or in a layer) and out-of-plane (between two layers) directions. The only limitation is that all the resins used alongside SLA are polymeric and are expected to introduce additional material complexities to this preliminary investigation. The Formlabs Form 2 printer is used for printing the specimen, and the resin used is based on the thermoplastic polymer, Acrylonitrile Butadiene Styrene (ABS) [119]. In addition to the resin used, the mechanical behaviour of the manufactured part is also influenced by print parameters such as layer thickness, part orientation during the print, and post-curing. Hence, for a preliminary assessment of the material and the effect of the print parameters on the final part, certain sample specimens were manufactured and characterised using tensile tests.

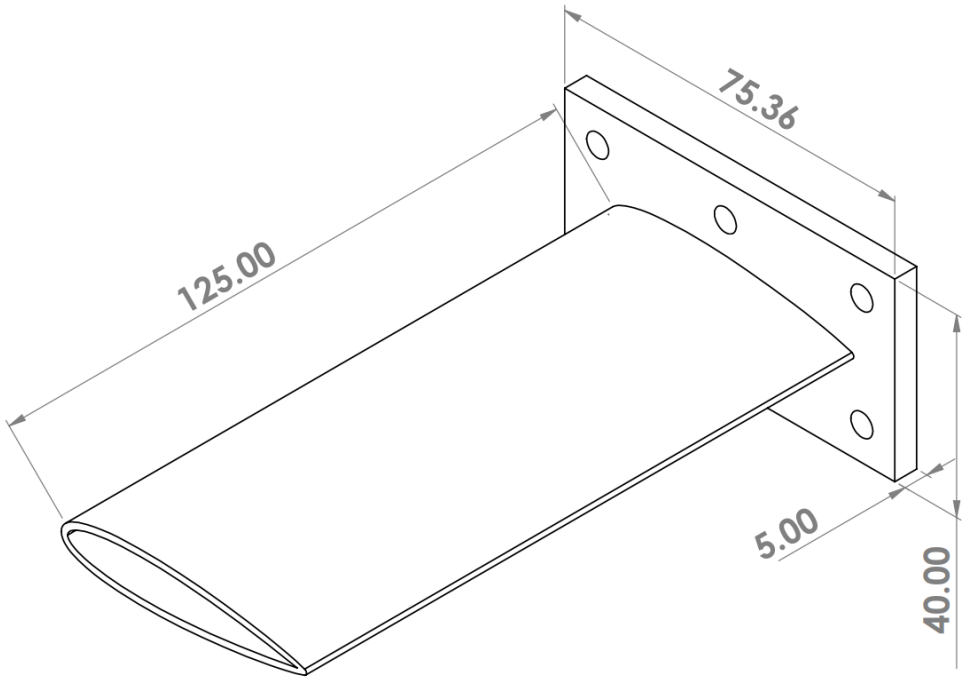

(a) Isometric view of the specimen

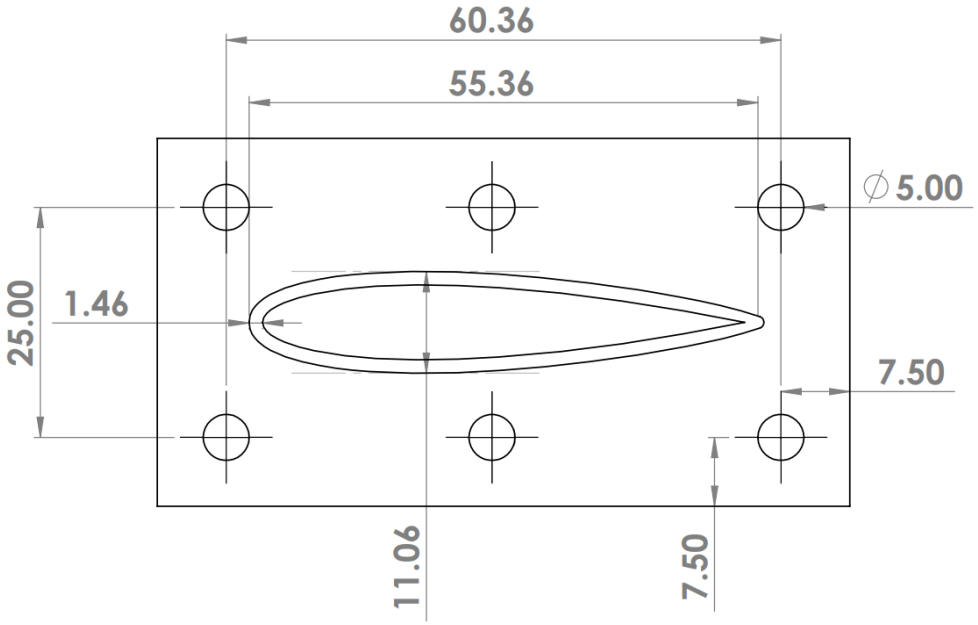

(b) Front view of the specimen

Fig. 5.10 Engineering drawings of the polymer beam specimen showing the beam profile attached to the flange which serves as the clamping system for the specimen; position and location of the clamping bolt holes are also shown (all dimensions indicated in the drawings are in mm)

Tensile Testing of Printed Specimens

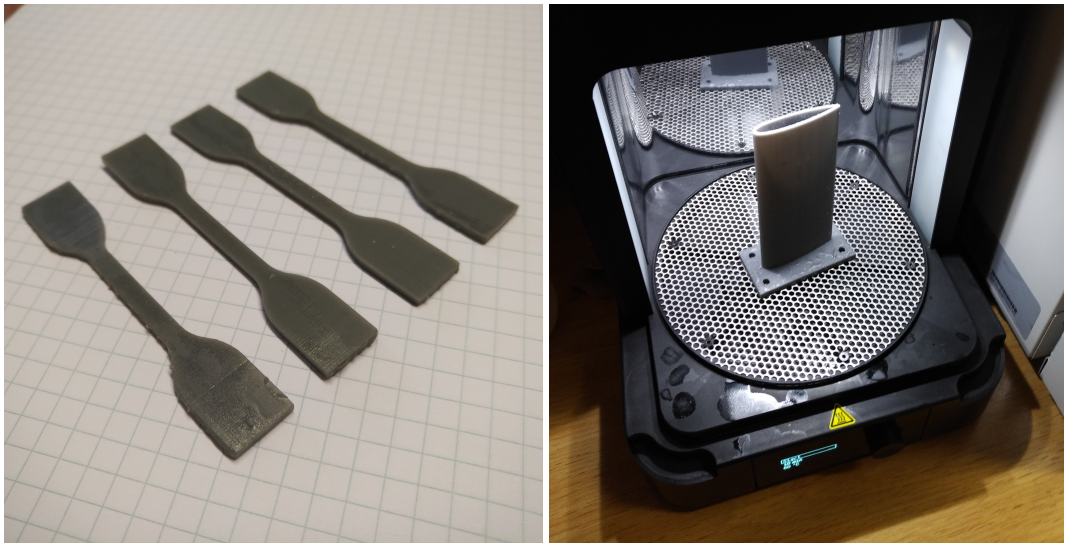

(a) (b)

Fig. 5.11 Additively manufactured ABS parts printed using the Formlabs Form 2 printer: (a) specimens printed for tensile test campaign to characterise material behaviour, and (b) final printed and post-cured airfoil beam specimen

The tensile testing of moulding and extrusion plastics is specified by the international standard ISO 527-2. Based on the standard, several test specimens are designed and manufactured, as shown in Fig. 5.11a. To ensure the optimal properties for the final part, the specimens are printed using a layer thickness of 0.05 mm, which is the minimum offered by the printer. Two different print orientations are also investigated: one where the print direction is along the longitudinal axis of the specimen (each layer is perpendicular to the print direction), and the second where it is perpendicular to the longitudinal axis. These orientations are specifically designed to test the tensile strength in a layer and between two layers. Once manufactured, the specimen is also treated to a post-curing procedure, where they are heated to a temperature of 60^0 C for a time of 30 mins and then allowed to cool naturally at room temperature. The post-curing process helps increase the tensile strength of the specimen but at the cost of depreciating ductility.

The tensile tests are performed at the Bio-inspired Nano Mechanics lab ("G.M. Pugno") in the Department of Structural, Geotechnical and Building Engineering, Politecnico di Torino. The MTS Insight testing machine is used with a loading rate of 0.3 mm/sec. Due to the two different print orientations, two loading conditions are also achieved: loading in-plane (Specimen-1) and transverse (Specimen-2) to a layer. Each specimen is loaded to failure, and the load and displacement data recorded is used to plot the stress-strain curves shown in Fig. 5.12.

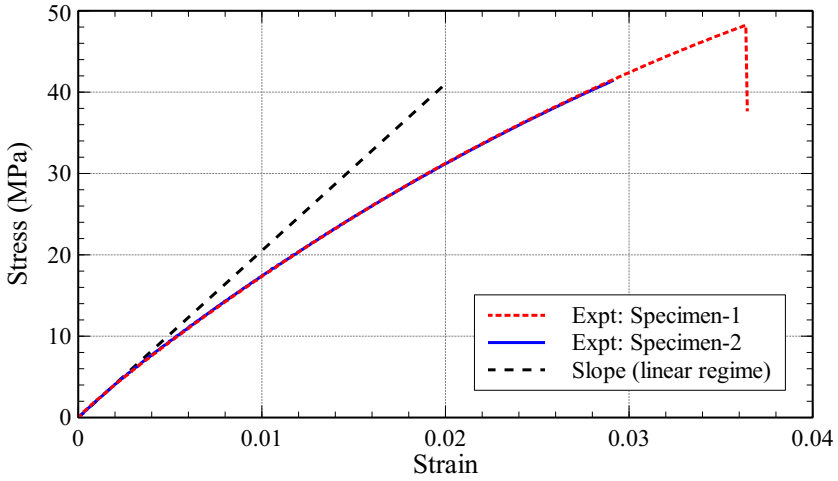

Fig. 5.12 Results of the tensile test campaign: stress-strain plots of the two polymer specimens; a line is also shown illustrating the slope of the linear regime of the curves

The tensile test results reveal no significant difference in mechanical behaviour between the two specimens, perhaps the only noticeable difference being the ultimate strength. Characteristic of polymeric materials, the stress-strain curves have a small linear-elastic regime (approximately strains $< 0.05\%$), followed by a large non-linear regime, eventually ending in material failure. The failure strength of the two specimens is reported in Table 5.2, revealing an average maximum tensile stress of ~ 44 MPa. The Young's modulus, estimated using the linear regime of the curve, is also seen to be similar for the two specimens, with an average value of 2.025 GPa. Estimating these material properties allows for a suitable experiment design for the airfoil beam specimen to ensure that applied loading lies with the linear-elastic regime of material behaviour (which is essential for the iFEM methodology investigated) and avoid specimen failure.

The results of the tensile test are instrumental in the final design of the airfoil beam (shown in Fig. 5.10.) The beam is manufactured using the same resin and under similar printing conditions with the print direction parallel to the beam axis. The final manufactured and post-cured beam specimen is shown in Fig. 5.11b.

Table 5.2 Results of the tensile test for the two specimens (θ_L represents the angle between the loading direction and plane of the layer)

Test Specimen	θ_L	Stress at Failure (MPa)	Strain at Failure	Young's Modulus (GPa)
1	0^0	48.2	0.036	2.0
2	90^0	41.3	0.029	2.05

Experimental Test of the Beam Specimen

As described before, the final beam prototype designed has a thin-walled symmetric airfoil profile (NACA 0016). It must be remarked that, compared to the numerical cases of Chapter 3, the trailing edge of the profile is slightly modified, where a sharp edge is replaced by a rounded edge for convenience of manufacturing and handling.

The beam is designed to be cantilevered and loaded at the tip by a concentrated load. In contrast to the C beam experiment, the present beam prototype is cantilevered using a flange printed at the root of the beam. The flange is printed with a series of holes through which it is bolted to a steel plate. As the stiffness of the steel plate is much higher than that of the beam specimen, deformations of the beam do not affect the plate, and hence the flange is assumed to be fixed. For a preliminary evaluation of the efficacy of this clamping strategy, a numerical model of the beam is developed in ABAQUS, using material properties reported in Table 5.2. The FEM results demonstrated negligible axial displacement at the beam root, thus approaching a fixed condition. Despite these reassurances, due to the novel nature of the setup, the present test also serves as an experimental validation of such a clamping strategy. The beam is loaded at the tip using a loading system consisting of a tip rib with three holes that act as loading points. The experimental deflection of the beam is measured using a single LVDT positioned on the beam surface near the tip. Images of the experimental setup are shown in Fig. 5.13b.

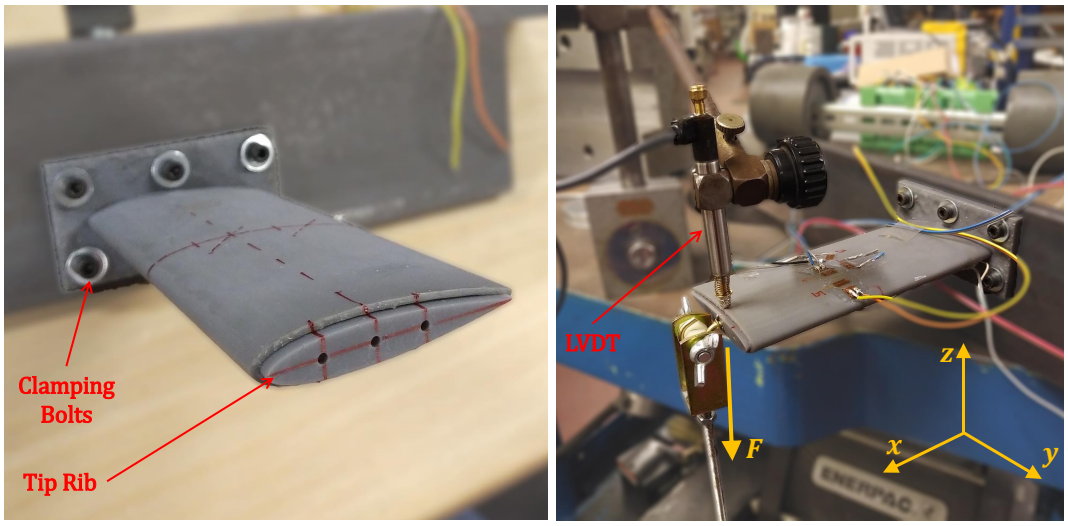

(a) (b)

Fig. 5.13 Images of the experimental setup: (a) beam specimen clamped onto a metallic base, (b) the instrumented sensors, loading setup and LVDT locations

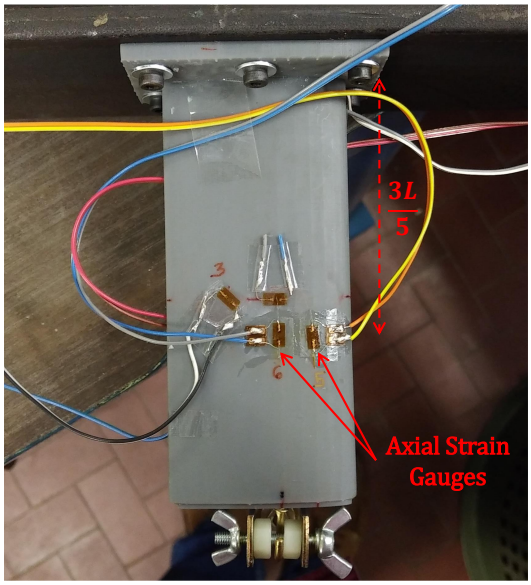

Fig. 5.14 Top view of the beam specimen showing the location of the axial strain gauges

Table 5.3 Number and location of strain gauges used for the iFEM analysis of the cantilevered polymer beam specimen subjected to a tip load

Beam Element	No. of Strain Gauges	Sensor Position
iEB2	3	$[(0.2^+, 0^+, -0.1^-), (\frac{3L}{5}), (0)]$

To ensure accurate strain measurements on the beam surface, the sensors have to be placed sufficiently far from both the root and tip of the beam. In the present case, as the beam length is relatively small, the number of sections and correspondingly sensors that can be instrumented is also limited. The beam is instrumented with three strain gauges close to the mid-section and oriented parallel to the beam axis (described in Table 5.3). Due to the preliminary nature of the investigation, only the iEB2 element is used for the iFEM analysis, and it requires sectional strains evaluated in at-least two sections. Using the sectional strains evaluated near the mid-section, $\{e_2^\varepsilon, e_3^\varepsilon\}_{\frac{3L}{5}}$, and assuming the condition: $\{e_2^\varepsilon, e_3^\varepsilon\}_L = 0$ at the beam tip, these sectional strains can be interpolated linearly over the beam element and evaluated at sections, $x = \frac{L}{3}, \frac{2L}{3}$. These strains are subsequently used for the iFEM analysis.

For a transverse beam tip load of 0.7 N, the time history of the measured strains are shown in Fig. 5.15. The plot shows that the magnitude of measured strain increases over time, displaying a phenomenon called creep. The entire strain time history can be subdivided into two parts: an instantaneous component corresponding to elastic deformation, followed by a viscoelastic deformation where the strain

changes as a function of time and eventually converges. Similarly, unloading leads to an instantaneous elastic, and subsequently, viscoelastic recovery of deformations.

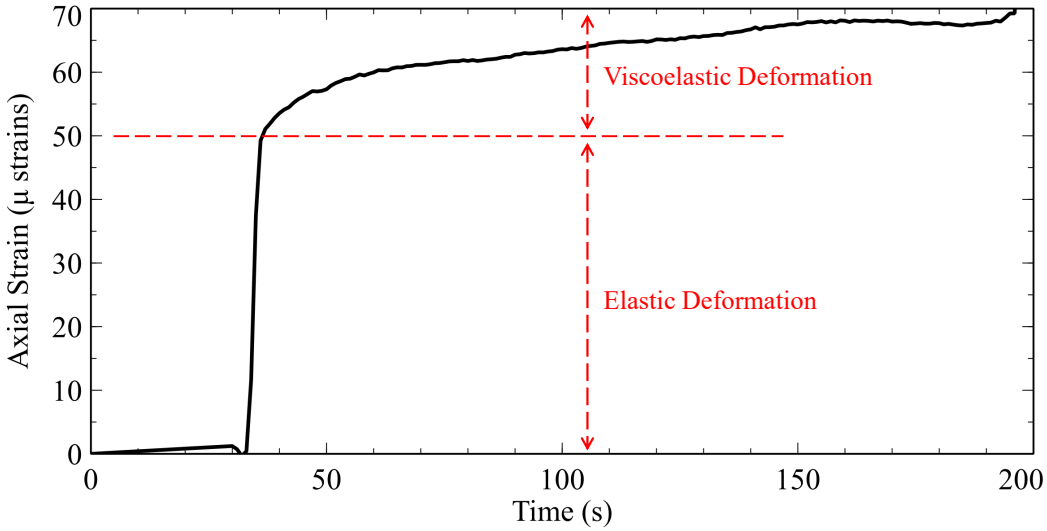

Fig. 5.15 Variation of strain measurement over time for the polymer beam specimen loaded at the tip by a force of 0.7 N; the elastic and viscoelastic deformation regions are shown

The viscoelasticity of the polymer used explains the material behaviour shown in Fig. 5.15, i.e. the constitutive relations are a function of the temperature and strain rate. Also, an increase in load produces a corresponding linear increase in strain, illustrating linear viscoelastic behaviour. As the loads applied restrict the beam to linear deformations, the measured strains are also confined to the linear regime, i.e., $<\sim 0.05\%$. The present polymeric beam specimen presents an ideal opportunity to investigate the effect of complex material behaviour on iFEM predictions. Experimental iFEM validations in existing literature have all been performed on either metallic or composite specimens that exhibit negligible viscoelastic behaviour. As material viscoelasticity is governed only by strain rate dependence on the constitutive relations, it is independent of the kinematic relations of the structure. Hence, iFEM predictions are expected to be unaffected.

Prior to implementing the 1D iFEM, it is necessary to verify the accuracy of the 'beam' assumption for the present structure. For bending about the $y-$axis (i.e., due to transverse loads perpendicular to the chord length), the ratio of beam length (125 mm) to section height (11.06 mm) is 11.3, lying within the technical definition of beams. However, the same cannot be claimed for bending about the $z-$axis. To verify the accuracy of this assumption for the experimental performed, a high-fidelity numerical FEM model of the structure is developed in ABAQUS and the FEM beam deflection are compared against those obtained using classical beam theories. When the structure is subject to a tip load perpendicular to the chord

length (parallel to $z-$axis), the numerical and shear corrected analytical tip deflection reveals a difference of only $\sim$2.5%. This proximity of the numerical and theoretical predictions is used to validate the beam assumption for the experimental loading condition and underpins the iFEM analysis of the airfoil beam using experimental strain data.

The iFEM analysis is performed using one iEB2 element, using experimental sectional strains at two separate sections of the beam ($x = \frac{L}{3}, \frac{2L}{3}$). A maximum tip load of 4.3 N is applied in six equal load steps. The loading cycle is followed by an unloading stage as well to assess the recovery behaviour of the beam. In both cases, the measured strains and deflections are allowed to converge before the next loading or unloading step. Availability of the complete time history of tip deflection measurements allows for an assessment of iFEM performance during both elastic and viscoelastic deformation regimes of the beam. Similarly, the deflection measurements during beam unloading provide an assessment of iFEM performance during the creep recovery stages. The time history of experimentally measured and iFEM reconstructed beam tip deflections over the complete loading and unloading cycle is shown in Fig. 5.16.

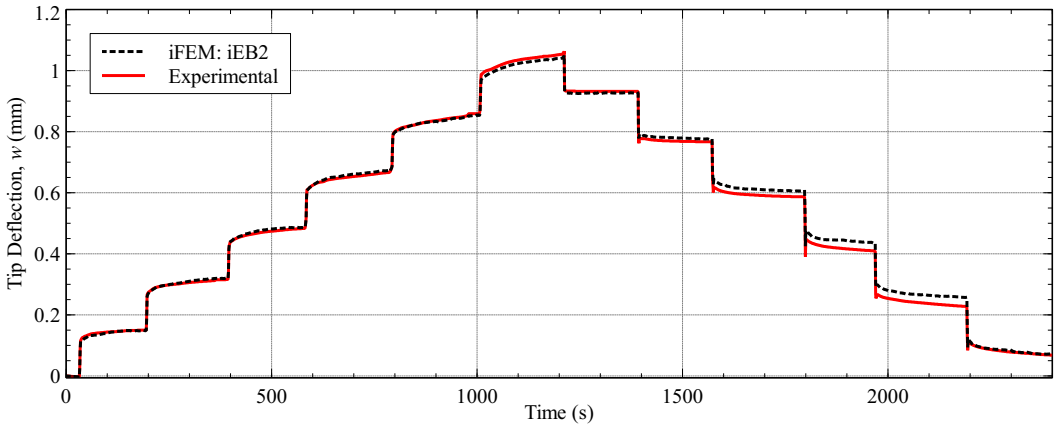

Fig. 5.16 Results of the experimental test on the polymer beam specimen: comparison of tip deflection time history measured using an LVDT, and reconstructed using the iEB2 element

Fig. 5.16 reveals the reconstructed tip deflections to be very accurate both during the elastic and viscoelastic deformation regimes of the beam. Similar but slightly lower levels of accuracy are seen during beam unloading. iFEM accuracy is quantified by calculating the percentage error in the tip deflection as a function of time, as shown in Fig. 5.17. The results are confirmed to be very accurate, with a percentage error in tip deflection $< 5\%$ across most of the loading and unloading phases. Higher errors ($\sim 10\%$) are seen close to the end of the unloading process. Minor error peaks are also seen, occurring between any two load steps. They are attributed to the high sensitivity of the LVDT combined with any experimental

errors during the handling of the beam due to imperfect loading and unloading of weights. Despite these minor issues, it can be concluded that the high accuracy of the reconstructed deflections present a clear validation of the material independence of the iFEM methodology used.

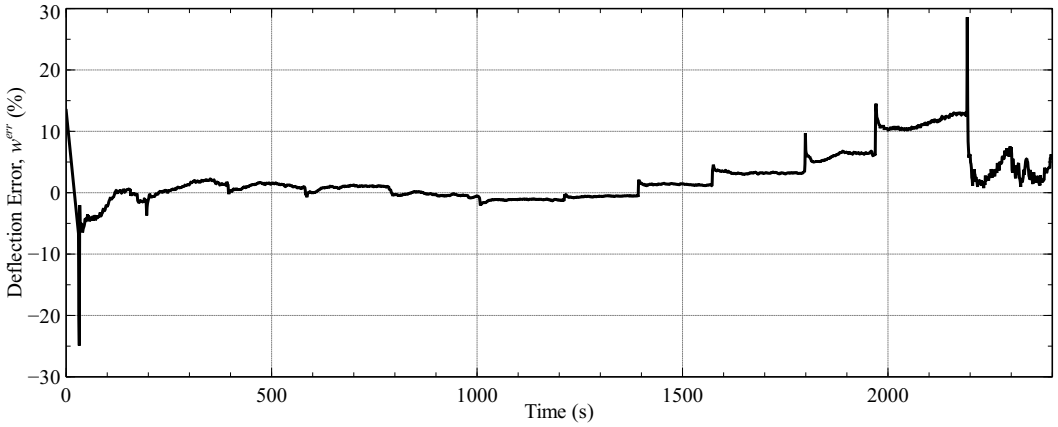

Fig. 5.17 Results of the experimental test on the polymer beam specimen: time history of percentage error in tip deflection reconstructed using the iEB2 element

An interesting feature of Fig. 5.16 is that, under similar loads, the magnitude of tip deflection during the loading and unloading cycles are not equal, indicating the presence of unrecovered elastic or plastic deformations in the beam. Perhaps more time at each load step or complete unloading of the beam is required to achieve full recovery. Additional investigations, e.g., creep or stress relaxation tests, are required to characterise this material behaviour fully. However, this is not the focus or within the scope of the present work.

iFEM results for the polymer airfoil beam are extremely encouraging, particularly for developing a more elaborate experiment involving a larger specimen. These results also validate the novel beam clamping setup adopted. Clamping using bolts and a flange printed directly on the specimen is effective and robust enough to mimic an ideal clamping situation. Based on these conclusions, a larger airfoil specimen is designed, manufactured and experimentally tested. These details are discussed in the next section.

5.2.2 Metallic Beam Specimen

The successful experimental shape sensing campaign on the polymer airfoil beam prompted further investigations on additively manufactured beam specimens. In particular, two key adaptions required for the new beam are identified:

- Longer length (with respect to section height) to better approximate beam behaviour and to provide sufficient surface area for sensor instrumentation;
- Use of a metallic material to avoid material complexities and focus primarily on the challenges to shape sensing caused by the geometrical complexity of the beam.

Based on these considerations, a new airfoil beam prototype is designed. It is meant to be a scaled-up version of the old design, using the same thin-walled NACA 0016 airfoil profile. The beam is 295 mm long, with an airfoil chord length of 76 mm and a wall thickness of 2 mm. The dimensions are given in more detail in Fig. 5.18.

As the new beam specimen is also meant to be additively manufactured, but now using a metallic alloy, SLA is no longer a viable option. Direct Metal Laser Sintering (DMLS) is chosen as the manufacturing technique for the present specimen. DMLS uses a high power laser aimed at a bed of very fine metallic powder, to melt and fuse the powder together and create a layer of the part. This process is repeated layer-by-layer to create the final part. The material used is an aluminium alloy: AlSi10Mg, a typical casting alloy with high strength, low weight, and good thermal, fatigue, and creep properties. It has a Young's Modulus, $E \approx 70$ GPa, and density, $\rho \approx 2670$ kg/m^3. Due to the nature of the manufacturing process, the in-layer strength is expected to be slightly higher than the out-of-layer strength. However, this orthotropic material behaviour is not expected to pose a significant problem for investigating shape sensing performance.

It must be noted that the actual mechanical behaviour of a DMLS printed part depends on the print parameters (such as layer thickness, orientation, etc.) and the local heating and cooling cycles experienced by the part. Hence, the final behaviour is expected to be highly dependent on the geometry of the part and can be different from those obtained from conventional tensile test experiments. The beam is designed considering the failure strength of the material (reported in Table 5.4) and with high safety of factor due to the uncertainties involved.

Table 5.4 Expected material properties of a part manufactured using DMLS with the aluminium alloy; the values reported are the lower limit, i.e., out-of-layer strength

Material	Young's Modulus (GPa)	Density (kg/m^3)	Yield Strength (MPa)	Strain at Break (%)
AlSi10Mg	70 ± 10	2670	240 ± 30	6 ± 5

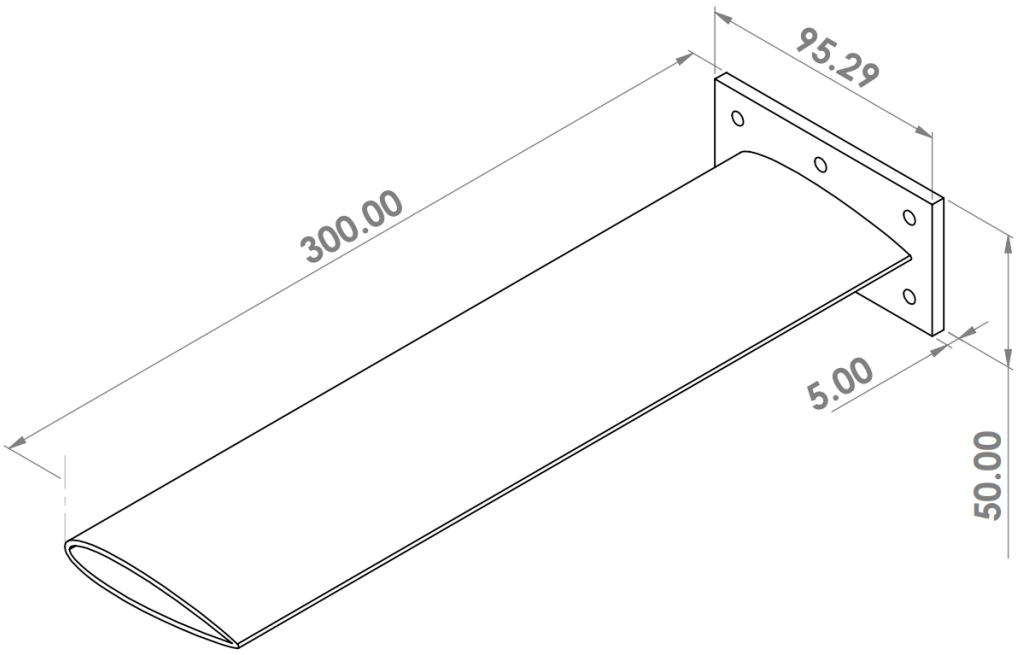

(a) Isometric view of the airfoil beam specimen

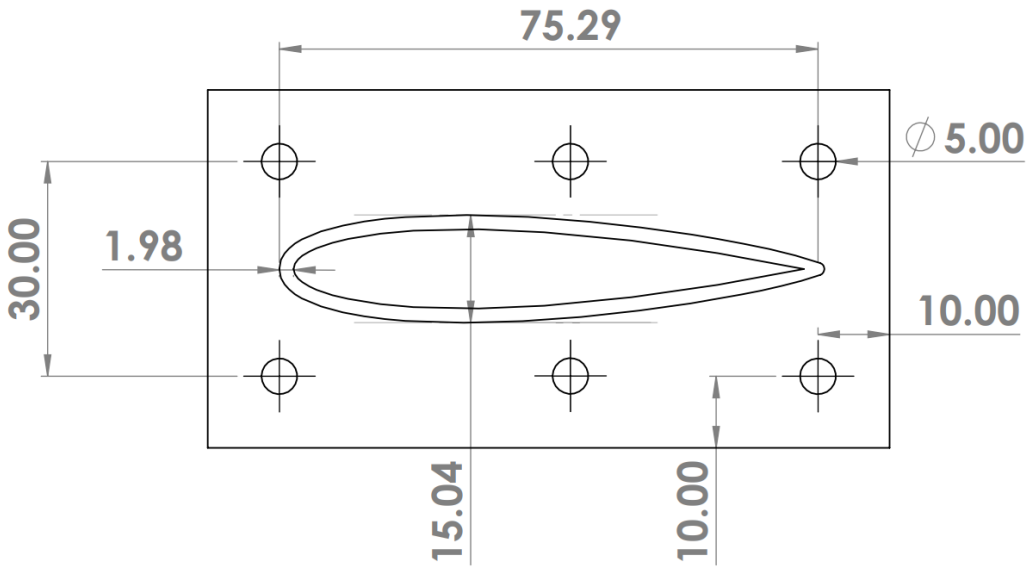

(b) Front view of the airfoil beam specimen

Fig. 5.18 Engineering drawings of the metallic airfoil beam specimen showing the beam profile attached to the flange which serves as the clamping system for the specimen; position and location of the clamping bolt holes are also shown (all dimensions indicated in the drawings are in mm)

Table 5.5 Number and location of in-situ strain measurements used for the iFEM analysis of the cantilevered metallic airfoil beam specimen subjected to a tip load

Beam Element	No. of Sensors	Sensor Position
iTM2D0	30	$[(\pm 0.2^{+}, 0^{-}), (\frac{L}{6}, \frac{L}{3}, \frac{L}{2}, \frac{2L}{3}, \frac{5L}{6}), (0)]$ $[(\pm 0.2^{-}, 0^{+}), (\frac{L}{6}, \frac{L}{3}, \frac{L}{2}, \frac{2L}{3}, \frac{5L}{6}), (45)]$

The surface strains on the beam are measured using both distributed fibre optic strain sensors and strain gauges, as shown in Fig. 5.19a. A 2 m long fibre optic cable (with an interrogator system provided by Luna Innovations) is instrumented for measuring the axial strains. The fibre creates three longitudinal sensor paths, two on the top and one on the bottom surface of the beam, as described in Table 5.5. Similarly, strain gauges are also instrumented on the beam to measure the contribution of the shear strains. A total of 15 strain gauges are used, uniformly placed at five axial sections of the beam (see Table 5.5). Hence, a total of six in-situ strain measurements are available in each section, three axial ($\beta = 0^0$) and three inclined ($\beta = 45^0$).

Similar to the previous case, the beam is cantilevered and loaded by a concentrated load at the tip, as shown in Fig. 5.19b. Due to the success of the clamping strategy adopted in the previous case, a similar approach is used here, and the beam is printed with a flange at its root. The flange is connected to a metallic base support structure using clamping bolts. As the aluminium beam is much stiffer than the polymer specimen, this base support structure is chosen to be much stiffer and heavier than the beam material to avoid any undesirable rigid body motion during beam loading. Here again, a numerical FEM model of the beam (developed in ABAQUS) is used to analyse the efficacy of clamping using this new stiffer material. The axial displacements at the beam root and on the flange are observed to be negligible, thus approximating a fixed condition.

For loading the beam specimen, a tip loading setup is designed. It consists of a top, bottom flange, and a core inserted in the beam. Combined, they effectively act as a rib at the tip of the beam, on which loads can be applied. The top and bottom flanges are connected using bolts for easy and effective mounting and unmounting. The beam tip deflection is measured experimentally using two LVDTs at two points on either side of the top flange of the tip rib. The LVDTs are mounted directly on the base support structure (similar to the beam) to avoid the measurement of any rigid body components due to the motion or rotation of the entire beam test setup. Considering a sufficient safety of factor, a maximum tip load of 49 N is estimated, with loads applied incrementally at steps of 4.9 N. Due to the metallic nature of the material used, the measured beam deflection is expected to be instantaneous without a time-varying component.

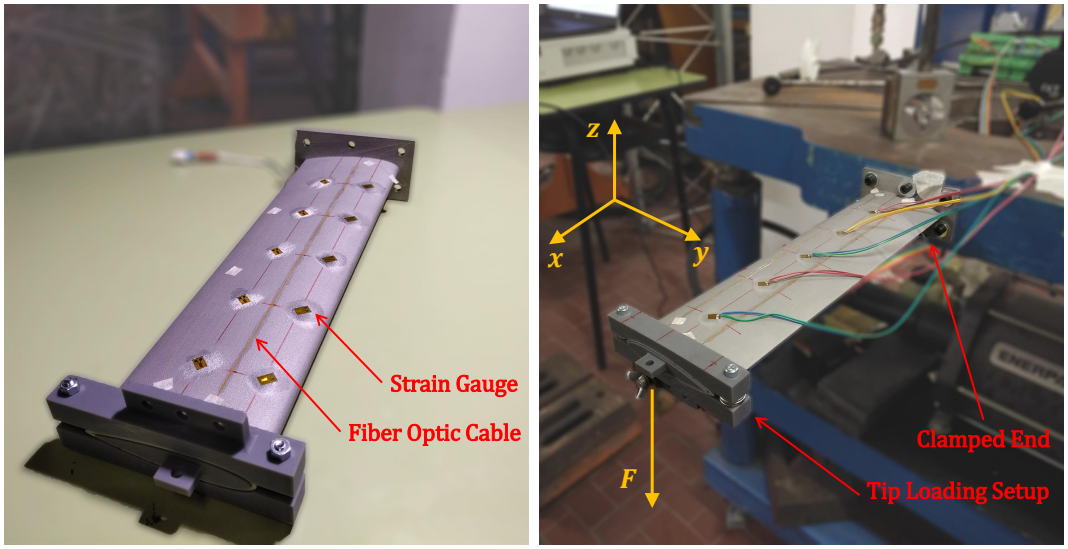

(a) (b)

Fig. 5.19 Images of the additively manufactured metallic airfoil beam: (a) printed specimen instrumented with strain sensors;root flange can be seen, and (b) the final setup of the beam specimen after clamping; tip loading setup and direction of the load applied is shown

Preliminary Shape Sensing Results

Similar to the airfoil beam of Section 5.2.1, the accuracy of the beam assumption is also assessed for the present structure. For bending about the $y-$axis, the ratio of beam length to section height is 19.6 (satisfying the beam assumption), while for bending about the $z-$axis, it is 3.9. A high-fidelity numerical FEM model of the structure is developed in ABAQUS, and for tip loading perpendicular to the chord length (parallel to $z-$axis), the numerical and shear corrected analytical tip deflections revealed a difference of only 0.3%. The proximity of these results helps validate the beam assumption for the metallic airfoil beam and subsequently the 1D iFEM is used to analyse the structure based on experimentally measured strains.

The iFEM analysis is performed with one iTM2D0 element, utilising the in-situ strain data described in Table 5.5. For the preliminary case, where the beam is incrementally loaded at the tip, close to the shear center of the beam, the iFEM reconstructed and measured tip deflection is reported in Table 5.6. Surprisingly, these results are extremely inaccurate, with an almost constant error in tip deflection of $\sim$50%. The results can be rationalised in two ways: either the 1D iFEM methodology applied is extremely inaccurate, and thus unsuitable for the present beam problem, or the error is due to an issue with the experimental setup. These results are alternatively presented as line plots in Fig 5.20a.

Table 5.6 Experimental and iFEM reconstructed tip deflection for the cantilevered metallic airfoil beam for different tip loads

Load (N)	Experimental Deflection (mm)	iFEM Deflection (mm)	Deflection Error (%)
4.9	-0.148	-0.072	50.91
9.8	-0.317	-0.157	50.39
14.7	-0.482	-0.229	52.46
19.6	-0.652	-0.308	52.72

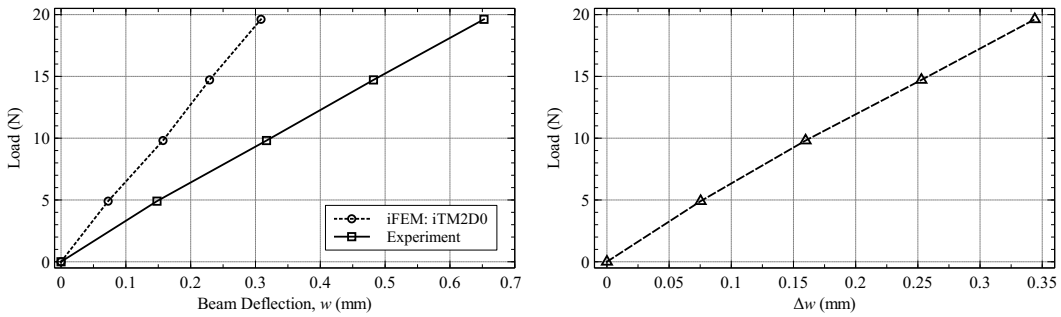

(a) (b)

Fig. 5.20 iFEM results for the metallic beam, obtained using the iTM2D0 element, compared against reference experimental results: (a) tip deflection, and (b) difference in tip deflection, plotted as a function of the tip load applied

The line plot presents some interesting conclusions: experimental and iFEM reconstructed tip deflections vary linearly with increasing load. The iFEM results also imply that the measured strains vary linearly. These results are not representative of any material or geometrical non-linear behaviour of the beam and hence are ruled out as a possible explanation. The difference between the experimental and iFEM deflections are also calculated and plotted in Fig. 5.20b, where the deflection difference is also seen to vary as a function of the load applied. This behaviour can be explained by a physical phenomenon that is both linear and elastic, given that the linear variation is observed both during beam loading and unloading.

A possible explanation is the rigid body motion of the beam, most likely due to imperfect clamping, that would generate an additional linear component of measured deflection without any corresponding strains. Based on this conclusion, the clamping system was reevaluated, during which the actual source of the errors was discovered. A closer inspection of the beam specimen revealed cracks at the root of the beam, between the beam section and the flange, as shown in Fig. 5.21a. The crack extended from the top to the bottom of the section, along the leading edge of the beam.

However, the depth of the crack was not easily discernable purely through visual inspection. Although the flange is rigidly fixed using clamping bolts, loading and unloading the beam leads to a corresponding opening and closing of the crack, respectively. Hence, the beam can no longer be assumed to be fixed as the crack acts as a source of rigid body rotation at the root of the beam.

The crack coincides with the location of the highest stress concentration expected on the beam, i.e., at the root and close to/along the leading edge where the section height is highest. The lack of a crack along the trailing edge of the airfoil section also attests to this theory. It is also possible that the sharp edge between the beam and the flange exacerbated the problem (by generating additional stress), in which case a possible solution is the use of a fillet.

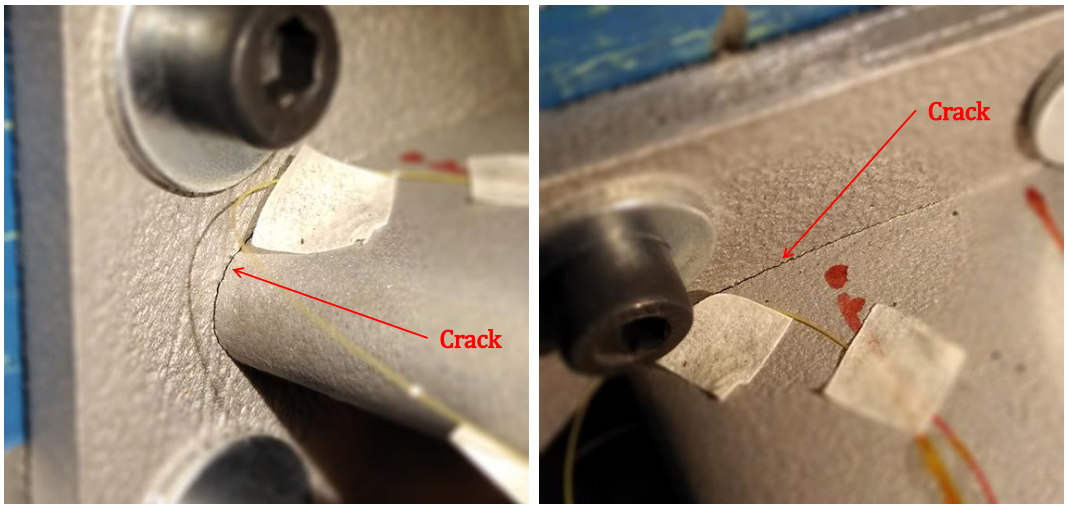

(a) (b)

Fig. 5.21 Images of the metallic airfoil with the crack observed at the root: (a) along the leading edge of the airfoil, and (b) extending from the leading edge to nearly half the chord length of the airfoil; notice that it does not extend further towards the trailing edge

However, given that the beam is designed and the loads were selected ensuring a very high safety of factor, the cause of the crack is not evident. A possible explanation can be found in the manufacturing strategy employed. As described at the beginning of this section, the final mechanical characteristics of the part are a function of the local heating and cooling cycles experienced. This can be influential when printing geometrically challenging areas, like the sharp change in the section near the root, potentially leading to poorer print quality. This depreciation in print quality will result in much lower mechanical properties at the root compared to those reported in Table 5.4. These are just some preliminary conclusions and observations derived from conversations with technicians who assisted in manufacturing the specimen. A definite cause of the crack and its absence in the polymer beam specimen can only

be established after a more elaborate investigation of both the printed parts and the materials. The present experience serves as a cautionary tale in the use of additive manufacturing, illustrating some of the potential limitations involved.

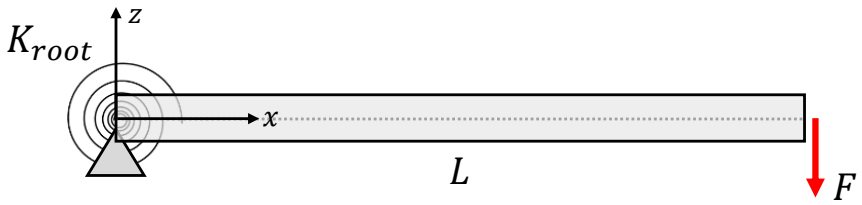

Fig. 5.22 Analytical model of the airfoil beam subjected to a tip load with the imperfect clamping condition modelled using a pinned support and a torsional spring

Shape Sensing an Imperfectly Clamped Beam

Despite these shortcomings, the present experimental campaign is used as an opportunity to model and investigate the influence of imperfect boundary conditions on iFEM reconstruction. Analytically, this imperfectly clamped beam can be modelled as a beam with a pinned support combined with a torsional spring at the root (shown in Fig. 5.22), where the spring stiffness governs the elasticity of the root. In the case of perfect clamping, the spring stiffness approaches infinity, while in the present case, it is a function of the size of the crack.

From the analytical model of Fig. 5.22, the total beam tip deflection can be written as a superposition of a rigid body component, w_{RB} and an elastic beam deformation component, w_e, as

$$\begin{aligned} w(x) =& w_{RB}(x, K_{root}) + w_e(x) \\ =& -\frac{FL}{K_{root}}x - \frac{FL}{2EI_{yy}}x^2 + \frac{F}{6EI_{yy}}x^3 \end{aligned} \tag{5.1}$$

where F is the tip load, L is the beam length, E is the Young's modulus of the material, I is the second moment of area, and K_{root} is the stiffness of the spring. The derivation of Eq. 5.1 is given in Appendix D. Based on this definition, Fig. 5.20b can now be interpreted a plot of w_{RB} as a function of F.

Assuming the veracity of this analytical model to perfectly capture experimental beam behaviour, the present study aims to filter the rigid body component from the experimentally measured deflections. As rigid body motion does not contribute to the measured strains, a comparison of iFEM reconstructed deflections with this 'filtered' experimental deflection would be a fair comparison of beam deformation. However, this cannot be achieved through a direct approach, as it would require knowledge

of the load applied and the spring stiffness, negating the proposed benefits of iFEM. Hence an inverse approach is proposed.

The analytical beam deflection of Eq. 5.1 is rewritten in terms of two unknown coefficients, a_1 and a_2 as,

$$w(x) = a_1 x + a_2 \left(x^2 L - \frac{x^3}{3} \right) \tag{5.2}$$

Given experimental deflection measurements, w_{exp}, at multiple axial locations, x_1 and x_2, Eq. 5.2 can be written in vector form as,

$$\begin{bmatrix} x_1 & x_1^2 L - \frac{x_1^3}{3} \\ x_2 & x_2^2 L - \frac{x_2^3}{3} \end{bmatrix} \begin{Bmatrix} a_1 \\ a_2 \end{Bmatrix} = \begin{Bmatrix} w_{exp}(x_1) \\ w_{exp}(x_2) \end{Bmatrix} \tag{5.3}$$

Eq. 5.3 can now be solved by simple matrix inversion to obtain these unknown coefficients. Using the coefficient values evaluated, the rigid body component is filtered from the measured deflection as,

$$\begin{aligned} w_f(x) =& w_{exp}(x) - w_{RB}(x) \\ =& w_{exp}(x) - a_1 x \end{aligned} \tag{5.4}$$

where w_f is called the filtered experimental beam deflection, representing the contribution due to beam deformation.

For the experimental implementation of this filtering approach, LVDTs are placed at three axial locations of the beam, x =0.43 L, 0.57 L, and 0.76 L, from the root, respectively. This is in contrast to the previous test, where the deflections were measured only at the tip of the beam. Similar to the previous test, the beam is incrementally loaded at the shear center up to a maximum load of 49 N, and one iTM2D0 element is used for the iFEM analysis. The iFEM results compared against experimental deflections are shown in Fig. 5.23a. Results of Fig. 5.23a reveal the iFEM predictions to be more accurate than previously demonstrated. Comparison with the unfiltered deflections reveals large errors similar to those observed in Fig. 5.20a. However, the filtered results correlate very well with the iFEM predictions at all three axial sections monitored. The iFEM results as a function of the load applied are shown in Fig. 5.23b. Although the reconstructed deflection remained linear, filtered deflections were not, because of which clear inaccuracies are observed at loads $\sim 30-40$ N. The lack of linearity possibility illustrates the sensitivity of the filtering approach in terms of the effect of noise or experimental errors (in the LVDT measurements) on the filtering results. More robust filtering strategies are expected to yield more accurate results.

iFEM accuracy is quantified in Fig. 5.24, where a percentage error less than 15% is observed over the majority of the loading cycle. Errors as high as 20% are also

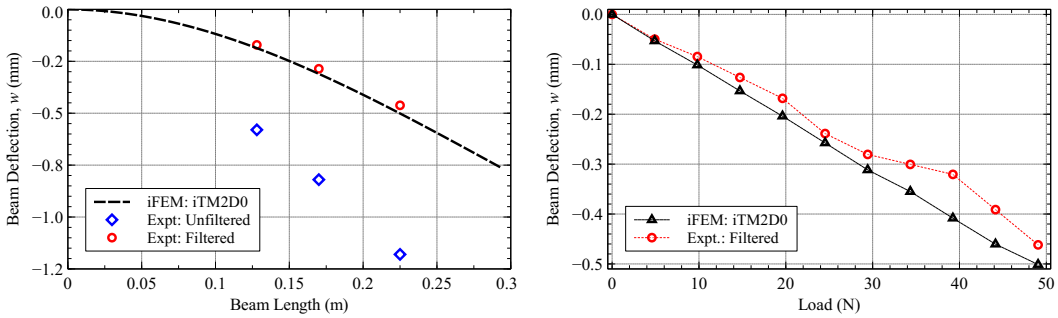

(a) (b)

Fig. 5.23 iFEM results, obtained using one iTM2D0 element, for the metallic airfoil beam: (a) reconstructed transverse deflection along the beam length for a tip load of 49 N, compared against filtered and unfiltered experimental measurements, and (b) iFEM and experimental transverse deflection at $x = 0.76\,L$, plotted as a function of the load applied

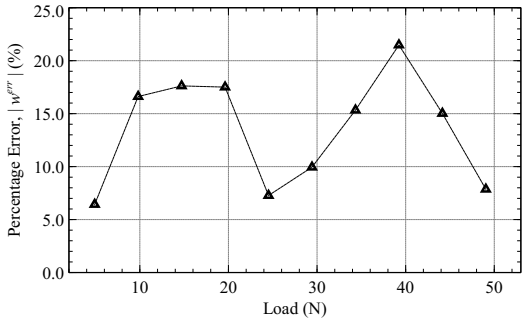

Fig. 5.24 iFEM results, obtained using one iTM2D0 element, for the metallic airfoil beam: percentage error in transverse deflection at $x = 0.76\,L$, as a function of the load applied

reported. Although not ideal, these results are a significant improvement on those presented in Fig. 5.20. Unfortunately, due to the high torsional stiffness of the beam, load cases where the beam undergoes combined bending and torsion could not be investigated effectively. Regardless of these limitations, the novelty of the present investigation should not be understated. These results present the first experimental application of iFEM for problems involving imperfect boundary conditions.

The main conclusions from this chapter describing experimental shape sensing using iFEM are briefly described below:

- The treatment of shear strains in the novel beam formulations is validated and demonstrated to be accurate for predicting the transverse shear and torsional deformation of beams with complex cross-sections;
- The iFEM formulation is demonstrated to be independent of the material properties of the analysed structure;
- A strategy based on filtering measured displacements can be used for analysing structures with imperfect boundary conditions.

Chapter 6

Control Strategy for Shape Morphing Structures

The need for efficient and robust shape sensing methodologies has underpinned the work presented in previous chapters. However, in addition to improving shape sensing performance, investigating potential applications is also vital for their maturation. Chapter 4 described an initial effort in the use of iFEM for SHM, specifically for damage detection in beams and plates. Another potential application is for the monitoring and control of shape morphing structures. However, previous efforts in this regard have been non-existent or limited at best.

This chapter describes initial efforts in developing a novel monitoring and operational framework for shape morphing structures using a control philosophy based on the iFEM methodology. Various control schemes are proposed considering structures which are isolated or under the effect of unknown external loads.

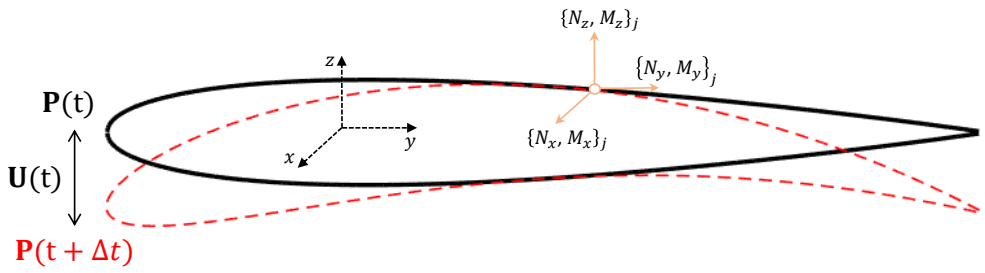

Fig. 6.1 The initial and final shape acquired by a shape morphing airfoil over a time period Δt; the nodal actuation loads can also be seen

6.1 Open-Loop Framework

The shape morphing beam or plate structure is considered to be defined in the three-dimensional orthogonal Cartesian coordinate system $\mathbf{x} \equiv \{x, y, z\}$. The control formulation is based on a finite element framework, where the structure is discretised using a finite element mesh, with a total of 'e' elements and 'n' nodes.

At any instant of time t, the location of a node, i, is defined by its coordinates, $\mathbf{P}_i(t) \equiv \{x, y, z\}_i^T$. The global shape of the structure is then given by the vector of nodal coordinates, $\mathbf{P}(t)_{[3n\times 1]} = \{\mathbf{P}_i(t)\}$ (the subscript $[* \times *]$ indicates the vector/matrix dimensions). Any change in shape of the structure over an interval of time Δt can be defined as the change in this nodal coordinate vector,

$$\mathbf{P}(t + \Delta t) = \mathbf{P}(t) + \mathbf{U}(t) \tag{6.1}$$

where, $\mathbf{U}(t)_{[3n\times 1]} = \{\mathbf{U}_i(t)\}$ is the global nodal displacement vector. The change in position of a node, $\mathbf{U}_i(t) = \{u, v, w\}_i^T$, is defined in terms of the variables, u, v, and w, representing the nodal displacements along the x, y, and $z-$axis, respectively.

The objective of the shape control strategy is to coordinate the change of shape from an initial to the desired state. This reference shape is defined by the vector of nodal coordinates, $\mathbf{P}_{ref}$, and the corresponding nodal displacements required for achieving this state is defined by, $\mathbf{U}_{ref}$. Assuming the reference shape to remain fixed or time-independent, the change from the initial to the desired state of the structure can be defined as,

$$\mathbf{P}(t + \Delta t) = \mathbf{P}(t) + \mathbf{U}_{ref}(t) \equiv \mathbf{P}_{ref} \tag{6.2}$$

where attaining $\mathbf{U}_{ref}$ is the primary goal for successful morphing.

Any change in the shape of the structure is initiated by a series of actuators instrumented within or on the surface of the structure (shown in Fig. 6.1). Using these actuators, concentrated forces and moments can be generated at any node, j; these nodal forces are represented by, $\mathbf{L}_j(t) = \{N_x, N_y, N_z, M_x, M_y, M_z\}_j^T$, where N_x, N_y, N_z, are nodal forces along the x, y, and $z-$axis, respectively, and M_x, M_y, M_z, are nodal moments about the x, y, and $z-$axis, respectively. The total nodal force vector can be written as, $\mathbf{L}(t)_{[6m\times 1]} = \{\mathbf{L}_j(t)\}$, where m represents the total number of nodes where actuation loads are present. In the most general case, $m = n$ and actuators are assumed to be present at all nodes of the structure.

At any time t, the instantaneous nodal displacements developed on the structure due to the action of these nodal actuation loads can be described as,

$$\mathbf{U}(t) = \mathbf{A}\mathbf{L}(t) \tag{6.3}$$

where $\mathbf{A}_{[3n\times 6m]}$ is a vector of influence coefficients. Each column of $\mathbf{A}$ represents the nodal displacements generated due to the independent action of a unit force or moment at a particular node of the structure. For example, the first column of $\mathbf{A}$ represents $\mathbf{U}$ due to a unit N_x load at node 1.

The objective of the present formulation is to identify the load vector, $\mathbf{L}$, that generates the desired nodal displacements, $\mathbf{U}_{ref}$. This is accomplished by a functional defined as the least-squares error between the actual and desired nodal displacements,

$$\Phi_m = ||\mathbf{U}_{ref} - \mathbf{U}(t)||^2 = \frac{1}{2}\mathbf{L}^T\mathbf{K}\mathbf{L} - \mathbf{L}^T\mathbf{F} + \mathbf{C} \tag{6.4}$$

where matrix $\mathbf{K}$ and vector $\mathbf{F}$ are similar to the stiffness matrix and force vector in the direct FEM. In the present scenario, $\mathbf{K}$ is only a function of the number and location of actuators used, while $\mathbf{F}$ is a function of the actuator position and final desired shape of the structure. They can be defined as,

$$\mathbf{K} = \mathbf{A}^T\mathbf{A} \qquad \mathbf{F} = \mathbf{A}^T\mathbf{U}_{ref} \tag{6.5}$$

Equation 6.4 is solved by minimising the functional with respect to the nodal actuation loads to obtain series of linear algebraic equations,

$$\mathbf{K}\mathbf{L} = \mathbf{F} \tag{6.6}$$

If $\mathbf{K}$ is a non-singular, Equation 6.5 can be solved by matrix inversion to obtain the nodal actuation loads, $\mathbf{L}$, required to achieve the desired shape at the next time step. The control flow in the present case is open-loop in nature. Prior knowledge of the influence matrix, $\mathbf{A}$, is key to implementing the present strategy. This can be measured experimentally or numerically, and any inaccuracies in its estimation can lead to poor results. The entire workflow of the open-loop control approach is shown in Fig. 6.2.

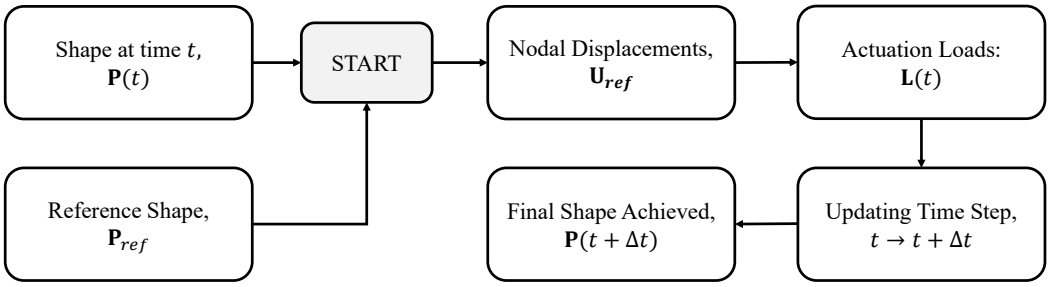

Fig. 6.2 Flow diagram illustrating the main steps of the open-loop framework for controlling the shape of a morphing structures

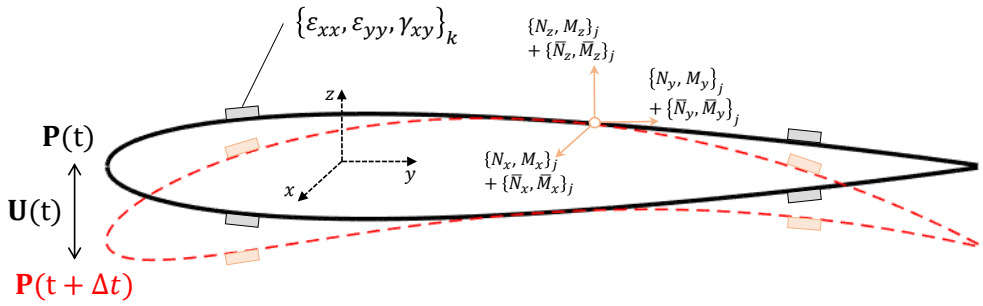

Fig. 6.3 The initial and final shape acquired by a shape morphing airfoil over a time period Δt; the nodal actuation loads and the surface instrumented strain sensors are shown

6.2 Closed-Loop Framework

In cases where the number of actuators used are low ($m << n$) or the structure is influenced by external loads, the actuation, $\mathbf{L}(t)$, calculated by Eq. 6.6 may not be successful in achieving the desired shape, i.e., $\mathbf{P}(t+\Delta t) \neq \mathbf{P}_{ref}$. Similar situations are also encountered when the desired shape is a function of time, $\mathbf{P}_{ref}(t)$, or of the operational conditions of the structure. For such problems, feedback information is required for taking further corrective actions, and the final shape may be achieved after multiple time steps.

The iFEM serves as a valuable tool in such situations, providing real-time information regarding the structural shape using surface strain measurements. Depending on the structure, both beam and plate iFEM can be used. The accuracy of the feedback information is dependent on the accuracy of the iFEM results. Hence, the previous framework is redefined by introducing an iFEM feedback-based shape correction capability.

In addition to the actuators, the structure is now assumed to be instrumented with strain sensors at discrete locations, $\mathbf{x}_k \equiv \{x,y,z\}_k$, $(k = 1,...,N)$, where N is the total number of strain sensors used. The sensors are used for measuring surface strains, $\{\varepsilon_{xx}, \varepsilon_{yy}, \gamma_{xy}\}_k$. The strain measurements at any time t, is used to compute the iFEM reconstructed shape, $\mathbf{P}_{iFEM}(t)$. This closed-loop framework is explained by considering two separate cases:a structure under external loads and morphing control using an insufficient number of actuators.

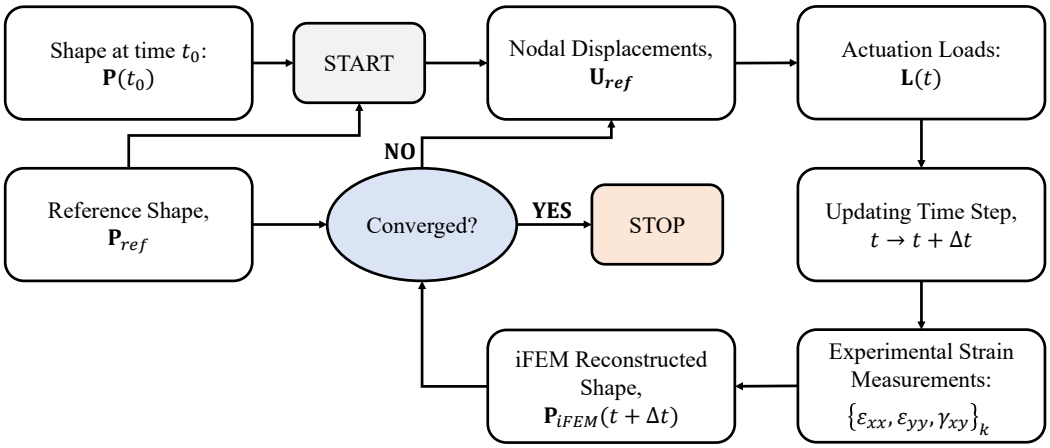

Fig. 6.4 Flow diagram illustrating the main steps of the iFEM-based closed-loop framework for controlling the shape of morphing structures

6.2.1 Structure Under External Loads

Assuming the structure during operation is influenced by external factors leading to loads being developed on its surface. The total load at any node j of the structure can be defined as the superposition of an actuation component, $\mathbf{L}_j(t) = \{N_x, N_y, N_z, M_x, M_y, M_z\}_j^T$, and nodal contributions due to the unknown external load, $\mathbf{M}_j(t) = \{\overline{N}_x, \overline{N}_y, \overline{N}_z, \overline{M}_x, \overline{M}_y, \overline{M}_z\}_j^T$. The corresponding global force vectors can be defined as, $\mathbf{L}(t)_{[6m\times 1]} = \{\mathbf{L}_j(t)\}$, and $\mathbf{M}(t)_{[6m\times 1]} = \{\mathbf{M}_j(t)\}$.

Considering the structure actuated at any time t by a force, $\mathbf{L}(t)$, calculated based on Eq. 6.6. The resultant nodal displacements generated can now be written as,

$$\mathbf{U}(t) = \mathbf{A}\left(\mathbf{L}(t) + \mathbf{M}(t)\right) \tag{6.7}$$

It is evident from Eq. 6.2 that the shape achieved at the next time step will not correlate with the desired shape,

$$\begin{aligned} \mathbf{P}(t+\Delta t) =& \mathbf{P}(t) + \mathbf{U}(t) \\ =& \mathbf{P}(t) + \mathbf{A}\left(\mathbf{L}(t) + \mathbf{M}(t)\right) \neq \mathbf{P}_{ref} \end{aligned} \tag{6.8}$$

At the time step, $t + \Delta t$, information regarding the new shape achieved is obtained as feedback from the iFEM results,

$$\mathbf{P}(t+\Delta t) \equiv \mathbf{P}_{iFEM}(t+\Delta t) \tag{6.9}$$

Given information regarding the initial and final states of the structure, the new vector of desired nodal displacements can be calculated as,

$$\mathbf{U}_{ref}(t+\Delta t) = \mathbf{P}_{ref} - \mathbf{P}_{iFEM}(t+\Delta t) \tag{6.10}$$

This new $\mathbf{U}_{ref}(t+\Delta t)$ is used in the least-squares functional of Eq. 6.6 to calculate the updated actuation load, $\mathbf{L}(t+\Delta t)$.

A claim can be made regarding the expected magnitude of the updated actuation load. As the shape inaccuracy is due to the external load, using Eq. 6.10, the change in actuation load at the new time step can be defined as,

$$\Delta\mathbf{L}(t+\Delta t) = \mathbf{L}(t+\Delta t) - \mathbf{L}(t) \approx \mathbf{M}(t) \tag{6.11}$$

Eq. 6.11 is only stated for theoretical understanding, and as $\mathbf{M}(t)$ is unknown, it cannot be employed directly in the control strategy. As mentioned previously, $\mathbf{L}(t+\Delta t)$ should be estimated inversely using Eq. 6.10 in Eq. 6.6. The flowchart of this iFEM based closed-loop control strategy is shown in Fig. 6.4.

Some interesting observations and conclusions from these results are briefly stated here. The equivalence of Eq. 6.11, i.e., $\Delta\mathbf{L}(t+\Delta t) \approx \mathbf{M}(t)$, is an ideal scenario that would ensure the successful achievement of the desired shape at the next time step, $\mathbf{P}(t+2\Delta t) = \mathbf{P}_{ref}$. However, it is contingent on the ability of iFEM to accurately reconstruct the updated shape of the structure (stated in Eq. 6.9). iFEM inaccuracies can lead to, $\mathbf{P}(t+2\Delta t) \neq \mathbf{P}_{ref}$, where further time steps are required to update the load and converge to the closest solution acceptable.

As mentioned previously, prior and accurate estimation of the influence matrix, $\mathbf{A}$, is key for the present control strategy. In cases where direct experimental or numerical estimation is difficult or impossible, the iFEM reconstructed nodal displacements due to individual actuation loads (applied experimentally) can be used to formulate the new iFEM-based influence matrix, $\mathbf{A}_{iFEM} \equiv \mathbf{A}$. Here again, the iFEM accuracy is a key factor influencing the final morphing results obtained.

6.2.2 Sparse Set of Actuators

When the structure is instrumented with only a sparse set of actuators ($m << n$), the desired shape may not be achieved at the next time step or, in certain cases, may never converge to an accurate solution regardless of multiple time updates. Although partially a failure of the morphing system, the control strategy can be redefined to optimise the results of structural morphing. This is accomplished through a weighted least-squares error functional.

For this present approach, a redefinition of Eq. 6.4 is used, where Φ_m is now defined as a weighted least-squares functional,

$$\Phi_m^{\lambda} = ||\mathbf{U}_{ref} - \mathbf{U}(t)||^2 = \frac{1}{2}\mathbf{L}^T\mathbf{K}^{\lambda}\mathbf{L} - \mathbf{L}^T\mathbf{F}^{\lambda} + \mathbf{C} \tag{6.12}$$

where λ indicates the functional formulated based on weighting each nodal displacement contribution. The new weighted $\mathbf{K}^{\lambda}$ matrix and $\mathbf{F}^{\lambda}$ vector are defined as,

$$\mathbf{K}^{\lambda} = \sum_{i=1}^{3n} \lambda_i \mathbf{A}_i^T \mathbf{A}_i \qquad \mathbf{F} = \sum_{i=1}^{3n} \lambda_i \mathbf{A}_i^T (\mathbf{U}_{ref})_i \tag{6.13}$$

where the subscript $(\bullet)_i$ represents the i^{th} row of a matrix or a vector, implying, $\boldsymbol{\lambda} = \{\lambda_i\}$, $\mathbf{A} = \{\mathbf{A}_i\}$ and $\mathbf{U}_{ref} = \{(\mathbf{U}_{ref})_i\}$.

Here, $\boldsymbol{\lambda}$ is the weighting coefficient vector, and is used to associate a value of weight, λ_i, to each nodal displacement component of $\mathbf{U}$. High ($\lambda_i = 1$) or low ($\lambda_i = 10^{-2} - 10^{-4}$) values can be used to enforce a stronger or weaker correlation between the initial and desired values of the nodal displacement in the error functional of Eq. 6.12. It should be stated that the use of constant weighting coefficient for all nodes is equivalent to the functional formulation of Eq. 6.4.

The present weighted formulation is useful when the overall morphing accuracy is poor. In such cases, weights can be used to redistribute the accuracy over the domain, i.e., specific nodal displacements with higher weights will better approximate the desired displacement value, compared to those with lower weights. Hence, the morphing performance of certain key areas of the structure can be given more emphasis, e.g. like the leading or trailing edge of an aircraft wing, to maximise structural performance.

Chapter 7

Conclusions

7.1 Summary

Real-time structural monitoring systems are an essential technology for ensuring the long-term health, safety, and performance of aircraft structures and can also play a vital role in the operation and control of the next generation of shape morphing structures. This work presents the development of 1D and 2D iFEM-based structural monitoring solutions to address some of the challenges that hinder existing systems from practical adoption.

The work primarily focused on improving existing 1D iFEM formulations and proposing novel inverse beam elements capable of modelling geometrically complex beam structures. A novel beam element formulation is proposed for analysing beams with complex cross-sectional profiles. This involved an accurate treatment of shear strains due to transverse and torsional loads, inherently a function of the beam section, and is accomplished using certain shear coefficients and functions. Numerical results reveal the novel formulation to be accurate in modelling transverse shear and torsional deformation. Further development of the formulation involves the analysis of thin-walled beams undergoing cross-sectional warping. The effect of axial displacements due to warping is modelled, and higher-order shape functions are proposed to capture the axial variation of torsional rotation. The developed elements are analysed numerically, revealing moderate success in reconstructing torsional deformation with the potential for further improvement.

The novel beam elements are also used for the experimental shape sensing of a cantilevered aluminium thin-walled C-beam subjected to tip loading. The experimental results demonstrate high iFEM accuracy in reconstructing the transverse deflection and torsional rotation of the beam, further validating the novel formulation. The experimental investigations on additively manufactured beam specimens are also a relative novelty in the domain of shape sensing research. Investigation of the

polymer beam specimen revealed iFEM to be effective in producing accurate results even under the influence of complex material properties, like creep and viscoelasticity, thus validating the material independence of the iFEM methodology. The challenges involved in testing and analysing the additively manufactured metallic beam specimen provided an ideal opportunity to assess the effect of imperfect boundary conditions on iFEM results. Despite the relative success of the method proposed to filter experimentally measured beam deflections, additional improvements are possible.

In parallel with the development and validation of novel inverse beam elements, existing 2D iFEM formulations are also investigated in terms of the number and position of strain sensors required for generating accurate results. Efficient strain sensor patterns are proposed, resembling the shape of commonly used load-bearing frame structures, for generating robust and accurate iFEM solutions. Numerical investigations demonstrated them to be effective for the shape sensing of a cantilevered plate, particularly for reconstructing the lower and higher vibrational mode shapes. Virtual sensor expansion, using the SEA, is demonstrated to be an effective strategy for accurately extrapolating in-situ strains. Coupling sensor patterns with virtual sensor expansion strategies led to the derivation of new reduced patterns, further reducing the number of sensors used without compromising iFEM accuracy. An iFEM-based damage detection and localisation strategy for thin plates is proposed and demonstrated numerically, and its performance is characterised using probability-based metrics. In this case, the use of virtual sensor expansion led to the development of more efficient solutions. Maximising the benefits and minimising the limitations of both 1D and 2D iFEM methodologies, an integrated Multi-Resolution monitoring approach is introduced and numerically demonstrated for the monitoring of a wing box structure.

Finally, this work also lays the theoretical foundation for an iFEM-based control framework for shape morphing structures, where iFEM results are used as feedback information for closed-loop shape control. The basic framework is introduced, and specific cases are discussed, such as structures under the influence of unknown external loads or those instrumented with a limited number of actuators leading to insufficient actuation performance.

7.2 Future Work

All investigations presented in this work are not meant to be exhaustive but rather place markers for ongoing research efforts. Further integration of 1D and 2D inverse elements would be effective from the perspective of iFEM accuracy and computational effort. In contrast to the Multi-Resolution approach described above, beam and shell elements can also be used in conjunction with the same inverse model

for modelling complex structures. Similar strategies are commonly adopted in direct FEM models and are expected to reduce the number of elements and sensors used and lower the computational effort.

Also, the proposed morphing framework is a preliminary work in this domain and requires further development. Numerical and experimental assessments can reveal the efficacy of this preliminary framework and highlight avenues for further development.

References

[1] W. J. Staszewski, C. Boller, and G. R. Tomlinson. *Health Monitoring of Aerospace Structures*. John Wiley & Sons, 2003.

[2] O. Benedettini, T. S. Baines, H. W. Lightfoot, and R. M. Greenough. State-of-the-art in integrated vehicle health management. *Proceedings of the Institution of Mechanical Engineers, Part G: Journal of Aerospace Engineering*, 223(2): 157–170, 2009. ISSN 09544100. doi:10.1243/09544100JAERO446.

[3] E. Baroth, W. T. Powers, J. Fox, B. Prosser, J. Pallix, K. Schweikard, and J. Zakrajsek. IVHM (Integrated Vehicle Health Management) techniques for future space vehicles. *37th Joint Propulsion Conference and Exhibit*, July, 2001. doi:10.2514/6.2001-3523.

[4] M. Esperon-Miguez, P. John, and I. K. Jennions. A review of Integrated Vehicle Health Management tools for legacy platforms: Challenges and opportunities. *Progress in Aerospace Sciences*, 56:19–34, 2013. ISSN 03760421. doi:10.1016/j.paerosci.2012.04.003. URL http://dx.doi.org/10.1016/j.paerosci.2012.04.003.

[5] C. R. Farrar and K. Worden. An Introduction to Structural Health Monitoring. *Philosophical Transactions of the Royal Society A: Mathematical, Physical and Engineering Sciences*, 365(1851):303–315, 2007. ISSN 1364503X. doi:10.1098/rsta.2006.1928.

[6] P. Cawley. Structural health monitoring: Closing the gap between research and industrial deployment. *Structural Health Monitoring*, 17(5):1225–1244, 2018. ISSN 17413168. doi:10.1177/1475921717750047.

[7] M. Gherlone, P. Cerracchio, and M. Mattone. Shape sensing methods: Review and experimental comparison on a wing-shaped plate. *Progress in Aerospace Sciences*, 99:14–26, April, 2018. ISSN 03760421. doi:10.1016/j.paerosci.2018.04.001. URL https://doi.org/10.1016/j.paerosci.2018.04.001.

[8] W. H. Prosser, S. G. Allison, S. E. Woodard, R. A. Wincheski, E. G. Cooper, D. C. Price, M. Hedley, M. Prokopenko, D. A. Scott, and A. Tessler. Structural health management for future aerospace vehicles. *Proceedings of the 2nd Australasian Workshop on Structural Health Monitoring, Melbourne, Australia*, pages 1–8, November, 2004.

[9] J. Valasek. *Morphing Aerospace Vehicles and Structures*. John Wiley & Sons, 2012.

[10] A.-M. R. McGowan, A. E. Washburn, L. G. Horta, R. G. Bryant, D. E. Cox, E. J. Siochi, S. L. Padula, and N. M. Holloway. Recent Results from NASA's Morphing Project [C]. *SPIE's 9th Annual International Symposium on Smart Structures and Materials*, 4698:97–111, 2002.

[11] S. Barbarino, O. Bilgen, R. M. Ajaj, M. I. Friswell, and D. J. Inman. A review of morphing aircraft. *Journal of Intelligent Material Systems and Structures*, 22(9):823–877, 2011. ISSN 1045389X. doi:10.1177/1045389X11414084.

[12] T. A. Weisshaar. Morphing aircraft systems: Historical perspectives and future challenges. *Journal of Aircraft*, 50(2):337–353, 2013. ISSN 15333868. doi:10.2514/1.C031456.

[13] A. Y. N. Sofla, S. A. Meguid, K. T. Tan, and W. K. Yeo. Shape morphing of aircraft wing: Status and challenges. *Materials and Design*, 31(3):1284–1292, 2010. ISSN 02641275. doi:10.1016/j.matdes.2009.09.011. URL http://dx.doi.org/10.1016/j.matdes.2009.09.011.

[14] A. Tessler and J. Spangler. Inverse FEM for Full-Field Reconstruction of Elastic Deformations in Shear Deformable Plates and Shells. *Proceedings of Second European Workshop on Structural Health Monitoring*, pages 83–90, 2004.

[15] A. Tessler and J. L. Spangler. A least-squares variational method for full-field reconstruction of elastic deformations in shear-deformable plates and shells. *Computer Methods in Applied Mechanics and Engineering*, 194(2-5 SPEC. ISS.):327–339, 2005. ISSN 00457825. doi:10.1016/j.cma.2004.03.015.

[16] R. Roy, M. Gherlone, and C. Surace. Damage localisation in thin plates using the inverse finite element method. *In: Wahab, M. (eds) Proceedings of the 13th International Conference on Damage Assessment of Structures. Lecture Notes in Mechanical Engineering. Springer, Singapore*, 2020. URL https://doi.org/10.1007/978-981-13-8331-1_14.

[17] R. Roy, M. Gherlone, and C. Surace. Shape sensing of beams with complex cross sections using the inverse finite element method. *In Proceeding of 12th International Workshop on Structural Health Monitoring, Stanford, CA*, 2019.

[18] R. Roy, A. Tessler, C. Surace, and M. Gherlone. Shape sensing of plate structures using the inverse finite element method: Investigation of efficient strain–sensor patterns. *Sensors*, 20:7049, 2020. URL https://doi.org/10.3390/s20247049.

[19] R. Roy, M. Gherlone, and C. Surace. A shape sensing methodology for beams with generic cross-sections: Application to airfoil beams. *Aer. Sci. and Tech.*, 110:106484, 2021. ISSN 1270-9638. URL https://www.sciencedirect.com/science/article/pii/S1270963820311664.

[20] R. Roy, M. Gherlone, C. Surace, and A. Tessler. Full-field strain reconstruction using uniaxial strain measurements: Application to damage detection. *Appl. Sci.*, 11:1681, 2021. URL https://doi.org/10.3390/app11041681.

[21] P. Cawley and R. D. Adams. A Vibration Technique for Non-Destructive Testing of Fibre Composite Structures. *Journal of Composite Materials*, 13 (2):161–175, 1979. ISSN 1530793x. doi:10.1177/002199837901300207.

[22] P. Cawley and R. D. Adams. The Location of Defects in Structures From Measurements of Natural Frequencies The Journal of Strain Analysis for Engineering Design. *The Journal of Strain Analysis for Engineering Design*, 14(2):49–57, 1979. ISSN 0309-3247.

[23] M. M. A. Wahab, G. D. Roeck, and B. Peeters. Parameterization of damage in reinforce concrete structures using model updating. *Sound & Vibration*, 228(4):717–730, 1999.

[24] C.R. Farrar and K Worden. *Structural Health Monitoring: A Machine Learning Perspective*. John Wiley & Sons Ltd., West Sussex, UK, 2013.

[25] C. Surace, R. Archibald, and R. Saxena. On the use of the polynomial annihilation edge detection for locating cracks in beam-like structures. *Comput. Struct.*, 114–115:72–83, 2013.

[26] N. Corrado, N. Durrande, M. Gherlone, J. Hensman, M. Mattone, and C. Surace. Single and multiple crack localization in beam-like structures using a Gaussian process regression approach. *JVC/Journal of Vibration and Control*, 24(18):4160–4175, 2018. ISSN 17412986. doi:10.1177/1077546317721418.

[27] C. Surace, R. Saxena, M. Gherlone, and H. Darwich. Damage localisation in plate like-structures using the two-dimensional polynomial annihilation edge detection method. *Journal of Sound and Vibration*, 333(21):5412–5426, 2014. ISSN 10958568. doi:10.1016/j.jsv.2014.05.047. URL http://dx.doi.org/10.1016/j.jsv.2014.05.047.

[28] M. Gherlone, M. Mattone, C. Surace, A. Tassotti, and A. Tessler. Novel Vibration-Based Methods for Detecting Delamination Damage in Composite Plate and Shell Laminates. *Key Engineering Materials*, 293-294:289–296, 2005. ISSN 1662-9795. doi:10.4028/www.scientific.net/kem.293-294.289.

[29] S. J. Wildy, A. G. Kotousov, and J. D. Codrington. A new passive defect detection technique based on the principle of strain compatibility. *Smart Materials and Structures*, 17(4), 2008. ISSN 09641726. doi:10.1088/0964-1726/17/4/045004.

[30] S. Wildy and J. Codrington. An Algorithm for Identifying a Crack Within a Measured Displacement Field. *Journal of Nondestructive Evaluation*, 36(2): 1–10, 2017. ISSN 15734862. doi:10.1007/s10921-017-0406-8.

[31] L. M. Bezerra and S. Saigal. A Boundary Element Formulation for inverse Elastostatics problem. *International Journal for Numerical Methods in Engineering*, 36:2189–2202, 1993.

[32] B. Gliši´c and D. Inaudi. *Fiber Optic Methods for Structural Health Monitoring*. John Wiley & Sons Ltd., West Sussex, UK, 2007.

[33] M. Domaneschi, S. Casciati, N. Catbas, G. P. Cimellaro, D. Inaudi, and G. C. Marano. Structural health monitoring of in-service tunnels. *Int. J. Sustainable Materials and Structural Systems*, 4:268–291, 2020.

[34] M. Mieloszyk and W. Ostachowicz. An application of Structural Health Monitoring system based on FBG sensors to offshore wind turbine support structure model. *Marine Structures*, 51:65–86, 2017. ISSN 09518339. doi:10.1016/j.marstruc.2016.10.006.

[35] O. J. Ohanian, M. A. Davis, J. Valania, B. Sorensen, M. Dixon, M. Morgan, and D. A. Litteken. Embedded fiber optic shm sensors for inflatable space habitats. *Accelerating Space Commerce, Exploration, and New Discovery Conference, ASCEND 2020*, pages 1–16, 2020. doi:10.2514/6.2020-4049.

[36] A. Güemes, A. Fernández-López, P. F. Díaz-Maroto, A. Lozano, and J. Sierra-Perez. Structural health monitoring in composite structures by fiber-optic sensors. *Sensors (Switzerland)*, 18(4):1–11, 2018. ISSN 14248220. doi:10.3390/s18041094.

[37] B. L. Martins and J. B. Kosmatka. Detecting damage in a UAV composite wing spar using distributed fiber optic strain sensors. In *Proceedings of the 56th AIAA/ASCE/AHS/ASC Structures, Structural Dynamics, and Materials Conference*, Kissimmee, FL, USA, 2015.

[38] T. M. Seigler, D. A. Neal, J. S. Bae, and D. J. Inman. Modeling and flight control of large-scale morphing aircraft. *Journal of Aircraft*, 44(4):1077–1087, 2007. ISSN 15333868. doi:10.2514/1.21439.

[39] R. Pecora. Morphing wing flaps for large civil aircraft: Evolution of a smart technology across the Clean Sky program. *Chinese Journal of Aeronautics*, 34(7):13–28, 2021. ISSN 10009361. doi:10.1016/j.cja.2020.08.004. URL https://doi.org/10.1016/j.cja.2020.08.004.

[40] N. Nazeer, X. Wang, and R. M. Groves. Sensing, actuation, and control of the smartx prototype morphing wing in the wind tunnel. *Actuators*, 10(6):1–20, 2021. ISSN 20760825. doi:10.3390/act10060107.

[41] C. C. Asins, V. Landersheim, D. Laveuve, S. Adachi, M. May, J. D. Wacker, and J. Decker. Analysis and design of a leading edge with morphing capabilities for the wing of a regional aircraft—gapless chord-and camber-increase for high-lift performance. *Applied Sciences (Switzerland)*, 11(6), 2021. ISSN 20763417. doi:10.3390/app11062752.

[42] C. E. Whitmer and A. G. Kelkar. Robust control of a morphing airfoil structure. *Proceedings of the American Control Conference*, 4:2863–2868, 2005.

[43] T. L. Grigorie, R. M. Botez, A. V. Popov, M. Mamou, and Y. Mébarki. A hybrid fuzzy logic proportionalintegral-derivative and conventional on-off controller for morphing wing actuation using shape memory alloy part 2: Controller implementation and validation. *Aeronautical Journal*, 116:451–465, 2012.

[44] T. Mkhoyan, N. R. Thakrar, R. D. Breuker, and J. Sodja. Design and development of a seamless smart morphing wing using distributed trailing edge camber morphing for active control. *AIAA Scitech 2021 Forum*, pages 1–16, 2021. doi:10.2514/6.2021-0477.

[45] F. Calkins and G Butler. Subsonic jet noise reduction variable geometry chevron. *Proceedings of 42nd AIAA Aerospace Sciences Meeting and Exhibit*, 2004.

[46] J. Valasek, M. D. Tandale, and J. Rong. A reinforcement learning - adaptive control architecture for morphing. *Journal of Aerospace Computing, Information, and Communication*, 2, 2005.

[47] W. L. Ko, W. L. Richards, and V. T. Tran. Displacement Theories for In-Flight Deformed Shape Predictions of Aerospace Structures. *NASA/TP-2007-214612*, 2007.

[48] W. L. Ko, W. Lance Richards, and V. T. Fleischer. Applications of Ko Displacement Theory to the Deformed Shape Predictions of the Doubly-tapered Ikhana Wing. *NASA/TP-2009-214652*, 2009.

[49] H. Xu, Q. Zhou, L. Yang, M. Liu, D. Gao, Z. Wu, and M. Cao. Reconstruction of full-field complex deformed shapes of thin-walled special-section beam structures based on in situ strain measurement. *Advances in Structural Engineering*, 23(15):3335–3350, 2020. ISSN 20484011. doi:10.1177/1369433220937156.

[50] J. Smoker and A. Baz. Monitoring the bending and twist of morphing structures. *Sensors and Smart Structures Technologies for Civil, Mechanical, and Aerospace Systems*, 6932:69321X, 2008. ISSN 0277786X. doi:10.1117/12.776433.

[51] W. Akl, S. Poh, and A. Baz. Wireless and distributed sensing of the shape of morphing structures. *Sensors and Actuators, A: Physical*, 140(1):94–102, 2007. ISSN 09244247. doi:10.1016/j.sna.2007.06.026.

[52] P. S. Heaney, T. G. Ivanco, and O. Bilgen. Distributed sensing of a cantilever beam and plate using a fiber optic sensing system. *2018 Applied Aerodynamics Conference*, pages 1–28, 2018. doi:10.2514/6.2018-3482.

[53] P. B. Bogert, E. Haugse, B. P. Works, R. E. Gehrki, and L. Martin. Structural shape identification from experimental strains using a modal transformation technique. *Proceedings of the 44th AIAA/ASME/ASCE/AHS Structures, Structural Dynamics and Materials Conference*, pages 1–18, April, 2003.

[54] N. S. Kim and N. S. Cho. Estimating deflection of a simple beam model using fiber optic Bragg-grating sensors. *Experimental Mechanics*, 44(4):433–439, 2004. ISSN 00144851. doi:10.1177/0014485104045431.

[55] S. Rapp, L. H. Kang, J. H. Han, U. C. Mueller, and H. Baier. Displacement field estimation for a two-dimensional structure using fiber Bragg grating sensors. *Smart Materials and Structures*, 18(2), 2009. ISSN 09641726. doi:10.1088/0964-1726/18/2/025006.

[56] R. Glaser, V. Caccese, and M. Shahinpoor. Shape Monitoring of a Beam Structure from Measured Strain or Curvature. *Experimental Mechanics*, 52 (6):591–606, 2012. ISSN 00144851. doi:10.1007/s11340-011-9523-y.

[57] L. H. Kang, D. K. Kim, and J. H. Han. Estimation of dynamic structural displacements using fiber Bragg grating strain sensors. *Journal of Sound and Vibration*, 305(3):534–542, 2007. ISSN 10958568. doi:10.1016/j.jsv.2007.04.037.

[58] C. G. Pak. Wing shape sensing from measured strain. *AIAA Journal*, 54(3): 1064–1073, 2016. ISSN 00011452. doi:10.2514/1.J053986.

[59] C. G. Pak. Shape sensing for wings with spars and ribs using simulated strain. *AIAA Scitech 2019 Forum*, 1:1–22, 2019.

[60] M. A. Davis, A. D. Kersey, J. Sirkis, and E. J. Friebele. Shape and vibration mode sensing using a fiber optic Bragg grating array. *Smart Materials and Structures*, 5(6):759–765, 1996. ISSN 09641726. doi:10.1088/0964-1726/5/6/005.

[61] C. J. Li and A. G. Ulsoy. High-precision measurement of tool-tip displacement using strain gauges in precision flexible line boring. *Mechanical Systems and Signal Processing*, 13(4):531–546, 1999. ISSN 08883270. doi:10.1006/mssp.1999.1223.

[62] H. J. Bang, S. W. Ko, M. S. Jang, and H. I. Kim. Shape estimation and health monitoring of wind turbine tower using a FBG sensor array. *2012 IEEE I2MTC - International Instrumentation and Measurement Technology Conference, Proceedings*, (3):496–500, 2012. doi:10.1109/I2MTC.2012.6229407.

[63] H. I. Kim, L. H. Kang, and J. H. Han. Shape estimation with distributed fiber Bragg grating sensors for rotating structures. *Smart Materials and Structures*, 20(3), 2011. ISSN 09641726. doi:10.1088/0964-1726/20/3/035011.

[64] M. Freydin, M. K. Rattner, D. E. Raveh, I. Kressel, R. Davidi, and M. Tur. Fiber-optics-based aeroelastic shape sensing. *AIAA Journal*, 57(12):5094–5103, 2019. ISSN 00011452. doi:10.2514/1.J057944.

[65] A. Derkevorkian, S. F. Masri, J. Alvarenga, H. Boussalis, J. Bakalyar, and W. L. Richards. Strain-based deformation shape-estimation algorithm for control and monitoring applications. *AIAA Journal*, 51(9):2231–2240, 2013. ISSN 00011452. doi:10.2514/1.J052215.

[66] R. Bruno, N. Toomarian, and M. Salama. Shape estimation from incomplete measurements: A neural-net approach. *Smart Materials and Structures*, 3(2): 92–97, 1994. ISSN 09641726. doi:10.1088/0964-1726/3/2/002.

[67] A. Tessler and J. L. Spangler. A Variational Principle for Reconstruction of Elastic Deformations in Shear Deformable Plates and Shells. *NASA/TM-2003-212445*, 2003.

[68] R.D. Mindlin. Influence of rotatory inertia and shear on flexural motions of isotropic, elastic plates. *J. Appl. Mech.*, 12:31–38, 1951.

[69] A. Tessler and T. J. R. Hughes. A three-node mindlin plate element with improved transverse shear. *Computer Methods in Applied Mechanics and Engineering*, 50(1):71–101, 1985. ISSN 00457825. doi:10.1016/0045-7825(85)90114-8.

[70] A. Kefal, E. Oterkus, A. Tessler, and J. L. Spangler. A quadrilateral inverse-shell element with drilling degrees of freedom for shape sensing and structural health monitoring. *Engineering Science and Technology, an International Journal*, 19(3):1299–1313, 2016. ISSN 22150986. doi:10.1016/j.jestch.2016.03.006. URL http://dx.doi.org/10.1016/j.jestch.2016.03.006.

[71] A. Kefal. An efficient curved inverse-shell element for shape sensing and structural health monitoring of cylindrical marine structures. *Ocean Engineering*, 188:106262, 2019. ISSN 00298018. doi:10.1016/j.oceaneng.2019.106262. URL https://doi.org/10.1016/j.oceaneng.2019.106262.

[72] A. Tessler and T. J. R. Hughes. An improved treatment of transverse shear in the mindlin-type four-node quadrilateral element. *Computer Methods in Applied Mechanics and Engineering*, 39(3):311–335, 1983. ISSN 00457825. doi:10.1016/0045-7825(83)90096-8.

[73] M. Gherlone, P. Cerracchio, M. Mattone, M. Di Sciuva, and A. Tessler. Shape sensing of 3D frame structures using an inverse Finite Element Method. *International Journal of Solids and Structures*, 49(22):3100–3112, 2012. ISSN 00207683. doi:10.1016/j.ijsolstr.2012.06.009. URL http://dx.doi.org/10.1016/j.ijsolstr.2012.06.009.

[74] F. Zhao, L. Xu, H. Bao, and J. Du. Shape sensing of variable cross-section beam using the inverse finite element method and isogeometric analysis. *Measurement: Journal of the International Measurement Confederation*, 158: 107656, 2020. ISSN 02632241. doi:10.1016/j.measurement.2020.107656. URL https://doi.org/10.1016/j.measurement.2020.107656.

[75] K. Chen, K. Cao, G. Gao, and H. Bao. Shape sensing of Timoshenko beam subjected to complex multi-node loads using isogeometric analysis. *Measurement: Journal of the International Measurement Confederation*, 184: 109958, 2021. ISSN 02632241. doi:10.1016/j.measurement.2021.109958. URL https://doi.org/10.1016/j.measurement.2021.109958.

[76] P. Savino, M. Gherlone, and F. Tondolo. Shape sensing with inverse finite element method for slender structures. *Structural Engineering and Mechanics*, 72(2):77–87, 2019. doi:https://dx.doi.org/10.12989/sem.2019.72.2.217.

[77] R. You and L. Ren. An enhanced inverse beam element for shape estimation of beam-like structures. *Measurement: Journal of the International Measurement Confederation*, 181:109575, 2021. ISSN 02632241. doi:10.1016/j.measurement.2021.109575. URL https://doi.org/10.1016/j.measurement.2021.109575.

[78] F. Zhao, H. Bao, J. Liu, and K. Li. Shape sensing of multilayered composite and sandwich beams based on Refined Zigzag Theory and inverse finite element method. *Composite Structures*, 261:113321, 2021. ISSN 02638223. doi:10.1016/j.compstruct.2020.113321. URL https://doi.org/10.1016/j.compstruct.2020.113321.

[79] P. Savino, F. Tondolo, M. Gherlone, and A. Tessler. Application of inverse finite element method to shape sensing of curved beams. *Sensors (Switzerland)*, 20(24):1–16, 2020. ISSN 14248220. doi:10.3390/s20247012.

[80] P. Savino, M. Gherlone, F. Tondolo, and R. Greco. Shape-sensing of beam elements undergoing material nonlinearities. *Sensors (Switzerland)*, 21(2): 1–17, 2021. ISSN 14248220. doi:10.3390/s21020528.

[81] K. Paczkowski and H. R. Riggs. An inverse finite element strategy to recover full-field, large displacements from strain measurements. *Proceedings of the International Conference on Offshore Mechanics and Arctic Engineering - OMAE*, 2:531–537, 2007. doi:10.1115/OMAE2007-29730.

[82] A. Tessler, R. Roy, M. Esposito, C. Surace, and M. Gherlone. Shape Sensing of Plate and Shell Structures Undergoing Large Displacements Using the Inverse Finite Element Method. *Shock and Vibration*, 2018, 2018. ISSN 10709622. doi:10.1155/2018/8076085.

[83] M. Alioli, P. Masarati, M. Morandini, G. L. Ghiringhelli, T. Carpenter, and R. Albertani. Nonlinear membrane inverse finite elements. *AIP Conference Proceedings*, 1648:1–5, 2015. ISSN 15517616. doi:10.1063/1.4912419.

[84] M. Alioli, P. Masarati, M. Morandini, T. Carpenter, N. B. Osterberg, and R. Albertani. Membrane shape and load reconstruction from measurements using inverse finite element analysis. *AIAA Journal*, 55(1):297–308, 2017. ISSN 00011452. doi:10.2514/1.J055123.

[85] M. Gherlone, P. Cerracchio, M. Mattone, M. Di Sciuva, and A. Tessler. Beam shape sensing using inverse finite element method: Theory and experimental validation. *Structural Health Monitoring 2011: Condition-Based Maintenance and Intelligent Structures - Proceedings of the 8th International Workshop on Structural Health Monitoring*, 1:578–585, 2011.

[86] Y. Zhao, J. Du, Q. Xu, and H. Bao. Real-time monitoring of the position and orientation of a radio telescope sub-reflector with fiber bragg grating sensors. *Sensors (Switzerland)*, 19(3), 2019. ISSN 14248220. doi:10.3390/s19030619.

[87] E. J. Miller, R. Manalo, and A. Tessler. Full-Field Reconstruction of Structural Deformations and Loads from Measured Strain Data on a Wing Test Article using the Inverse Finite Element Method. *NASA/TM—2016–219407*, 2016.

[88] A. Kefal, I. E. Tabrizi, M. Tansan, E. Kisa, and M. Yildiz. An experimental implementation of inverse finite element method for real-time shape and strain sensing of composite and sandwich structures. *Composite Structures*, 258: 113431, 2021. ISSN 02638223. doi:10.1016/j.compstruct.2020.113431. URL https://doi.org/10.1016/j.compstruct.2020.113431.

[89] D. Oboe, L. Colombo, C. Sbarufatti, and M. Giglio. Shape Sensing of a Complex Aeronautical Structure with Inverse Finite Element Method. *Sensors*, 21:1388, 2021. doi:https://doi.org/10.3390/s21041388.

[90] P. Cerracchio, M. Gherlone, and A. Tessler. Real-time displacement monitoring of a composite stiffened panel subjected to mechanical and thermal loads. *Meccanica*, 50(10):2487–2496, 2015. ISSN 15729648. doi:10.1007/s11012-015-0146-8.

[91] M. Esposito and M. Gherlone. Composite wing box deformed-shape reconstruction based on measured strains: Optimization and comparison of existing approaches. *Aerospace Science and Technology*, 99:105758, 2020. ISSN 12709638. doi:10.1016/j.ast.2020.105758. URL https://doi.org/10.1016/j.ast.2020.105758.

[92] A. Kefal and E. Oterkus. Displacement and stress monitoring of a Panamax containership using inverse finite element method. *Ocean Engineering*, 119: 16–29, 2016. ISSN 00298018. doi:10.1016/j.oceaneng.2016.04.025. URL http://dx.doi.org/10.1016/j.oceaneng.2016.04.025.

[93] A. Kefal, J. B. Mayang, E. Oterkus, and M. Yildiz. Three dimensional shape and stress monitoring of bulk carriers based on iFEM methodology. *Ocean Engineering*, 147:256–267, 2018. ISSN 00298018. doi:10.1016/j.oceaneng.2017.10.040. URL https://doi.org/10.1016/j.oceaneng.2017.10.040.

[94] M. Esposito and M. Gherlone. Material and strain sensing uncertainties quantification for the shape sensing of a composite wing box. *Mechanical Systems and Signal Processing*, 160:107875, 2021. ISSN 10961216.

doi:10.1016/j.ymssp.2021.107875. URL https://doi.org/10.1016/j.ymssp.2021.107875.

[95] A. Tessler. Structural analysis methods for structural health management of future aerospace vehicles. *Key Engineering Materials*, 347:57–66, 2007. ISSN 16629795. doi:10.4028/0-87849-444-8.57.

[96] S. L. Vazquez, A. Tessler, C. C. Quach, E. G. Cooper, J. Parks, and J. L. Spangler. Structural Health Monitoring Using High-Density Fiber Optic Strain Sensor and Inverse Finite Element Methods. *NASA/TM-2005-213761*, 2005. URL https://ntrs.nasa.gov/search.jsp?R=20050185211.

[97] C. C. Quach, S. L. Vazquez, A. Tessler, J. P. Moore, E. G. Cooper, and J. L. Spangler. Structural anomaly detection using fiber optic sensors and inverse finite element method. *Collection of Technical Papers - AIAA Guidance, Navigation, and Control Conference*, 6:4799–4806, 2005. doi:10.2514/6.2005-6357.

[98] L. Colombo, C. Sbarufatti, and M. Giglio. Definition of a load adaptive baseline by inverse finite element method for structural damage identification. *Mechanical Systems and Signal Processing*, 120:584–607, 2019. ISSN 10961216. doi:10.1016/j.ymssp.2018.10.041. URL https://doi.org/10.1016/j.ymssp.2018.10.041.

[99] M. Li, A. Kefal, B. C. Cerik, and E. Oterkus. Dent damage identification in stiffened cylindrical structures using inverse Finite Element Method. *Ocean Engineering*, 198:106944, 2020. ISSN 00298018. doi:10.1016/j.oceaneng.2020.106944. URL https://doi.org/10.1016/j.oceaneng.2020.106944.

[100] M. Li, A. Kefal, E. Oterkus, and S. Oterkus. Structural health monitoring of an offshore wind turbine tower using iFEM methodology. *Ocean Engineering*, 204:107291, 2020. ISSN 00298018. doi:10.1016/j.oceaneng.2020.107291. URL https://doi.org/10.1016/j.oceaneng.2020.107291.

[101] A. Kefal, I.E. Tabrizi, and M. Yildiz. Real-Time monitoring of crack propagation in fiber-reinforced composite plates using iFEM methodology. *Developments in the Analysis and Design of Marine Structures*, pages 345–353, 2021. doi:10.1201/9781003230373-40.

[102] A. Kefal and A. Tessler. Delamination damage identification in composite shell structures based on Inverse Finite Element Method and Refined Zigzag Theory. *Developments in the Analysis and Design of Marine Structures*, pages 354–363, 2021. doi:10.1201/9781003230373-41.

[103] L. Colombo, D. Oboe, C. Sbarufatti, F. Cadini, S. Russo, and M. Giglio. Shape sensing and damage identification with iFEM on a composite structure subjected to impact damage and non-trivial boundary conditions. *Mechanical Systems and Signal Processing*, 148:107163, 2021. ISSN 10961216.

doi:10.1016/j.ymssp.2020.107163. URL https://doi.org/10.1016/j.ymssp.2020.107163.

[104] U. Papa, S. Russo, A. Lamboglia, G. Del Core, and G. Iannuzzo. Health structure monitoring for the design of an innovative UAS fixed wing through inverse finite element method (iFEM). *Aerospace Science and Technology*, 69:439–448, 2017. ISSN 12709638. doi:10.1016/j.ast.2017.07.005. URL http://dx.doi.org/10.1016/j.ast.2017.07.005.

[105] M. Li, Z. Wu, D. Jia, S. Qiu, and W. He. Structural damage identification using strain mode differences by the iFEM based on the convolutional neural network (CNN). *Mechanical Systems and Signal Processing*, 165:108289, 2022. ISSN 10961216. doi:10.1016/j.ymssp.2021.108289. URL https://doi.org/10.1016/j.ymssp.2021.108289.

[106] A. Kefal, C. Diyaroglu, M. Yildiz, and E. Oterkus. Coupling of peridynamics and inverse finite element method for shape sensing and crack propagation monitoring of plate structures. *Computer Methods in Applied Mechanics and Engineering*, 391, 2022. ISSN 00457825. doi:10.1016/j.cma.2021.114520.

[107] A. Kefal and M. Yildiz. Modeling of sensor placement strategy for shape sensing and structural health monitoring of a wing-shaped sandwich panel using inverse finite element method. *Sensors (Switzerland)*, 17(12), 2017. ISSN 14248220. doi:10.3390/s17122775.

[108] M. Esposito and M. Gherlone. Composite wing box deformed-shape reconstruction based on measured strains: Optimization and comparison of existing approaches. *Aerospace Science and Technology*, 99:105758, 2020. ISSN 12709638. doi:10.1016/j.ast.2020.105758. URL https://doi.org/10.1016/j.ast.2020.105758.

[109] Y. Zhao, J. Du, H. Bao, and Q. Xu. Optimal Sensor Placement for Inverse Finite Element Reconstruction of Three-Dimensional Frame Deformation. *International Journal of Aerospace Engineering*, 18, 2018. ISSN 16875974. doi:10.1155/2018/6121293.

[110] Y. Zhao, J. Du, H. Bao, and Q. Xu. Optimal sensor placement based on eigenvalues analysis for sensing deformation of wing frame using iFEM. *Sensors (Switzerland)*, 18(8), 2018. ISSN 14248220. doi:10.3390/s18082424.

[111] A. Tessler, H. R. Riggs, and S. C. Macy. A variational method for finite element stress recovery and error estimation. *Computer Methods in Applied Mechanics and Engineering*, 111(3-4):369–382, 1994. ISSN 00457825. doi:10.1016/0045-7825(94)90140-6.

[112] A. Kefal, I. Emami, M. Yildiz, and A. Tessler. A smoothed iFEM approach for efficient shape-sensing applications : Numerical and experimental validation on composite structures. *Mechanical Systems and Signal Processing*, 152: 107486, 2021. ISSN 0888-3270. doi:10.1016/j.ymssp.2020.107486. URL https://doi.org/10.1016/j.ymssp.2020.107486.

[113] D. Oboe, L. Colombo, C. Sbarufatti, and M. Giglio. Comparison of strain pre-extrapolation techniques for shape and strain sensing by iFEM of a composite plate subjected to compression buckling. *Composite Structures*, 262:113587, 2021. ISSN 02638223. doi:10.1016/j.compstruct.2021.113587. URL https://doi.org/10.1016/j.compstruct.2021.113587.

[114] S. Timoshenko. *Strength of Materials*. Van Nostrand Company Inc, Princeton, USA, 1956.

[115] V. Z. Vlasov. *Thin-Walled Elastic Beams*. Fizmatgiz, Moscow, 1959.

[116] S. P. Timoshenko. Theory of bending, torsion and buckling of thin-walled members of open cross section. *Journal of the Franklin Institute*, 239 (3):201–219, 1945. ISSN 0016-0032. doi:https://doi.org/10.1016/0016-0032(45)90093-7. URL https://www.sciencedirect.com/science/article/pii/0016003245900937.

[117] H. R. Riggs, A. Tessler, and H. Chu. C1-continuous stress recovery in finite element analysis. *Computer Methods in Applied Mechanics and Engineering*, 143 (3-4):299–316, 1997. ISSN 00457825. doi:10.1016/S0045-7825(96)01151-6.

[118] A. Tessler, H. R. Riggs, and M. Dambach. Novel four-node quadrilateral smoothing element for stress enhancement and error estimation. *Collection of Technical Papers - AIAA/ASME/ASCE/AHS/ASC Structures, Structural Dynamics and Materials Conference*, 1:124–136, 1998. ISSN 02734508. doi:10.2514/6.1998-1713.

[119] F. W. Billmeyer. *Textbook of Polymer Science*. John Wiley & Sons, New York, USA, 1984.

[120] S. P. Timoshenko and J. N. Goodier. *Theory of Elasticity*. McGraw–Hill, New York, USA, 1970.

[121] C. Y. Wang. Exact torsion solutions for certain airfoil shapes. *AIAA Journal*, 55(12), 2017.

[122] J. B. Kosmatka. Flexure-torsion behavior of prismatic beams, part i: Section properties via power series. *AIAA Journal*, 31(1):170–179, 1993. doi:doi:10.2514/3.11334.

[123] A. Carpinteri. *Structural Mechanics Fundamentals*. CRC Press, FL, USA, 2013.

Appendix A

Element Shape Functions

A.1 Euler-Bernoulli Beam Element

The shape functions for the iEB2 element defined as a function of the axial coordinate, $x \in [0, L_e]$,

$$\begin{aligned} L_1(x) &= 1 - \frac{x}{L_e} & L_2(x) &= \frac{x}{L_e} \\ M_1(x) &= 1 - \frac{3x^2}{L_e^2} + \frac{2x^3}{L_e^3} & M_2(x) &= x - \frac{2x^2}{L_e} + \frac{x^3}{L_e^2} \\ M_3(x) &= \frac{3x^2}{L_e^2} - \frac{2x^3}{L_e^3} & M_4(x) &= -\frac{x^2}{L_e} + \frac{x^3}{L_e^2} \end{aligned} \tag{A.1}$$

where L_e is the element length, and $x = 0$, and $x = L_e$ represents the element limits.

A.2 Timoshenko Beam Element

The shape functions for the iTM2D0 and iTM2D1 elements are defined in the element natural coordinates,$\eta \in [-1, 1]$, and are stated below.

The Lagrange polynomial of order-1:

$$L_1^{(1)}(\eta) = \frac{1}{2}(1-\eta) \qquad L_2^{(1)}(\eta) = \frac{1}{2}(1+\eta) \tag{A.2}$$

The Lagrange polynomial of order-2:

$$L_1^{(2)}(\eta) = \frac{1}{2}\eta(\eta-1) \qquad L_r^{(2)}(\eta) = (1-\eta^2) \qquad L_2^{(2)}(\eta) = \frac{1}{2}\eta(\eta+1) \tag{A.3}$$

The Lagrange polynomial of order-4:

$$\begin{aligned} L_1^{(4)}(\eta) &= \frac{1}{6}\eta(4\eta^2-1)(\eta-1) \qquad L_q^{(4)}(\eta) = \frac{4\eta}{3}(1-\eta^2)(2\eta-1) \\ L_r^{(4)}(\eta) &= (1-\eta^2)(1-4\eta^2) \\ L_s^{(4)}(\eta) &= \frac{4\eta}{3}(1-\eta^2)(2\eta+1) \qquad L_2^{(4)}(\eta) = \frac{1}{6}\eta(4\eta^2-1)(\eta+1) \end{aligned} \tag{A.4}$$

Anisoparametric interpolations for the iTM2D0 element [73]:

$$\begin{aligned} N_1^{(3)}(\eta) &= \frac{L_e}{24}(1-\eta^2)(2\eta-3) \qquad N_r^{(3)}(\eta) = -\frac{L_e}{6}\eta(1-\eta^2) \\ N_2^{(3)}(\eta) &= \frac{L_e}{24}(1-\eta^2)(2\eta+3) \end{aligned} \tag{A.5}$$

Anisoparametric interpolations for the iTM2D1 element [73]:

$$\begin{aligned} M_1^{(3)}(\eta) &= \frac{4}{3L_e}(1-\eta^2)(4\eta-3) \qquad M_q^{(3)}(\eta) = -\frac{8}{3L_e}(1-\eta^2)(8\eta-3) \\ M_r^{(3)}(\eta) &= \frac{32}{L_e}(1-\eta^2)\eta \\ M_s^{(3)}(\eta) &= -\frac{8}{3L_e}(1-\eta^2)(8\eta+3) \qquad M_2^{(3)}(\eta) = \frac{4}{3L_e}(1-\eta^2)(4\eta+3) \end{aligned} \tag{A.6}$$

Appendix B

Numerical Estimation of Transverse Shear Strain

This section provides a detailed explanation of the calculation of shear functions, $\{f_1, f_2, f_3\}$, and coefficients, $\{k_{ty}, k_{\varepsilon y}, k_{tz}, k_{\varepsilon z}\}$, introduced in Section 2.1.2. These quantities are estimated using results from a high-fidelity FEM model of the structure in Section B.1, and other numerical or analytical strategies that can be used are summarised in Section B.2.

B.1 Estimation using a FEM Model

The estimation of shear functions and coefficients using FEM results is demonstrated for the case of a prismatic airfoil beam with a NACA 0016 airfoil profile, similar to the one analysed in Section 3.1. The beam is 20 m long with a chord length of 1 m. It is clamped at the root and loaded by concentrated forces at the tip. A high-fidelity FEM model of the beam is developed in ABAQUS, with 8490 C3D8R (linear brick) elements per cross-section and 100 elements along the beam length. Discretisation of the solid beam cross-section is shown in Figure B.1.

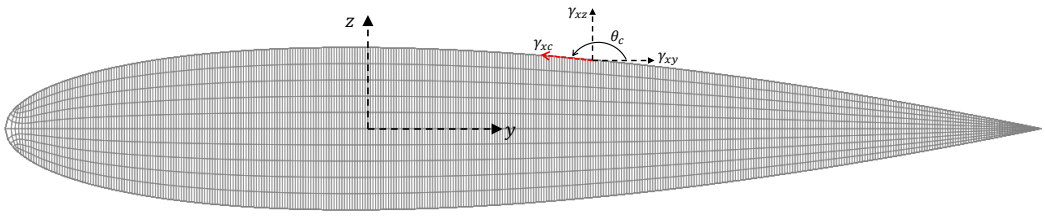

Fig. B.1 FEM element discretisation of the solid NACA 0016 airfoil beam cross-section

Similarly, thin-walled beam models are discretised using the four-node shell elements (S4R) and utilise 150 shell elements along the beam length. The number of element divisions per cross-section (or along the thin-walled profile) and along the beam length for both solid and thin-walled beams are reported in Tables B.1 and B.2, respectively.

Table B.1 FEM element discretization details of the solid beam models

	Element Discretisation		
NACA Profile	per cross-section	per beam length	Total
0016	8490	100	849000
6516	8710	100	871000

Table B.2 FEM element discretization details of the thin-walled beam models ($t = 5$ mm)

	Element Discretisation		
NACA Profile	along profile	per beam length	Total
0016	4828	150	724200
6516	4495	150	674250

For calculating shear function, f_1, and coefficients, $\{k_{tz}, k_{\varepsilon z}\}$, the FEM beam model is subjected to a unit tip load along the z-axis, and numerical stresses and strains are extracted at all elements of the mid-beam cross-section. Undesired contributions due to end effects, such as beam clamping or loading, are avoided by considering elements at the mid-beam section. The stresses and strains are extracted at the centroid of each element with the assumption that they are a constant within each element. The total shear strain energy per unit length is calculated by integrating the product of shear stresses and strains over the entire beam cross-section,

$$\begin{aligned} \phi_{SE}^{FE} &= \frac{1}{2}\int_{A_b} (\tau_{xz}^{FE}\gamma_{xz}^{FE} + \tau_{xy}^{FE}\gamma_{xy}^{FE})dA \\ &= \sum_{i=1}^{N_e} (\tau_{xz}\gamma_{xz} + \tau_{xy}\gamma_{xy})_i A_i^e \end{aligned} \tag{B.1}$$

where, A_b is the area of the beam cross-section, N_e is the total number of cross-sectional elements, A_i^e is the projected area of each element, i, and $\{\tau_{xz}, \gamma_{xz}, \tau_{xy}, \gamma_{xy}\}_i$ are the transverse shear strains and stresses extracted at the element centroid.

For any node, j, lying on the perimeter of the beam section, the tangential shear strain can be calculated as,

$$(\gamma_{xc})_j = (\gamma_{xy})_j \cos((\theta_c)_j) + (\gamma_{xz})_j \sin((\theta_c)_j) \tag{B.2}$$

where, θ_c at a node is the angle between the horizontal and the local tangent as shown in Fig. B.1. Iterating through all the discrete nodes along the perimeter, a continuous variation of γ_{xc} is estimated as a function of c (using a suitable Fourier series or polynomial function),

$$\gamma_{xc}(c) = \gamma_{xy}(c)\cos(\theta_c(c)) + \gamma_{xz}(c)\sin(\theta_c(c)) \tag{B.3}$$

and the maximum of Eq. B.3 represents the tangential shear strain maxima for a transverse load along the z-axis,

$$\gamma^z_{xc,max} = \gamma_{xc}(c)|_{max} \tag{B.4}$$

Using Eqs. B.1 and B.4, the shear coefficients, $\{k_{tz}, k_{\varepsilon z}\}$ can be calculated using Eqs. 2.30 and 2.32. The variation function, $f_1(c)$, is obtained by rewriting Eqs. B.3 as,

$$\gamma_{xc}(c) = \gamma^z_{xc,max} f_1(c) \tag{B.5}$$

A similar process can be used to calculate coefficients, $\{k_{ty}, k_{\varepsilon y}\}$ and function, $f_2(c)$, using a FEM beam model with a unit tip load along the y-axis. For this case, use of Eq. B.3 results in,

$$\gamma_{xc}(c) = \gamma^y_{xc,max} f_2(c) \tag{B.6}$$

To calculate the function, $f_3(c)$, a unit torsional strain is applied at the tip of the FEM beam model. For this case, use of Eq. B.3 results in,

$$\gamma_{xc}(c) = f_3(c) \tag{B.7}$$

For the NACA 0016 airfoil profile discussed in this section, the shear coefficients and functions calculated using the above procedure are provided in Tables B.3 and B.4, respectively. A similar procedure is used to compute these quantities for other solid and thin-walled, symmetric, and cambered airfoil profiles. These details are also reported in the following tables.

Table B.3 Shear coefficients computed for some airfoil beam profiles analysed in Chapter 3 (the thin-walled sections have a wall thickness of 5 mm)

NACA Profile	Section Type	k_{ty}	k_{tz}	$k_{\varepsilon y}$	$k_{\varepsilon z}$
0016	Solid	0.91	0.31	0.84	1.24
0016	Thin-walled	0.75	0.03	0.85	3.93
6516	Solid	1.01	0.28	0.81	1.15
6516	Thin-walled	0.83	0.03	0.73	3.06

Table B.4 The shear function for the solid NACA 0016 airfoil profile

Profile	f_1	f_2	f_3
NACA 0016	$\sin\left(\frac{3}{2}\pi\frac{c}{p}\right)$	$\sin\left(\pi\frac{c}{p}\right)$	$0.9\sin(2.3c+0.4)+0.24\sin(12.6c-1.6)$

B.2 Alternate Numerical and Analytical Methods

The previous section described the estimation of shear coefficients and functions using a high fidelity 3D FEM model of the beam. A key drawback of this approach is the high computational cost due to the high fidelity discretisation used. In this context, alternative analytical and numerical approaches offering similar accurate solutions at lower computational cost are discussed.

An analytical solution of transverse shear strain for the bending or torsion of a prismatic beam can be derived based on the theory of elasticity. The torsion problem can be solved using Saint-Venant's Semi-Inverse Method, by considering the axial displacement to be a function of the warping function, $\psi(y,z)$. The warping function is described in terms of a stress function,$\Phi(y,z)$, satisfying the Poisson's equation,

$$\Phi_{,yy}+\Phi_{,zz}=-2G\theta_{x,x} \tag{B.8}$$

where G is the shear modulus of the beam. The Semi-Inverse Method can also be applied for beam bending problems, with an assumption regarding the stress distribution across the beam. The shear stresses can be represented using a suitable stress function, satisfying the equilibrium equations, boundary conditions, and compatibility conditions. However, closed-form solutions for Saint-Venant's bending and torsion problems exist only for a few sections (e.g., circle or rectangle [120]). Due to this difficulty, numerical and semi-analytical methods are considered for more general beam profiles.

For the torsional problem of Eq. B.8, a specific definition of the stress function can be used to achieve closed-form solutions for a specific family of airfoils. Wang [121] defined the stress function using specific terms of a power series,

$$\Phi = G\theta_{x,x}\Big(-\frac{y^2+z^2}{2} + a_0 + a_2(y^2-z^2) + a_4(y^4 - 6y^2z^2 + z^4)\Big) \tag{B.9}$$

where the values for a_0, a_2, and a_4 are chosen such that Eq. B.8 is satisfied, and the condition, $\Phi = const = 0$, defines the boundary of the profile. A suitable choice of a_0, a_2, and a_4 can lead to the boundary representing a family of airfoils. The sole limitation is that these closed-form solutions for a function, f_3, are only available for specific symmetric airfoil profiles, and hence the method is not generalisable.

Kosmatka [122] describes another approach, based on power series, for solving both bending and torsion problems. In this case, the warping function is defined as a double power series represented in terms of the coordinates of the beam profile,

$$\psi(y,z) = \sum_{m=0}^{\infty}\sum_{n=0}^{\infty} C_{mn} y^m z^n \tag{B.10}$$

where the total warping function, ψ, is a linear combination of warping contributions due to beam bending and torsion, and coefficients, C_{mn}, are calculated using the principle of minimum potential energy. A numerical implementation of this approach requires a discretisation of the beam area using a series of finite elements, where the equations are solved for each element. All the shear coefficients and functions can be computed using this approach, with the additional advantage of applicability to any general beam cross-section.

For the specific case of closed thin-walled beam profiles undergoing torsion-less bending, the Jourawski formula [123] offers a way to compute functions,$\{f_1, f_2\}$. An advantage of this approach is that relatively simple and complex (e.g., multiply connected sections) thin-walled beams can be analysed. However, the results are constrained by the initial assumptions made, and hence more accurate solutions are obtained for profiles with smaller wall thickness. A further simplification can be made in the case of a thin-walled beam for computing $f_3(c)$ when the wall thickness tends to zero ($t \to 0$). For such profiles, the through-thickness variation of shear strain can be considered uniform with a value equal to that along the center-line [123], and the product of tangential shear strain along the section wall, $f_3(c)$, and the wall thickness, $t(c)$, is a constant. Hence, for a thin-walled section with a uniform wall thickness, the function, $f_3(c)$, can be considered a constant.

Although some analytical and numerical techniques have been described above, this list is by no means exhaustive, and other suitable methods might also be available in the literature. For the case of the NACA 0016 airfoil profile, the results using these strategies are compared and plotted in Fig. B.2. Results are similar, except

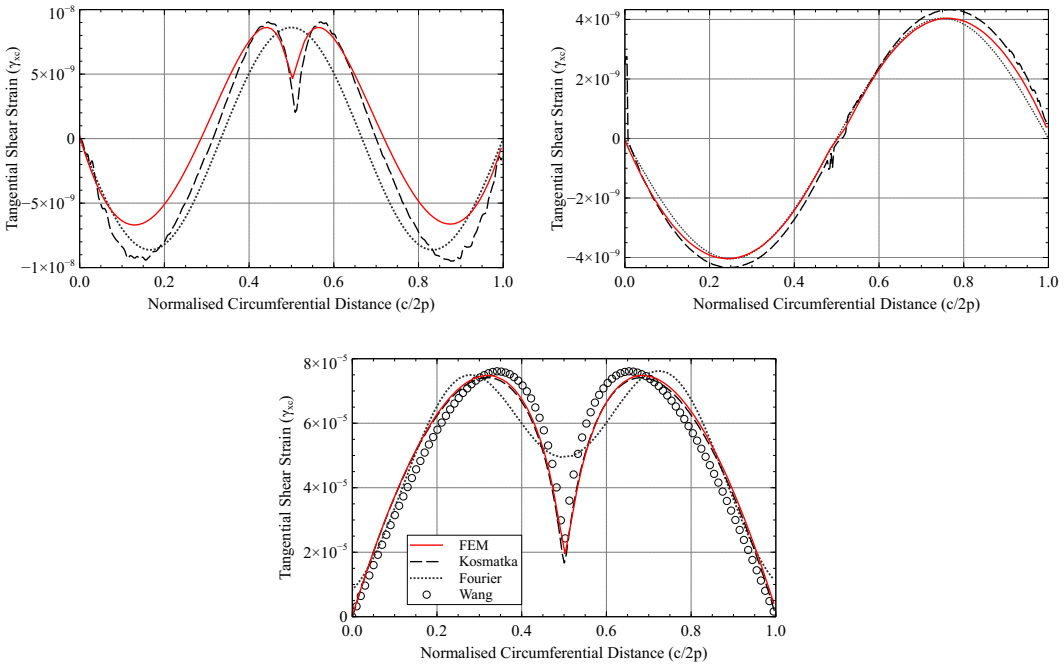

Fig. B.2 Tangential shear strain variation for a solid NACA 0016 airfoil profile corresponding to: (a) transverse load along x-axis, (b) transverse load along y-axis, and (c) torsional strain about z-axis, computed using the different methods

for those using the Fourier series approximation. Similar results are also observed for different airfoil beams profiles and for the evaluation of the shear coefficients as well.

For the numerical problems of Chapter 3, FEM results are used to compute the shear coefficients (reported in Table B.3). The variation functions $\{f_1, f_2, f_3\}$, are evaluated using a combination of methods because the FEM results do not provide a direct analytical expression. Instead, a Fourier series expansion is required to fit the data, leading to potential inaccuracies. For all solid airfoil beam problems of Chapter 3, functions, f_1 and f_2, are computed using the numerical approach of Kosmatka [122] and the torsion function,f_3, using the analytical approach of Wang [121]. For thin-walled beams, the Jourawski formula is used for computing functions,$\{f_1, f_2\}$, and a constant variation of f_3 is assumed (corroborated by FEM results). As no one method is ideal for all problems, depending on the beam geometry, the method offering the greatest ease of application, without depreciating accuracy, is used.

Appendix C

Computing Virtual Strain Data

C.1 Virtual Sensor Expansion using the 2D SEA

Smoothing or expanding the in-situ strain measures for the reduced sensor patterns of Section 4.1.2 is performed using the three-node smoothing element (SEA3) developed by Tessler et al. [111]. Independent SEA3 meshes are used for smoothing the strains along each sensor path (along the plate length, width, and diagonals), and the elements used are arranged in a cross-diagonal pattern. Each mesh is designed based on the specific distribution of sensors along each path, i.e., along the plate length, the SEA3 mesh is finer closer to the clamped end, while along the plate width and diagonals, a uniform mesh is used. These elements are robust enough to produce accurate results even when some elements of the mesh do not have in-situ strain data. The smoothed strains are computed at all inverse element centroids corresponding to the instrumented elements in CFG-B.

The smoothed strain fields are compared against reference FEM strains to assess their feasibility as accurate substitutes for in-situ strain measurements on the plate. These comparisons are made using line plots along sections C-C' and D-D' (defined in Fig. C.2). These results (normalized with respect to the maximum FEM curvature along each path), are presented in Sections C.1.1 and C.1.2.

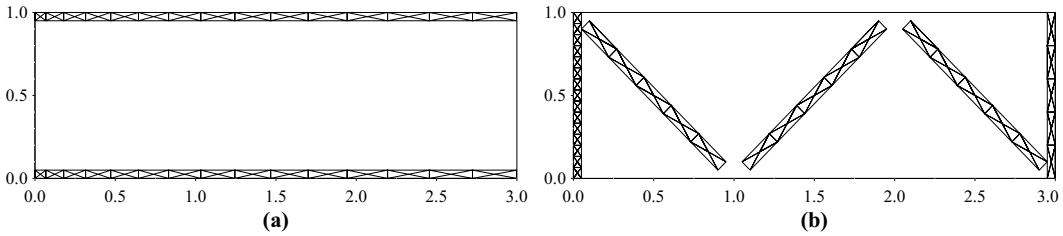

Fig. C.1 The SEA3 meshes used for expanding the measured in-situ strain data

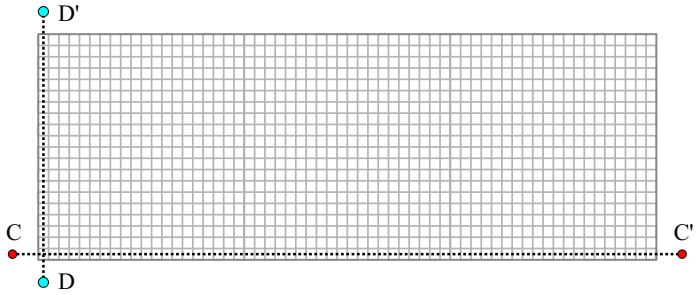

Fig. C.2 The sections along which the 2D SEA results are reported

The SEA results for modes 5 and 6 are shown in Figs. C.3 and C.4, respectively, and the maximum percentage error along each section are reported in Tables C.1 and C.2. The results are accurate, with an average error of less than 5% over the majority of the sensor paths.

Local high error peaks are observed close to the plate tip, as the SEA3 mesh used and the number of sensors used along the plate length is coarser towards the plate tip, and near the plate corners at the clamped end, as the curvature distribution is quite complex along the clamped, which necessitated the very fine mesh used.

The accuracy of the smoothing results corresponds well with the number of sensors used, with R1 results more accurate than R2 and R3. Overall, these results are deemed to be very accurate substitutes for in-situ strains in the iFEM analysis.

Table C.1 Percentage error in SEA results along each section for Mode 5

Variable	Section C-C'			Section D-D'		
	R1	R2	R3	R1	R2	R3
$\kappa_x^{err}\|_{max}$	1.12%	2.29%	2.29%	0.14%	0.14%	0.14%
$\kappa_{xy}^{err}\|_{max}$	0.40%	1.10%	-	5.15%	5.15%	5.15%
$\kappa_y^{err}\|_{max}$	4.23%	8.51%	-	4.50%	4.50%	4.50%

Table C.2 Percentage error in SEA results along each section for Mode 6

Variable	Section C-C'			Section D-D'		
	R1	R2	R3	R1	R2	R3
$\kappa_x^{err}\|_{max}$	1.01%	3.94%	3.94%	0.14%	0.14%	0.14%
$\kappa_{xy}^{err}\|_{max}$	0.71%	1.55%	-	3.63%	3.63%	3.63%
$\kappa_y^{err}\|_{max}$	1.35%	5.88%	-	3.94%	3.94%	3.94%

C.1.1 Results for Mode 5

The virtual sensor expansion results for Mode 5, along sections C-C' and D-D', are compared against reference FEM results and shown in Fig. C.3.

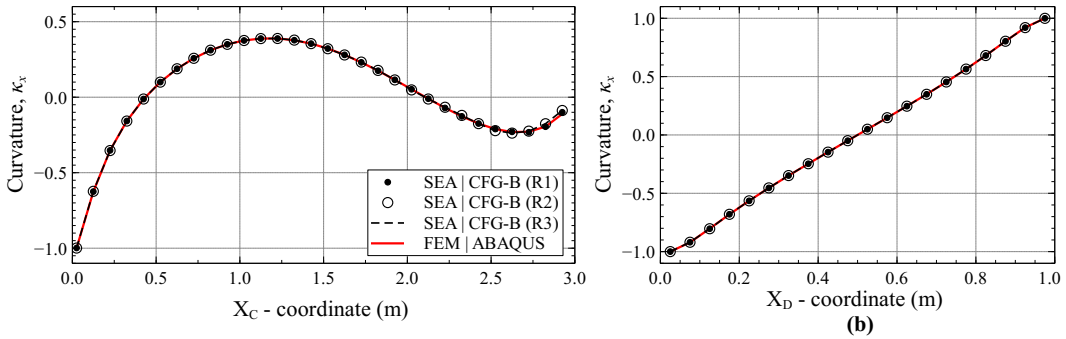

(a) Line plots of curvature, κ_x, along section C-C' and D-D'

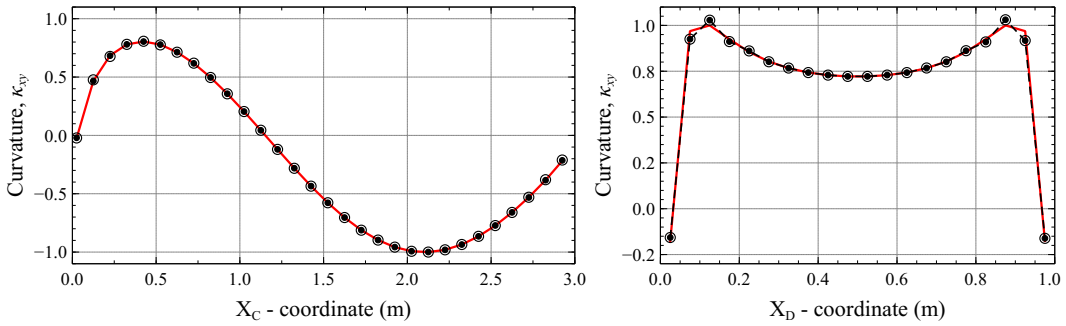

(b) Line plots of curvature, κ_{xy}, along section C-C' and D-D'

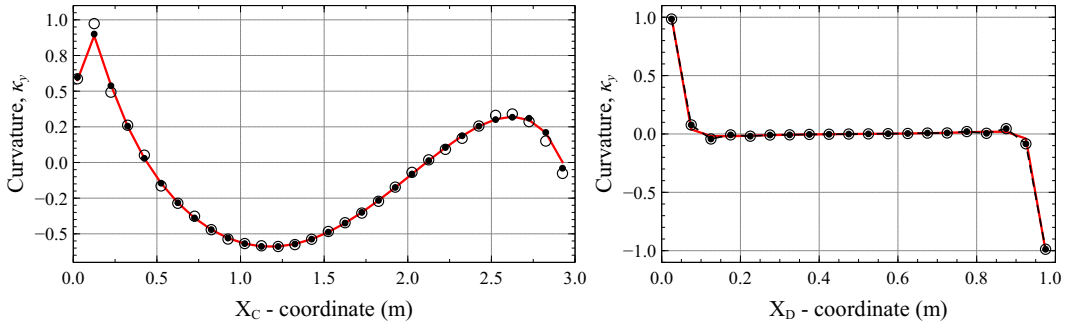

(c) Line plots of curvature, κ_y, along section C-C' and D-D'

Fig. C.3 Line plots of SEA smoothed curvatures for Mode 5 using in-situ strain measurements corresponding to the reduced sensor patterns

C.1.2 Results for Mode 6

The virtual sensor expansion results for Mode 6, along sections C-C' and D-D', are compared against reference FEM results and shown in Fig. C.4.

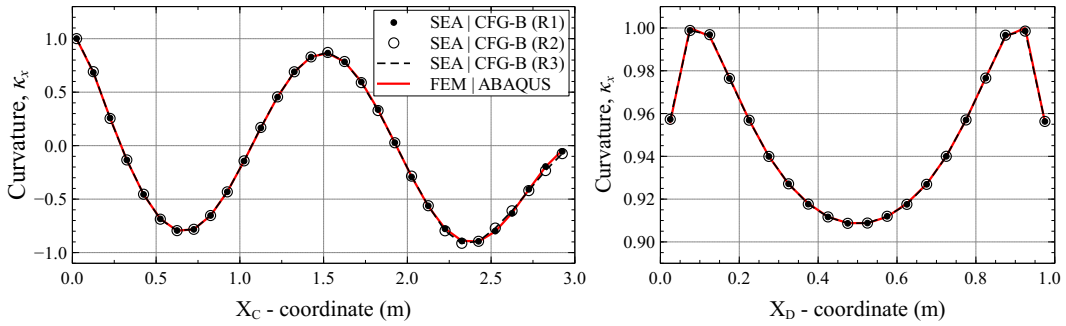

(a) Line plots of curvature, κ_x, along section C-C' and D-D'

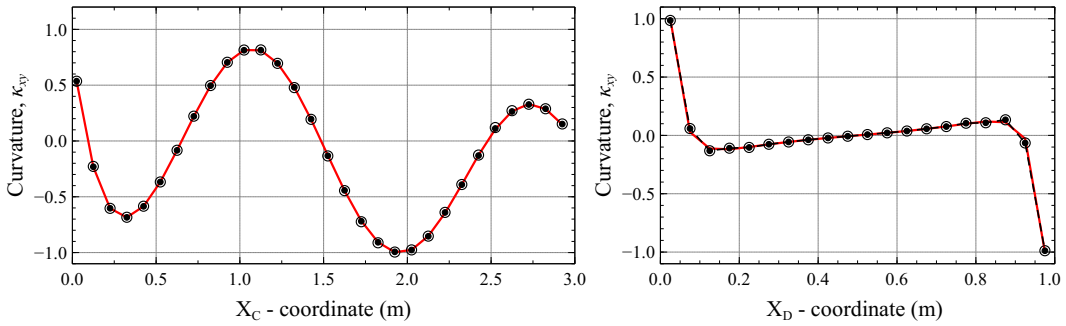

(b) Line plots of curvature, κ_{xy}, along section C-C' and D-D'

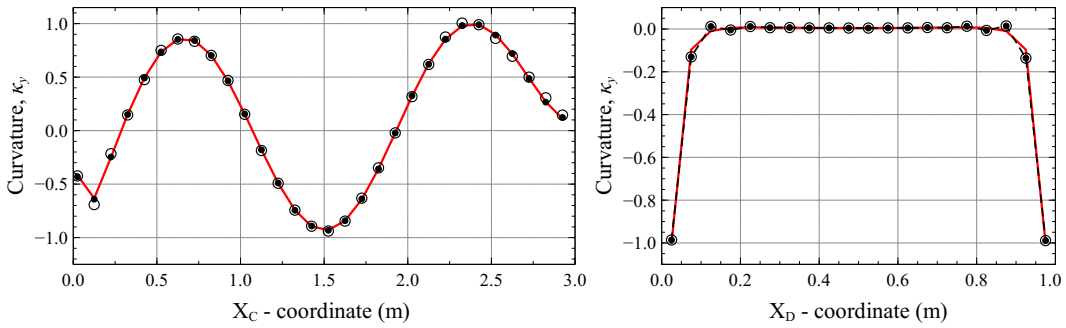

(c) Line plots of curvature, κ_y, along section C-C' and D-D'

Fig. C.4 Line plots of SEA smoothed curvatures for Mode 6 using in-situ strain measurements corresponding to the reduced sensor patterns

C.2 Reduced Patterns: Reconstructed Rotations

(a) Contour plot of rotation, θ_x, for Mode 5

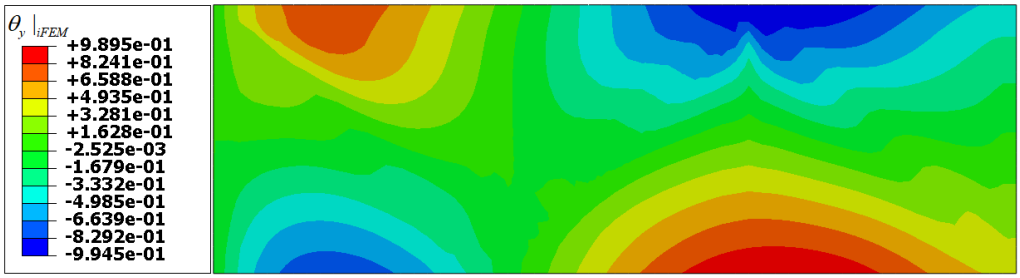

(b) Contour plot of rotation, θ_y, for Mode 5

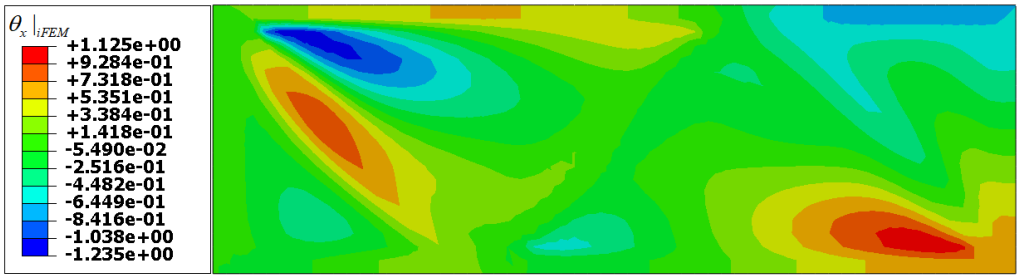

(c) Contour plot of rotation, θ_x, for Mode 6

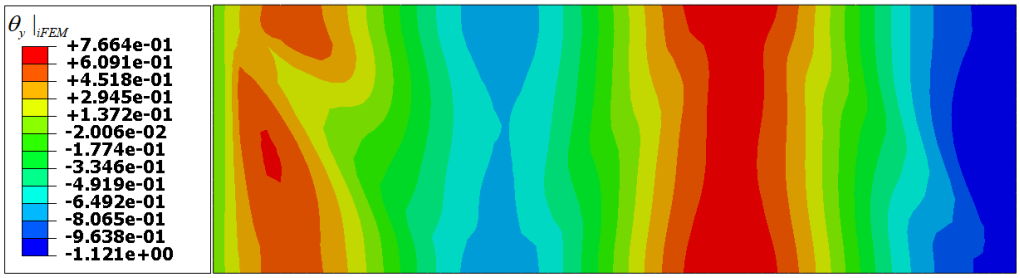

(d) Contour plot of rotation, θ_y, for Mode 6

Fig. C.5 The contour plots of iFEM reconstructed rotations for modes 5 and 6 using the R3 sensor pattern

C.3 Virtual Sensor Expansion using the 1D SEA

The in-situ strain measurements alone were insufficient to produce accurate iFEM results for the two FOSS-based patterns. Hence, an expansion of the in-situ strains is proposed for each case to achieve a final strain data set approaching the benchmark case. The 1D SEA is the expansion strategy used, and its application to the in-situ strains of CFG-2 is described in this section.

The smoothing strategy for CFG-2 is shown in Fig. C.6. Two horizontal and three vertical smoothing lines are used, lying along those sensor paths having elements not instrumented with sensors. Along each smoothing line, multiple 1D elements are used, with at least one in-situ strain data point per element. As CFG-2 measures all three components of in-plane strain at an element centroid, all three components are also expanded. Although the SEA results are not presented here, they were observed to be sufficiently accurate and hence used as input for the iFEM analysis.

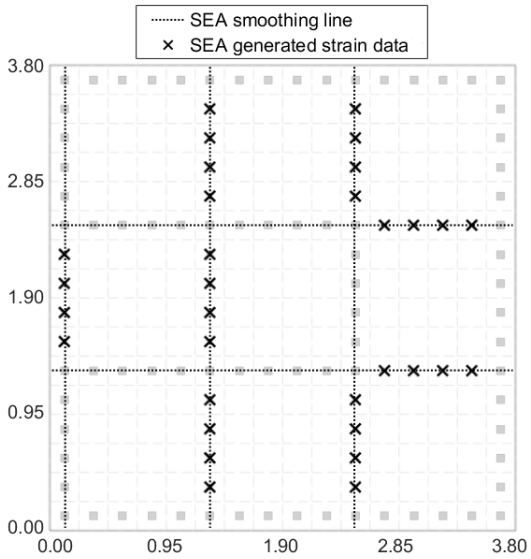

Fig. C.6 The smoothing lines used for expanding the in-situ strains of CFG-2; the in-situ and expanded strain locations are also shown

A similar strain expansion is performed for CFG-1 as well. However, in this case, a limitation is the lack of in-plane shear strain measurements. This is solved by assuming the in-plane shear strain to be a constant throughout the plate. This constant value is computed by introducing a few strain rosettes at discrete locations of the plate and computing the average of their in-plane shear measurements. This strategy presented a convenient solution for the present problem, where the plate is under relatively simple in-plane loading. For more complex problems, this assumption is likely to produce highly inaccurate results.

Appendix D

Analytical Equations for an Imperfectly Clamped Beam

This section presents the derivation of the analytical equations for the imperfectly clamped experimental airfoil beam of Section 5.2.2. Considering a thin beam of length L, having a section with the second moment inertia about the y-axis, I_{yy}, and made of a material with Young's modulus, E. The beam root is not completely fixed, but due to the nature of the imperfect clamp, it induces a resultant elastic rigid body rotation to the entire beam. This support condition at the beam root is modelled as a pinned support connected with a torsional spring of stiffness, K. Similar to the experimental load conditions, the beam is loaded at the tip by concentrated force F along the negative z-axis.

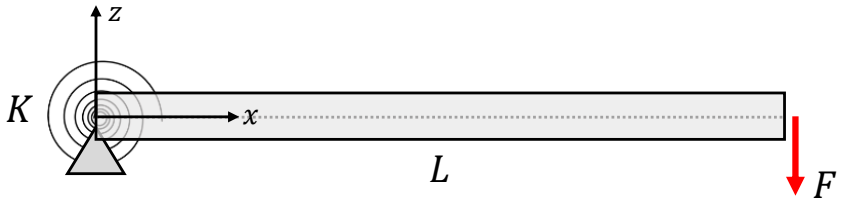

Fig. D.1 Illustration of the imperfectly clamped beam; it is pinned at the root and connected by a torsional spring

The analytical equations for beam deformation can be derived based on the assumptions of the Euler-Bernoulli beam theory. For a thin beam undergoing pure bending, the resultant bending moments and transverse deflection can be related as,

$$M_y = EI_{yy}\frac{\partial^2 w}{\partial x^2} \tag{D.1}$$

Due to the concentrated load at the tip, the bending moment variation along the beam length is linear. Substituting this in Eq. D.1 we get,

$$-F(L-x) = EI_{yy}\frac{\partial^2 w}{\partial x^2} \tag{D.2}$$

Integrating Eq. D.2, we get the variation of transverse deflection along the beam length,

$$w(x) = -\frac{FL}{2EI_{yy}}x^2 + \frac{F}{6EI_{yy}}x^3 + c_1 x + c_2 \tag{D.3}$$

Constants c_1 and c_2 can be solved by applying the boundary conditions.
Boundary condition-1: $w(0) = 0$,

$$w(0) = c_2 = 0 \tag{D.4}$$

Boundary condition-2: $\frac{\partial w}{\partial x}(0) = \frac{FL}{K}$,

$$c_1 = -\frac{FL}{K} \tag{D.5}$$

Substituting Eqs. D.4 and D.5 in Eq. D.3, the final deflection field of the beam can be written as,

$$w(x) = -\frac{FL}{2EI_{yy}}x^2 + \frac{F}{6EI_{yy}}x^3 - \frac{FL}{K}x \tag{D.6}$$